Development and Application of Magnetic Modelling to the Design of Power Devices

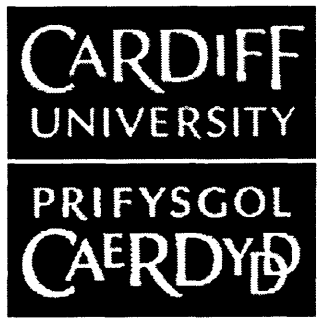

Aghuinyue Esaindang Umenei

Wolfson Magnetics Research,

School of Engineering,

Cardiff University.

A thesis submitted for a degree of

Doctor of Philosophy

September 27th , 2010.

Project Sponsored by Zenergy Power Inc.

ProQuest LLC
789 East Eisenhower Parkway
P.O. Box 1346
Ann Arbor, MI 48106-1346

Acknowledgements

'I can do all things through Christ which strengtheneth me 'Phillipians 4:13 (KJV)

I thank God for the grace, opportunities and gifts that have enabled me to come this far. Without Him, I really can do nothing. I never have been perfect, but I have always tried to live with, and for Him.

Special thanks to my supervisor Dr. Yevgen Melikhov, for always being there with a patient answer and an insightful solution to my endless and sometimes unnecessary questioning. I owe a lot of what I know in this line of science to your acumen and guidance. I say thanks to Prof. D.C. Jiles for giving me perspective and keeping me scientific and professional.

A lot of my gratitude goes to Zenergy Power Inc. for providing the funding for this research project, and providing all the data and support I needed. To Franco, Bert and Dr. Darmann, I say, thanks for your help and support.

I will forever be grateful to my Mom and Dad, Rev. and Mrs. Umenei for the sacrifices they have made all through, both financially and otherwise to see that I became the best I could be. There's no way that I could pay you back, but my plan is to show you that I understand –you're appreciated. To my brother and friend Fon; my sister and literary counterpart Navoma; my sister and like-minded world citizen Viv – you all have in different ways helped me through it all and I will spend a lifetime making it worth your while.

To my Wolfson Centre colleagues– we had a good and memorable run. And finally to my friends and all those who love and care for me, I say thank you, God bless you, and please don't stop now!

'... whether the wrath of the storm tossed sea,
Or demons, or men, or whatever it be,
No waters can swallow the ship where lies,
The Master of Ocean, and Earth, and Sky!
They all shall swiftly obey My will,
"Peace, be still"'

Abstract

This thesis examines the use of electromagnetic modelling techniques in the development of realistic models for a saturable core fault current limiter (FCL), which can be extended to other electromagnetic power devices. It includes the use of mathematical, analytical and FEM tools which incorporate magnetic properties of the FCL with the properties of the electrical circuit in which it is placed.

Two independent models for a saturable core FCL have been developed on different platforms, validated against measured results, and compared with each other for consistency. The models were incorporated into a time-domain circuitry representation of a power distribution network to assess their performance as predictive representations of the actual device. The electromagnetic models incorporate analytic representations of the non-linear soft ferromagnetic material used in the magnetic cores of the devices obtained from sample measurements. Particular attention is paid to the effects and changes needed by the non-linear equations and data, due to the high-field applications in which they are used. The models also include an improved analytic magnetic field distribution function developed for calculating the variation of magnetic field H in magnetic cores that combines accuracy and speed of computation and offers advantages over conventional finite element calculations.

Three dimensional finite element modelling was also used for developing structural improvements to the FCL, such as the effect of various design configurations on the performance of the FCL in the power circuit.

A comparative study of the modelling methods employed shows the advantages of each modelling method while underlining some of the challenges faced during the model development. This has provided solutions to problems which invariably arise in the modelling design of such electromagnetic devices for applications.

Contents

List of Figures

List of Tables

List of abbreviations

AC	Alternating Current
DC	Direct Current
MV	Medium Voltage
FCL	Fault Current Limiter
SFCL	Superconducting Fault Current Limiter
SCFCL	Saturable Core Fault Current Limiter
VDM	Voltage Driven Model
SLE	Straight Line Extrapolation
LAS	Law of Approach to Saturation
ELE	Exponential Law of Extrapolation
SC	Search Coil
MPMS	Magnetic Property Measurement System
mmf	Magnetomotive force
emf	Electromotive force

List of Symbols

V	Volume [m^3]
m	Magnetic moment [Am^2]
B	Magnetic flux density [T]
B_s	Saturation flux density [T]
H	Magnetic field strength [A/m]
H_c	Coercive field [A/m]
M	Magnetisation [A/m]
M_s	Saturation magnetisation [A/m]
μ	Relative permeability
μ_0	Permeability of vacuum [N/A^2]
Φ	Flux linkage [Wb]
L	Inductance [H]
I,i	Current [A]
E	Electric field [V/m^2]
J	Current density [A/m^2]
ξ	Emf [V]
ω	Frequency [Hz]
R	Resistance [Ohms]

Chapter 1. General Introduction

1.1. Introduction and Aim

With increasing demand being placed on the interconnectivity of power networks and renewable generation, innovative technologies are needed to help control the faults currents in the power grid [1], [2]. Such devices also increase the longevity of other protective equipment present in these power systems by improving the stability and robustness of the power networks [3], [4], [5]. Many electromagnetic technologies are being developed for this purpose one of which is the fault current limiter (FCL). Some FCLs depend on the inherent non-linear behaviour of ferromagnetic core materials to enable the devices to automatically adjust the impedance of an electric power circuit so that at low currents the circuit has low permeability and low impedance, while at high currents it has high permeability and high impedance. This change in impedance limits the propagation of fault currents throughout the power grid.

Development and design of these devices requires an understanding of the electromagnetic behaviours of the constituent elements, and an ability to use this knowledge in improving the design and assessing the performance of such devices. Furthermore, the use of computational electromagnetic techniques in the design process has become increasingly prominent due to their ability to solve large-scale problems in short time periods [6], compared with the use of approximate mathematical models.

However, given the insight and simplicity that can be provided by analytic mathematical models, a comprehensive approach to modelling such devices like the fault current limiter has been taken in this thesis. This includes a combination of both numerical and analytic methods. This multi-physics approach has been

successfully used in the design of electromagnetic devices such as power transformers and fault current limiters [7], [8], [9]. Furthermore, the effects of very high fields and currents on the assumptions and equations used in creating these analytic models have not been properly investigated.

The aim of this thesis is to use a electromagnetic multiphysics approach to modelling in the design of a saturable core fault current limiter (SCFCL). This includes the use of analytic mathematical models and FEM techniques, combined with the use of electromagnetic property information obtained from laboratory measurements, to improve understanding and design of the device. The work also provides an examination of the electromagnetic equations and methods used in these modelling and how they change with the modelling of power devices. This has resulted in models which are reliable representations of the real device and which can be used in the design, analysis and performance of FCLs in power system models.

1.2. Thesis Outline

The thesis is organised into nine chapters that cover the development and analysis of the SCFCL models developed.

Chapter 2 provides a fundamental background of the underlying scientific, magnetic and engineering concepts used in the thesis. It describes the magnetic properties of ferromagnets and introduces their use in the design of fault current limiters, which are the devices of interest in this thesis. A literature review of the attempts at electromagnetic modelling of this device has also been carried out. An introduction to the finite element modelling method has been given, including how it is used in engineering applications.

Chapter 3 includes the data measurements and equipment setup for the thesis. The chapter shows the preparation of the data obtained from measurements for their use in material selection and also device modelling in the mathematical and FEM software either by way of direct data inclusion or by curve fitting to obtain material representative curves.

Chapter 4 outlines some critical problems and challenges faced in obtaining and processing magnetic property data for representation of magnetic materials. These include finding appropriate extrapolation methods for ferromagnetic materials, and also problems with the standard Ampere's Law formulation equation generally used in calculation and measurement.

Chapter 5 details the development of a mathematical model for the FCL. The model provided a basis for studying the FCL functionality and performance directly in a network, and formed a basis from which improvements in material selection. The core design and structural modifications could be further investigated by simply changing the model parameters.

Chapter 6 uses the finite element method in the structural analysis and modification of the electromagnetic FCL. Improvements due to this static solver analysis approach are sought for the different designs of the FCL.

Chapter 7 uses FEM static and transient solvers to improve the understanding and performance assessment of the device. The inductance calculations performed in the work are examined in order to find the most appropriate method of comparing the inductances of various FCL design models. The insertion inductance of the FE models were compared to those measured from actual prototypes in order to authenticate the FCL models. The performance of various models and design modifications were then assessed.

Chapter 8 presents the development of another model in a commercial power system simulator PSCAD. It analyses the unique problems faced in building a module in this software and uses the model that has been developed to assess the performance of the device in real MV networks. A comparison is also performed between the two models developed in the thesis.

Chapter 9 concludes the work with a summary of the achievements and conclusions from the research, along with suggestions for future work.

[1] D. Cvoric, S.W.H de Haan; J.A Ferreira, Comparison Of The Four Configurations Of The Inductive Fault Current Limiter, IEEE Power Electronics Specialists Conference, PESC 2008

[2] Lin Ye , Liang Zhen Lin , Study Of Superconducting Fault Current Limiters For System Integration Of Wind Farms, IEEE Trans. Applied Superconductivity, Issue 3, Pg. 1233 – 1237, June 2010

[3] S.B Rafi., M. Fotuhi-Firuzabad , T.S. Sidhu , Reliability Enhancement In Switching Substations Using Fault Current Limiters, PMAPS 2006, Pg. 1.5, June 2006

[4] Agheli, Ali; Abyaneh, Hossein Askarian ; Chabanloo, Reza Mohammadi ;Dezaki, Hamed Hashemi , Reducing The Impact Of DG In Distribution Networks Protection Using Fault Current Limiters, Power Engineering And Optimization Conference (PEOCO), 2010, Pg. 298 - 303 June 2010

[5] Sjostrom, M. ;Cherkaoui, R.; Dutoit, B., Enhancement Of Power System Transient Stability Using Superconducting Fault Current Limiters, IEEE Trans. Applied Superconductivity, Vol.9, Pg. 1328 – 1330,June 1999

[6] S. Ratnajeevan , H. Hoole, Computational Electromagnetics, Elsevier Science Publishing, 1989, Pg. 6

[7] Tihanyi, V. ;Gyore, A. ;Vajda, I., Multiphysical Finite Element Modeling Of Inductive Type Fault Current Limiters And Self Limiting Transformers, IEEE Trans. Applied Superconductivity,Vol 19, Pg.1922-1925, June 2009

[8] Sharifi, Reza ;Heydari, Hossein, Optimal Design Of Superconducting Fault Current Limiters For Electrical Systems, Second International Conference On Engineering Systems Management And Its Applications (ICESMA), 2010 ,Pg. 1.6, April 2010

[9] Liang Zou ;Hongshun Liu ;Qingmin Li ;Wah Hoon Siew, Analysis And Simulation Of The PMFCL Based On Coupled Field-Circuit Modeling Methodology, International Conference On High Voltage Engineering And Application, 2008.,Pg. 498-502, Nov. 2008

Chapter 2. Technical Background

2.1. Magnetic Material Classification

Classifying magnetic materials traditionally has been done by an examination of their macroscopic susceptibilities [1], or their relative permeabilities [2]. Some magnetic materials show such minimal magnetic effects that they are essentially considered "non-magnetic". A method of quantifying 'magnetic effects' is by examining materials on the basis of their magnetic susceptibility (i.e. how their magnetic dipole moments behave in the presence of a magnetic field). With this definition, magnetic material classes can be distinguished as shown in Fig. 2.1 to include:

- *Diamagnetism*: These are materials with no net dipole moment in the absence of an applied field magnetic, but can acquire a weak magnetic moment in the presence of an applied magnetic field, and the direction of that magnetic moment opposes the applied field. A typical example is Bismuth.
- *Paramagnetism*: These materials possess a net magnetic moment even without the influence of an external magnetic field. An application of an external field will cause the moments to align themselves with the direction of the external field. Examples include Aluminium and Manganese.
- *Ferromagnetism*: Such materials benefit from a quantum phenomenon called 'exchange coupling', which greatly facilitates the alignment of their moments into rigid parallel configurations over regions called domains. It can also be

considered that the moments in ferromagnets are 'ordered' in domains. As such, they can have very high net magnetic moments without an applied field. They do however, lose this capacity above a critical temperature called the *Curie temperature*, after which they become paramagnetic. Examples include Iron and Cobalt.

- *Antiferromagnetism*: Here, the magnetic moments of adjacent atoms though same in magnitude, align themselves antiparallel to each other when the temperature is low enough. As such they have a net magnetic moment of zero in the absence of an external field. This arrangement of domains is unaltered in the presence of an external field. An example is Manganese oxide.
- *Ferrimagnetism*: In these materials the adjacent atomic moments are aligned in opposition but are unequal. Hence there is a net moment but not as strong as those in ferromagnets. A special class of these materials, called *ferrites*, also possess low electrical conductivity and hence are useful in inductor cores and ac applications. An example is magnetite or Fe_3O_4. [3]

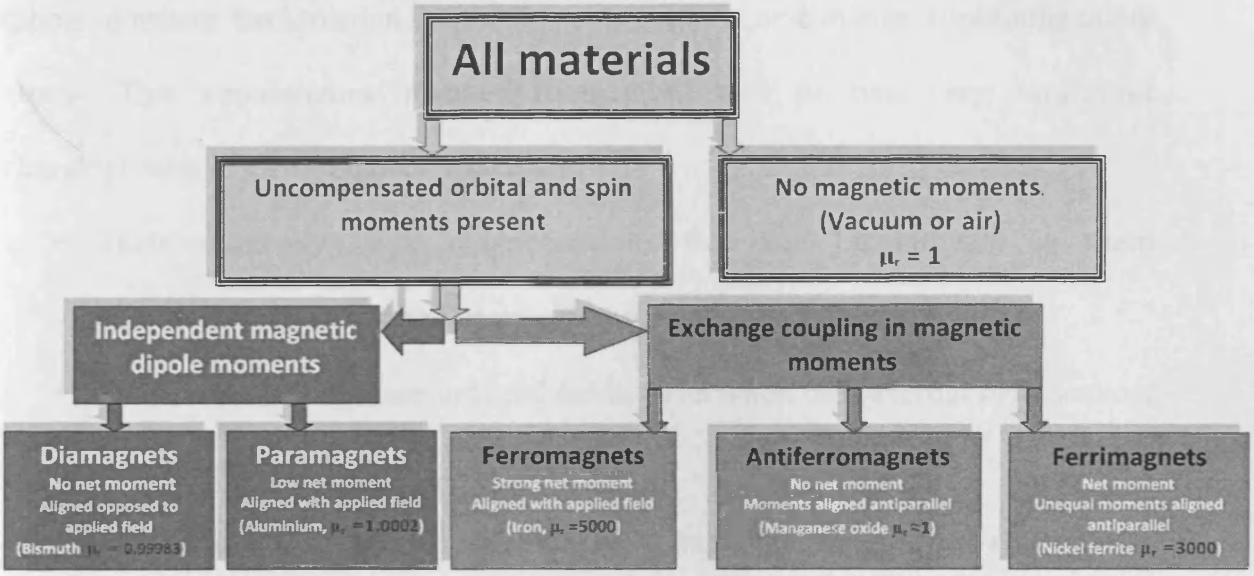

Fig. 2.1: Classification of materials by their alignment of their magnetic dipole moments.

Further sub-classes like superparamagnetism, helimagnetism can be defined with the principle of ordered moments introduced in ferromagnetism. This thesis will focus on the most important class of magnetic materials, which is ferromagnetism, as they are the materials, which are most practically used in science and industry.

2.2. Ferromagnetic Material Properties

2.2.1. Introduction

Ferromagnetism is the term used to characterise strong magnetic behaviour (i.e. large susceptibility) exhibited by some materials. This is understood to be due to spontaneous magnetisation [4], a phenomenon that occurs due to the unforced parallel alignment of spin dipole moments of constituent adjacent atoms. The atomic

dipole moments tend to align themselves over regions, or domains, containing many atoms. This spontaneous magnetisation gives rise to two very important characteristics of ferromagnets, which are:

- Their relatively large magnetisations that can be induced in them spontaneously or by comparatively low fields.
- Their retention of these induced fields, even when the external field sources are removed. [5]

These two factors are responsible for the most important magnetic characteristics observed from ferromagnets on a macroscopic scale. Characterising ferromagnets provides a way of comparing these materials, and how these magnetic materials can be described in models for their application, such the devices to be modelled in this thesis. These important factors used in the characterisation of magnetic materials are now examined.

2.2.2. Characteristic Features In Ferromagnetism

2.2.2.1. Magnetisation and Magnetic Induction

When an external magnetic field **H** is applied to a material, the response of the material is called its magnetic induction **B,** which physically can be understood as the magnetic flux density in the medium. In some materials and in free space, this relationship is linear, but in most cases it is more complicated and non-linear, and sometimes not even single-valued [6]. The equation relating **B** and **H** in SI units is:

$$B = \mu_0(H + M) \qquad (2.1)$$

where $\boldsymbol{M}$ is the magnetisation of the medium, and $\mu_0 = 4\pi * 10^{-7} \mathrm{Hm}^{-1}$ is the permeability of free space, a universal constant. **M** is defined as the magnetic moment ($\boldsymbol{m}$) of the constituent atoms or molecules, per unit volume ($\boldsymbol{V}$) of the materials

$$M = \frac{m}{V} \qquad (2.2)$$

In this thesis the unit convention adopted for magnetic field H will be Amps per meter (A/m), and for the magnetic induction **B** will be Tesla (T).

The line or curve showing the relationship between **H** and **B** for any given material is called a *magnetisation curve.* If the values of **H** are increased monotonically from zero and the magnetisation **M** starts from zero, then the curve is termed an *initial* magnetisation curve, which is one type of magnetisation curve commonly used to represent the magnetic material in the modelling of devices. If **H** is increased indefinitely, the magnetisation eventually reaches *saturation* at a value designated $\mathbf{M_S}$. At this point, it is understood that all the magnetic dipoles are aligned in the direction of the magnetic field; hence any further increase in field produces no increase in magnetisation **M.** Fig. 2.2 illustrates the effects of a field on the domains (groups of similarly aligned magnetic moments), as it re-orients all the domains in its applied direction. Saturation is attained when all such domains are aligned in one direction.

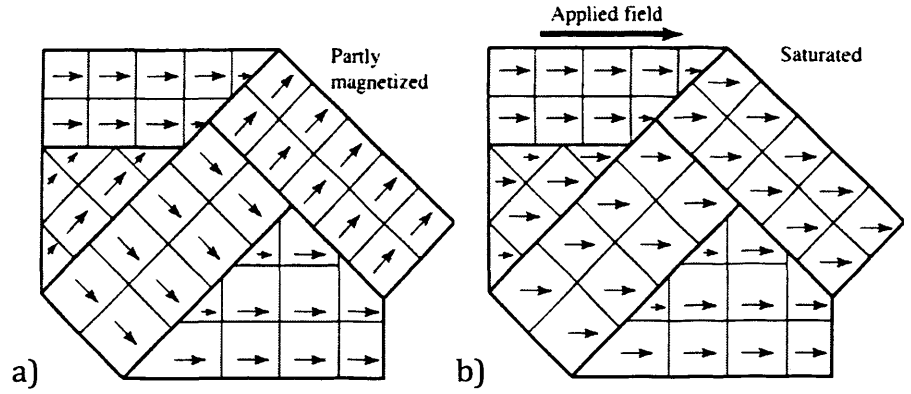

Fig. 2.2: Stages of magnetisation of a ferromagnet with a) domain alignment with no field and b) saturation magnetisation with all domains magnetised in direction of external field [7].

2.2.2.2. Permeability

By far the most useful characteristic of ferromagnetic materials used in modelling is the permeability (or absolute permeability) of the material. Permeability is the ratio between the magnetic induction **B** and the magnetic field **H**. It provides a measure of how easily a material allows flux through it. A material that concentrates a high amount of flux density in its interior is said to have high permeability, as is the case with most ferromagnetic materials:

$$\mu = \frac{B}{H} = \mu_0 \mu_r \qquad (2.3)$$

where μ is the permeability and μ_r is the relative permeability of a material.

It should be noted that the permeability of a material is not constant as a function of field. A more useful quantity is the relative differential permeability $\frac{dB}{dH}$, which is

determined by the small change in induction by a change in field around the point of interest, as the field tends to zero. Mathematically speaking:

$$\frac{dB}{dH} = \lim \Delta H \rightarrow 0 \quad \frac{B(H + \Delta H) - B(H)}{\Delta H} \qquad (2.4)$$

taken at any point of interest on the magnetisation curve.

Any subsequent reference to "permeability" in this thesis will refer to this definition, except where otherwise stated. The relative differential permeability will hence be termed relative permeability, or simply permeability. Eqn. 2.4 gives two useful kinds of permeability descriptions viz – the *maximum permeability, max* μ_r (or μ_{max}), which is the relative permeability from the line of steepest slope on the initial magnetisation curve, and the *initial permeability, initial* μ_r, which is taken as the slope of the initial magnetisation curve at the origin. These two descriptions are more commonly used in relating and comparing materials for their appropriateness for usage in magnetic devices. Fig 2.3 illustrates the differences between the various types of permeability measurements possible, and their values relative to their position on the initial magnetisation curve of Iron.

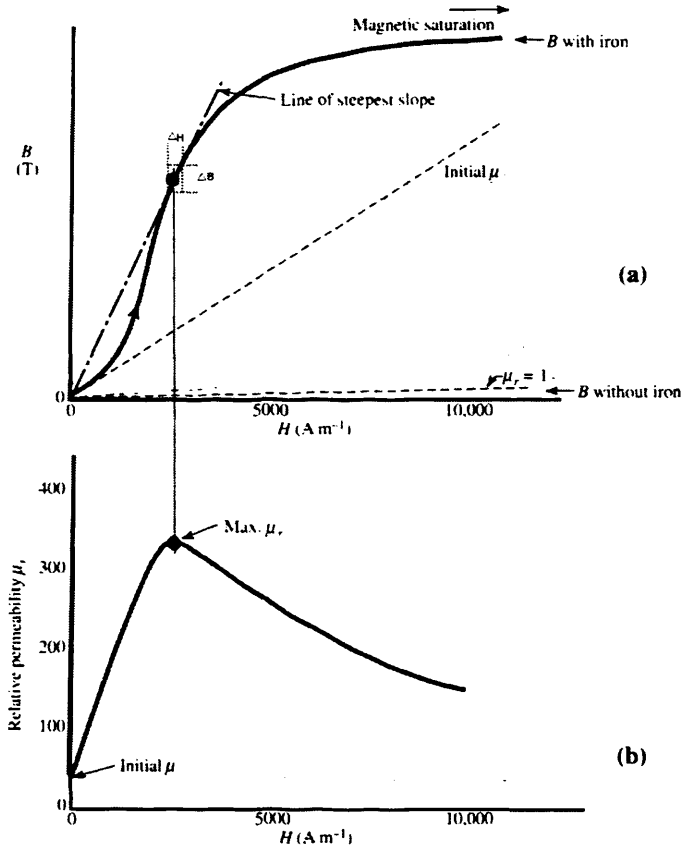

Fig. 2.3: a) Initial magnetisation curve and b) relative permeability curve for iron illustrating the different aspects and methods of measuring permeability.

2.2.2.3. Coercivity and Remanence

The ***coercive field*** *(sometimes called the* ***coercivity)*** of a ferromagnetic material is defined as the field strength necessary to reduce the magnetisation of the material to zero. This is a reverse field $\mathbf{H_c}$, which is strongly affected by external factors like heat and stress.

The ***remanence*** on the other hand, is the remaining magnetic induction in a magnetic material when the external field applied to such a material is reduced to

zero. It is the residual flux that is due to the ordering of the intrinsic domains in a ferromagnet, and it is denoted $\mathbf{B_r}$.

These are two characteristics that are used to determine the hardness or softness of a ferromagnetic material. This shall be examined in more detail later on in this Chapter.

2.2.2.4. Hysteresis

Hysteresis, which means 'lag behind' [8], is the terms used in describing the behaviour of ferromagnets wherein the magnetisation always seems to lag behind the applied field. This phenomenon is observed during the cyclic variation of field **H,** which results in a non-identical magnetisation curve for increasing and decreasing values of **H**. Such cyclic loops of B vs **H** are called a *hysteresis loop or **B-H** loop*. The loop shows that the magnetisation of a material is not only dependent on the external field, but also on the history of changes in magnetic field undergone by the material. Hysteresis loops are plotted by increasing the field from zero (of the demagnetised sample) till the material attains positive saturation ($\mathbf{B_s}$) (called the initial portion of the hysteresis loop), and then reducing the field through zero till the sample attains negative saturation ($\mathbf{-B_s}$) (termed the upper branch), before finally increasing it back into positive saturation (termed the lower branch). This cyclic process produces a *major hysteresis loop*, also called **B-H** loops, whose main characteristics are shown in Fig. 2.4. Such loops are usually sigmoidal in shape and symmetric about the origin. Other cyclic measurements not required to reach

positive and or negative saturation also produce loops, usually referred to as *minor loops.*

For any given ferromagnetic material, the **B-H loop** is a useful representation in that it provides a limiting boundary for all possible states that can be attained by the material in the B-H space, as any points outside the loop can never be reached for the particular material. Hence the **B-H** loop provides a complete set of all the possible states of a magnetic material. The suitability of magnetic materials for applications is generally determined from the magnetic characteristics shown by their respective hysteresis loops. This is why the hysteresis loop is so important; because it contains information on all the magnetic parameters that have been discussed earlier like coercivity, remanence, saturation magnetisation, power loss and permeability. This completeness and all-inclusiveness, makes the hysteresis loop the single most important representation for ferromagnetic materials for technical applications.

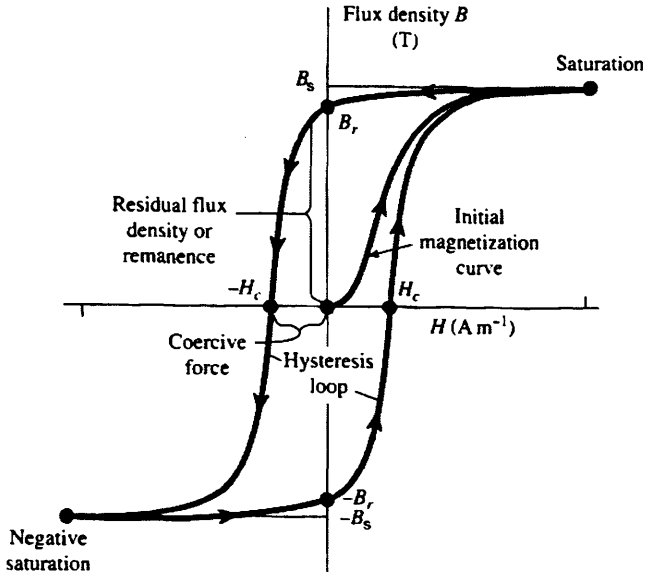

Fig. 2.4: Typical hysteresis loop showing various magnetic material characteristics [9]

Historical empirical facts about hysteresis like the fact that the addition of non-magnetic elements to iron increase the hysteresis loss and coercivity, or that an increase in coercivity is observed when iron is subjected to cold working, seem to point towards imperfections (such as dislocation or impurities) as the main agents responsible for hysteresis. There are other contributing factors like anisotropy and stress in a material [10]. It is beyond the scope of this thesis to examine the theories behind this phenomenon, and hence it shall suffice that the study simply makes use of the fact of hysteresis and the role it plays in device modelling.

2.2.2.5. Anhysteretic Magnetisation

Assuming the earlier mentioned hypothesis about hysteresis being caused by imperfections, it is conceivable to acquire some additional material information

from a reference curve that has no hysteresis. This kind of magnetisation is the anhysteretic curve, which by definition for every material, is single-valued for all values of **H.** Given that such a flawless material is practically impossible to find, the only way of obtaining such a magnetisation curve, is by cyclic decaying magnetisation with an alternating field at every point on the curve determined by a DC bias field, using minor loops such that the extremes of the minor loops – both positive and negative – lie on the anhysteretic curve [11]. The anhysteretic curve which is independent of the history of the sample is reproducible. It is always above the initial magnetisation curve and does not feature an inflection point or Raleigh region as seen on an initial magnetisation curve [12]. Fig. 2.5 shows the low field regions of a ferromagnetic material (Fe-Si), magnified to show the difference between the anhysteretic curve and the initial magnetisation curve in the first positive quadrant. At high fields leading towards saturation, both curves coincide.

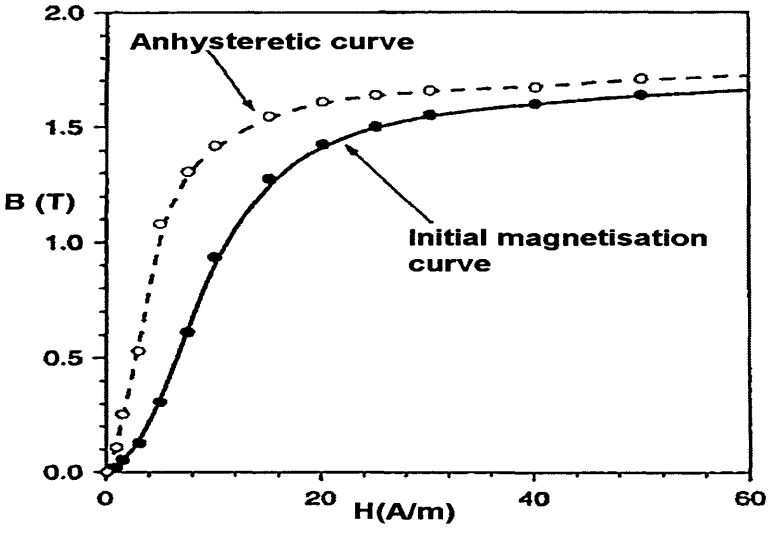

Fig. 2.5: Initial magnetisation curve and anhysteretic curve of grain-oriented Fe-Si, showing differences at low fields [13]

With the complexity of hysteresis modelling incorporation in power applications, sometimes the anhysteretic curves are used for modelling instead of the initial magnetisation curves, especially in ferromagnets where the difference between anhysteretic curves and initial magnetisation curves are negligible [14] for many modelling purposes.

2.2.3. Analytic Representation of Ferromagnetic Materials

Considering the initial assertion about the completeness of the hysteresis loop in capturing the important properties of magnetic materials, it follows that accurate magnetic material modelling will entail finding mathematical descriptions and models for these hysteresis loops. This problem has been tackled extensively in the literature, with the Jiles-Atherton model, and the Preisach model of hysteresis being the most popularly accepted and used, due to their simplicity and applicability across a wide range of engineering problems [15].

The application of these elaborate hysteresis models and algorithms in electromagnetic design is fraught with substantial difficulties and disadvantages. Not only do they require large amounts of computing resources, but the appreciation and determination of the model parameters is not easily achieved. In fact, the existing models are not universal with one model being more readily applicable to specific material types than others [16]. Therefore most electromagnetic modelling is carried out with simpler approximations like the anhysteretic expressions for ferromagnetic materials. Such an approximation is

made possible due to the narrow hysteresis loops of soft magnetic materials. Hence over a wide field range, such B-H curves can adequately be approximated as a single-valued function. Neglecting the effects of hysteresis in such cases gives reasonably good results faster and with more flexibility to investigation, providing another reason why the assumption is desirable. Thus finding expressions for the anhysteretic curves of ferromagnets is of particular importance to this study.

In principle, for the approximation of an idealised anhysteretic curve, one can use any function that adequately describes the achievement of saturation, and quite many have been researched in literature. One such equation was developed independently by Frohlich and Kennelly [17]:

$$M = \frac{\alpha H}{1 + \beta H} \tag{2.5}$$

and,

$$a + bH = \frac{1}{\mu - \mu_0} \tag{2.6}$$

where **α , β ,a, b are constants such that** $\alpha/\beta = Ms = 1/(\mu_0 b)$, *and* $1/\alpha = \mu_0 a$.

A series expansion of Eqn. 2.5 will lead to the more generalised form of the anhysteretic equation

$$M = M_s \left[1 - \frac{cM_s}{H} + \left(\frac{cM_s}{H} \right)^2 - \left(\frac{cM_s}{H} \right)^3 \cdots \right] \tag{2.7}$$

Another very similar relation which is mostly applicable at high fields is the Law of Approach to Saturation as given by Becker and Doring [18]. These two relations approach each other asymptotically as the field increases.

For isotropic materials, an analogous relation like that proposed for paramagnets by using the Langevin –Wiess function [19], is used for modelling ferromagnets

$$M = M_s\left[\coth\left(\frac{H_e}{a}\right) - \frac{a}{H_e}\right] \qquad (2.8)$$

and for uniaxially anisotropic materials,

$$M = M_s \tanh\left(\frac{H_e}{a}\right) \qquad (2.9)$$

where H_e is the effective magnetic field as introduced by Weiss to account for ferromagnetism and $a = {k_B T}/{\mu_0 m}$, is a material parameter that depends on temperature T, k_B is the Boltzmann constant and m is the magnetic dipole moment per atom [20].

These analytic functions have their limitations as to how accurately they can represent one ferromagnet or the other, but their widespread use suggests that they

are good enough representations to be used in modelling of applications that contain ferromagnets.

2.3. *Soft Magnetic Materials*

Ferromagnets are popularly classified with respect to their properties for applications in engineering. One of such classifications is on the basis of their coercivity. The two simple groupings on this basis are soft (easy to magnetise and demagnetise) materials with low coercivities (typically <1 kA/m), and hard (difficult to demagnetise and magnetise) materials with high coercivities (typically >10 kA/m) [21]. This difference in coercivity is illustrated in Fig. 2.6:

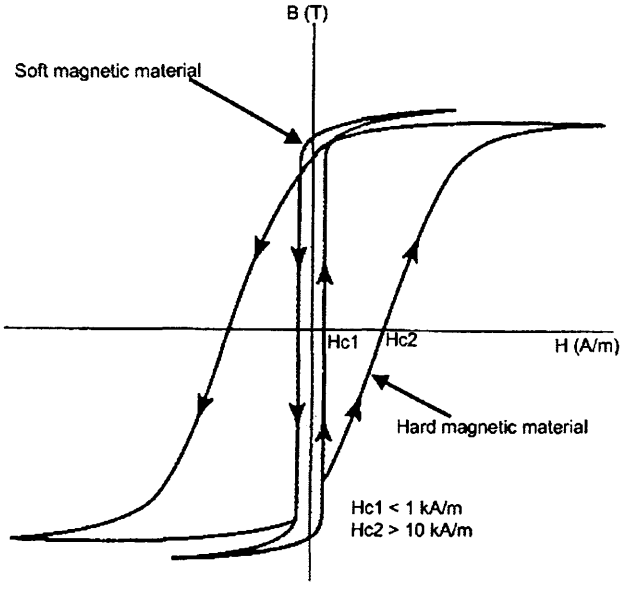

Fig. 2.6: Characteristic hysteresis loop for soft and hard magnetic materials of typical coercivities Hc_1 and Hc_2 respectively.

Hard magnetic materials are characterised by broad B-H loops, higher hysteresis losses, high coercivities, low permeability and susceptibility, high eddy current loss (due to low resistivity), and usually have larger lattice defects and impurities. Examples include NdFeB, chromium steel, $Sm_2 CO_{15.}$ Their primary characteristics of retaining magnetisation once magnetised and their high retentivity makes them useful as permanent magnets in motors, generators, loudspeakers etc. Semi-hard materials are used in data storage applications. Their material properties however make them undesirable for high power applications (high time-varying magnetic fields) where their high losses will be major sources of inefficiency and potential danger to the equipment due to overheating. Because of these issues, hard magnetic materials will not be the materials of focus in this research.

On the other hand, soft magnetic materials are characterised by thinner and steeper B-H loops (hence lower hysteresis loss), high permeability and susceptibility, low coercivity, high resistivities (and hence low eddy current loss), and low impurities. Examples include silicon-iron alloys, low carbon steels, nickel-iron alloys, cobalt-iron alloys, amorphous alloys etc. These materials' properties enable their usage as flux multipliers due to high permeability [22] in transformers, electromagnetic relays, generators, and fault current limiters amongst others. Their low hysteresis and eddy current losses make them appropriate for high power devices. This thesis shall hence focus on the magnetic modelling of soft magnetic materials in power applications with particular interest in their applications in fault current limiters and induction heaters.

2.4. *Magnetic Circuits and Material Property Measurements*

2.4.1. *Magnetic Circuits*

The study of magnetic materials and their uses in electromagnetic devices is best understood from the perspective of magnetic circuits. Some important aspects of these circuits will now be highlighted in order to aid the understanding of the subsequent discussions on electromagnetic modelling.

Magnetic circuits are generally described as a combination of magnetic materials that form a complete path for magnetic lines of force or magnetic flux [23]. Most of this flux stays in its intended path, while some of it flows out of the intended path and is termed *leakage flux.* In magnetic calculations, such leakage flux are either usually ignored or empirically accounted for. Magnetic circuit design is largely concerned with two principal issues. First of all, is the issue of how to determine the excitation (magnetomotive force - ***mmf***) needed in producing the magnetic flux Φ or magnetic field **H,** required in the application. This can be through permanent magnets or electromagnets (current carrying coils and solenoids). Secondly is the aspect of determining the flux effects or the flux density **B** at any particular point in the application. This is achieved by the use of the constitutive electromagnetic equations (Maxwell's equations). Taking the analogy from electric circuits, it is

useful to the study to define the ***reluctance*** R_m, of a magnetic circuit as the resistance of the material to the flow or passage of magnetic flux. It is defined as:

$$R_m = \frac{l}{\mu.A} \qquad (2.10)$$

where, l is the magnetic path length , μ is the absolute permeability of the material and A is the cross-sectional area of the material.

The relation provides an invaluable tool in designing devices, as it combines geometric quantities with the intrinsic material property of permeability.

In magnetic circuits, the magnetic field produced by a current carrying conductor can be described analytically using **Ampere's circuital law** which states that the field around a closed path is equal to the sum of the currents in an area enclosed by the path *C*. Ampere's law is easily derivable from Maxwell's third law. In integral form it is represented as,

$$\oint_C H.dl = \sum I \qquad (2.11)$$

where dl is the vector element of length, tangential to the path direction. This equation governs the generation of magnetic fields using current carrying coils or electromagnets that are essential in power device design.

The effect of a magnetic field H on materials is usually measured in terms of the magnetic flux density B. Hence for any given field **H** applied to a magnetic material, the relation between the flux and the flux density is represented by the surface integral such that:

$$\Phi = \oint_A B.n\,dA \qquad (2.12)$$

where ***n*** is the unit vector normal to the elementary area ***dA***.

These two constitutive equations give a platform from which magnetic material measurements can be performed.

2.5. *Methods of Magnetic Material Measurements*

Magnetic characterisation is the process of measuring the intrinsic magnetic parameters of magnetic materials such as saturation magnetisation and Curie temperature. It also is the determination of the constitutive law of the material, that is, the dependence of the magnetisation on the effective field in the form of magnetisation curves and hysteresis loops. Different techniques have been developed for these purposes. They generally make use of:

- *Forces and mechanical torques* wherein a non-uniform field generates a translational force on a magnetised sample.
- *Inductive methods* wherein signals induced on the magnetic material samples by Faraday-Maxwell laws are picked up and integrated to provide material magnetisation.

- *Magneto metric methods* which are techniques based on the measurement of stray fields emitted by a magnetised open sample.
- *Magneto-optical* techniques like the Kerr Effect hysteresisgraphs.
- *Magnetostrictive* techniques based on measuring the magnetisation-related dimensions of the sample.
- *Magnetic resonance methods* based on the resonant frequency energy emission of magnetic nuclei due the applied magnetic field strength.

Due to the fact that this thesis is focused principally on soft magnetic materials, the inductive technique of characterisation will be the technique of choice as it is the most appropriate when dealing with this class of magnetic materials [24].

2.5.1. Closed and Open Magnetic Circuit Configurations

Closed magnetic circuits are those in which there is a complete flux path, through magnetic materials. This usually means with no inclusion of airgaps. Closed magnetic circuit measurements are by far the preferred method of material characterisation and measurement because magnetic testing usually depends on the direct vector relationship between **B or M,** and **H.** Such a relationship is not immediately evident in open circuits and as a consequence the measured properties will depend on how the magnetic circuit is realised, in more than one dimension. As such, toroidal samples will provide very good measurement samples for closed circuits as uniform mmf and field can be ensured, by wrapping both magnetising and sensing coils uniformly around such a sample. The toroid ensures flux closure

and since this configuration provides the least reluctance path, leakage flux and fringing are held at a minimum, thus improving the accuracy of the measurements.

But in practical terms, preparation of toroid samples is extremely laborious, and the field strength achievable with the primary windings is limited. Also, such closed toroidal samples have a field gradient from the inner to the outer diameters that can be a problem for measurement accuracy.

Because of these limitations on doing toroidal closed sample measurements, the more accepted closed circuit measurement standard is one made by a square assembly of suitable ferromagnetic magnetic material sample strips, cut along the desired testing direction. This is the **Epstein frame** configuration, defined under IEC 60404-2, and used for power frequency measurements (0-10kHz), used predominantly for the measurement of electrical steels [25]. Test material strips are cut with dimensions 30x3x0.03 cm and placed in an Epstein frame in sets of four. This frame consists of four solenoid pairs; each with 700 turns primary (external) and 700 turns secondary (internal) uniform coil windings assembled to produce a uniformly distributed field. Overlapping the strip edges ensures flux continuity at the edges of the strips, and placing 1 Newton weights on these joints improves reproducibility of flux measurements. The magnetic path length for the standard 25cm Epstein frame is $\boldsymbol{lm}$ = 0.94m. The structure of the Epstein frame measurement unit is shown in Fig. 2.7.

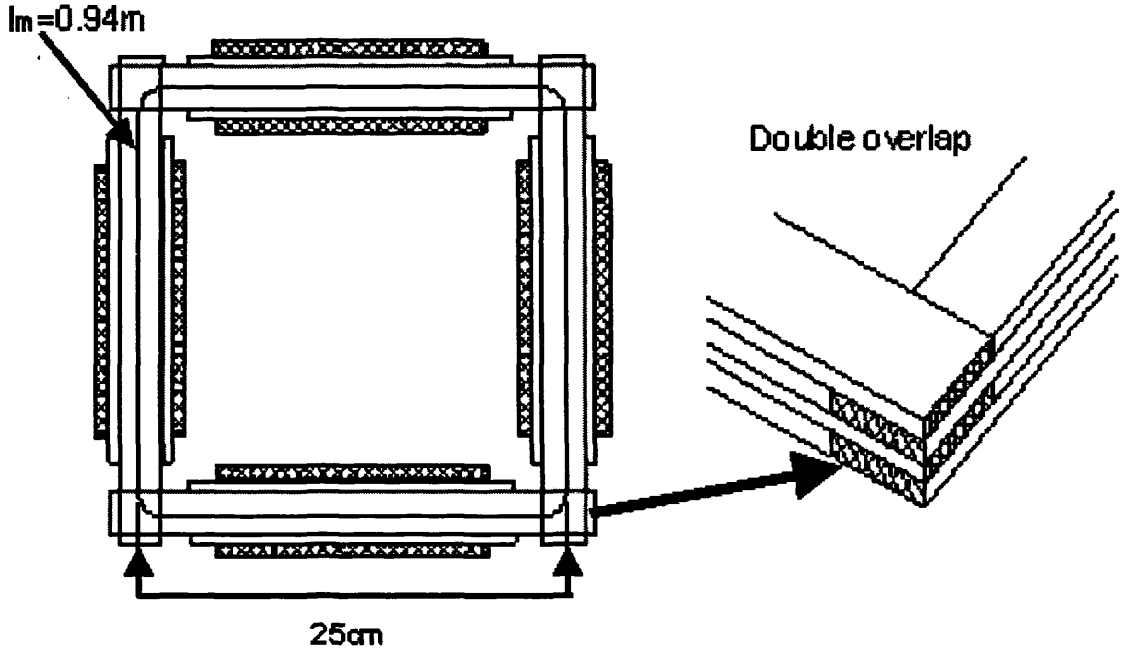

Fig. 2.7: Epstein frame setup showing double overlap of samples to ensure close flux path.

Not only have the Epstein frame results proven to be reproducible, but the system also offers easy usage [26]. Other closed circuit methods include using very soft material in a yoke that provides a near zero reluctance flux path for the sample which is magnetised by wrapping both the primary (excitation), and secondary (sensing coils) directly on the specimen. Alternatively, an electromagnet with high permeability poles can be used to magnetise samples. A hall-effect probe is used to detect the magnetic field strength and a sensing coil wrapped on the sample gives the magnetic induction readings.

Open circuit measurements, which are measurements performed on materials without a determined closed flux path, are also used in material characterisation.

They do however suffer from particular problems like demagnetising factor considerations and spurious field effects (earth's magnetic field), which make determining the effective field on the sample problematic. With this in mind, this thesis will use the closed circuit method of material measurements as its de facto measurement method, unless otherwise stated. There are many power applications which use both the characterisation methods and material modelling techniques we have examined so far in this thesis.

2.6. *Fault Current Limiters*

2.6.1. *Introduction*

The focus of this thesis will be on a special class of devices which use soft electromagnetic material cores, called fault current limiters.

A fault current limiter is a device that prevents fault current reaching damagingly high levels in a power network. For example, a EU study has estimated that there are about 150 faults per year per 100 km of transmission line occur in the distribution network of Europe [27]. In today's operating environment, the ability to control fault levels without paying a penalty in the system flexibility is economically attractive. The fault level management problem is particularly acute in large conurbations (urban areas) where fault levels are already close to the design limits of switchgear. The ever-increasing connection of short circuit contributing

distributed generation (DG) in these areas requires some action to be taken, such that fault levels remain within the design ratings of existing switchgear.

Several methods are used to control fault current levels in power systems. These including grid splitting, upgrading switchgear and using fault current limiters. Grid splitting is not very desirable, due to the decreased flexibility and larger network failures that result due to reduced redundancy in power systems. The possibility of uprating switchgear and other equipment will require enormous financial overhead. Consequently, designing and introducing fault limiting devices into the already existing infrastructure is a matter of intense economic and scientific interest, as these devices do not contain the inherent disadvantages of the other methods

Fig. 2.8 gives a brief overview of the various types of fault limiters available in industry and research, presenting the categories under which they are characterised.

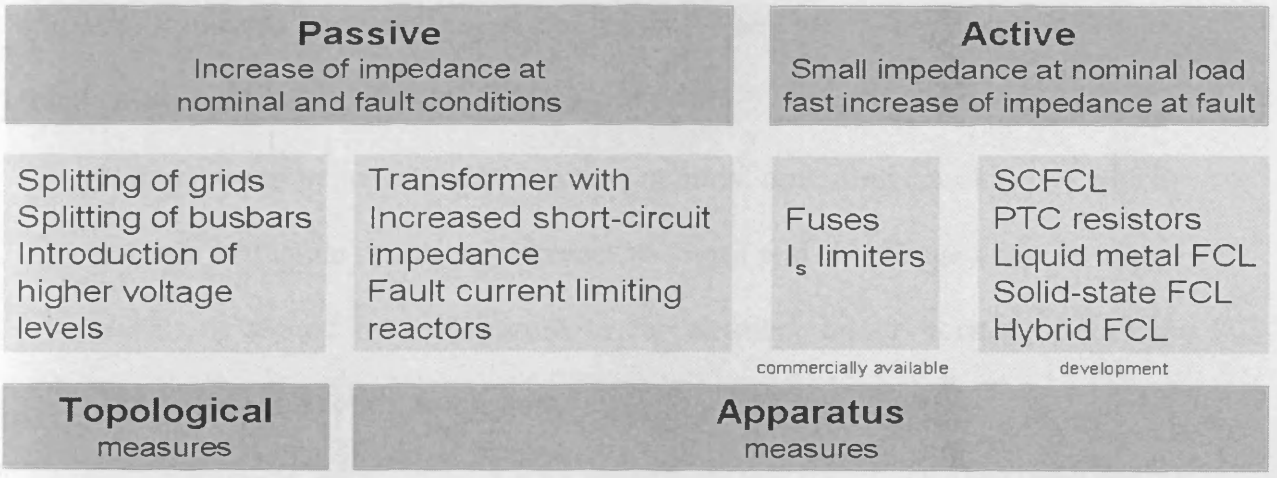

Fig. 2.8: Overview of characterization of fault current limiters [28].

Passive FCLs limit a fault current by providing different current paths with different impedances at nominal and fault conditions. Therefore, they generate losses and voltage drops under fault conditions.

Active FCL devices on the other hand, show a highly non-linear behaviour and quickly increase the impedance in the current path only during the fault. These include the PTC (Positive thermal coefficient) resistors, and different FCL models. This is usually by inclusion of a non-linear ferromagnetic material in their operational elements [29]. They intelligently add impedance to a power system in the advent of a fault. Examples include hybrid FCLs and superconducting FCLs (SFCL) which are among the most promising of fault limiting prospects. Of particular interest to this study are the saturable-core type fault current limiters (SCFCLs), which contain ferromagnetic cores.

Industrial standards have set the requirements for any FCL being designed. These include [30];

- Negligible insertion impedance under nominal operating conditions – which include negligible resistive and reactive losses and no voltage drop. In other words, it should be transparent to the network under normal operating conditions, and return to the same state after limiting a fault.

- Fast and multiple response – the first peak of short-circuit current (<5 ms) must be limited in order to limit the magnetic forces on the other equipment on the network. Also, the device should be able to automatically recover within a short period of time to respond to multiple fault cycles.
- Selectivity – It should not limit motor start currents and not respond to transients or capacitor switching currents; this should be achieved by FCL configuration. The current for coordination with protective devices has to be provided, so that existing protection concepts do not need to be modified.
- High reliability and fail safety –the FCL must correctly operate under any fault magnitude and any fault phase condition. Correct response must reliably occur after a long duration without fault events as well as in cases of consecutive multiple faults. A failure of the device should not disrupt the power network.
- Compact size, long lifetime, maintenance-free and low cost.

2.6.2. Operating Principles of FCLs and FCL types.

A fault current limiter can limit a fault current passing through it within the first half cycle. Their fundamental principle of function is either by amplitude reduction or switching before peak value of fault is attained. The use of fault current limiters allows equipment to remain in service even if the prospective fault current exceeds its rated peak and in case of circuit-breakers also its rated short-circuit current.

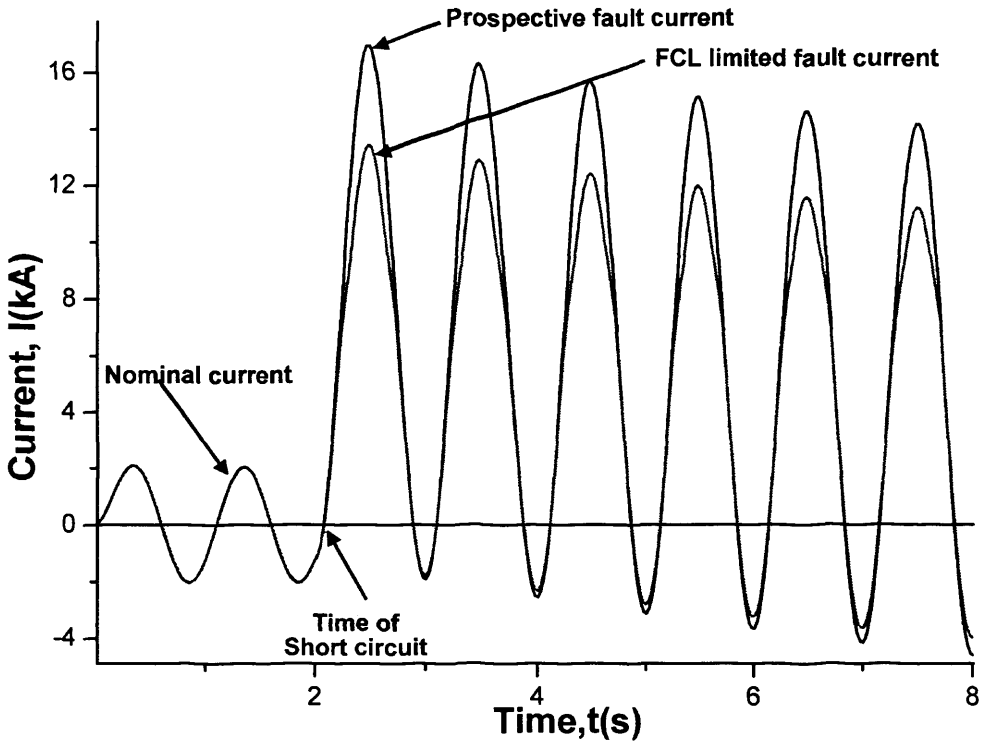

Fig. 2.9: Typical waveform for FCL limiting current.

When no limiting action takes place - depending on the type of fault in the system (short circuit) -a fault current waveform as shown in Fig. 2.9 will flow (prospective fault current) in the system. However, when an FCL is put in the network, and there is a fault current, it inserts an impedance of a high enough value into the circuit in order to limit the fault right from the first half cycle.

Designing such devices at high voltages usually implies the use of special materials like ferromagnets and superconductors where their highly nonlinear characteristics can be exploited to dynamically alter the impedance of the circuit.

2.6.2.1. Types of FCLs

FCLS are broadly categorized into the resistive and inductive varieties. Ferromagnets are usually included in these FCLs as flux concentrators and for their high nonlinear permeability. A brief description of these types will provide an insight into their functioning and how they introduce impedance onto a network.

- ***Resistive FCLs*** use nonlinear material to insert a resistance into the circuit configuration. For example, resistive superconducting FCLs (SFCLs) make use of a superconducting nonlinear resistive element (Rvar) put into a circuit of AC voltage u. Superconductors have the unique property of being able to rapidly switch from zero resistance state to the resistive state of a normal conductor. This may be achieved through the application of a transport current greater than the superconductor critical current, I_c (current at which change of state is effected). The operation of this device is based on the principle that if a fault occurs causing a current I to become larger than I_c, normal state resistivity is established and current limiting occurs. Here, the actual fault duration has to be shorter than the permissible fault duration for the superconducting element, beyond which it could be damaged (thermal effects).

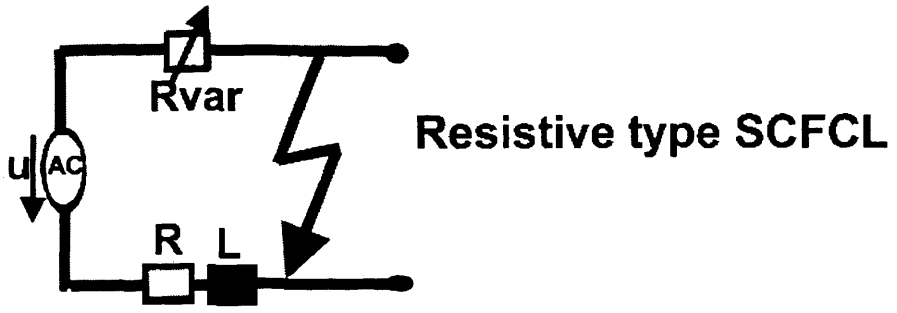

Fig. 2.10: Circuit diagram for resistive SCFCL.

Fig. 2.10 shows a schematic of the nonlinear variable resistance (representing the FCL) in a circuit with load resistance R, and inductance L.

The resistive FCL is challenged by two important practical difficulties which restrict its potential for application. Firstly, the quenching process of the superconducting elements introduces thermal and mechanical instabilities which have still not be properly understood or circumvented. Secondly, the long recovery time for the element to return to superconducting state after limiting a fault, are still too long for industrial standards [31].

- ***Inductive FCLs*** (FCL) are those FCLs which insert an inductance into the current circuit using the special characteristics of its constituent materials. An example is the saturable core fault current limiter (SCFCL) which makes use of the transducer principle that, as an inductive device goes into or out of

saturation, its impedance changes significantly due to the nonlinear increase in its permeability.

From basic principles, the inductance of a coil carrying a current ***i***, with a flux linkage **Φ**, can be written as,

$$L = \frac{\Phi}{i} \qquad (2.13)$$

Substituting a derivation of Eqn. 2.13 with **BA= Φ**, and Eqn. 2.3, and considering the induction changes for every time step due to the nonlinear core, the equation becomes

$$L_{(t)} = \frac{\mu_0 \mu_{r(t)} A H_{(t)}}{i_{(t)}} \qquad (2.14)$$

Hence a change in the permeability at any point in time will increase or decrease the inductance, depending on the total magnetising field on the core.

To achieve current limiting in both halves of a cycle, two inductive cores (inductors) are required per phase as shown in Fig. 2.11. These are driven into saturation by a DC bias field supplied in the case of interest of this thesis, by a superconducting coil because of its ability to supply a permanent ampere turns to magnetise the core almost with no losses [32]. The AC line to be protected is therefore wound around two inductor cores. During a fault, the inductive cores are driven alternately out of saturation by the fault current. The large magnetomotive force (mmf) produced by

the AC winding, drives the core out of saturation on one half cycle, automatically inserting large impedance and limiting the magnitude of the fault current. Limiting on the reverse half-cycle is achieved by the use of the second inductor connected in series with the first and is saturated in the opposite direction. To protect all three phases, six inductors are therefore required. The saturated inductor design is attractive because the superconducting component (the field winding) is external to the circuit being protected, hence transition from normal to fault operation is gradual and without interruption of the superconducting state of the winding. Fig. 2.11 gives a circuital representation of this device.

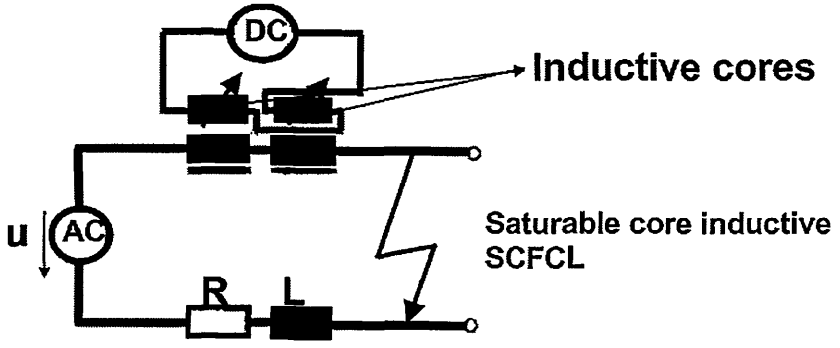

Fig. 2.11: Transducer principle of the inductive-type saturated iron core FCL.

Given the inherent advantages of the SCFCL and its promise in ongoing research, this type of FCL was the focus of this thesis in examining how magnetic modeling can be used in its design and testing.

2.6.3. Modelling Considerations for FCLs

The design and implementation of FCLs is a complex issue because it involves not only different materials but a balance between electric and magnetic requirements and circuitry, and more importantly, a set of industrial requirements every prototype or device must meet. Modelling becomes an integral process in achieving these aims, both in the design process, and also in the implementation of the FCL in tests and analysis. Therefore a detailed understanding of the operation of the FCL and how to convert this into accurate analytic and mathematical models that represent the actual device is needed, in choosing the right parameters and making the right assumptions, for successful device design.

The complexity is further enhanced by the acute nonlinearity of the materials (superconductors and ferromagnets) most commonly used in these devices. Previous work in modelling FCLs has followed vastly different methodology in producing mathematical models for their respective configurations. A broad ranging literature search of these different attempts, points towards two general stages at which the modelling was carried out.

2.6.3.1. Material Modelling

Material modelling is the process of finding analytic or numerical methods of representing the behaviour of the constituent materials in the FCL – the superconducting and the ferromagnetic components of the devices. For SFCLs,

material modelling entails the analysis of the electric field – current density (E-J) characteristic for the particular superconductor element being utilised. Many modelling attempts for these FCLs follow the same method as Langston *et al.* [33] . In their theoretical modelling of a SFCL, they resort to approximating the E-J characteristic of the Y-123 superconductor being used into 3 regions, each represented by a different power law. This approximation in a piecewise representation gives a faster analytic incorporation of the FCL in the general model. The resistance by the superconductor R_{sc} generated during a short circuit at every time step is then measured as

$$R_{sc}(t) = \frac{E(t)l_s}{I_{sc}(t)} \qquad (2.15)$$

where I_{sc} is the fault current , and l_s is the length of the superconducting element.

In other models the HTS material is modelled by a more general analytic and continuous temperature-dependent function for the resistivity, obtained from the V-I characteristic of the superconductor. The resistance introduced into the network during the fault is then calculated using

$$R_{sc} = \frac{\rho(i,T)l_s}{A} \qquad (2.16)$$

Where $\rho(i,T)$ is an analytic representation of the resistivity of the FCL, A is its cross sectional area, and l its length.

The inductive type FCLs models pay particular attention to the ferromagnetic material within the device. Modelling ferromagnets usually involve a choice of which ferromagnetic material representation is appropriate for use. Given that the hysteresis loops carry the most information about magnetic materials, some application models were built to represent hysteresis using models like the Jiles-Atherton model for hysteresis, in order to obtain the differential permeability at each field point on the B-H curve for the ferromagnetic material, $\frac{dB}{dH}$. The model parameters are obtained from measured hysteresis curves [34]. These instantaneous values for permeability at every time step were substituted in the generalized equation for inductance to find the reactance added to the circuit by the coil in order to limit the fault. The fault inductance gained L_{sc} per time step were obtained from;

$$L_{sc}(t) = \frac{\mu_0 N^2 A}{l} \frac{dB}{dH(t)} \qquad (2.17)$$

where, ***N*** is the number of turns of coil on the ferromagnet and ***l*** is the mean magnetic path length of the magnetic circuit.

This process requires a lot of processing time. Moreover it requires complex spatial formulations as the hysteresis model is not single-valued and will have to be specified for spatial location and direction at each modeling time step.

A less complicated method of modelling a hysteresis loop in an FCL system is by replacing the continuous loop with linear piecewise approximations, as proposed by Hoshino *et al. [35]* shown in Fig. 2.12

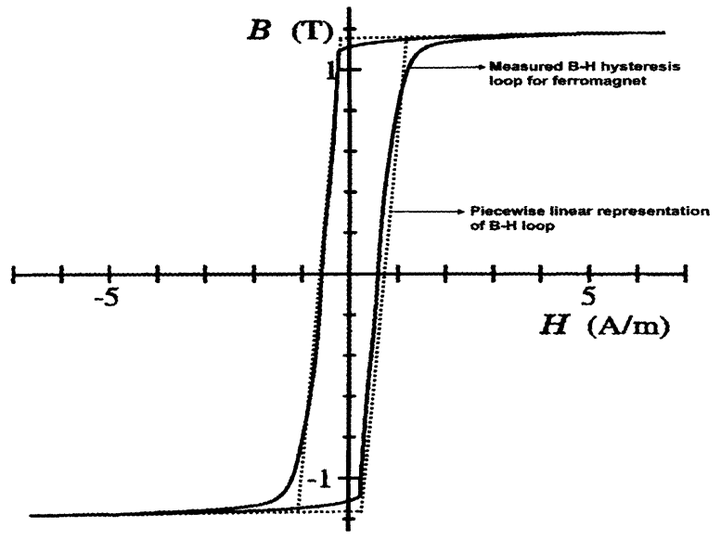

Fig. 2.12: Piecewise representation of B-H loop for modelling of magnetic material.

This idea cuts down on the modelling resources needed for the magnetic material, but still has to deal with the complexities of spatial differentiation and double-valued functions.

With the complexities introduced by directly trying to model hysteresis into FCL systems, many researchers resorted to using single-valued representations of ferromagnets in FCL modelling on the assumptions that soft magnetic materials have such low hysteresis loss that it can be neglected and hence replaced by their

anhysteretic curves. This idea is also made attractive by the amount of modelling resources conserved by making this assumption. Secondly, finding an analytic representative function for the material eases its incorporation into both analytic and numeric model analyses. Such an approach was used by Abbott *et al. [36]*, in modelling an SCFCL where they modelled the permeability of the core by fitting it to an arbitrary function of the form

$$\frac{dB}{dH} = e^{a} H^{c} e^{\frac{b}{H}} \qquad (2.18)$$

where ***a, b*** and ***c*** are constants representing the magnetizing properties of the steel core laminations.

To determine the terminal inductance of the FCL, the nonlinear **B–H** characteristics of the laminated steel core for this model were represented within the 0–30 kA/m region. This approach brings even more simplicity to FCL modelling as it obviates the need to find the permeability directly from the material characteristics, and it produces an easily utilised well-behaved function to find the inductance during the fault. It is however very problem specific and the functions involved have no magnetic meaning or representation. This means that they cannot be adapted for other materials and devices apart from the specific material used in that particular FCL model. Furthermore, there is uncertainty as to how such an arbitrarily chosen

function will behave past the range for which it was fitted, if ever the FCL reaches higher fields than the 30kA/m range specified.

A lack of magnetic information also brings in the handicap of not being able to use the equation to improve the model by investigating the actual effects of the equations' parameters on the magnetic core. Such flexibility, where the parameters are mapped to the behaviour of the material characteristic can be useful to the researcher as it would immediately offer the possibility of researching other closely-related materials using the same model. This type of reverse engineering is very useful in design, as the analytic material function could be used to find exactly the type of parameters a target material needs to have in order to give the best performance. Such material predictions can thus help the designers to find a more appropriate material than that which they started off with. This dynamic material representation helps in an effort to improve the design and performance of the FCL, without having to do multiple measurements and curve fittings. This will be the path taken in this thesis, as it offers the best compromise between modelling complexity, flexibility and maintaining adequate magnetic integrity in material representation.

2.6.3.2. Equivalent Circuit Modelling

The next stage in device modelling is integrating the material representation adopted, into the generalised electromagnetic circuitry of the system in which the

FCL is placed. The circuit modelling varies vastly from one model to the other due to factors that include amongst others:

- The type of FCL being modelled – resistive or inductive.
- The type of configuration being used - that is, open core (airgaps) or closed core [37].
- The arrangement of the primary and secondary coils [38].
- General assumptions made about the circuit like neglecting of mutual impedances, or neglecting leakage flux.

The device models usually are fitted into differential equations that describe the physical systems, which are then solved for their electrical outputs like voltage and current.

2.7. Finite element modelling techniques and methods

2.7.1. Introduction

When engineering problems comprise simple systems, solving and modelling them is generally done using the equivalent circuit approach, which is easy and fast. Moreover, it is physically readable, in the sense that an equivalent circuit represents quantities familiar to the engineer, such as voltage or current. Physical electromagnetic systems are often more complex and are usually represented by means of systems of partial differential equations which exhibit time- and/or space-boundary conditions. These systems, in general, cannot be solved with the simplistic analytic equivalent circuit modelling approaches.

A technique largely shared with other branches of engineering consists of the *discretisation* of the system governing equations (breaking down a large complex system into smaller subsystems which are mathematically easier to analyse), which entails substituting the system of differential equations with a system of algebraic equations. This process is the basic idea behind the use of finite element modelling in device modelling. Not only does this engineering technique aid with providing a holistic view of how a device functions at any particular point in time, it also has a solution space from which analysis of many different physical properties can be carried out. It provides more detail to the designer than would have been available through the basic analytic equivalent circuit approach.

2.7.2. Finite Element Modelling Of Electromagnetic Devices

Finite Element Method (FEM) is one of the most widely used methods for the realisation of system discretisation. It allows one to convert a constructed model problem into a system of equations that is suited for computer resolution. The finite element method is based on the concept of dividing the original problem domain into a group of smaller elements called finite elements, and applying a numerical formulation based on interpolation theory to these elements [39]. In this process of discretisation or meshing a problem domain, it is necessary to choose elements of given shape.

Several element shapes are used including the triangular, quadrilateral and curvilinear shapes. This process of making the elements small is important in order that the field potentials in the elements can be safely approximated by linear terms. Sometimes, higher order terms are used where necessary. The collection of these elements or their associated expansions or shape functions, can model arbitrarily large complex fields and potentials in terms of unknown coefficients. Equations to find these unknown coefficients are constructed by enforcing the boundary values on the various elements and nodes, hence forming a solution matrix [40] .This process can be carried out in either the Galerkin method (weighted residuals) or the Rayleigh-Ritz method (energy functional) [41]. However, the idea is to hypothesize the local behaviour of the unknown space (or time) quantity, and to transform the differential equations into algebraic equations, which can be solved for the quantities of interest in a solution space. Fig 2.13 presents a schematic of the FEM mathematical process of solving equations.

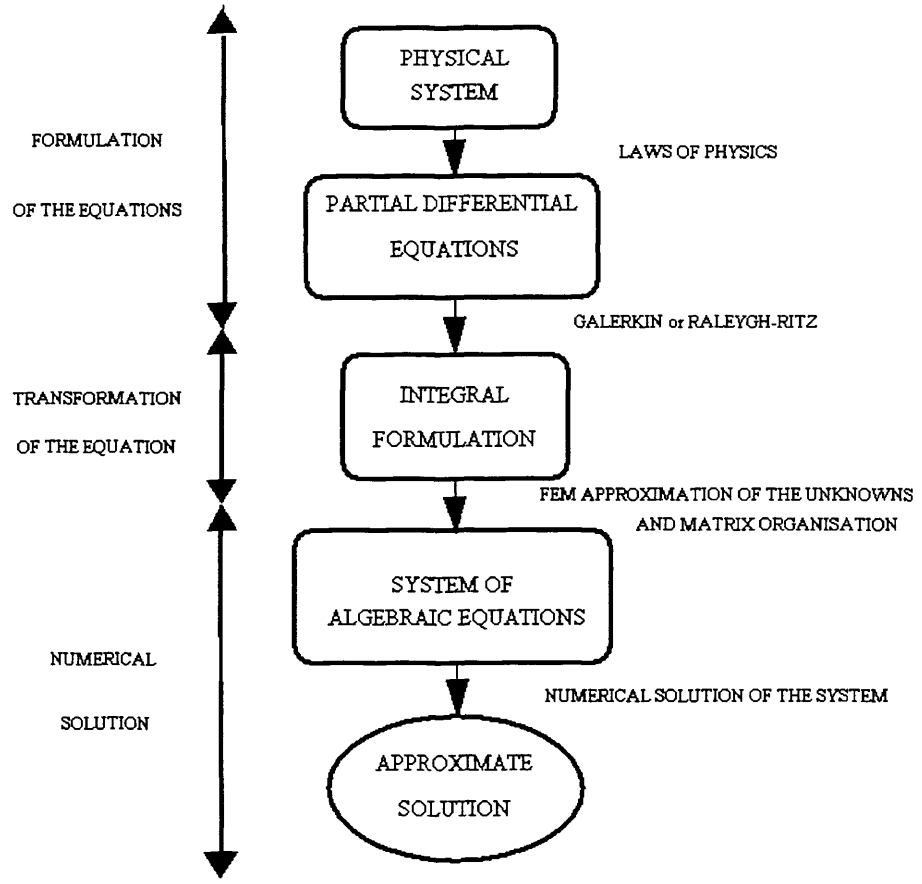

Fig. 2.13: FEM schematic showing path to arriving at a numeric solution.

The method of weighted residuals is more popular in electromagnetics due to its simplicity and accuracy. It is summarised below in the following steps:

i. **Meshing**: The computational domain is discretized in small contiguous cells called ***elements***.

ii. **Base functions approximation**: The unknown fields are approximated on each element using a finite set of pre-determined *base functions* with unknown coefficients. These functions are based on the edges or nodes of

the elements, with the requirement that the solution must be continuous across inter-element boundaries.

iii. **Elementary systems construction**: This step involves the model equations, which are valid on the entire computational domain, and in particular on each element taken separately. On each element, the unknown fields are replaced in the model equations by their corresponding base function elemental approximation constructed in Step 2. The model equations are then multiplied by weight functions and integrated over the element, thereby generating a system of equations for the element.

iv. **Global matrix assembly**: The elementary systems of all the elements, as well as the boundary conditions, are then assembled into a global matrix system **S[x]=b**.The order N of the matrix system corresponds to the total number of unknown field values at mesh nodes.

v. **Linearization of the global system**: if the matrix system is non-linear, e.g. the device involves non-linear magnetic materials, $\boldsymbol{S} = \boldsymbol{S}(\boldsymbol{x})$ and $\boldsymbol{S}$ depends on the 'a-priori' unknown solution $\boldsymbol{x}$. In such a case, $\boldsymbol{S}$ must be linearized before one can proceed with the resolution (or inversion $\boldsymbol{x}=\boldsymbol{S}^{-1}\cdot\boldsymbol{b}$) of the system.

vi. **Solving**: The solution $\boldsymbol{x}$ of the linearized matrix system finally provides the value of the fields at all the nodes.

vii. **Post-processing**: The solution is analyzed from the calculated global quantities and field plots.

2.7.3. FEM Software Processes

From a problem-solving perspective, there are three major stages in FEM modelling in every FEM software package; from defining the problem space to obtaining the required solutions. These stages include:

- ***Pre-processing*** – Model description and geometry construction. This phase includes definition of the boundary conditions of the physical system, and material modelling. It also entails the discretisation or meshing procedure of the total problem space.

- ***Solving*** – This phase is transparent to the user of FEM package. It includes the finite element processes of finding the numerical solution to the constituent differential equations and potentials for all the nodes of the problem set. Depending on the physical system input during pre-processing the solver algorithm can either be magnetostatic (no time variation), time harmonic (linear materials with sinusoidal excitation) or time transient (non-linear time varying systems). The constituent equations will change as per which solver is used, as will be explained in later.

- ***Post-processing*** – This phase involves interrogating the solver output for required quantities, and presenting them in required formats. Further calculations can also be performed on the solutions obtained from the solver.

2.7.4. Equations in Electromagnetic Fields Analysis for FEM

Electromagnetic modelling is focused on solving the differential equations that arise from field theory. The study of electromagnetic fields can be fully performed by means of five vector quantities and one scalar quantity viz: electric fields (**E** [V/m]), magnetic fields(**H** [A/m]), electric flux density(**D** [C/m^2]), magnetic flux density (**B** [T]), current density (**J** [A/m^2]), and the scalar electric charge Q [C/m^3]. These quantities are governed by the four partial differential equations known as Maxwell's equations:

$$\text{curl}\,\mathbf{H} = \mathbf{J} + \frac{\partial \mathbf{D}}{\partial t} \quad \textit{(Ampere's Law),} \qquad \textit{(2.19)}$$

$$\text{curl}\,\mathbf{E} = -\frac{\partial \mathbf{B}}{\partial t} \quad \textit{(Faraday's Law),} \qquad \textit{(2.20)}$$

$$\text{div}\mathbf{D} = \rho \quad \text{(Gauss's Law),} \qquad (2.21)$$

$$\text{div}\,\mathbf{B} = 0 \quad \textit{(Gauss's Law),} \qquad \textit{(2.22)}$$

together with the constitutive equations involving the material properties:

$$\mathbf{D} = \varepsilon_0 \mathbf{E} + P, \qquad \textit{(2.23)}$$

$$\mathbf{B} = \mu_0 (H + M), \qquad \textit{(2.24)}$$

$$\mathbf{J} = \sigma \mathbf{E}. \qquad (2.25)$$

With **P** being the polarisation of the electric poles.Static fields imply no time variation; setting the time derivatives to zero in Eqns. 2.19 and 2.20 give

$$\text{curl}\,\mathbf{E} = 0 \qquad (2.26)$$

$$\text{curl}\,\mathbf{H} = \mathbf{J} \qquad (2.27)$$

These are the uncoupled equations of static fields; the electrostatic field is determined from the solution of Eqns. 2.20, 2.23 and 2.24 with specified applied potentials or charges, and the magnetostatic field from the solution of Eqns. 2.19, 2.24 with specified current sources.

When the fields vary with time, the electric and magnetic fields are no longer independent but are coupled through the time derivatives in Eqns. 2.19 and 2.20. At low frequencies, such as the power frequencies where our devices of interest reside, the displacement current term $\frac{\partial \mathbf{D}}{\partial t}$ in Eqn. 2.19 is negligible in comparison with **J**, but Eqn. 2.20 shows that there is an induced electric field **E** associated with a time-varying magnetic field **B**. This in turn gives rise to an induced current-density **J** through Eqn. 2.25 if the material has a finite conductivity.

Eddy-current problems are readily solved when the applied excitation – usually **J**– is a sinusoidal time-varying quantity. The problem is then described as time harmonic. As with AC circuits, the problem is simplified by transforming to the frequency domain where time-varying quantities are replaced by time invariant complex quantities, and time derivatives are replaced by jω. The time-harmonic

FEM solvers return the real and imaginary parts of the complex potential from which the corresponding field may be calculated.

Most electromagnetic simulations are conducted using the scalar or vector approaches, depending on the quantities in the physical system. For the electrostatic field, Eqn. 2.26 implies that the electric field strength $\vec{E}$ can be expressed as the gradient of a scalar potential ***V***:

$$\vec{E} = -gradV \qquad (2.28)$$

This is the familiar electric potential, which is calculated by the electrostatic solver in FEM software. For example,, in 2-D problems with the z-direction assumed to be the same, the Cartesian components of **E** are given by the derivatives

$$\mathrm{E}_x = \frac{dV}{dx},\ \mathrm{E}_y = \frac{dV}{dy} \qquad (2.29)$$

Thus the electric field magnitude **E** is zero along any equipotential – contour of constant V – so the electric field lines are orthogonal to the equipotentials, and symmetry in the z-direction.

In a current-free region, where ***J***= 0, Eqn. 2.27 shows that it is likewise possible to express the magnetic intensity ***H*** as the gradient of a scalar potential Ω :

$$\vec{H} = -grad\Omega \qquad (2.30)$$

In the majority of magnetostatic problems the current density J is not zero, so the field cannot be expressed in terms of a scalar potential. It is beyond the scope of this thesis to exhaustively look through all the variations of the Maxwell's equations, but there is a reason for examining the vector potential in two-dimensions. Most high power devices such as transmission lines, electrical machines and transformers, exhibit some kind of symmetry; usually an axial symmetry that enables the potentials to be treated as two-dimensional.

Instead of the scalar potentials shown above, Eqn 2.31 is used to express the flux density B in terms of another vector A, through the equation

$$\vec{\mathbf{B}} = \text{curl}\vec{\mathbf{A}} \qquad (2.31)$$

where **A** is known as the **magnetic vector potential**. Simililarly in 2-D, the current and therefore the vector potential is in the z-direction. The components of **B** are then given by

$$B_x = \frac{\partial A}{\partial y}, \quad B_y = -\frac{\partial A}{\partial x} \qquad (2.32)$$

where $A=A_z$ is the magnitude of the vector potential. It follows from Eqn 2.31 that equipotentials – lines of constant A – are flux lines. Moreover, the magnetic flux between any two points in the x-y plane, for a depth d in the z direction, is given by

$$\phi = d(A_1 - A_2) \tag{2.33}$$

where ***A1*** and ***A2*** are the values of ***A*** at those points.

With this definition of flux, it is easier for engineers to define their systems in two dimensions, and this can ultimately help limit solving resources and also help reduce the pre-processing with use of symmetry. A similar extension, which makes the electromagnetic models closer to reality, is extending the above reasoning with potentials, into the third dimension. The equations and matrices become larger and more complex, but the basic ideas used above for the two-dimensions remain the same.

For the work carried out in this thesis, the FEM software which has been used is the MagNet package designed by Infolytica [42]. The use of any other package will be expressly stated where appropriate. The MagNet package was chosen because of its ease of use, and its flexibility in incorporating other specialised software like Matlab.

2.8. Summary

This section provided an overview of the technical background for the work carried out in the subsequent Chapters of this thesis. It has covered the basic magnetic material properties and how they are used in electromagnetic devices. An introduction to the methods of modelling used in current research has been examined. Of particular interest was the modelling of SCFCLs, wherein different methods used for its modelling were examined. The relative merits and demerits of

some of the methods were highlighted from the literature search, and the direction which will be pursued by this work in modelling a saturable core limiter was mapped out.

The concept of finite element modelling which will be used in conjunction with analytic modelling throughout this thesis was introduced to give a basic understanding of the underlying equation which will be encountered during the modelling work carried out in this thesis. Having examined the basic technical background of the thesis statement, the next Chapter will delve into the material selection and characterisation for the purpose of modelling the saturable-core fault current limiter.

[1] D.C. Jiles, Introduction To Magnetic Materials, Chapman & Hall,1998, Chapter 4, Pg 89

[2] R.K Rajput, Textbook For Electrical Engineering, Laxmi Publications, 2003,Chapter 5, Pg 245

[3] J. Kraus. D. Fleisch, Electromagnetics With Applications, WCB McGraw-Hill,1999, Chapter 7, Pg 405

[4] P. Weiss, J. Phys. 6 , 1907 , Pg 661

[5] D.D. Polluck, Physical Properties Of Materials For Engineers, CRC Press, 1993, Chapter 9, Pg 317

[6] N. A. Spaldin, Magnetic Materials: Fundamentals And Device Applications, Cambridge University Press, 2003, Chapter 2, Pg 11

[7] J.Kraus. D. Fleisch, Electromagnetics With Applications, WCB McGraw-Hill,1999, Chapter 8, Pg 421

[8] Ewing, J. A, Magnetic Induction In Iron And Other Metals,3rd Edition The Electrician Publishing Co. London, 1900.

[9] J.Kraus. D. Fleisch, Electromagnetics With Applications, WCB McGraw-Hill,1999, Chapter 8, Pg 424

[10] D.C. Jiles, Introduction To Magnetic Materials, Chapman & Hall,1998, Chapter 5, Pg 114.

[11] J. Takacs , Mathematics Of Hystetesis Phenomena, Wiley-VCH Verlag,2003, Chapter 6, Pg 55

[12] E. T. De Lachiesserie, Magnetism : Fundamentals, First Springer Science, 2003, Chapter 4, Pg 230

[13] Giorgio Bertotti, The Science Of Hysteresis, Elsevier Academic Press, 2007,Chapter 1, Pg 28

[14] Forbes T. Brown, Engineering System Dynamics: A Unified Graph-Centred Approach, CRC Press, 2007 Chapter 9, Pg 661

[15] J. Takacs , Mathematics Of Hysteresis Phenomena, Wiley-VCH Verlag,2003, Chapter 8 , Pg 150

[16] A. Krawczyk, S. Wiak, Electromagnetic Fields In Electrical Engineering, IOS Press, 2002, Pg 531

[17] A.E. Kenelly,IEE Trans., Am.,8, Pg 485, 1891

[18] R. Becker , W. Doring, Ferromagnetismus, Springer Berlin, 1938

[19] Yi Liu, David J. Sellmyer, D. Shindo, Handbook Of Advanced Magnetic Materials, Vol. 1,Springer, 2006,Chapter 8, Pg 391

[20] G. A. Maugin, Mechanics Of Electromagnetic Materials And Structures, IOS Press, Chapter 4, Pg 61

[21] Alex Van Den Boscche, Inductors And Transformers For Power Electronics, CRC Press, 2005, Chapter 1,Pg. 12

[22] Marikani, Engineering Physics, Raj Press, 2009, Chapter 8 , Pg 297

[23] I. J. Nagrath ,Electric Machines, Tata-McGraw Hill, 2004,Chapter 1, Pg 18

[24] F. Fiorillo, Measurement And Characterisation Of Magnetic Materials, Elsevier Press, 2004, Chapter 6, Pg 280

[25] S. Tumański, Principles Of Electrical Measurement, CRC Press, Chapter 1, Pg 30

[26] J. Sievert,Recent Advances In The One And Two Dimensional Magnetic Measurement Technique For Electrical Sheet Steel, IEEE Trans. Magn., Vol 26, Pg 2553-2558, 1990

[27] New Fault Current Limiter For Utility Substations , By Frank Darmann , Tim Beales , Australian Superconductors Report , 2005

[28] CIGRE WG A3.10, Fault Current Limiters – Fault Current Limiters In Electrical Medium And High Voltage Systems, CIGRE Technical Brochure, No. 239, 2003

[29] CIGRE WG A3.16, Guideline On The Impacts Of Fault Current Limiting Devices On Protection Systems, A3-06 (SC) 33 IWD, Final Draft, 2006

[30] CIGRE WG A3.10, Fault Current Limiters – Fault Current Limiters In Electrical Medium And High Voltage Systems, CIGRE Technical Brochure, No. 239, 2003

[31] B.W. Lee, J. Sim, K.B. Park, I.S. Oh, Practical Application Issues For Superconducting Fault Current Limiters In Electric Power Systems, IEEE Trans. Applied Superconductivity,Vol. 18, NO. 2, June 2008

[32] B. P. Raju, K. C. Parton, And T. C. Bartram, A Current Limiting Device Using Superconducting D.C. Bias Applications And Prospects, IEEE Trans. Power Appar. & Syst., Vol. 101, Pg. 3173–3177, 1982

[33] J. Langston Et Al., A Generic Real Time Computer Simulation Model For Fault Current Limiters And Its Application To System Protection Studies, IEEE Trans. Applied Superconductivity, Vol. 15, NO 2, June 2005

[34] Z. Xuhong, Z. Youqing, Z. Zhifeng, Design Of Saturated Iron Core Superconducting Fault Current Limiter Based On Numerical Calculation, IEEE/PES Transmission And Distribution Conference & Exhibition, Pg 1-5, 2005

[35] Tsutomu Hoshino , Salim, K.M.; Kawasaki, A.; Muta, I.; Nakamura, T.; Yamada, M.; Design Of 6.6 KV, 100 A Saturated DC Reactor Type Superconducting Fault Current Limiter, IEEE Trans. On Applied Superconductivity, Vol. 13, Pg 2012-2015, June 2003

[36] S. B. Abbott Et Al., Simulation Of HTS Saturable Core-Type FCLs For MV Distribution Systems, IEEE Trans. On Power Delivery, Vol. 21, NO. 2,Pg 1013 – 1018, April 2006

[37] T. Janowski Et Al.,Properties Comparison Of Superconducting Fault Current Limiters With Closed And Open Core', IEEE Trans. On Applied Superconductivity, Vol. 13, No. 2, Pg. 2072 – 2075, June 2003

[38] D. Cvoric, S. W. H. De Haan And J. A. Ferreira, New Saturable-Core Fault Current Limiter Topology With Reduced Core Size, IEEE Power Electronics Specialists Conference, 2008, Pg 3967 – 3973, June 2008

[39] A. Polycarpou, Introduction To Finite Element Method In Electromagnetics, Morgan & Claypool, 2006, Chapter 1, Pg. 3

[40] J. L. Volakis, A. Chatterjee, L. C. Kempel, Finite Element Method For Electromagnetics, IEEE Press , 1998, Chapter 3, Pg 66

[41] By J. Bastos, N. Sadowski, Electromagnetic Modelling By Finite Element Methods, Crc Press, 2003, Chapter 3, Pg 123

[42] MagNet™,Infolytica Corp.,www.infolytica.com, 2007

Chapter 3. Characterisation, Measurement and Data Preparation for Material Modelling

3.1. Introduction

In order to find the appropriate materials for the design and development of an electromagnetic application such as a fault current limiter, characterisation and modelling of the candidate ferromagnetic material, is one of the first steps in the process. These initial steps help not only in identifying the appropriate soft ferromagnetic material and assessing its suitability for the particular application, but it also provides data for use in the FEM simulations and model development. This thesis focuses on the saturable core inductive fault current limiter (SCFCL), its design, and material selection. The material selection aspect entails finding the appropriate ferromagnet for this device.

When examining how the FCL functions in Chapter 2, it follows that the selected material should fulfil two important prerequisites:

- The desired material should have low hysteresis losses.
- The desired soft ferromagnetic material needs to have low differential permeability in the region of normal operation and high differential permeability in the region of fault limiting operation. From this a maximum amount of change in inductance should occur between the saturated and unsaturated states of the material.

These requirements amongst others, let to the selection of grain-oriented high permeability electrical steels, specifically M4 steel (1.25-1.40% Carbon (C), 0.15-0.40% Manganese (Mn), 0.20-0.45% Silicon (Si), 3.75-4.75% Chromium (Cr), 0.3% Nickel (Ni), 4.25-5.50% Molybdenum (Mo), 5.25-6.50% Tungsten (W), 3.75-4.50% Vanadium (V), 0.25% Copper (Cu), 0.03% Phosphorus (P), 0.03% Sulphur (S), and the base metal Iron (Fe)).

Such steels have high permeability and low losses, and hence can prove challenging in characterisation and measurement using generic measurement systems. Since providing data for modelling is one of the principal reasons for these measurements, a system was designed using a closed magnetic circuit design as an immediate way of studying the intrinsic properties of the material, without incorporating the additional effects (classical and excess losses) that result with AC measurements. These measurements are useful for the comparative purposes, however it is understood that DC curves represent the rate independent B-H behaviour, which is related only to the sequence of values attained by a quasi-static applied field, and not the rate of change of that field [1].

It was also important to measure the materials properties under time varying AC fields, given that this is the condition under which the core will be operated in the actual fault current limiter.

The approach taken in this research was first to get the intrinsic characterisation with DC measurements for a number of materials for comparison, and subsequently, to take AC measurements for a few selected materials in order to have more appropriate data for the operating conditions.

3.2. DC Measurement Setup

3.2.1. DC Permeameter System Overview

The measurements performed on M4 steel samples, were taken on a customised **DC** permeameter measurement system (Fig. 3.1). This system provided a flexible DC measurement platform for a wide range of soft magnetic materials. It was built because of the need in this project to characterise the ferromagnetic candidate material by precisely measuring hysteresis loops. The aim was to have

magnetisation data with high data point density for the samples over the whole measurement range.

The system hardware was controlled by custom written software in LabView™ to provide control for a bipolar current source (from the power supply amplifier unit), that was used in generating the magnetising current needed. This could either drive the primary magnetizing winding in the Epstein system described in Chapter 2, or control the field in the electromagnet.

The magnetising field was changed continuously, but at 0.25 Hz to avoid eddy current effects. This essentially makes the method more appropriately termed a quasi-static measurement, instead of a DC measurement. The data acquisition (DAQ) card receives input from the fluxmeter, which integrates the flux picked up by the secondary coils in the Epstein frame. The fluxmeter and gaussmeter were connected by GPIB connectors.

The magnetic field strength at the surface of the test sample was either measured by a Hall probe connected to the gaussmeter (best practice), or in some cases by measuring the voltage across a precision resistor in the ground return of the magnetising winding. The magnetic flux density was measured by connecting an integrating fluxmeter to a second winding wound tightly around the sample (in the case of the electromagnet) in order to minimise measurement errors due to magnetic flux in the region between the sample and the winding.

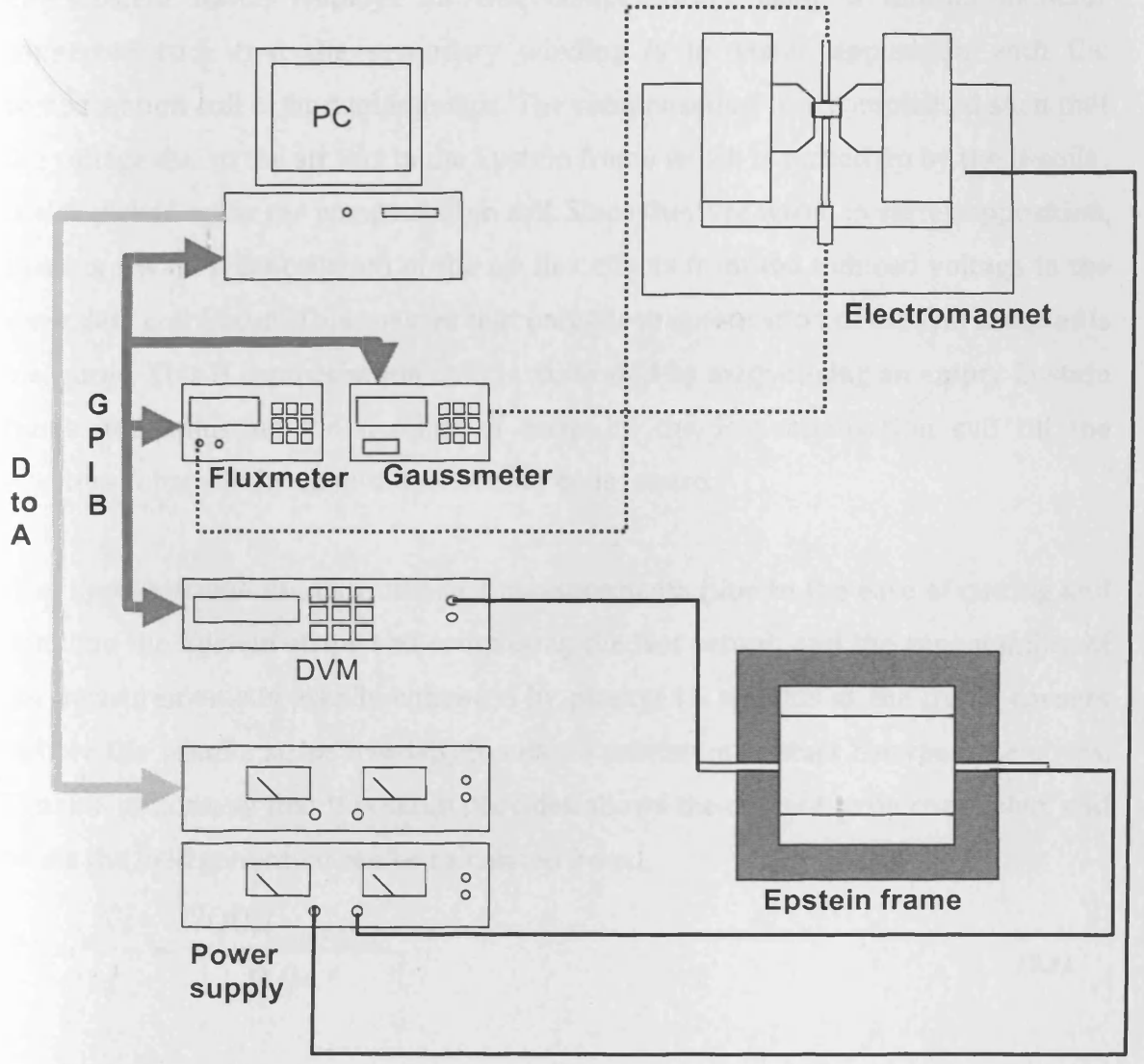

Fig. 3.1: Schematic of the DC Permeameter showing closed circuit measurement systems using Epstein frame and electromagnet.

3.2.2. *Epstein Frame System Measurements*

In this system, the test circuit is formed by a closed circuit Epstein frame (which is defined to meet the international standard IEC 404-2). In the setup, the DC permeameter system measures 30x3x0.03 cm strips of M4 material, cut in the direction of interest (usually the rolling direction) and inserted in sets of four into the 2T Epstein frame with 700 turns for each of the primary and secondary coils.

The Epstein frame employs air flux compensation using a mutual inductor connected such that the secondary winding is in series opposition with the compensation coil or mutual inductor. The compensation is accomplished such that the voltage due to the air flux in the Epstein frame which is picked up by the B-coils , is also picked up by the compensation coil. Since they are wired in series opposition, there is always a cancellation of the air flux effects from the induced voltage in the secondary coil circuit. This ensures that only the magnetisation of the test samples is measured. This H compensation coils is calibrated by magnetising an empty Epstein frame and adjusting the number of turns on the H-compensation coil till the effective voltage induced in the secondary coils is zero.

The Epstein frame used ensures fast measurements (due to the ease of cutting and handling the Epstein strips and completing the test setup), and the repeatability of the measurements is usually enhanced by placing 1N weights at the frame corners (where the sample strips overlap) to ensure maximum contact between the strips. The flux uniformity that this setup provides allows the current to be controlled, and hence the field generated can be calculated from:

$$H = \frac{NI}{l} = \frac{700.I_{controlled}}{0.94} \qquad (3.1)$$

where $I_{controlled}$ is the current supplied by the computer-regulated power amplifier, and l is the standard mean magnetic path length for a 25 cm Espstein frame [2].
The secondary sensing coils pick up an induced emf from the flux linking these coils through the sample. This emf is generated following Faraday's law,

$$\xi = -N\frac{d\phi}{dt} \qquad (3.2)$$

where N is the number of turns in the sensing coil, ξ is the induced emf, and ϕ is the flux linkage of the coil. For a sample cross-sectional area, **A** (obtained by

measuring the total sample weight and length and assuming the density), the linked flux density can be calculated as B= ϕ/A. Hence for the stationary sense coils, the emf induced leads to the calculation of the flux density by the fluxmeter using

$$B = -\frac{1}{NA}\int \xi dt \qquad (3.3)$$

It is worth noting at this juncture that the flux density measured in an Epstein frame test will differ from that which could be measured by placing the sense coil directly on the sample (as is in the electromagnet). This difference might introduce some inherent differences in the measured curves from the manufacturer information sheet, and hence need a correction in order to be able to correlate them. To understand this, it is essential to start from the general equation of magnetic induction

$$B = J + \mu_0 H \qquad (3.4)$$

where $\boldsymbol{B}$ is magnetic flux density, J =μ_0M (such that when M=M_s J=B_s= $\mu_0 M_s$) is magnetisation and H is magnetic field.

Fig. 3.2(a) represents an idealistic case of the electromagnet wherein the search coil is wrapped in a close configuration around the sample. However, in the case of the Epstein frame system, the sample does not occupy the whole cross-sectional area of the search coil as is shown in Fig.3.2 (b). In this configuration, there still exist a layer of air between the sample and the search coil, and at high fields this will play a role as well. It is because of this that an air flux compensation coil is introduced in series with the sensing coil. The formula for the magnetic flux density at magnetic fields can now be written as:

$$B = J_{sample} + \mu_0 H_{SearchCoil} \qquad (3.5)$$

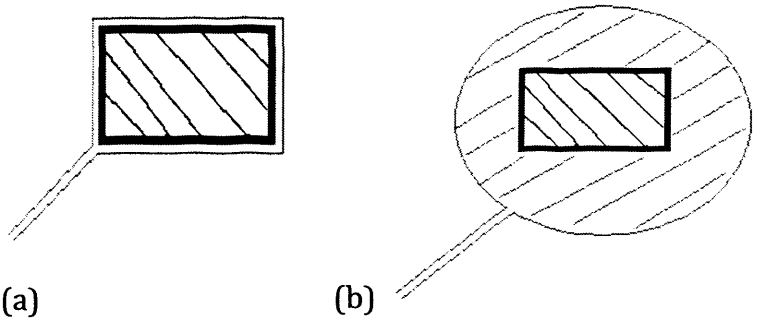

Fig. 3.2: Cross-sectional areas of search coil position (red) relative to sample position (black) for measurements for the case with (a) close configuration (electromagnet) and (b) loose configuration (Epstein frame)

Due to the presence of the air gap, compensating coils are used in the Epstein frame system, such that it incorporates negative flux from the air around the coil:

$$B_{measured} = J_{sample} + \mu_0 * H_{SearchCoil} - \mu_0 * H_{SearchCoil} = J_{sample} \qquad (3.6)$$

What is being measured in the Epstein frame system has units of Tesla, but it is actually magnetisation **M**. Hence the saturation magnetization $\mathbf{M_s}$, is the maximum reading obtainable from the Epstein frame system.

For the purposes of this thesis, measuring B-H far into saturation is the main objective given that the devices to be modelled function at high fields. Consequently the Epstein frame was used to measure **J** (or ***M***) vs ***H*** till saturation, and the term $\mu_0 H_{sample}$ was added to find **B**.

Secondly, the magnetic field **H** in the Epstein frame system is not measured directly using a Hall probe, but is instead calculated using Eqn. 3.1. At high magnetic field strengths when the relative permeability of the material comes very close to 1 (the permeability of air), the mean path length *l* increasingly becomes a function of he applied field and Eqn.3.1 is no longer valid [3]. Furthermore, at higher magnetisation fields, more feedback systems are required which introduce higher levels of complexity in the setup. These reasons therefore limit the magnetic

induction level for which the Epstein frame can be confidently used to do magnetic measurements to below 1.9T only, otherwise the errors mentioned above become difficult to quantify and account for.

With these issues in mind, the DC permeameter was used up to about 1.9T and the B-H curves obtained were used for material characterisation purposes, as the fields generated were not strong enough to take the M4 samples into the expected magnetic induction regimes for the actual device (> 2T). Such high field measurements were made using the electromagnet with a Hall-effect probe to measure the H-field and a sensing coil wrapped tightly around the sample. This allowed for measurements at higher field strengths.

3.2.3. Measurement System Calibration

The fluxmeter in the DC permeameter setup is highly sensitive but prone to the problem of drift, which is the change over time of the zero reference point for the magnetic flux integration. This is caused by leakage currents and stray fields from the wires in the circuitry around the integrator (or fluxmeter) [4]. If calibration of the fluxmeter is not done, it will continually integrate a small out of balance voltage with time, giving an erroneous varying magnetic induction **B**.

The DC permeameter measurements need a reference point for the sample under investigation, and the reference point for these measurements is usually the demagnetised state of the specified sample. This state is achieved by applying an alternating decaying field with no DC offset to the test sample with its amplitude starting from a high field so as to insure technical saturation. Another practical method used in correcting drift is linear numeric compensation wherein the **B** obtained from the air coil is recorded, and this value is introduced as a negative offset to all measured values. The offset is consistently subtracted from the integrated induction. The processes described above ensure that the calculations

performed give correct values that are closer to the actual value of the B-field than the raw data because they take into account the effects of drift.

3.3. Magnetisation Curve Measurement Procedure

Before a test run was started, it was essential that the test sample was fully demagnetised. The test control program can operate in two distinct modes. The first mode drives the current such that the rate of change of magnetic field strength is constant and measures the field strength and flux density at a predefined set of evenly spaced discrete fields. This mode is inappropriate for very soft materials such as the grain oriented M4 steel samples because the discrete spacing of the field is not fine enough in resolution to measure many points at the highest slope region of the hysteresis loop. Hence a more complex adaptable fine control algorithm is required over the magnetising current at low values of field (less than 40 A/m).

This fine control is not easy to achieve and obtaining an appropriate number of data points on the magnetisation curve becomes very difficult. Therefore a second mode is preferred that uses a predefined set of discrete flux densities, at appropriate increments (0.1T for example). This mode uses a variable rate of change of magnetic field strength which is dependent on the rate of change of flux density. Depending on the feedback acquired, the rate of change of the discrete field values can be altered in order to ensure that a measurement is obtained at any particular point. The control of the flux density rate is accomplished by an adaptive digital negative feedback algorithm [5] incorporated into the software.

Hysteresis loops were then obtained for several values of maximum field. After each test run, the sample was routinely demagnetised, by selecting a demagnetising field value greater than the maximum field value attained by the previous measurement. Fig. 3.3 shows one of such loops obtained at maximum field value of 1kA/m.

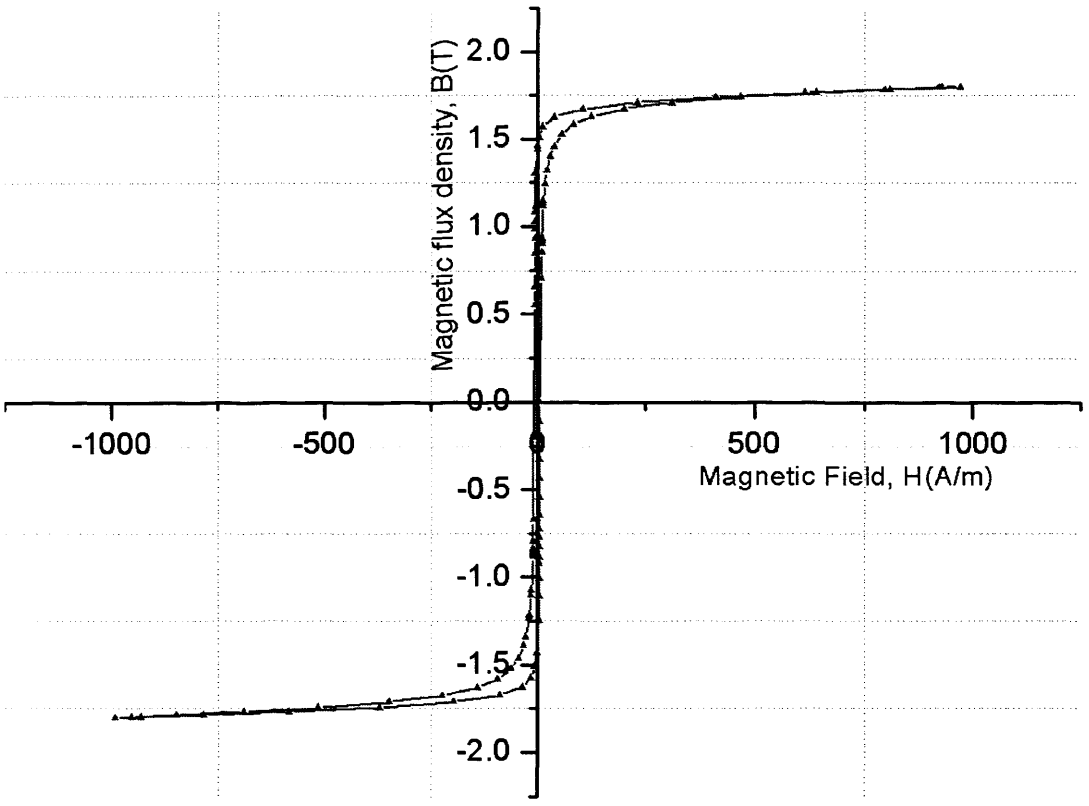

Fig. 3.3: Epstein frame measurement of M4 steel sample up to the maximum field value 1kA/m

Fig.3.3 shows a DC B-H loop measurement for M4, showing little hysteresis loss and symmetry with the appropriate correction of drift. The initial hysteresis loops taken were used to determine fluxmeter drift which was apparent from the non-symmetry of the B-H loop. The offset in ***B*** was calculated from such loops and used for subsequent set of measurements on for the sample, resulting in symmetrical zero-offset loops like that shown in Fig. 3.3.

3.4. Anhysteretic and Initial Magnetisation Measurements

As earlier argued in Chapter 2, the modelling representation of soft magnetic materials, (in our case M4 steel) can often be adequately represented by the anhysteretic magnetisation curve for such a material. The measurements in Fig.3.3 actually confirm this assumption for M4 steel as even at a maximum field of only 1 kA/m, the loop is very thin, with very little hysteresis. If the maximum field range is increased, this loop only appears thinner as it has more data points from negative to positive saturation, to which its anhysteretic curves becomes a very good approximation. Thus hysteresis loop measurements described above were not only to characterise the material, but also be used to construct their anhysteretic equivalent [6].

The process involves separating the loop into two single-function curves $f(x^+)$ (curve from negative saturation to positive saturation) and g(x-) (curve from positive to negative saturation); inverting g(x) (by changing the sign on the values) to get $Inv(g(x^-))$; adding both curves and diving by two to get the new calculated anhysteretic curve, Anhyst(x) passing through the origin.
Symbolically,

$$Anhyst(x) = \frac{f(x^+) + Inv(g(x^-))}{2} \qquad (3.7)$$

This alternative algorithm, although only an approximation, is used instead of a direct measurement for reasons of convenience. Furthermore the problems faced with measuring the anhysteretic curves of very soft magnetic materials such as silicon iron, and controlling the rate of change of field during the anhysteretic measurements makes the procedure described above more attractive, as it provides a faster and acceptable alternative. This process yielded the anhysteretic curve for M4 steel as shown in Fig. 3.4.

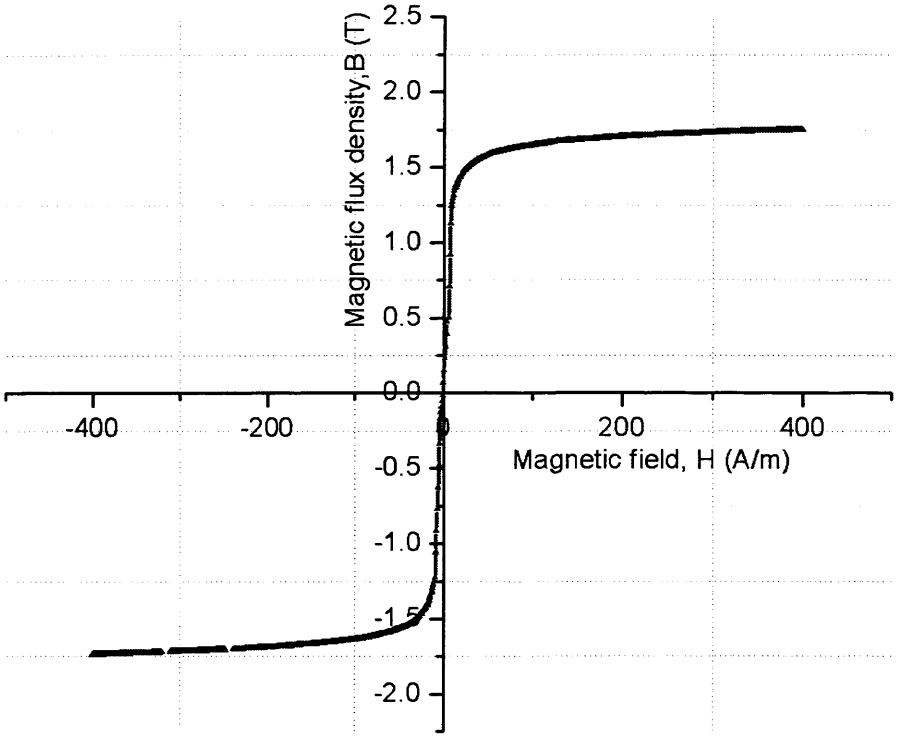

Fig. 3.4: Anhysteretic curve for M4 obtained from hysteresis loop by applying anhysteretic algorithm in Eqn. 3.7.

Another dataset of interest that was measured using the permeameter, was the initial magnetisation curve. As earlier mentioned in Chapter 2, in soft magnetic materials such as the M4 steel under investigation, the anhysteretic curve and the initial magnetisation curves are quite similar and for most modelling purposes can be used interchangeably.

Obtaining the initial curve required demagnetising the M4 steel samples, and then slowly magnetising the sample strips to the highest possible magnetic fields. Given the field generation limitations of the Epstein frame test for high field magnetisation, an M4 steel sample was inserted into an electromagnet measurement system, wherein fields up to 15 kA/m were obtained. The effective field on the sample was measured using a Hall probe mounted on the surface of the sample to detect the tangential field. For validation purposes, these initial

magnetisation curves were compared with the magnetisation curve information obtained from the industrial manufacturers' manual. A direct comparison was made between the two measurements as show in Fig. 3.5.

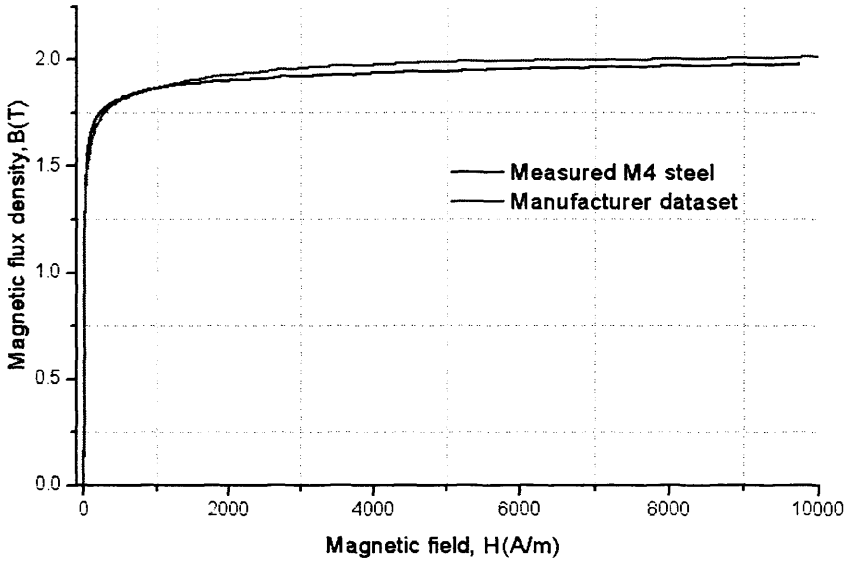

Fig. 3.5: Measured initial magnetisation for M4 steel from electromagnet compared with manufacturer dataset.

Fig. 3.5 shows that the permeameter measurement is comparable with the manufacturer data, especially at the major regions of interest (the knee point where $d^3B/dt^3 = 0$ provides the largest permeability change, and the origin), hence suggesting that the measurements are adequate enough for use in modelling the M4 steel.

3.5. AC and DC Measurement Comparison

In performing the DC measurements, the primary motive was to obtain accurate data for characterisation of the candidate material and to obtain the material parameters necessary to incorporate a model of the material in software simulators. Another area of interest to the thesis was to find out how the material behaved under AC conditions given that the high power devices of interest in this thesis make use of ferromagnetic cores which necessarily function under AC conditions.

Furthermore, performing AC measurements provides more information on the relevant material properties beyond those already obtained, hence providing more parameters and magnetic information needed in confirming the choice of material for this particular application. It is one objective of this thesis to ascertain that the analytic expressions obtained for the DC anhysteretic curves were still valid in representing the ferromagnetic material even in an AC environment, and to make any necessary adjustments or corrections.

To achieve this aim, AC measurements were made and the results compared with the DC measurements. It follows that because of classical eddy current losses and excess losses, the AC measurements will necessarily have wider hysteresis loops than the DC measurements, but the expectation was that the general shape of the loops curve obtained from the AC measurements would correlate with those from the DC measurements, such that an anhysteretic curve derived from either of these loops would be an appropriate representation of the material. This will validate the use of the parameters and analytic the representation of the M4 steel obtained from these measurements, in the modelling of the device.

The permeameter equipment set up to measure the DC B-H loops was also appropriate for use in obtaining AC measurements up to the 50-60 Hz power frequency range, with a few modifications. This is so because these frequencies used are still sufficiently low for the effects of stray capacitances and leakage inductances on the circuit to be ignored. Attention was paid to some aspects which needed alteration from the DC system as follows:

Firstly, the rate of change of field was increased in the LabView system control software configuration to the appropriate level (50Hz) for AC measurements. Also, the Epstein frame standard is valid and reproducible at this frequency (under the IEC-60604-2 standard) and adequate data acquisition is ensured by using high sampling rate data acquisition cards (DAQs). Secondly, due to the thermal

coefficients of all the copper wiring involved, calibration of the fluxmeter was done frequently, especially after maximum magnetisation (high current) test runs.

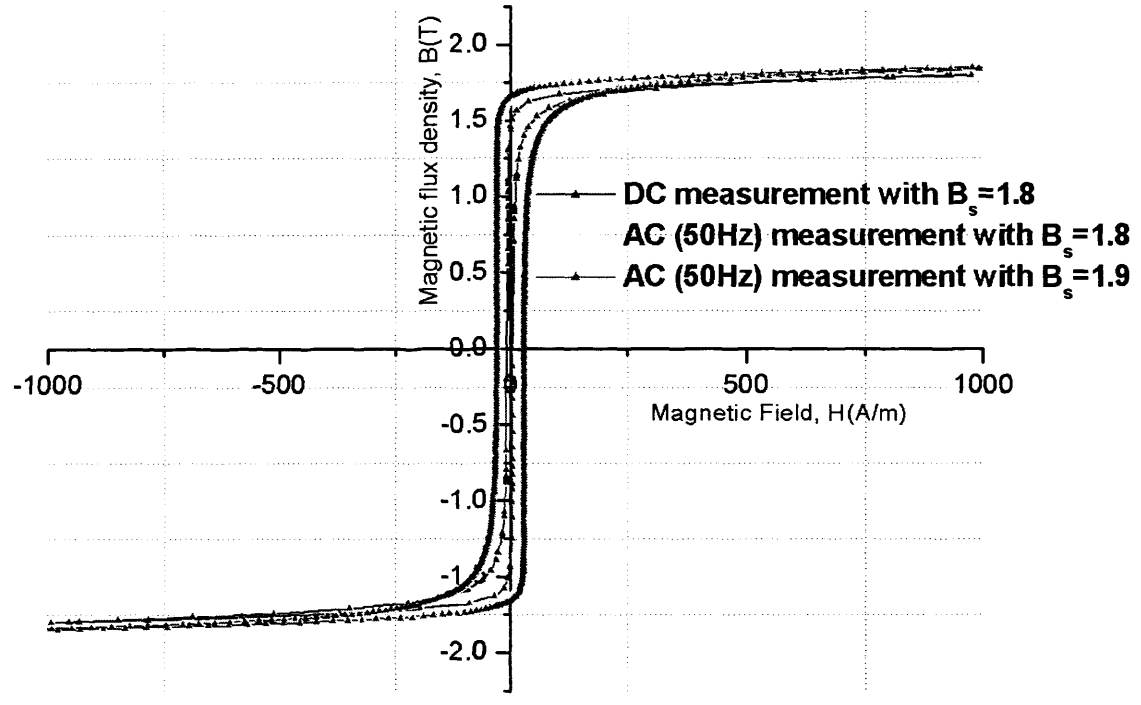

Fig. 3.6: B-H loop comparison between DC measurements and AC measurements (Bs= 1.9T and 1.8T)

The measured AC hysteresis loop results in a wider loop due to higher hysteretic losses as expected. Furthermore, a slight difference in magnetisation is noticed (a 0.08% difference between the flux density values at 500 A/m), which is expected, depending on the maximum value of B_s used in the particular measurement.

These differences will have little effect to the choice of the analytic function used to represent the material in the model, as the 'knee' slope and maximum magnetisation do not vary significantly, especially over the large range of magnetic fields for which the model functions will be used. This assertion, that the slight variance of the material parameters will not affect the general representation of our material is investigated in a subsequent Chapter.

3.6. Curve Fitting for Analytic Anhysteretic Curve Representation

After obtaining the anhysteretic curves at various maximum magnetic field strengths, and also obtaining data for the initial magnetisation curves, the next step towards obtaining a representative function for the mathematical models was to find the most suitable analytic expression for the data obtained. This was to facilitate the inclusion of the model of the material into the mathematical model of the engineering simulator for fast calculation, which is essential at the initial stages of design.

Non-linear anhysteretic representations of the M4 steel core material that was measured above entails ideally devising closed form functions, which represents the magnetic characteristics of the FCL core as closely as possible throughout its performance cycle. Usage of these closed form functions will allow quick calculations in assessing the performance and functionality of the FCL. Data analysis and curve fitting were carried out to identify mathematical expressions that could adequately represent this specific dataset with as much accuracy as possible.

Various mathematical expressions are commonly used in the magnetic property modelling theory, some of which were examined in Chapter 2, and two of such functions in particular were investigated to find the best fit for the M4 steel dataset obtained from the measurements. Attention was directed towards the particular regions of interest on these curves, which are the 'knee' point of maximum curvature (where $d^3B/dt^3 = 0$), the origin, and the approach to saturation of the anhysteretic curve. This was in order to improve the magnetic representation of the curve at low fields while also adequately representing the curve as the magnetisation values increase into high field regimes.

This process also served to extract the material parameters (the $\boldsymbol{a}$-parameter and the $\boldsymbol{B_s}$-parameter) that could be used to analyse the behaviour of the material, and

examine the macroscopic effect of such material parameters on the performance of the device when they are investigated in the mathematical model.

The hyperbolic functions along with modifying parameters were judged to be the most adequate to use in a non-linear representation of the soft ferromagnetic data. As discussed in Chapter 2, the two viable candidate functions are the tanh(x) function for uniaxially anisotropic materials, and the Langevin-Wiess formulation (from here-on called the modified Langevin function) for isotropic materials. Figs. 3.7 & 3.8 show how these functions fit the measured data after the data was point correlated and interpolated for point step uniformity.

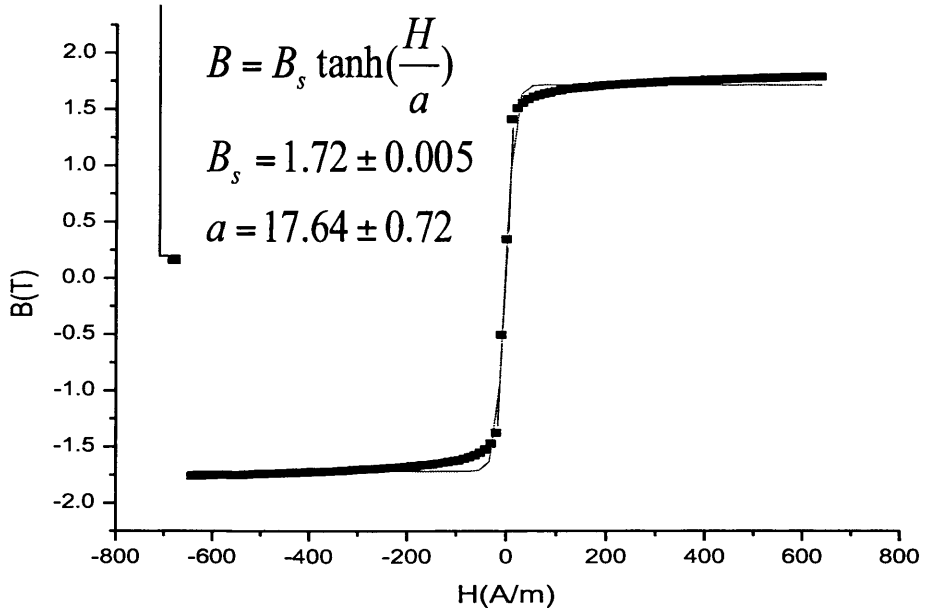

Fig. 3.7: Fitting of Tanh(x) function (red) to measured data (black), showing error margin of extracted parameters **Bs** *and* **a**

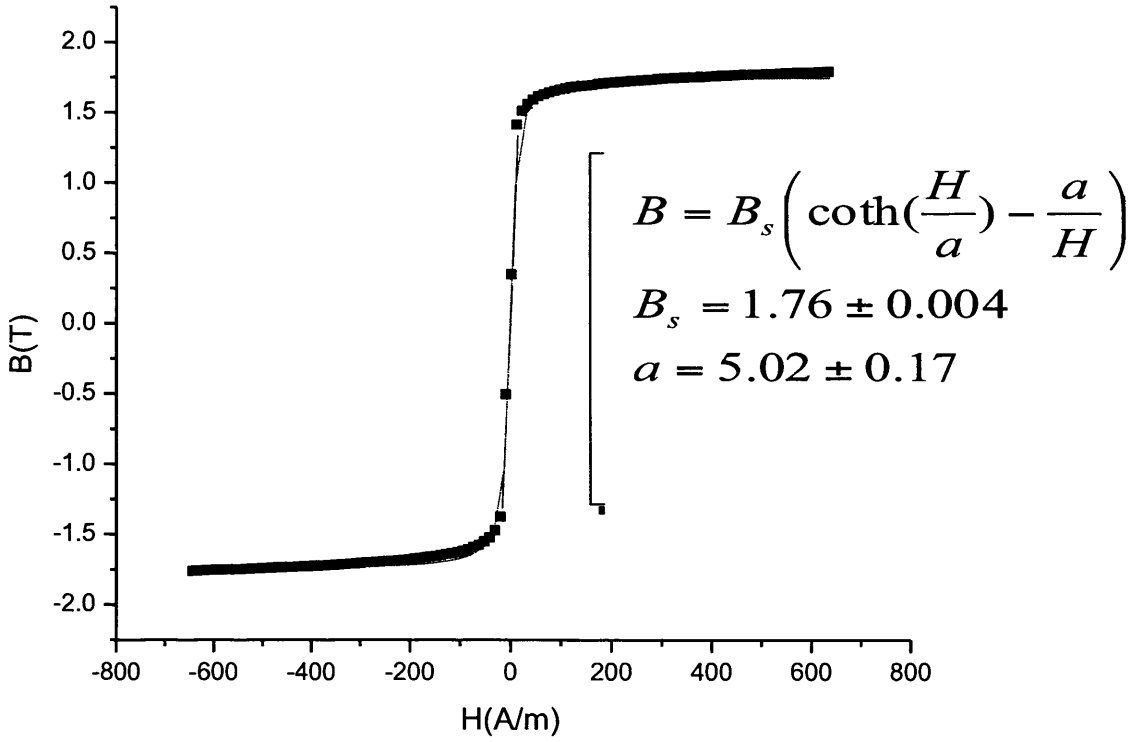

Fig. 3.8: Fitting of modified Langevin function (red) with measured data (black)

The modified Langevin function showed a better fit to the data as shown in Fig. 3.8. It gives better representation at the regions of interest as compared to the Tanh(x) function. The fundamental parameters of interest - $\mathbf{B_s}$ and **a** - are directly calculated from fitting the function to the anhysteretic magnetization data. These parameters will be investigated to observe their effects on device performance. They provide a method of determining how the changes in the material properties affects the performance of the whole device system, and how to select the best material for the application by modifying these parameters to get optimum performance from the device.

3.7. Summary

In this Chapter, the various measurement configuration used for obtaining the data for the M4 steel samples were examined and the types of measurements needed were presented. A contrast between the AC and DC setups and results was given and

comparisons for validation between measured graphs and manufacturer-provided information were undertaken. Furthermore, various analytic representations of soft magnetic materials were fitted to the data to obtain the best functional representations for modelling, and the important magnetic parameters necessary for building an analytic equivalent circuit model for the FCL were also determined.

Furthermore, the methods used for characterisation and measurements of the M4 electrical steel material were detailed. The limits of the laboratory experimental setup were analysed, and how these limitations reflected on the data obtained.

[1] Fausto Fiorillo, Measurement And Characterisation Of Magnetic Materials, Elsevier Academic Press, Chapter 7, Pg. 337

[2] H. Czichos, T. Saito, L. Smith, Springer Handbook Of Materials Measurement Methods, Volumes 978-20786, Springer , Chapter 10. Pg 503

[3] P. Marketos, S. Zurek, A.J. Moses, A Method Of Defining The Mean Path Length Of An Espstein Frame, IEEE Trans. Mag. , Vol 43, Issue 6, Pg. 2755-2757, 2007

[4] American Society For Testing And Materials, Direct-Current Magnetic Measurements For Soft Magnetic Materials, Chapter 1, Pg. 14, 1970

[5] Zurek, S., Marketos,P.;Meydan, T.;Moses, A.J.,Use Of Novel Adaptive Digital Feedback For Magnetic Measurements Under Controlled Magnetizing Conditions, IEEE Trans., Magn., Vol. 41, NO. 11, Nov 2005

[6] D.C. Jiles, J.B. Thoelke, M.K Devine, Numerical Determination Of Hysteresis Parameters For The Modeling Of Magnetic Properties Using The Theory Of Ferromagnetic Hysteresis, IEEE Trans. Mag.,Vol 28,Issue 1,Pg 27-35, 1992

Chapter 4. Problems Associated With Measurements and Data Processing for Modelling At High Flux Densities

4.1. Introduction

In this Chapter some of the intrinsic challenges and shortcomings noticed in measurement of magnetic fields and flux densities in high field regimes were examined. The challenges faced in measuring electromagnetic parameters for this study were detailed and the proposed solutions used to circumvent these problems were analysed.

Also, the Chapter examined material data preparation for use in FEM modelling of the ferromagnetic core. It highlighted some of necessary modifications to the process of data calculation and acquisition commonly used in data handling in an effort to improve on the general accuracy of the material representation, and data acquisition process for devices that function at high flux densities.

The use of the ferromagnetic M4 steel in either the FCL systems on which this Thesis focuses, make use of the property of ferromagnets as flux concentrators because of their high permeability and consequently low reluctance. In the FCL, it is desirable to saturate the core for the device to function properly, with a low inductance under normal operating conditions, and hence finding the B-H characterisation at high fields is essential. In this case, the design has a closed magnetic circuit. Consequently, the analysis of the problems encountered in measurement and data modelling will be examined from a perspective of a closed circuit made up of a ferromagnetic M4 steel core. Firstly examination of some theoretical limitations of the laboratory setup was carried out, and then a description of how these problems were solved is described. The underlying equations and assumptions used in the

software will also be analysed to show their shortcomings and better equations were developed for this particular case to improve the accuracy of modelling. Finally a discussion of the techniques developed for extrapolation of the data to higher flux densities than can be measured was undertaken, with a description of the most suitable methods that were adopted for the data modelling of the magnetic properties of the test samples.

4.2. Measurements Close to Saturation for Electrical Steels

While taking the closed circuit measurements of the samples of M4 steel, it was of interest to determine the permeability of the material at high induction levels of 2T and above, given that the FCL need to operate at these high flux densities. Performing laboratory measurement to such high fields with the permeameter presented some difficult challenges.

4.2.1. Field Generation Limitations

One of the principal problems encountered during measurement, was the inability to generate the amount of ***H***-field necessary to magnetise the samples in order to obtain B-H data at the flux densities required for the operation of such power devices. To illustrate the problem, consider the saturation magnetisation (B_s) for M4 electrical steel at 2.03 T (the manufacturer's specification). Assuming that the saturation of the core is reached at an arbitrarily high magnetic field 100kA/m (a safe assumption given how soft the material is, as per the measurements obtained in Chapter 2), the magnetic induction will be:

$$B = B_s + \mu_0 H = 2.03 + 0.126 = 2.156\,T \qquad (4.1)$$

If the operational range of the device is taken above 2T, the magnetic field required to achieve such values is:

$$B = B_s + \mu_0 H \quad \rightarrow \quad \mu_0 H = B - B_s \quad \rightarrow \quad H = \frac{B - B_s}{\mu_0} \qquad (4.2)$$

Therefore, for M4 with target B = 2.3 T and B_s = 2.03T saturation magnetisation, the required applied field will be:

$$H = \frac{2.3 - 2.03}{\mu_0} = 215\ kA/m \qquad (4.3)$$

The usual standard formula used for calculating magnetic fields in a closed magnetic circuit is:

$$H = \frac{NI}{l} \qquad (4.4)$$

This formula represents an average field and does not allow for non-uniform distribution of the field due to leakage flux, geometrical variations and the non-uniform distribution of magnetomotive force (mmf).

For further illustration of this example, values for a SCFCL prototype core design were used, with number of turns, ***N*** = 171, magnetising current, ***I***= 77 A. and, mean magnetic path length, ***l***= 2.8m

Using Eqn. 4.4, the average field strength generated, H = 4.7 k/Am. This is only slightly over 2% of the 215 kA/m that is required to reach 2.3 T according to calculations (Eqn. 4.3). Moreover, given that the field generating coil is not uniformly wrapped on the FCL or induction heater, the field distribution is uneven around the core and hence the values for the ***H***-field could be lower or higher at different parts of the core.

Another problem is encountered when the ferromagnetic core is modelled in the FEM software MagNet™. The underlying material representation in the software for

the M4 steel only has values up to H= 40 kA/m. The permeability calculated from B and H values is shown in Fig. 4.1

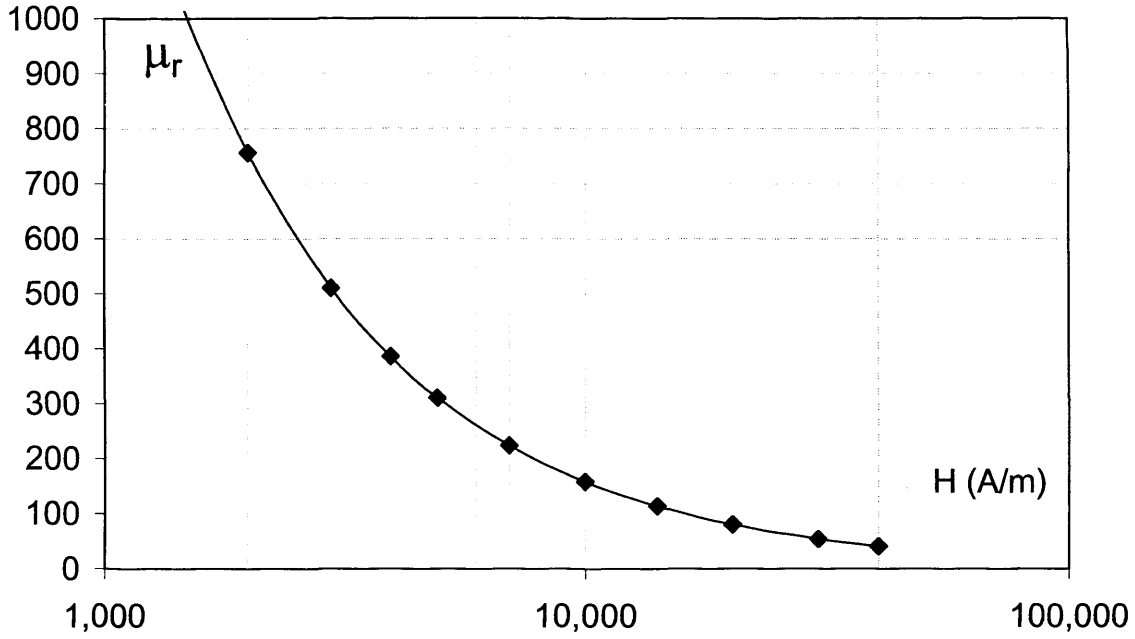

Fig. 4.1: μ-H characteristic for M4 steel used in FEM software MagNet

From Fig. 4.1, it is estimated that at H = 40 kA/m the relative permeability is 41. It can be seen that the saturation phase (defined herein as reducing the relative differential permeability to that of air, $\mu_r(air) = 1$) is estimated to be reached at H = 100 kA/m. Moreover, using Eqn. 4.4, the magnetomotive force (***N***x***I***) needed to attain H = 100 kA/m will have to be approximately 280 kAmp-turns , which for a current of 77 A would require 3,636 turns; that is 47 times more than the number of turns quoted at the start of this analysis.

In fact, the situation may be even worse, because if the graph is plotted on a log scale, as in Fig.4.2, a straight line extrapolation shows that it is possible that magnetic field values required for actual saturation could reach H = 2 MA/m.

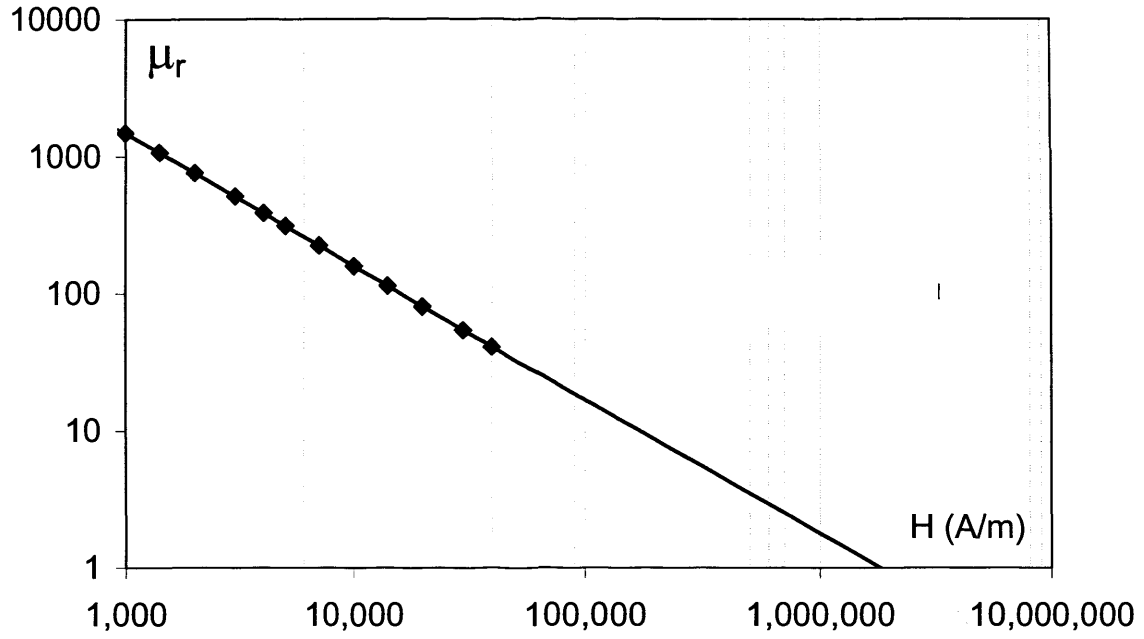

Fig. 4.2: μ-H characteristic for M4 steel used in FEM (log scale) linearly extrapolated to saturation (μ_r= 1)

This analysis shows not only the difficulty in actually obtaining measurements as far into saturation as is required for modelling the device, but also the discrepancies that exist between calculated FEM H-field values for the M4 steel and measurements taken for the same material.

Hence a step taken towards improving on the general efficiency of modelling was to use the same data set measured in Chapter 3 for the subsequent modelling of the ferromagnetic material, ignoring the representation of the B-H curve supplied in the 'library' file of the FEM software.

4.2.2. Inadequacy of Average Field Equations Used In Measurement

Another difficulty of measuring the magnetic properties at high fields for soft magnetic core samples lies in the fact that in the actual devices, the magnetic field is generated non-uniformly around the core. Fig 4.3 shows a typical core schematic for

the SCFCL with the magnetising solenoid located on only part of the core. Full saturation of the core is desirable hence the permeability in all parts of the core, especially the limb furthest from the magnetising coil (herein called the unmagnetised limb) would have to equal 1. However, due to the practical limitations of the design such as the finite length of the solenoid which limits it to less than the entire length of the core, the material on the limb covered by to the coil (herein called the magnetised limb) will be exposed to a higher H-field. Hence this region of the core will approach saturation faster than the rest of the core. Therefore there will be more leakage flux through the air as the magnetisation increases, because the air becomes increasingly favourable as a return flux path. So, as more flux leaks through the air, there is less increase in the flux in the unmagnetised limb, making it even more difficult for it to attain saturation. This is explained by the fact that the of the reluctance of air, which is determined by the path length and the permeability (Eqn.. 2.10),becomes increasingly lower due to its shorter path length as opposed to the full length of the core. This thus provides a more favourable path for the flux instead of going all round the core.

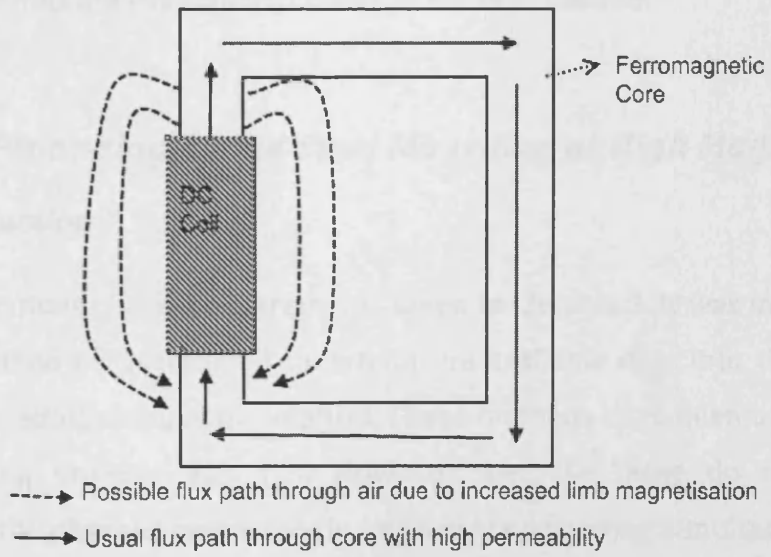

Fig. 4.3: Schematic of magnetised core showing possible flux paths (dashed lines) at high saturation of magnetised limb

Finally, if the whole core is fully saturated, then the permeability equals unity everywhere and the flux just spreads around the coil as the saturated region of the core becomes equivalent to air.

In Fig. 4.3, it would seem to be impractical to generate a magnetic field strong enough to achieve complete saturation of the core – that is, permeability equal 1 throughout. Thus a practical compromise implemented in framing the problem was to pick a target operating point which is on the unsaturated part of the core (unmagnetised limb), and measure the magnetisation up to that point.

Considering the issues introduced above, a compromise method was used wherein, the best possible measurements were taken with the existing permeameter measurement system (up to H = 14 kA/m), and extrapolation methods based on the available magnetic information were used to extend the data into the higher field regimes. Furthermore, a number of ways of expressing the field in the calculations as a function of location around the core were researched, in order to improve on the 'standard' field generation equation that is usually used (Eqn.. 4.4). These modelling solutions are examined in detail in the next section.

4.3. Data Processing for M4 Steel Modelling at High Magnetic Fields

4.3.1. Introduction

Given the limitations of the measurements taken in Chapter 3, it was imperative that a different method be formulated to extend the available data into the field range needed for modelling using extrapolation. These methods have been used before for other modelling projects. [1], [2]. However, because these do not take into consideration the physical magnetisation processes occurring simultaneously in the materials at higher fields they can result in significant errors in the predictions [3]

The more common techniques for numeric extrapolation include the straight line extrapolations (SLE) using the last few measured data points of a dataset and the Richardson method of data extrapolation which uses interpolation polynomials and the power law [4], amongst others. These algorithms have been compared and recommendations made on a per problem basis for extrapolation [5]. Though numerically efficient, these methods do not add any insight into the high magnetic regime processes or provide any supplementary magnetic information to the single-value nonlinear B-H curves measured for use to represent the M4 steel. Furthermore because these do not take into consideration the physical magnetisation processes occurring simultaneously in the materials at higher fields they can result in significant errors in the predictions [6]

Furthermore, most FEM modelling packages ignore magnetic phenomena like hysteresis and do not usually model the Rayleigh region of the initial magnetisation curves used in material representation (due to large changes in slope which put a burden on both the precision limits and computational resources of most computers) [7]. Hence it can be argued that there is a need to retain as much magnetic information as is possible within the present mathematical and convergence limitations of the software. Better extrapolation techniques, including physically realistic models and more reliable measurements constitute areas where such improvements can be introduced.

For the purposes of this Thesis, the extrapolation methods were analysed and used on the measured data, before using this new data set in the FEM software for modelling.

4.3.2. Preliminary Measurements and Sample Preparation

The initial magnetisation curve of M4 steel measured in the DC permeameter system was used as the starting point for the extrapolation method assessment, with maximum achieved field of H = 14kA/m. The straight line extrapolation (SLE) method is the most common method used in extrapolating magnetic material data, especially when the last measurement points are assumed to be in saturation. This was the first procedure used to predict B-H data measured (initial magnetisation curve) outside the range of the original measurement data. This was used to establish a baseline against which all the other procedures could be compared.

In order to get the high magnetisation data required for validation of the data extrapolation procedures, a SQUID (Superconducting Quantum Interference Device) magnetometer in combination with a superconducting magnet called a Magnetic Properties Measurement System (MPMS), which is a commercial measurement system was used to measure initial magnetisation curves for a 7.04g M4 steel sample in an open circuit test. The MPMS from Quantum Design can reach magnetic field strength values of 4 MA/m (or close to 50 kOe), with a sensitivity of up to 10^{-8} emu for the measurement of magnetic moments [8]. As analysed in Section **4.2.1**, such a field is enough to get the material into saturation, and hence this system was suitable to measure points in the saturation magnetisation range of interest in the material.

However, the difference between this type of MPMS measurement and the Epstein frame measurements used so far, is that the MPMS measures samples in an open circuit as opposed to the close circuitry of the Epstein frame system. The data obtained from both systems is shown in Fig. 4.4.

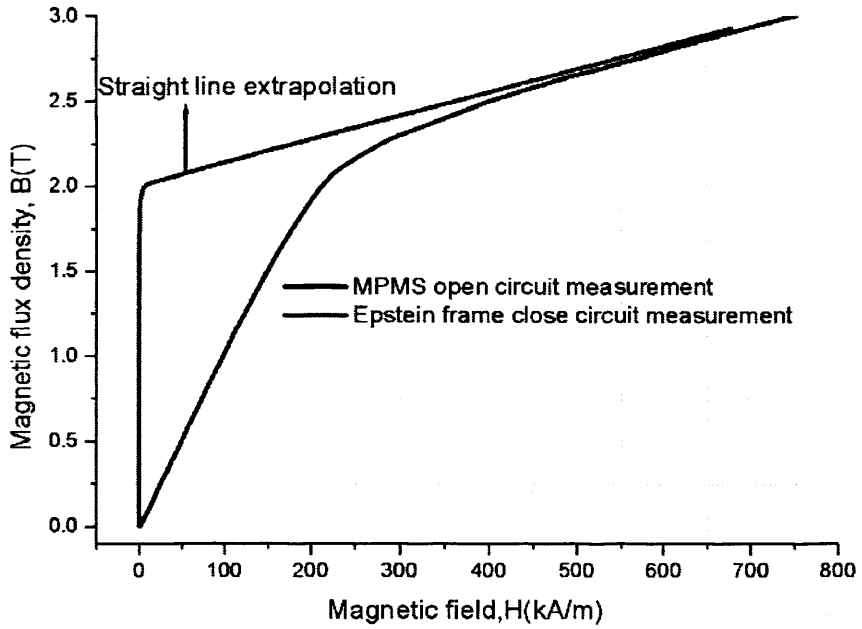

Fig. 4.4: Uncorrected MPMS and Epstein frame test measurement with a straight-line extrapolation

The major differences between the two measurements were in the geometry and measurement type [9], and hence a demagnetising correction of the data obtained is required.

Given this need to compare open and closed circuit measurements, the demagnetisation field $H_d = N_dM$ was estimated, and used in correcting for the effective field using the equation:

$$H_{effective} = H_{applied} - H_d \qquad (4.5)$$

Considering that the soft magnetic material used in this experiment approaches saturation at relatively low fields compared to other magnetic materials, it was assumed that the open and closed circuit measurements far into the saturation region would be comparable if not equal, after demagnetising factor corrections to the measured fields were made using Eqn. 4.5. This was not the case as Fig. 4.5 shows.

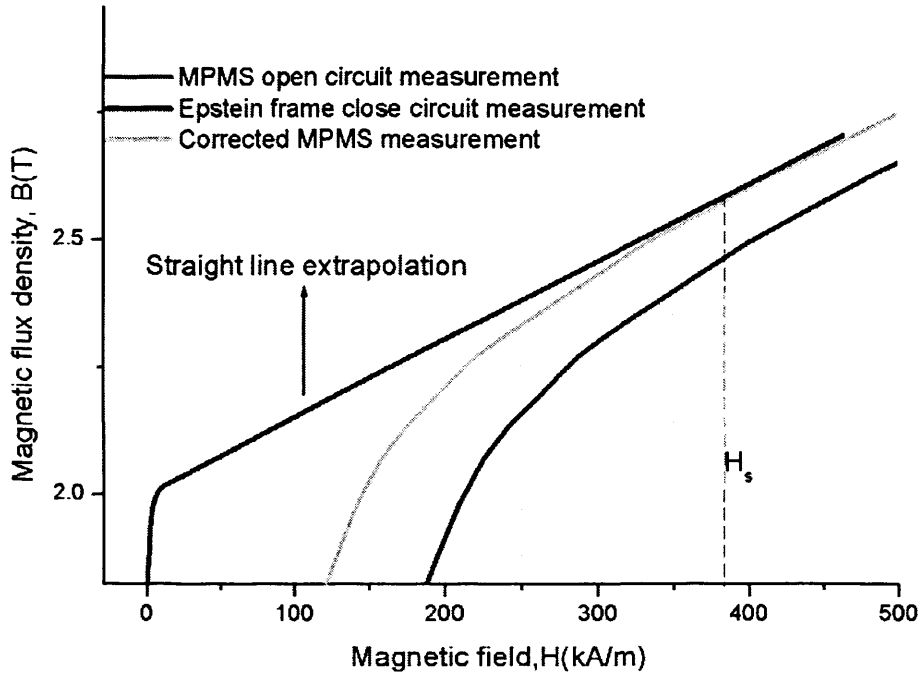

Fig. 4.5: Corrected open circuit measurement compared with SLE to obtain reference point

From the graph it is seen that the demagnetisation correction does bring the open and close circuit measurements in alignment in saturation. But this correction is not adequate when the measurements are not in saturation as seen by the discrepancy in the curves below our saturation reference point.

From the measurements at high fields using the MPMS, a reference point in the saturation region was found at which it was assumed maximum magnetisation occurs. From this point, it was ascertained by comparison, which algorithms come closest to predicting the correct value of the reference point. In this way such a reference point was used a developmental tool for a formulated extrapolation algorithm.

The field value of H_{smax} = 385 kA/m was determined as the field at which maximum magnetisation occurred (maximum field value obtained) and was set as the

reference point for saturation. With these preliminary measurements and basic assumptions, various procedures were examined and compared with the SLE.

4.3.2.1. Procedure 1: Law of Approach to Saturation Extrapolation (LAS)

The first procedure that was investigated was the LAS, as a data extension algorithm. The LAS as obtained experimentally by Becker and Döring [10] is,

$$M = M_S\left[1 - \frac{a}{H} - \frac{b}{H^2}\right] + \kappa H \qquad (4.6)$$

where a and b are curve fitting coefficients, M_S and H are the saturation magnetisation and applied field respectively, and κH is the forced magnetisation term which is small.

This procedure assumes that the measured Epstein data is correct, and the measurements are taken close enough to actual saturation such that the Law of Approach is applicable. From Eqn. 4.6, it is further assumed that constants a (due to the absence of reversible rotation components of magnetisation in saturation) and κ (assuming there is no significant forced magnetisation caused by the external magnetic field at these fields strengths) can be neglected. These assumptions reduce Eqn..4.6 to the following simplified form:

$$M = M_S\left[1 - \frac{b}{H^2}\right] \qquad (4.7)$$

Combining Eqn.. 4.7 and the expression for magnetic induction $B = \mu_0(H+M)$, and then differentiating, the following system of equations is obtained:

$$\begin{cases} B = \mu_0\left(H + M_S - M_S\dfrac{b}{H^2}\right) \\ \dfrac{dB}{dH} = \mu_0\left(1 + 2M_S\dfrac{b}{H^3}\right) \end{cases} \qquad (4.8)$$

Solving this system of equations simultaneously using the last data points on the measured data curves obtained from the Epstein tests (H_{last}, B_{last}, μ_{last}) = (14209, 2.02, 1.18), gives values of $\boldsymbol{b}$ = 1.66 x $10^5 A^2m^{-2}$, and $\boldsymbol{M_S}$ = 1.6 x 10^6 A/m, where μ_{last} is the relative differential permeability.

Substituting these into Eqn. 4.7 provides an analytic function for extrapolating the B-H curve to larger field strengths beyond the range of measurements. Fig. 4.6 shows the LAS extrapolation of the measured curve up to 300 kA/m, compared with the SLE.

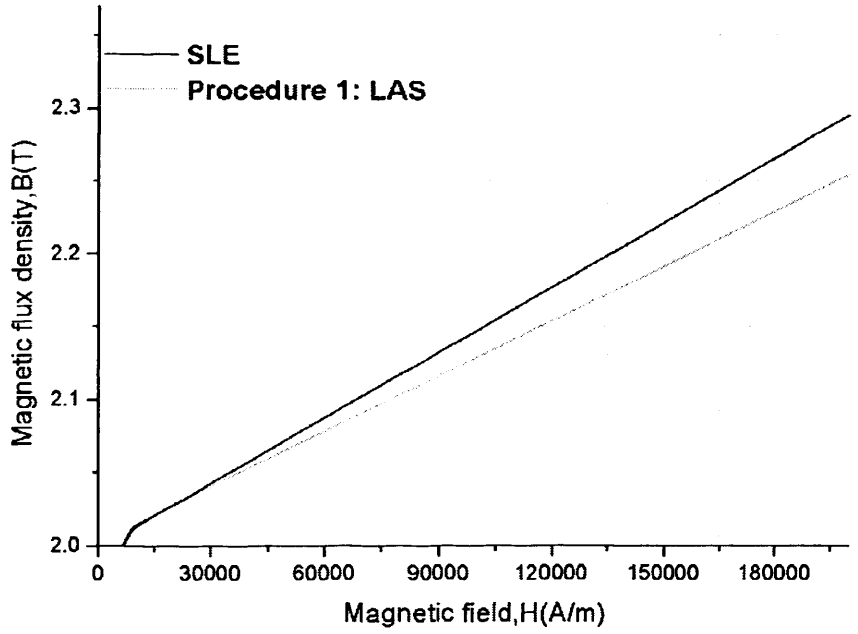

Fig. 4.6: Extrapolation curves obtained using the LAS procedure and SLE, added to measured data from 14 kA/m.

In Fig. 4.6 it is seen that the Law of Approach gives a curve with lower magnetic induction for all extrapolated values of field compared with the SLE algorithm. This is due to a lower derivative dB/dH of the material. For example, at an arbitrary value of magnetic field of H = 160 kA/m, a discrepancy of about 0.04 T in magnetic flux density is noticed between the two predictions. This difference gets larger as the fields increase.

4.3.2.2. Procedure 2: Saturation Field Extrapolation (SFE)

By including an assumption that at some reference point H_S the material must have reached saturation, another extrapolation procedure can be constructed which is herein referred to as the Saturation Field Extrapolation (SFE).

Starting from the Epstein test measurements, the data set uses an adjacent point differentiation to obtain a dB/dH versusH dataset as shown in Fig. 4.7.From this data, an algorithm for the extension of this curve can be developed from the last data point (H_{last}, B_{last}, μ_{last}) if the saturation field H_S is known. These saturation values are such that H = H_S, B = B_S, and μ_r = 1 (H_S, B_S, 1). Therefore, for all field strengths above this relative differential permeability value will be equal to 1. In addition, the functional dependence of permeability on increasing magnetic field strength has to be specified for this procedure. It is then possible to extrapolate (by integration) B-H data for the M4 steel, up to any field required.

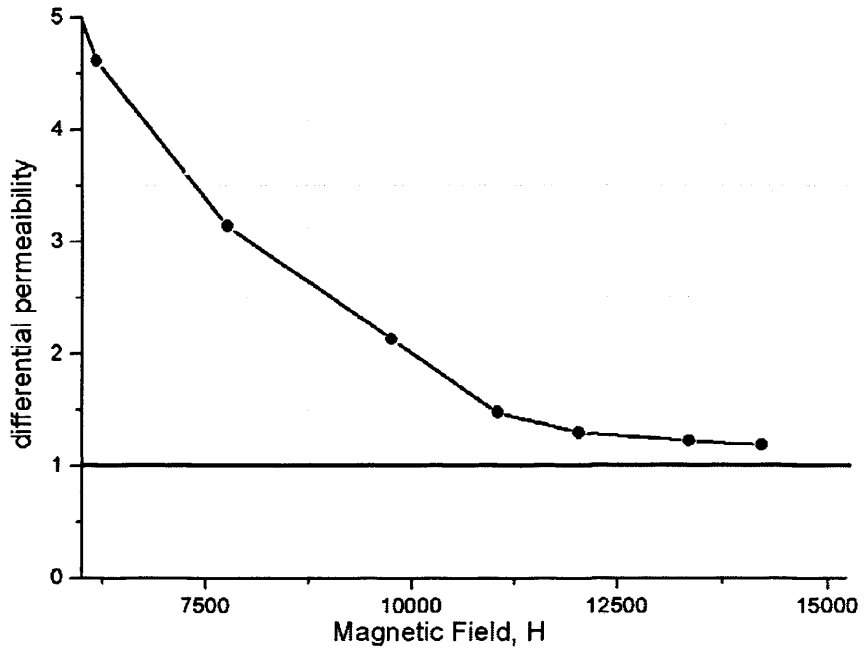

Fig. 4.7: Differential permeability as a function of magnetic field for M4 steel, showing slope and the asymptote relative permeability for free space μ_r =1

It is possible to estimate both a minimum (H_{SMIN}) and a maximum (H_{SMAX}) magnetic field value for saturation to occur by combining the measured values of the Epstein and MPMS measurements.

In the case where the decrease in the differential permeability is linear until the value of differential permeability reaches 1, the value of H_{SMIN} can be obtained using the two measurement data points at the two highest field strengths, H_{last} and H_{last-1} as shown in the Fig. 4.8. In this case the equation for H_{SMIN} is:

$$H_{SMIN}=H_{last}+\left(\frac{\mu_{last}-1}{\mu_{last}-\mu_{last-1}}\right)\cdot\left(H_{last}-H_{last-1}\right) \qquad (4.9)$$

This equation was obtained from the equation of a straight line using the last two points on the permeability vs field graph. H_{SMIN} = 19 kA/m was estimated by a straight line extension of the last measured slope of the curve dB/dH.

The other extreme case is to take a value of the magnetic field at which saturation must have assuredly occurred. This value was taken from the MPMS measurements and is H_{smax} = 385 kA/m.

These procedures place both upper and lower bounds on the saturation field H_S: $H_{smin} < H_S < H_{smax}$ and therefore, identifies the bounds of the range of possible extrapolations as shown in Fig. 4.8

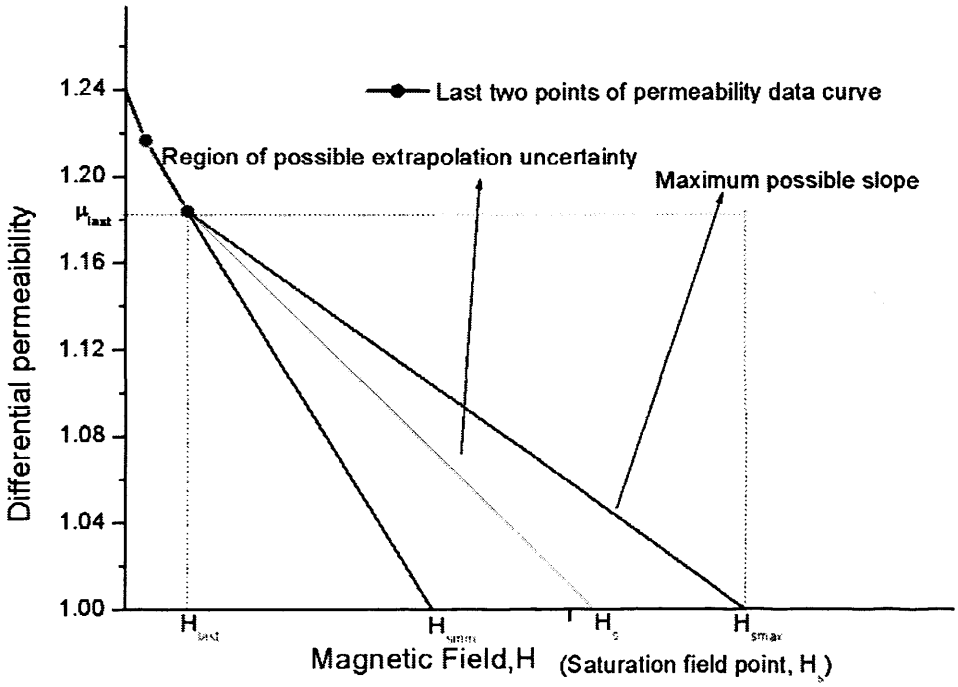

Fig. 4.8: Illustration of the concept behind the SFE. After the last measured point, (H_{last}, B_{last}, μ_{last}), differential permeability decreases to 1. (H_{last} = 14 kA/m, H_{smin} = 19 kA/m, H_{smax} = 385 kA/m). The actual saturation field, H_S, must lie between H_{smin} and H_{smax}

As a first approximation to this algorithm, a linear decrease of the differential permeability from the last measured point (H_{last}, B_{last}, μ_{last}) to the saturation point (H_S, B_S, 1) is such that

$$\frac{dB}{dH}=\mu_0\cdot\left(\mu_{last}-\left(\frac{H-H_{last}}{H_S-H_{last}}\right)\cdot(\mu_{last}-1)\right) \qquad (4.10)$$

Therefore in the field range until saturation field H_S is reached, the magnetic flux density is,

$$B = \frac{\mu_0 H}{2}\left(\frac{2H_{last} - H + (H - 2H_S)^* \mu_{last}}{(H_{last} - H_S)}\right) \qquad (4.11)$$

After the saturation magnetic field has been reached, magnetic flux density increases linearly with field with permeability equal to that of free space.

Fig. 4.9 shows the difference in extrapolation curves for different chosen values of H_S.

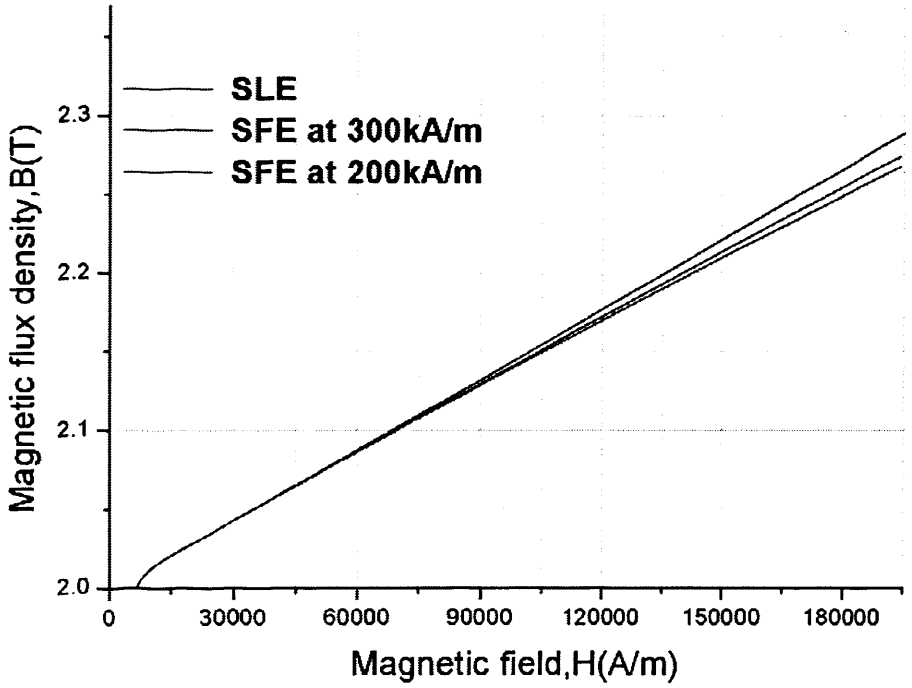

Fig. 4.9: Extrapolation curves following the SFE procedure for different values Hs, compared to the SLE.

A robustness test for the SFE algorithm provided above was carried out by varying the value of H_S by as much as 100kA/m (H_S = 200 kA/m to 300 kA/m), to assess the sensitivity of the curve to variations or errors in data. Fig. 4.9 shows that there is a less than 0.05 T difference between the extrapolated curves (compared arbitrarily at

160 kA/m). This shows that the algorithm is quite stable, and still markedly different from the SLE. It is important to note, however, that depending on various factors like the geometry of the sample, the saturation may actually occur at higher field strengths. Therefore, a good estimate is needed for H_{SMAX}.

4.3.2.3. Procedure 3: Exponential Law Extrapolation (ELE)

In this procedure it is assumed that the magnetisation of the material continues into saturation following an exponential function [11] which can be written as

$$\begin{cases} B = \mu_0 \left(M_S \left[1 - e^{-\beta H} \right] + H \right) \\ \dfrac{dB}{dH} = \mu_0 + \mu_0 M_S \beta e^{-\beta H} \end{cases} \qquad (4.12)$$

where M_S is the saturation magnetisation and β is an exponential coefficient. Solving this system of equations simultaneously by using the last point on the Epstein data curve it is possible to find both M_S and β. In this case (H_{last}, B_{last}, μ_{last}) is (14209, 2.02, 1.18) respectively and, therefore, β = 6.07 x 10^{-4} m/A and M_S = 1.59 x 10^6 A/m.

Substituting the calculated values into Eqn. 4.12 makes it possible to extrapolate the B-H curve to high field strengths. Fig. 4.10 shows such an extrapolation compared with the linear extrapolation procedure.

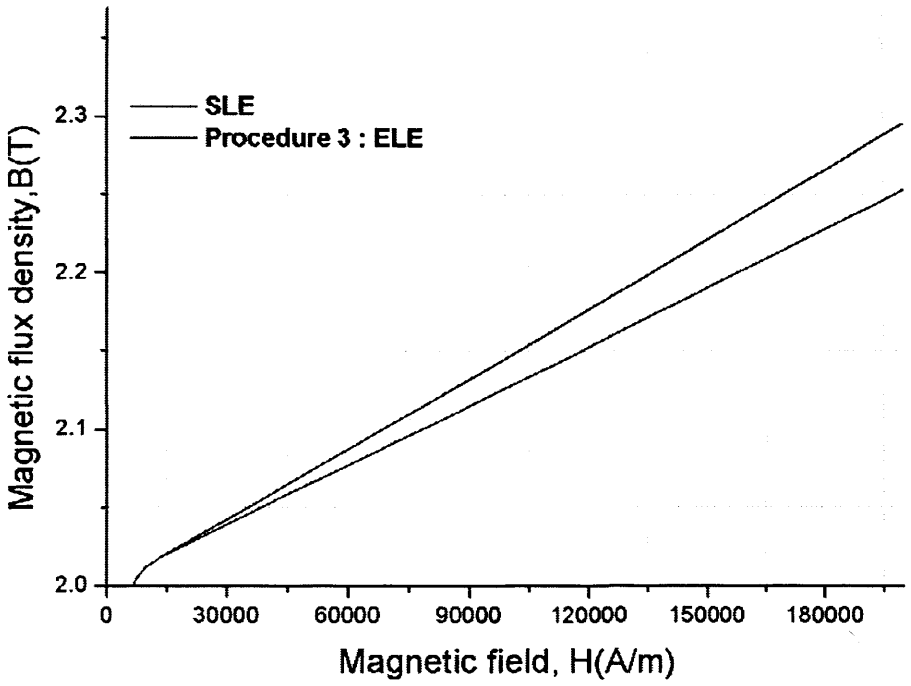

Fig. 4.10: Extrapolation curve obtained from the ELE procedure, added to the 15kA/m measured data, compared to the SLE

By comparing the different extrapolation procedures proposed above, a baseline for the highest and lowest slope acceptable for the extrapolation of the data has been established. It is seen that all three procedures result in lower B-H values than are achieved using the algorithm presently used in most software. Fig.4.11 compares the results of all the procedures discussed above.

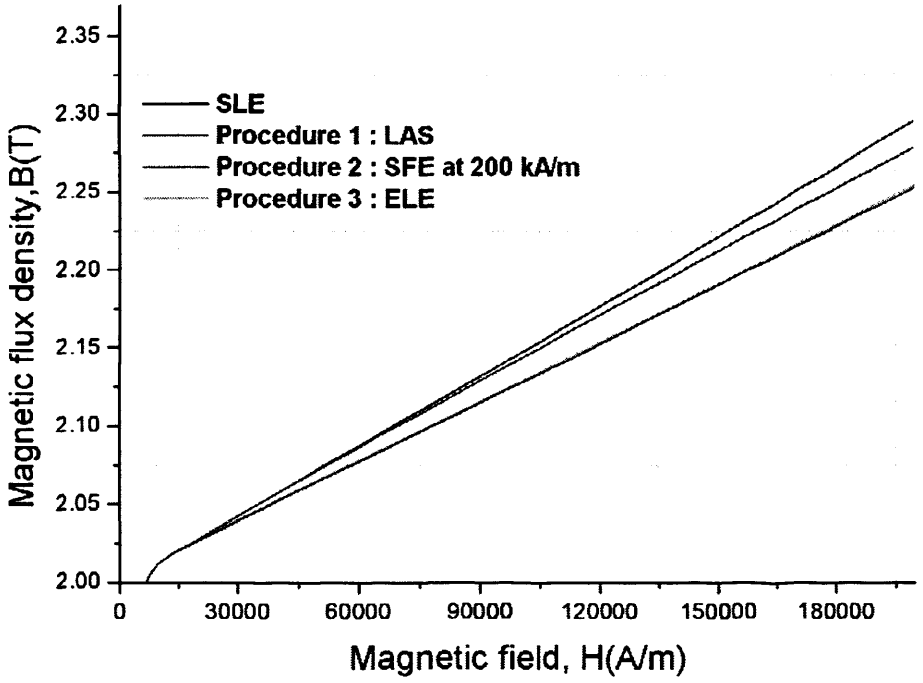

Fig. 4.11: Various extrapolation procedures compared, using the same measured data.

Given the deviation that all three procedures show from the standard straight line extrapolation, it suggests that the magnetic considerations used in the procedures all have the effect of reducing the slope with which magnetisation curves are extrapolated in FEM software. The difference in slope also gives an indication of the errors that are likely to be introduced in the model calculations if an appropriate extrapolation procedure for the specific application is not used. This is especially critical when used in simulation of ferromagnetic materials in models requiring high power and high magnetic fields, as these errors are magnified with increase in field, as the analysis have demonstrated.

The SFE (procedure 2) can be used if data far into saturation can be obtained from other measurements. However, the procedure can only be used if we can make the critical assumption that at some point deep in saturation, the open and closed circuit measurements from which the datasets are obtained are considered comparable.

This approach can be used for various ferromagnetic materials to seamlessly combine open and closed circuit measurements to form a consistent extrapolated B-H representation.

Furthermore, two of the procedures investigated – the LAS and ELE - have overlapping extrapolation curves. This may indicate that these methods of extrapolation, though independently developed, take into consideration the appropriate behaviours of the material at high magnetic fields better. Consequently, the LAS procedure was implemented as the choice for extrapolation for the purposes of this Thesis.

4.4. The Standard Measurement Ampere's Law Extension

4.4.1. Introduction

Another challenge that was evident in the modelling process was the integrity of the measurement data when transcribed from a uniform mmf laboratory specification to a real device design, which invariably included non-uniform mmf cores. Essentially, the idea to quantify what error was introduced by assuming that the material representation for a uniform emf around the actual magnetic core was adequate for modelling non-uniform field distribution was considered. This is an important consideration which is most usually ignored, and hence could lead to significant error in both the analytic modelling (finding the proper equation to represent the H-field in the equivalent circuit models), and the testing and measurements in prototypes (the algorithms implemented in measurement systems to measure the H-fields in device prototypes).

One of the principal predictive tools used in this regard is Finite Element Modelling (FEM) which requires meshing of the spatial domain, including the device and surrounding air boundaries, and providing solutions in 3D. During the initial stages

of device modelling, the analytic models were usually more important to use in order to get an understanding of the likely behaviour of the device. At this stage, detailed analysis of the device is not necessary, and hence analytic models that are quick, are preferred to FEM, which is too time-consuming and detailed for this initial analysis [12].

For these reasons, and the fact that this problem seemed to not have been adequately researched before, this Thesis takes a detailed look into the shortcomings of the uniform mmf assumption which leads to errors in the calculation of the field around a core. A procedure is then proposed which gives a more realistic variation of the field around the core that can be used in measurement algorithms and mathematical models of devices.

4.4.2. Standard Ampere's Law Derivation Problem

As earlier mentioned in the Chapter, the Ampere's circuital law in materials, which is widely used in field calculations, [13] provides a relationship between the magnetic field H, around a current carrying conductor and its current source. The more standard derivation for this equation usually used in applications is

$$H = \frac{N.I}{l} \qquad (4.13)$$

The equation has the assumption of uniform mmf , and is constant for all parts of a core. Practical cores in devices on the other hand, generally do not have this uniform distribution due to the location of the energising coils due to practical device design limitations and requirements. With uneven mmf in such cases, a non-uniform field profile around the core is a consequence, and Eqn.. 4.13 which is widely employed for such calculations and representations, cannot be used.

This failure is even more significant in terms of the error magnitudes when calculations are needed in higher field regimes for simulation or design for power devices such as FCLs and induction heaters. The fact that in such devices the mmf produced by the applied current source is non-uniform and non-local, applying Eqn.. 4.14 to field calculations or measurements for such devices that require accurate values for magnetic field for their proper calibration and functioning, can lead to significant error in design and prototyping.

4.4.3. Prototype Design and Measurements for Ampere's Law Derivation Problem Investigations

The Amperian approach to field generation is most commonly used in laboratory closed circuit measurements for ferromagnetic materials, due to their practicality and the ease of current-controlled field generation. In some device models, the exact spatial field distribution variation along their component cores is needed for calculations such as inductance and magnetic induction, B. For example, in the FCL modelled in this Thesis, a localised magnetising coil that does not extend over the entire core accomplishes the magnetisation of the M4 steel cores. This results in non-uniform mmf around the core, and hence uneven field distribution across the cores, thus violating the principal assumptions of the Ampere's law derivation, given in Eqn..4.13.

Furthermore, most field calculations using this standard equation are made with the magnetising coil as a reference point instead of at the point where the electromagnetic interactions and calculations of inductance on FCLs, are performed. Consequently, for larger ferromagnetic cores, the field distribution can become

highly non-uniform and hence vastly different from the analytically calculated values using Eqn. 4.14.

To illustrate the problem, a scaled-down prototype of a ferromagnetic core stack was built from standard laminated Epstein-size strips of M4 non-oriented steel, 30x30x0.03 cm as shown in Fig.4.12. The stack was 0.3cm thick. Only one limb had a magnetising 1000-turn DC coil around it, referred to as the magnetising limb. Several search coils (SC) were wrapped at various points around the length of the core. A power amplification system comprising two cascaded KepCo 36V/12A bipolar power supplies was used to generate the magnetising current which was measured over a 0.1 Ohm resistor in series. The H-field was calculated using Eqn. 4.13.

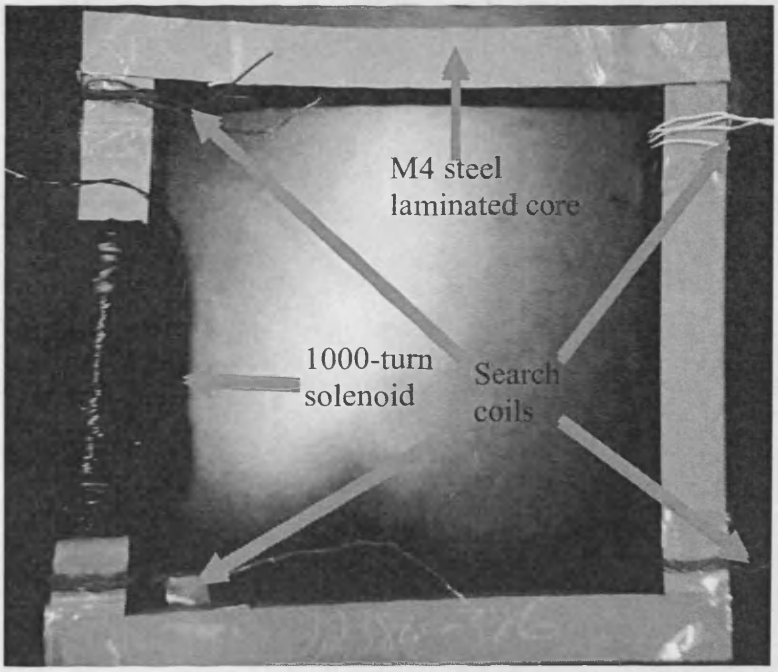

Fig. 4.12: Picture of prototype core 30x30x3 cm, made from Epstein laminated strips

A similar core was 'built' in FEM software MagNet to highlight the differences in H-field values obtained using Eqn. 4.13 and those obtained from the finite element calculations. Fig. 4.13 highlights the search coil locations and the axis of reference for the calculations.

As shown in the schematic, the field distribution was taken as a function of displacement, ***x***, around the core, starting from the middle of the magnetising limb. The core was first demagnetised using a cyclic decaying field over 240 seconds and then the current in the magnetisation was gradually increased

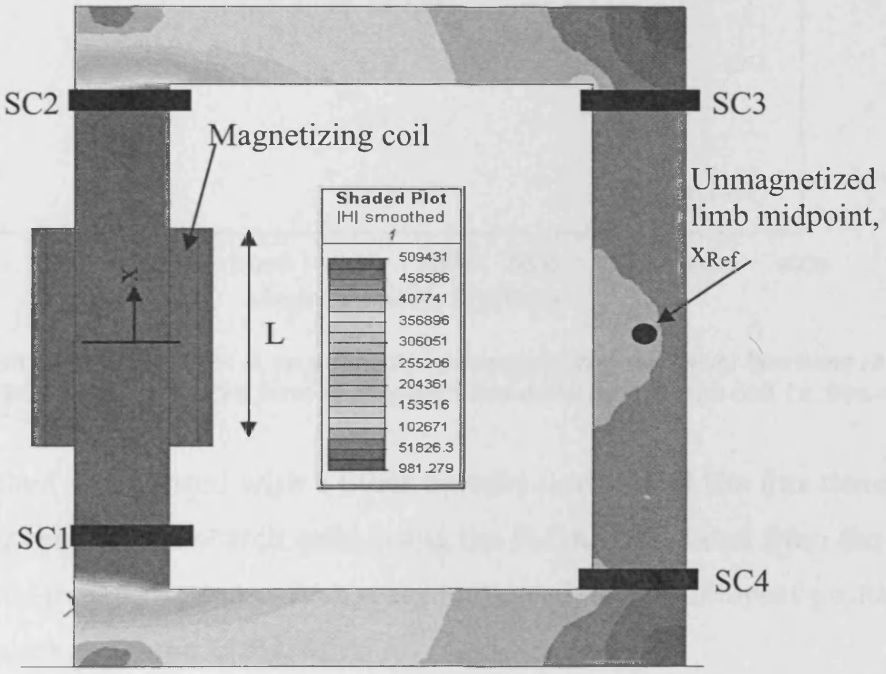

Fig. 4.13: FEM of magnetic field in a core, showing difference in H-field distribution on opposite limbs.

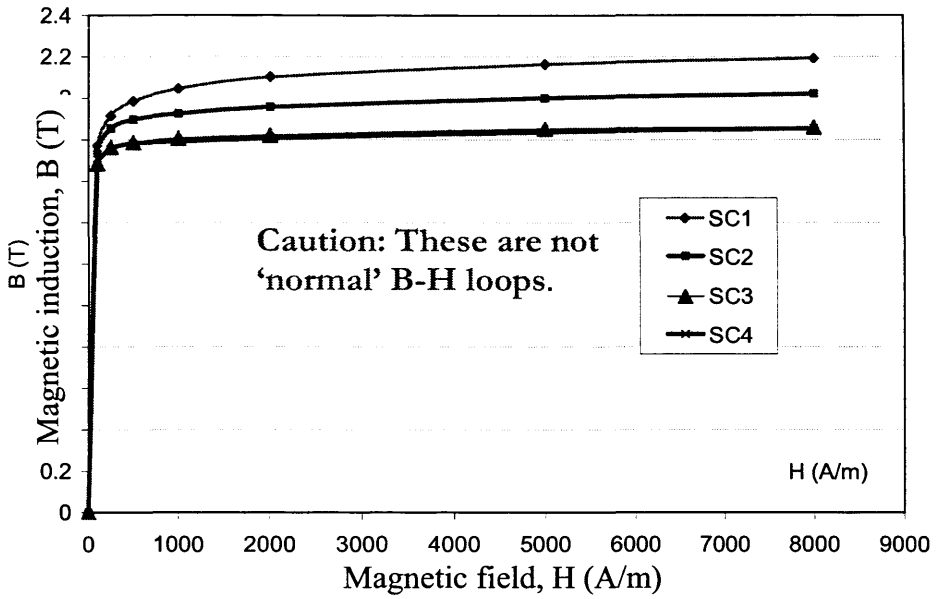

Fig. 4.14: Flux density measurements, B, on miniature prototype core at various locations vs field values, H, obtained using the standard form of Ampere's law derivation, at the coil, i.e. Eqn. 4.13.

The setup was then magnetised with a 50Hz current source, and the flux densities are measured by the various search coils, using the H-field calculated from the line current, the initial magnetisation curves were measured, at the different positions, SC1-SC4, on the core as shown in Fig. 4.13.

Fig.4.14 shows the problems involved in obtaining B-H measurements in such situations. Different curves are obtained when the measurements are taken at different parts of the core. This is because the assumption of uniform mmf around the closed circuit is not met. The magnetic field H is inhomogeneous around the closed path of the core, varying significantly from the prediction of Eqn. 4.13, and hence the H-values calculated at the coil location are not the effective H-values at the various search coils.

Eqn. 4.13 relates the average H-values produced by the current carrying conductor over the length of the solenoid, but accounts neither for the finite dimensions of

most practical solenoids, nor the geometric effects of the core and coil location on the field distribution. Thus, magnetic field values at some parts of the core can drop to less than 2% of their peak value between the magnetized and un-magnetised limbs. The FEM model calculated in Fig 4.13 illustrates this clearly as the H-field values ranged from 50.9 kA/m to less than 1 kA/m.

A proposed alternative to accurately calculate the effective magnetic field at a particular location of a core evidently is essential, given the errors that can arise for the primary B-H loop measurements and also for derived or secondary measurements like inductance.

4.4.4. Improved Generalised Ampere's Law Extension for Core H-field Calculations.

In order to overcome the problem detailed above, an approach was used in this Thesis based on a combination of measurements and modelling to form a procedure that provides a better solution, especially at high fields and flux densities where the shortcomings of Eqn. 4.14 are more prominent.

The first step of the procedure was accomplished by taking accurate B-H loop data and extended it using the LAS extrapolation method investigated above. The B-H information obtained herein was then incorporated into FEM and H-field distribution profiles were obtained over a large range of current values around the core (0-25kA). Calculation of field distributions were made, starting from the middle of the magnetized limb and tracing the displacement, x, around the core to an arbitrary point of interest, x_{Ref}, along the core length (for this case, taken as the midpoint of the unmagnetised limb due to symmetry, as shown in Fig. 4.13).

The closed core path was then transformed conformally as that for a non-uniform media into a straight core, since both structures are planar (z-direction potentials are unchanged) and the analytic function representing the transformation is well-behaved [14]. Therefore, the edge or fringing effects are to be accounted for by an analytical function, which is denoted as w=f(x). The H-l graph which results from this transformation, was then plotted alongside the Ampere's law derivation function for the same current value range as shown in Fig. 4.15.

The hypothesis for this method is that the magnetic field is better calculated with the analytic solution for a finite solenoid extension of Ampere's equation [15] instead of the usual averaged Ampere's law extension of Eqn. 4.13, for field profile around the non uniform mmf core. This hypothesis is now considered.

The formula for a straight finite solenoid provides an expression for determining the magnetic field H at a distance ***x*** from the centre of the solenoid in a linear axis. It also takes into consideration the solenoid characteristics like length ***L***, diameter ***D*** and number of turns, ***N***.

$$H=\frac{N.I}{L}\left[\frac{(L+2x)}{2\sqrt{D^2+(L+2x)^2}}+\frac{(L-2x)}{2\sqrt{D^2+(L-2x)^2}}\right].f_{shape}(x) \qquad (4.14)$$

where H is the on axis field, ***x*** is the displacement around the core along the axis from the centre of the coil mapped into a linear distance equivalent to the path length, ***l***.

The shape function $f_{shape}(x)$ is introduced to allow for the effect of the shape and fringe effects (equivalent to w=f(x)) of the core on the field as transcribed by the conformal mapping procedure. For a first approximation, let $f_{shape}(x)=1$. The

expression was then compared to FEM calculated data over the core profile as shown in Fig. 4.15.

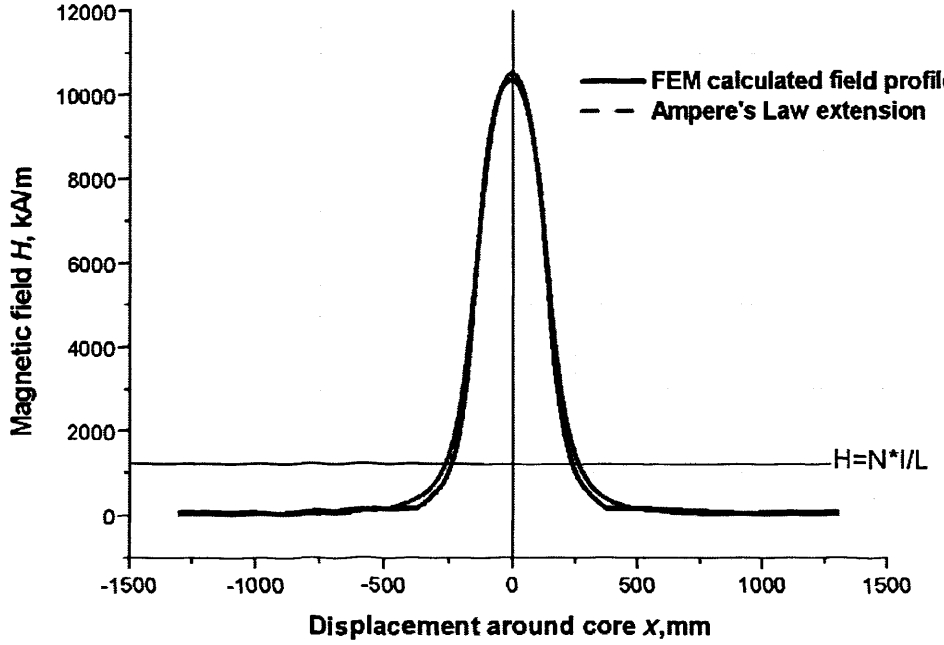

Fig. 4.15: Magnetic field profile around core (FEM calculated) compared to the new generalised Ampere law extension (Eqn. 4.15) and the usual Ampere's law derivation (Eqn. 4.14).

The Fig. 4.15 shows excellent agreement between the FEM measured data and the modified Ampere's Law extension. It also highlights the disparity between the commonly used standard derivation of Ampere's law, which is essentially an average value, as compared to the detailed variation around the core given by the modified equation.

It is clearly seen in Fig. 4.15 that the standard Ampere's Law derivation produces values which deviate markedly from the actual values at all points in the profile except directly under the solenoid. Ideally, it would be useful to have the description of the field over the whole range of variation of the current; however, the H-I dependence was only investigated in two regions: low and high magnetic field (low and high applied current respectively)

4.4.5. Investigation of Function Validity over Large Magnetic Field Range

A detailed investigation into possible functions to represent the H-l relationship was carried out, to support the claim that Eqn. 4.15 could be used extensively over a large current range. This is needed because in order to be able to use this new extension, it has to be proven robust and applicable for the whole current range for which it needs to be used. Thus, current values were recorded at the reference point, and compared with both the FEM calculated and the standard ampere's law equation. The idea was to search for a valid relationship between the field and the current and how it varied over time. For this purpose, the H-field profile is split arbitrarily into a low-level magnetic field range (< 500 A/m) and a high-level magnetic field range (> 500 A/m).

At low magnetic fields, there is need for high accuracy in determining both H and B because at these field strengths exists the highest core inductance and, hence, the inductance of the device is very sensitive to the changes (or errors) in permeability. The correct description of the field in this region is very in determining the validity of the model for predicting the functioning of the device. As a first approximation, the square root function was used arbitrarily to fit the region for lower magnetic field (low applied current) because it provided the best fit for the data:

$$H = P_1\sqrt{I} \qquad (4.15)$$

where H is the magnetic field value , I is the current and P_1 is an adjustable parameter.

Fig. 4.16 shows how the low magnetic fields corresponded with the square foot function fitting. Also shown in Fig 4.16 is the comparison with the values obtained if the standard Ampere's derivation was used. These are clearly in serious error.

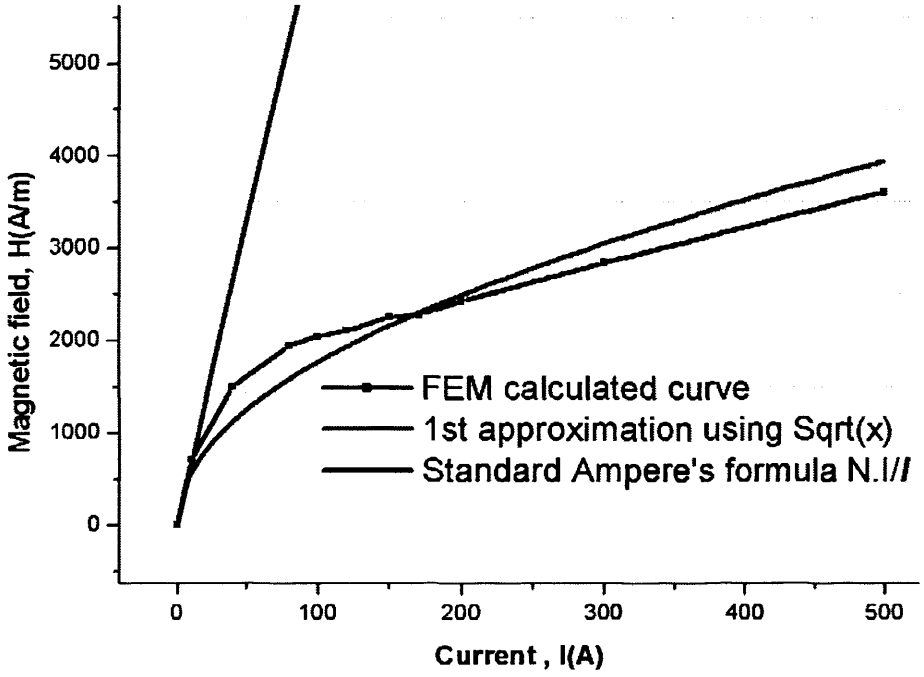

Fig. 4.16: Low H-field calculations with FEM, standard calculation ($H = \frac{N*I}{l}$), and first approximation with P_1=178.4

Extending this relation into higher fields proves problematic as the extension only increased the deviation of the value obtained from the analytic function and the FEM-calculated values.

Hence a search was initiated to find a function that might be applicable over a wider which might not be as accurate for the low fields as Eqn. 4.15, but will better fit the complete data range.

Consequently, at the reference point x_{Ref}, the range of applied currents was extended from zero to 25kA. A linear dependence of field H, on current I, was obtained by fitting the proposed equation (Eqn. 4.15) to H-field values produced over a more complete field ranges.

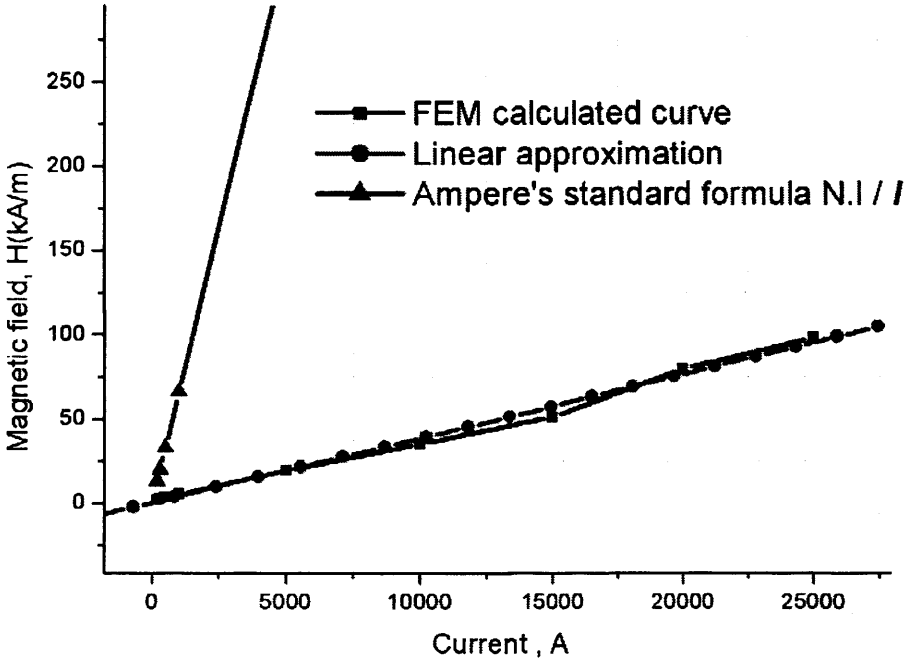

Fig. 4.17: New generalized linear extension (Eqn.. 4.14) fitting for H-I data contrasted with standard Ampere's derivation (Eqn.. 4.13) results for H-field values(FEM calculated) over large coil current range.

The agreement shown in Fig.4.17 between FEM-calculated values and Eqn. 4.15 is remarkable and proves not only how consistently the new generalised equation models the field distribution over a large range of current or field values, but also the difference between the calculated values based on this equation and those based on the usual Ampere's law derivation equation.

Fig. 4.17 shows the FEM generated field distribution profile of the core, compared to the Ampere's law equation and the modified Ampere's Law extension in Eqn. 4.15. It confirms the fact that modified the Ampere's law extension introduced here can be used for a larger range of field values – from low to high fields –with more accuracy than the original Ampere's law equation.

The accuracy of this modified analytic expression cuts down on the time resources needed for magnetic field computations using complex FEM analysis. Furthermore,

the edges of both graphs show that our first approximation of the shape function as unity, though good, has room for improvement. This makes the analytic function even more adaptable, accurate and applicable to various specific core geometries. An analytic function with such a high level of accuracy in predicting the field distribution on a closed core can easily be incorporated into larger system modelling.

This function was investigated particularly because of its usefulness in mathematically modelling a ferromagnetic closed core for the FCL. Analytic formulations such as this are model/problem-specific, but the approach can be extended to other core models, and is certainly faster than relying on FEM calculations alone.

4.5. Summary

In this Chapter, some critical problems and challenges faced in obtaining and processing magnetic property data for representation of magnetic materials have been examined in detail. This includes finding appropriate extrapolation methods for ferromagnetic materials, and also problems with the standard Ampere's Law formulation equation generally used in calculation and measurement. A procedure for the derivation of a better extension of this law was proposed, and proven to be more accurate than the previously used equation.

The Thesis will now proceed to consider how these material data and representations can be used in formulating the models for the FCL device being investigated. A detailed look into the formulation of the mathematical model will be undertaken, and the direct relationship between the material properties and their effects on the functionality of the device will be examined. This knowledge is

essential in making the choice of a ferromagnetic core material for use and also to assess the effects of material properties on device functionality.

[1] H. Hauser, D.C.Jiles, Y. Melikhov, L. Li, R. Grossinger, An Approach To Modeling The Dependence Of Magnetization On Magnetic Field In High Field Regime, Jour. Magn. Magn. Mat., No. 300, Pg.273-283, 2006

[2] G. Bertotti, Hysteresis In Magnetism, Academic Press, London, 1998

[3] R. Becker, G. Martinez, A.V.D. Weth, Improvement Of Magnetic Field Calculations By Extrapolation, Nuclear Instruments And Methods In Physics Research, A 519, Pg.49-52, 2004

[4] M. Clemens, M. Wilke, T. Wieland, Extrapolation Strategies In Numerical Schemes For Transient Magnetic Field Simulations, IEEE Trans., Mag. Vol.39,Pg. 1171-1174, 2003

[5] S. Chikazumi, Physics Of Ferromagnetism, 2nd Ed. Oxford, Uk.: Oxford Univ. Press, Pg.503–508, 1997

[6] R. Becker, G. Martinez, A.V.D. Weth, Improvement Of Magnetic Field Calculations By Extrapolation, Nuclear Instruments And Methods In Physics Research, A 519, Pg. 49-52, 2004

[7] B.D. Cullity, Introduction To Magnetic Materials, Reading Ma, USA: Addison-Wesley Pub. Co., Pg. 347, 1972

[8] MPMS measurement system ,Quantum design www.qdusa.com/products/mpms.html, 2008

[9] E.Fernandez; A. Garcia-Arribas; S.O. Volchkov, G.V. Kurlyandskaya; J.M. Barandiaran, Differences In The Magneto-Impedance Of Feni/Cu/Feni Multilayers With Open And Closed Magnetic Path, IEEE Trans Magn., Vol. 46, Pg. 658-661, 2010

[10] S. Chikazumi, Physics Of Ferromagnetism, 2nd Ed. Oxford, Uk.: Oxford Univ. Press, Pg. 503–508, 1997

[11] A. Hubert, R. Schafer, Magnetic Domains: The Analysis Of Magnetic Microstructures, Springer-Verlag Berlin Heidelberg, 1998

[12] P. Virtic, P. Pisek, T. Marcic, M. Hadziselimovic, B. Stumberger, Analytical Analysis Of Magnetic Field And Back Electromotive Force Calculation Of An Axial-Flux Permanent Magnet Synchronous Generator With Coreless Stator, IEEE Trans Magn., Vol. 44, Pg 4333-4336 2008.

[13] D.C. Jiles, C.C.H. Lo, The Role Of New Materials In The Development Of Magnetic Sensors And Actuators, Sensors And Actuators A 106,Pg. 3-7, 2003

[14] Roland Schinzinger, Patricio A., A.Llaura, Conformal Mapping: Methods And Applications, Dover Publications, 2003, Chapter 6, Pg 186

[15] D.C. Jiles, Introduction To Magnetic Materials, Chapman & Hall, 1998, Chapter 1, Pg 25

Chapter 5. Functional Algorithm Design and Mathematical Modelling of EM Devices: Case of the Fault Current Limiter

5.1. Introduction

This Chapter will focus on the development of such a model for the saturable core fault current limiter (SCFCL) under development in this Thesis. It will focus on building the model in the time domain,- with time as an independent explicit variable - as this method of electromagnetic analytic modelling is not only computer efficient but more suiting to such devices where the states of the constituent materials and underlying equations change with time [1]. It will examine the limitations of the underlying equations, analyse the effects of the material parameters on the functioning of the FCL and also propose solutions to problems usually encountered with such models.

Such modelling usually entails incorporating measurement data, and the physical operational principles of the device using a set of mathematical tools and equations that describe the system under investigation. This kind of modelling is usually used because it provides a fast method of understanding the full system. Furthermore, in the case under study, it is also an easy way of investigating circuit and material parameters for their effects and optimum values for the functioning of the device. This can lead to a simplification of the device or electromagnetic system, by discarding the unimportant features to gain this deeper understanding of the system [2]. Due to the intrinsic limitations of trying to represent physical systems with purely mathematical tools, such models are usually approximate in nature and are used more for qualitative than quantitative purposes.

5.1.1. Principle of Operation of SCFCL

The SCFCL functions on the principle of increasing the inductance of a circuit in which it is connected in series, in order to limit an incoming fault current. This is accomplished by biasing the FCL core with a DC circuit such that the normal operating point lies as far into saturation as is necessary for the device to provide little or no impedance to the system (the so-called 'transparency' condition). Here, the operating point refers to the state of core as characterised by a position on its B-H curve, determined by the total magnetic fields acting on the core, at a particular point in time.

The AC coil is wound around both ferromagnetic cores such that the flux produced by the AC or line current is in opposition to the flux generated by the DC coil bias. Thus a fault current will oppose such a bias and move the operating point of the core into the region of high differential permeability, and hence high inductance and impedance. Fig. 5.1 gives a schematic of a prototype of this device.

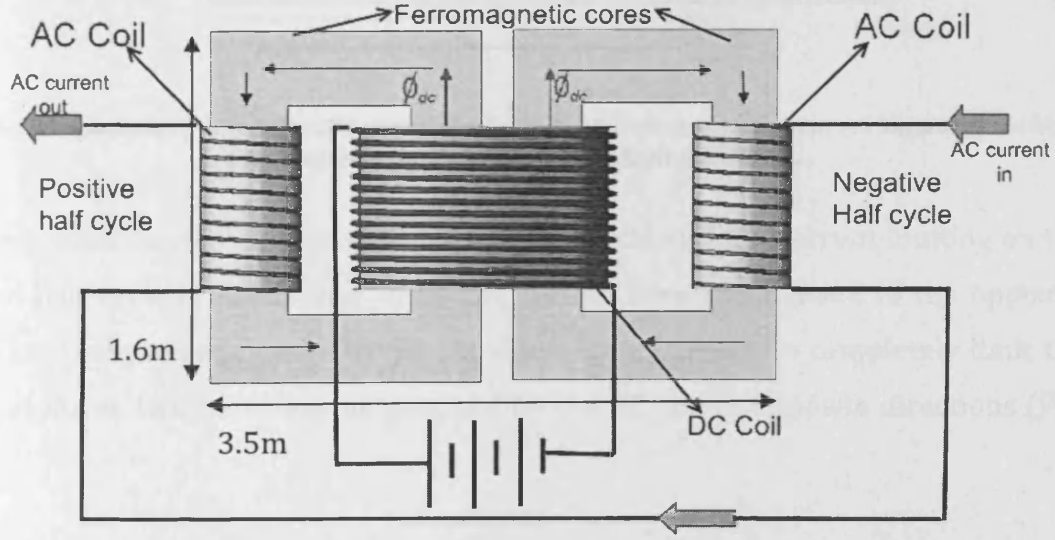

Fig. 5.1: Schematic of prototype SCFCL showing wiring configuration and placement of DC coil generating flux Φdc , in both ferromagnetic cores (from Zenergy power report).

By Ohm's law, increase in inductance will limit the fault current seen by the power system. When the fault current is removed from the system (either by circuit breakers or other protection equipment), the DC-generated field restores the core back to its original operating point in saturation. The annotated diagram in Fig. 5.2 of an anhysteretic representation of the M4 steel core in the first quadrant shows the various processes that occur for a simple AC waveform.

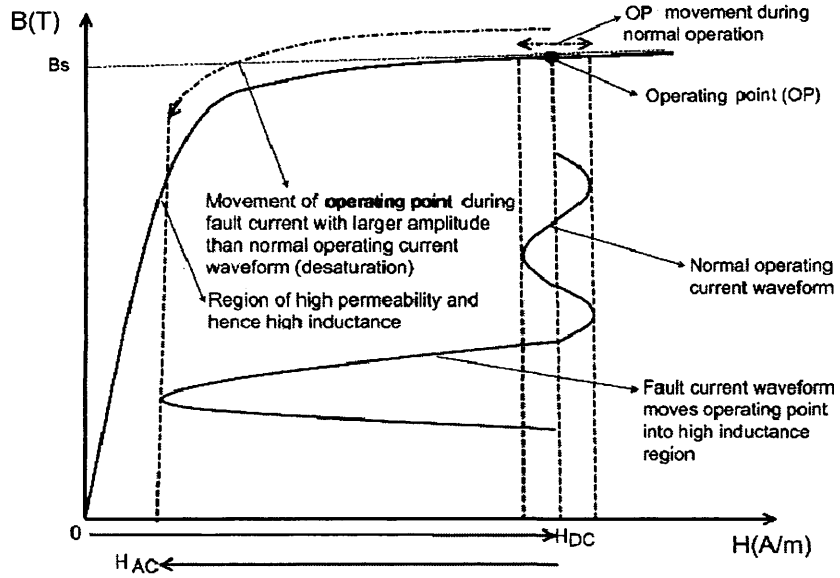

Fig. 5.2: Schematic of anyhsteretic curve showing the movement of the operating point during normal operating conditions and fault conditions.

The processes in Fig. 5.2 take place in one half cycle and the current limiting on the second half cycle is taken care of by the second core, magnetised in the opposite direction (anhysteretic curve in the third quadrant). Hence to completely limit the full waveform, two cores are magnetised by the DC coil in opposite directions (Fig. 5.1).

5.2. *Mathematical Model Formulation for SCFCL*

5.2.1. *Equivalent Circuit for Electrical System Implementation of FCL*

Formulating a mathematical model for the SCFCL required the creation of an equivalent circuit for the FCL in a simple electrical circuit. This leads to the formation of a first order ordinary differential equation, which is then solved for the quantities of interest (line current and or voltage). The equivalent circuit model incorporates the functional magnetic material representation equation along with the dimensions of the FCL, into an electrical system model, which is comparable to that in which the device will be used.

For this particular device, a voltage driven electrical model (VDM) was devised, and for simplicity, a couple of assumptions were made. Firstly, the structure of the prototype (Fig. 5.1), shows that the coils, being on different sides of the core are far from each other. Hence leakage inductances (or mutual inductances) are neglected in the analysis. This assumption is usually made for non-concentric coils [3]. Hence for a simple inductive circuit, the ordinary differential equation (ODE) representation is,

$$V_s \sin \omega t = iR + L\frac{di}{dt} \qquad (5.1)$$

The diagram in Fig. 5.3 is a representation of the basic components of the voltage driven equivalent circuit.

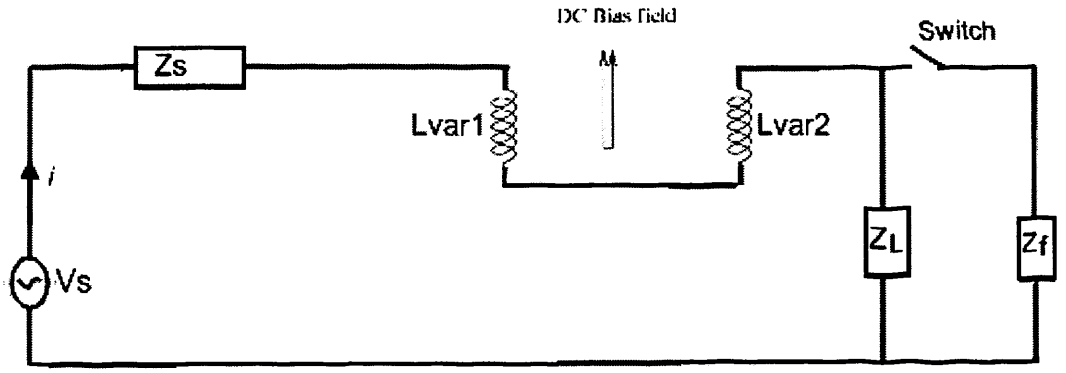

Fig. 5.3: Circuit diagram for the voltage driven equivalent model for FCL circuit implementation

The simplified circuit consists of an AC voltage source V_s, a source impedance $Z_s = R_s + i\omega L_s$ and a purely resistive load $Z_L = R_L + i\omega L_L$ (circuit capacitances are assumed negligible for this analysis). In the setup, the FCL is introduced as a variable inductor whose value changes depending on the AC line current. The inductance from both cores is independently factored into the circuit as two separate inductances, both producing variable values of inductance depending on the differential permeability at the operation point on the ferromagnetic cores.

The fault is introduced as a very small resistance $Z_f = R_f$ in paralled with the load, which results in a short circuit across the load. A switch is used to insert the fault after the current waveform for normal operating conditions has been established and stabilised. The total current waveform is initially obtained without the FCL in the circuit to establish the expected circuit behaviour before and after the fault is introduced, in the absence of the FCL. This waveform will be called the base current or base, to which all other waveforms will be compared.

In order to solve these model ODEs, a program using the Mathematica™ [4] platform was implemented as follows:

When the FCL is not included in the circuit, the Eqn.. 5.1 ODE becomes;

$$V_s \sin \omega t = \left(R_s + \frac{R_f R_L}{R_f + R_L} \right) i + (L_s + L_L) \frac{di}{dt} \qquad (5.2)$$

where current ***i*** has to be found as a function of time ***t***. R_f is a fault resistance which is made very large with $R_f = 10^6$ Ohms (by turning off the switch in Fig. 5.3) when there is no fault, and takes a value of $R_f = 0.08$ Ohms when there is fault present (by turning on the switch in Fig. 5.3). Let R_{t1} be total resistance under normal operation and L_{t1} be total inductance under normal operating conditions.

When the FCL is introduced, the ODE becomes:

$$V_s \sin \omega t = \left(R_s + \frac{R_f R_L}{R_f + R_L} \right) i + (L_s + L_{\text{var}1} + L_{\text{var}2} + L_L) \frac{di}{dt} \qquad (5.3)$$

where the conditions relating to R_f are the same as above. Let R_{t2} be total resistance during the fault condition and L_{t2} be total inductance under fault conditions. The variable inductances L_{var1} (inductance due to the positive half cycle limiting process of the FCL) and L_{var2} (inductance due to the negative half cycle limiting process of the FCL) are both functions of current ***i*** because the permeability of the core changes with the total magnetic field which is in turn controlled by the line current. The total magnetic field is represented by the cumulative sum the fields generated by the AC line current, and the DC bias coil current. Symbolically,

$$H_{total}(t) = \begin{cases} H_{DC} + H_{AC}(t) & \textit{for positive half cycle} \\ -H_{DC} + H_{AC}(t) & \textit{for negative half cycle} \end{cases} \qquad (5.4)$$

where H_{DC} is the DC bias generated field, and $H_{AC}(t)$ is the field generated by the AC line current per time step. The analytic equation used to represent the H-field here is the generalised Ampere's extension Eqn. 4.14 proposed in Chapter 4, with the

exception of the shape function $\mathbf{f_{shape}(x)}$ being represented as a numerical variable factor (***ACMultfac***). As a consequence,

$$H(t) = ACMultfac\frac{Ni(t)}{L}\left[\frac{(L+2x)}{2\sqrt{D^2+(L+2x)^2}}+\frac{(L-2x)}{2\sqrt{D^2+(L-2x)^2}}\right] \quad (5.5)$$

where the variables ***N, L, I, D*** and ***x*** depend on the generating coil – either AC or DC. It should be noted that since the electromagnetic interactions are taking place at the AC coils, $x_{AC}=0$ and hence the equation reverts to the standard Ampere's derivation of Eqn. 4.14 when dealing with the AC coils on both cores.

Another physical significance of the factor ACMultfac is that it is used to determine the appropriate bias level for the DC coil. A requirement of the FCL is that during normal operating conditions, the magnetic cores have to be deeply saturated so that the AC winding impedance is low enough for the device to be considered transparent to the network [5]. Usually, the required value of the DC mmf can be determined from the requirement that the maximum limiting process occurs when the DC bias field is brought to zero by the AC line current induced field H_{AC}. That is,

$$N_{DC}I_{DC} \cong ACMultfacN_{AC}I_{AC} \quad (5.6)$$

Thus for either core, the FCL average inductance calculated is,

$$L_{\mathrm{var}(1or2)}(t) = \mu_0 \frac{A_{AC}.N_{AC}^2}{l}\mu_r\left(H_{total}(i(t))\right) \quad (5.7)$$

where N_{AC} is the number of AC coil turns, A_{AC} is the surface area of the AC coil, and l is the mean magnetic path length around the core. It should be noted that the inductance here depends on the current values and also the time value of the waveform. The inductance is thus represented by an expression for the differential permeability obtained from the B-H expression in Eqn. 2.14 of Chapter 2.

$$\mu_r(t) = \frac{dB}{dH(t)} = \mu_0 \left(\frac{B_s}{\mu_0} \left(\frac{a}{H_{total}(t)^2} - \frac{1}{a} \operatorname{cosech}^2 \left(\frac{H_{total}(t)}{a} \right) \right) + 1 \right) \quad (5.8)$$

Implementing these equations in the section above into the circuit ODE provides an equivalent circuit model that incorporates the FCL and its parameters.

5.3. *Piecewise Formulation of Material Representation and Analysis of Effects in SCFCL*

5.3.1. *Piecewise Function Determination*

Given the complexity and interdependence of the constitutive equations of the ODEs and the output variables, the resulting differential equation was initially difficult to solve analytically. This was due to the cyclic dependence of the variables as was evident with the fact that the inductance L_{var} of the equation depended on the value of the current at any particular solution time step, and this current value was in turn depended on the total inductance of the circuit. Furthermore, the nonlinear resultant inductance that was added through the functioning of the FCL does not have a direct analytic expression and hence was difficult to implement in the software due to solver limitations. This level of complexity was initially circumvented in order for an initial solution to the circuit ODE to be obtained.

The method used to solve this equation was to replace the continuous material representation B-H characteristics with a piecewise function, with linear constituent equations. This traded some degree of accuracy, but resulted in an initial solvable differential equation.

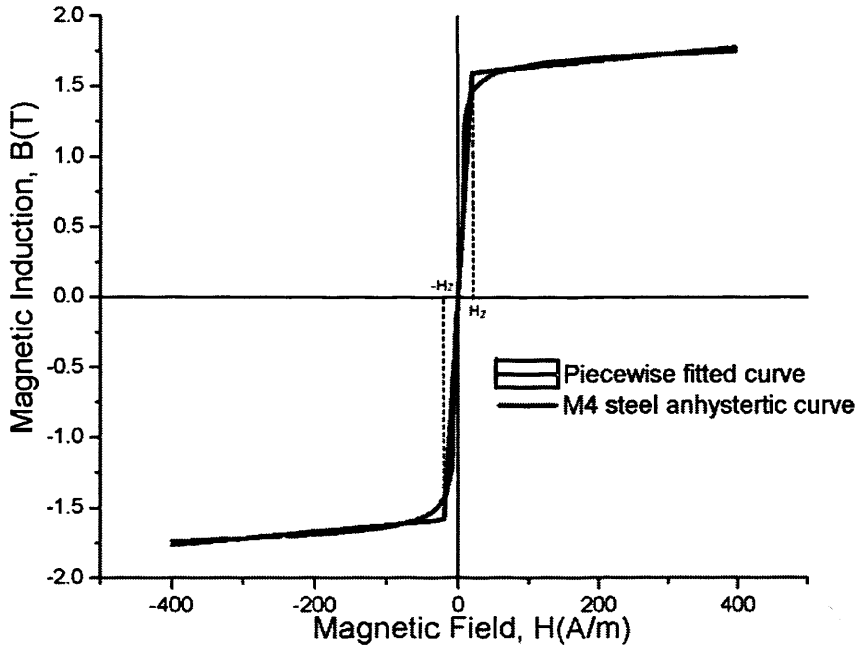

Fig. 5.4: Piecewise representation of the M4 steel anhysteretic curve.

The piecewise equation obtained from the fitting was:

$$B(H)=\begin{cases} B_s+\mu_0 H & when\ H<-H_z \\ \dfrac{B_s H}{3a}+\mu_0 H & when\ -H_z \le H \le H_z \\ -B_s+\mu_0 H & when\ H>H_z \end{cases} \qquad (5.9)$$

The value for $H_z \approx$ 3a was estimated from the closest fitting with the modified Langevin function (obtained as the slope of the curve at the origin) representation of the anhysteretic curve. From this B-H function, a function for the differential permeability is thus obtained by piecewise differentiation as

$$\frac{dB(H)}{dH} = \begin{cases} -\mu_0 & when \quad H < -H_z \\ \dfrac{B_s}{3a} + \mu_0 & when \quad -H_z \le H \le H_z \\ \mu_0 & when \quad H > H_z \end{cases} \qquad (5.10)$$

This provides a constant permeability for every part of the piecewise equation that represents one of the three regions of the curve as shown in Fig. 5.4. Hence an analytic model can be formulated by solving the ODEs under normal operating conditions and during the fault condition.

The general solutions for Eqns. 5.2 and 5.3 give a complete solution to the current wave equation. Let the time of fault inception be t_f, and if $F_4=N^2_{AC}.A_{AC}/l$, then the general solution is,

When $t < t_f$,

$$i(t) = Ke^{\frac{R_{t1}}{L_{t1}}t} + \frac{V_s\left[-L_{t1}\omega\cos\omega t + R_{t1}\sin\omega t\right]}{R_{t1} + L_{t1}.\omega^2}$$

When $t \ge t_f$,

$$i(t) = \begin{cases} Ke^{\frac{R_{t2}}{F_4\mu_0 + L_s}t} + \dfrac{V_s\left[-(F_4\mu_0 + L_s)\omega\cos\omega t + R_{t1}\sin\omega t\right]}{R_{t1} + (F_4\mu_0 + L_s).\omega^2}, & H < -3a \\ Ke^{\frac{R_{t2}}{F_4(\frac{B_s}{3a} + \mu_0) + L_s}t} + \dfrac{V_s\left[-(F_4(\frac{B_s}{3a} + \mu_0) + L_s)\omega\cos\omega t + R_{t1}\sin\omega t\right]}{R_{t1} + (F_4\mu_0 + L_s).\omega^2}, & -3a \le H \le 3a \\ Ke^{\frac{R_{t2}}{F_4\mu_0 + L_s}t} + \dfrac{V_s\left[(F_4\mu_0 + L_s)\omega\cos\omega t + R_{t1}\sin\omega t\right]}{R_{t1} + (F_4\mu_0 + L_s).\omega^2}, & H > 3a \end{cases}$$

(5.11)

Using initial boundary condition such that i(t)=0 at t=0, C can be found and substituted in Eqn. 5.11.

The mathematical implementation model incorporating above solutions and expressions was then analysed in the voltage driven model, to check its the functionality and the limits of its applicability.

The initial circuit parameters and FCL prototype values used were:

- AC voltage supply, at 60 Hz, $V_s(t) = \sqrt{2}\ 7.96 \sin(\omega t)$
- Source inductance, L_s=0.002 H
- Source resistance, R_s=0.1 Ohms
- Load inductance, L_L=0.008 H
- Load resistance R_L=10 Ohms
- Fault resistance R_f=0.08 Ohms

For the AC side of the system:

- Number of turns on AC side, N_{AC} = 20
- Cross sectional area of AC coil, A_{AC} = 0.015m^2
- Height of AC coil, H_{AC} = 0.35 m
- Diameter of AC coil, D_{AC} = 0.2m

For the DC side of the FCL system:

- Current in DC coil, I_{DC} = 400A
- Number of DC turns, N_{DC} = 300
- Cross sectional area of DC coil, A_{DC} = 0.0225m^2;
- Height of DC coil, H_{DC} = 0.35m
- Diameter of DC coil, D_{DC} = 0.2m

with the initial fitted values for the M4 steel magnetic material parameters :

- B_s=1.7 T

- a=5 A/m

These values were input into the voltage model and preliminary tests were run with different variations to the parameters under investigation

5.3.2. *Investigation of Model Parameters With Piecewise Model Implementation*

In order to investigate how the parameters under investigation (material parameters a and B_s, and model parameter ***ACMultfac***) influence the functioning of the FCL model, the initial prototype values were input into the VDM coded in Mathematica™ and the parameters under investigation were input with ranges above and below the initial input value, to test its effects on the current waveform. The system was implemented such that normal operating conditions were in place from the start of the test run, till the fault was inserted at 0.1s, and allowed to run indefinitely.

5.3.2.1. *Waveform investigation at ACMultfac of 100*

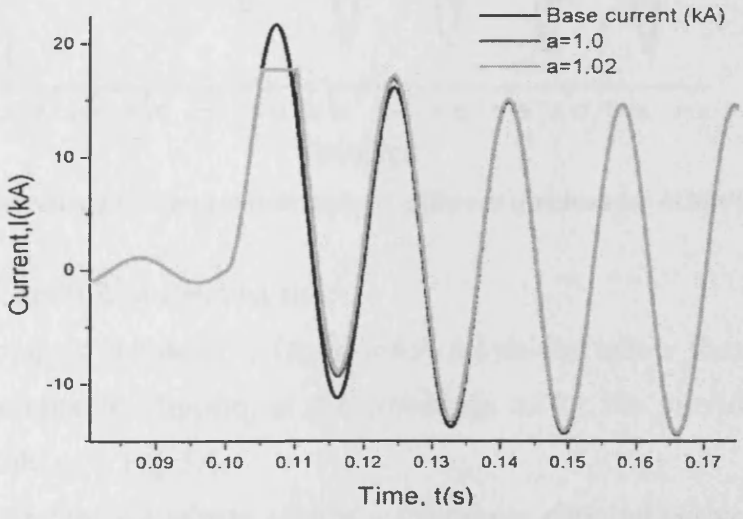

Fig. 5.5: Piecewise function comparison at different **a***-values for ACMultfac = 100*

Points to note from the waveform:

i.) The current waveform clipping is apparent only from *a=1*, as any values below this resulted in no apparent clipping of the waveform;

ii.) The clipping was almost instantaneous at 17.7 kA (not a gradual progressive clipping);

iii.) Above *a=1.05*, the waveform was distorted or destroyed by the algorithm.

5.3.2.2. Investigation at ACmultfac of 5000

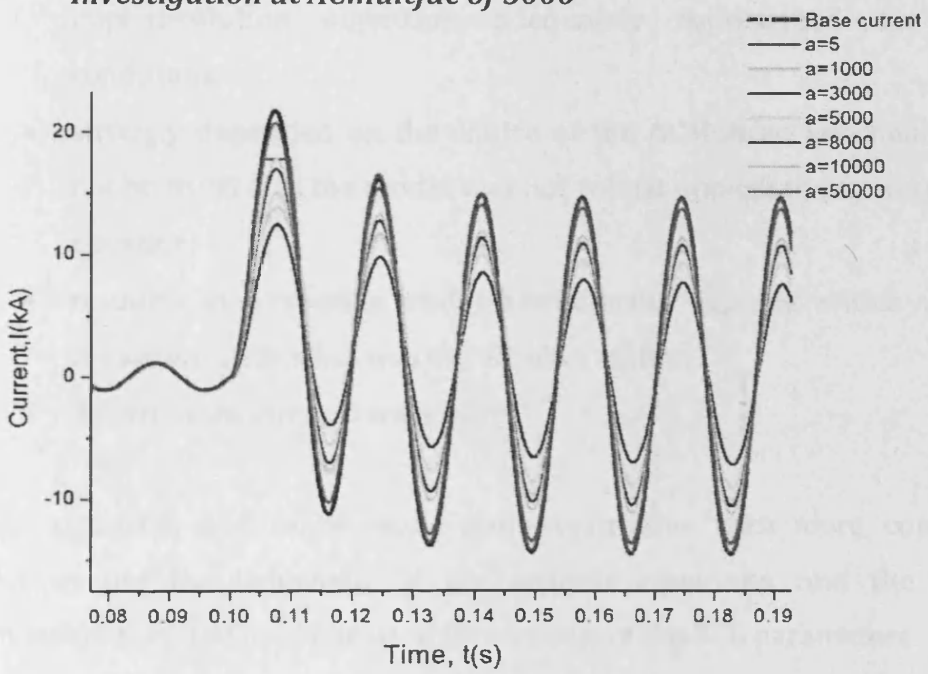

Fig. 5.6: Piecewise function comparisons at different a-values for ACMultfac = 5000

Points to note from this model test run:

i.) Clipping is visible only from *a=4.9*. All values below that resulted in no instantaneous clipping of the waveform as for the previous value of the ACMultfac in Fig. 5.6;

ii.) The current waveform attains a maximum clipping between *a=3000* and *a=5000;*

iii.) For increasing values of the ***a***-parameter above 5000, there is continuous current clipping although the magnitude of this clipping reduces with increasing value of the ***a***-parameter;

Numerous tests carried out with these initial factors using the piecewise function revealed that the voltage model with the piecewise implementation:

- provided a proof of concept for the model, showing that the implementation algorithm adequately represented the circuit conditions.
- strongly depended on the choice of the ACMultfac, and hence could not be trusted as the model was not robust enough to represent a real situation.
- resulted in a sudden and instantaneous clipping which was not consistent with what was expected in reality;
- distorted the current waveform .

Hence, the algorithm had to be made more restrictive with more constraints introduced, as per the behaviour of the analytic equations, and the current waveform before the VDM could be used for analysis of the FCL parameters.

5.4. Refinement and Mathematical Limitations of Model Equations

An important part of describing the voltage driven model (VDM) was to be able to predict and control the clipping levels. This ultimately included finding analytic tools that could describe the clipping that was realised and which could be included in the model.

The piecewise function, enabled this part of the research by providing a starting point for such an endeavour, but as seen above the model needed more restrictive

equations in order to provide better functionality. The sudden clipping of the waveform seen is due to the fact that the initial assumptions were made for a knee point for the B-H characteristic representation having sharp change from one linear equation to the other, instead of the smooth continuous curvature of the B-H curve which is more representative of reality.

More assumptions had to be made for a consistent mathematical formulation to result. Firstly, effective current clipping is assumed to start at a particular value of field, H_z, which is determined from the anhysteretic piecewise curve by comparison to the modified Langevin function. The expressions were incorporated into the equivalent circuit system by using the idea that clipping will start immediately after the DC field H_{DC} is pushed by the AC contribution H_{AC} past the field H_z in either direction. This condition supposes that the clipping capacity of the FCL is concentrated at the steepest part of the curve and hence taking the curve to this steep part gives the highest inductance gain. Mathematically:

$$H_{DC} - H_{AC} = H_z \qquad (5.12)$$

Now, the clipped current waveform I_{clip} which is the current at H_z will be calculated using the standard Ampere's Law derivation

$$H_{AC} = \frac{N_{AC}}{l} i_{clip} \qquad (5.13)$$

because the interaction is assumed to be inside the AC coil and hence the uniform mmf. Therefore the general equation for determining the clipping current level will be,

$$i_{clip} = \frac{H_{DC} - 3a}{ACMultfac} \frac{l}{N_{AC}} \qquad (5.14)$$

But for most practical purposes and the majority of the materials being investigated at the moment, $H_{DC} >> 3a$. Hence it can be asserted that the line current should conform to the analytic expression,

$$i_{clip} \approx \frac{H_{DC}}{AcMultfac} \frac{l}{N_{AC}} \qquad (5.15)$$

Secondly, the test runs showed that when clipping of the current occurred, depending on the inductance, there was an overshooting of the solution current waveform, as illustrated in the magnified diagram in Fig. 5.7

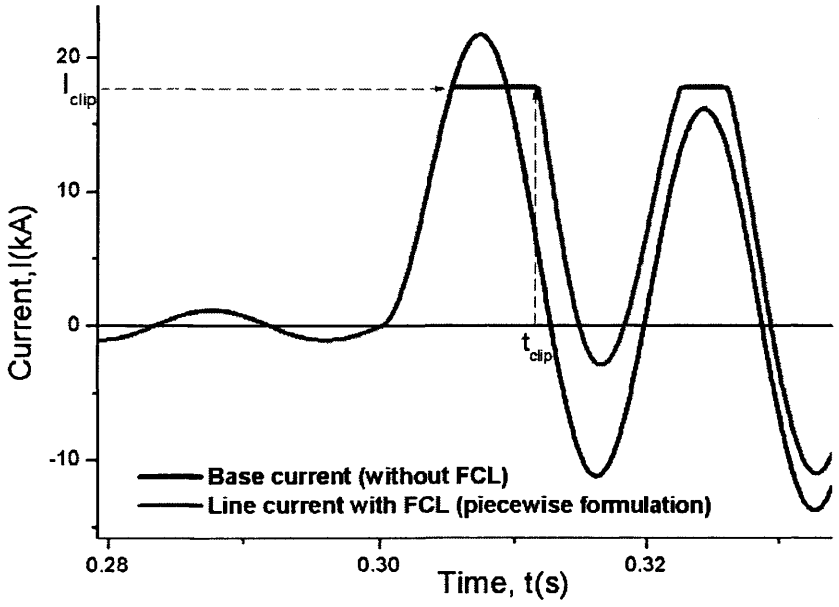

Fig. 5.7: Modelled current-time graph showing the overshoot properties of I_{clip} *at* t_{clip}

The clipped current waveform overshoots the base current waveform, and this anomaly increases with increase in inductance. This effect stops the expected sinusoidal pattern of the solution waveform for a couple of cycles, essentially converting it into a quasi-DC response. This observation is due to modelling equation approximations and errors

To remedy this, there have to be restrictions placed on the inductance-current waveform interaction, so that such large increases in inductance that cause the

destruction of the sinusoidal waveform be avoided, and hence the AC line current and the base current should be identical in both phase and amplitude.

Thus the further assumption that at the start of fault, before the clipping sets in , the FCL inductance is essentially negligible (L $\approx$0) is made. Substituting this into the Eqn. 5.14, and circuit ODEs from the circuit equation, Eqn. 5.1 gives,

$$t_{clip} = \arcsin\left(\frac{H_{DC}.l.R_f}{AcMult.N_{DC}.V_0}\right) \qquad (5.16)$$

This is a new analytic constraint to determine the approximate time at which the clipping should stop occurring on an appreciable scale.

Using Eqn. 5.16 to solve the ODE in order to insure a sinusoidal solution current waveform, results in a constraining equation between the network parameters and the inductance, Eqn. 5.17. Solving and simplifying the results in a complex condition which has to be satisfied for the solution current to stay in coherent oscillation with the base current:

$$L\left[\frac{\left(1-e^{\frac{R_f}{L}(2t_{clip}-\frac{\pi}{\omega})}\right)}{\left(1+e^{\frac{R_f}{L}(2t_{clip}-\frac{\pi}{\omega})}\right)}\right] = \frac{R_f}{\omega}\coth(\omega t_{clip}) \qquad (5.17)$$

It is clear from this equation given that t_{clip} exist on both sides that, that L can only be solved iteratively using numerical methods, one of which is the Newton-Raphson method of iteration.

With these mathematical constraints incorporated into the algorithm, the analysis of the device by varying the parameters under investigation to see their effects on the clipping point was undertaken.

5.5. *Study of Material Parameters on Functionality of SCFCL at Fault Inception*

In order to represent the non-linearity of the core material, the continuous anhysteretic equation was used instead of piecewise approximation for the further study of the FCL functional model.

Except where otherwise stated, the following parameters under investigation, were held constant at these values: B_s = 1.5 and a = 5, but the X/R ratios of the circuit was changed to 44 and the source voltage increased to 100V such that the peak fault current changed to 270 kA from 2kA nominal current, in order to get a more asymmetric fault current. This helps in providing a higher fault peak, and hence makes it easier to see the effect of the various parameters investigated. Also, the time for the fault inception was changed to 0.3s to allow for stability of the circuit.

5.5.1. *Effect of the ACMultfac*

The first parameter investigated in the setup was the ACMultfac numerical factor. This ratio is defined as the factor that incorporates the differences in the core geometry and fringe effects into the magnetic field distribution. It can also be considered as the factor between the DC and AC mmfs, used in locating where the operating point should be.

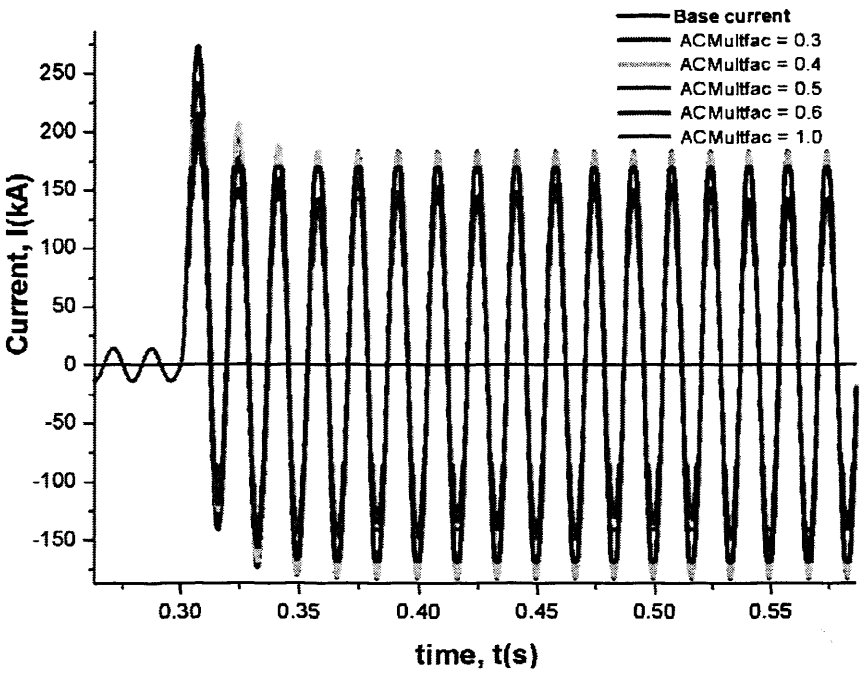

Fig. 5.8: Comparison of different current waveforms in circuit after fault inception, with FCL having different AC coil turns ratios

The waveforms are now properly sinusoidal and moreover, the clipping of the line current is continuous and not instantaneous. This shows that the additional constraints and improvements incorporated as discussed earlier have made the model more realistic in modelling the current clipping of the FCL.

As seen in Fig. 5.8, there is increased clipping of the waveform for increased ACMultfac values. Moreover, the ACMultfac variation has been reduced significantly compared with what was previously seen in the piecewise interpretation. These point to the fact that the model has become more accurate and robust as a tool to be used in studying the FCL.

But there is a peculiar occurrence with ACMultfac =1, where the current clipping levels become uneven even after the fault level has stabilised. These results are better explained in terms of how the total magnetic field varies during the same time period.

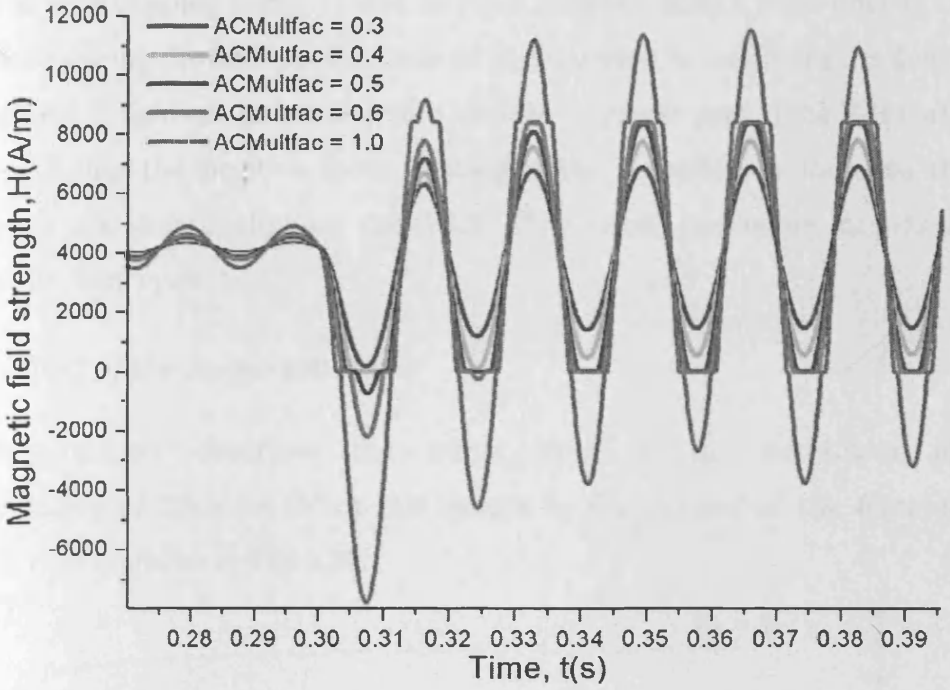

Fig. 5.9: Comparison of different H-field values for different AC coil ratios plotted in the same time period.

It is noticed in Fig. 5.9 that, as the ACMcultfac is increased, a point is reached where the total field waveform goes through a point of inflection before continuing in a sinusoidal path. These points coincide with the areas of unevenness in the clipping of the current waveforms. When the model allowed the total magnetic field to be pushed past the origin into the negative part of the material representative curve (overshoot), there is a violation of the initial operating condition for clipping of the FCL established earlier such that

$$H_{AC} \pm H_{DC} \sim 0 \qquad (5.18)$$

This violation does not necessarily disrupt the clipping but reveals an important design possibility. For added clipping, Eqn. 5.17 can be relaxed in design as long as it does not take the core into reverse saturation, such that the positive cycle can be moved into the negative part of the curve by H_{ac}, but stays in the region of high permeability. It is noticed though, that the uneven clipping waveform occurs below

the initial peak clipping current value as Fig. 5.8 shows. Hence if the uneven clipping is tolerable during the fault period, it could be an option to configure the device such that the total H-field can go beyond zero into the negative part of the B-H curve. This happens during the positive fault limiting cycle, in order to increase the gain inductance and hence clipping capability. The same procedure occurs for the negative limiting cycle.

5.5.2. Effect of the B_s-parameter

The B_s-parameter describes the upper limit of the non-linear material representation of the core. What this means in the context of the ferromagnetic material type is shown in Fig. 5.10.

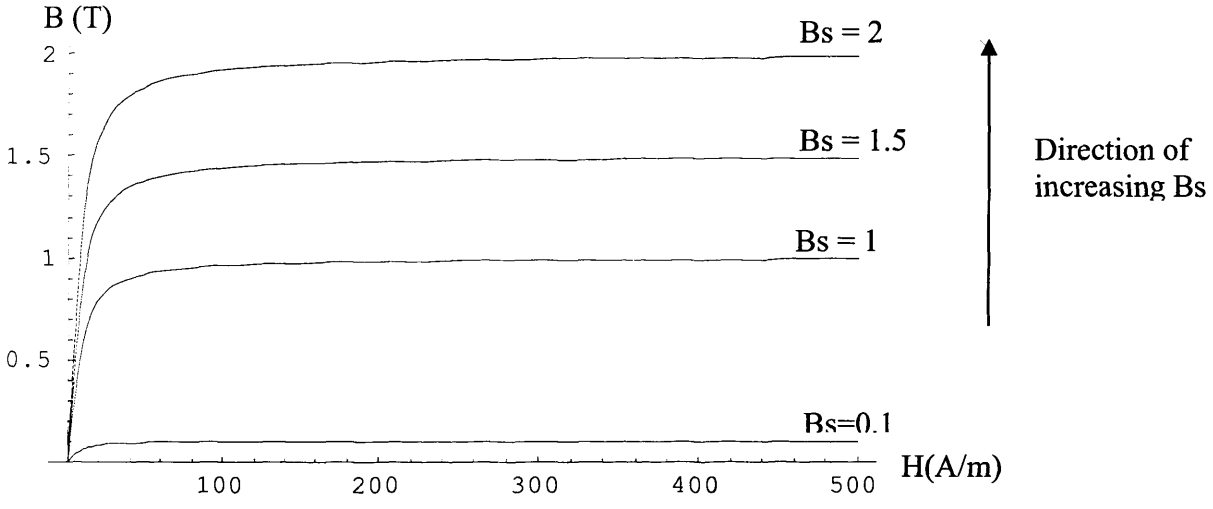

Fig. 5.10: Non-linear anhysteretic curve (1st quadrant) representation for M4 steel with different values of the B_s.

The effect of different values of B_s on the line current is shown in Fig. 5.11.

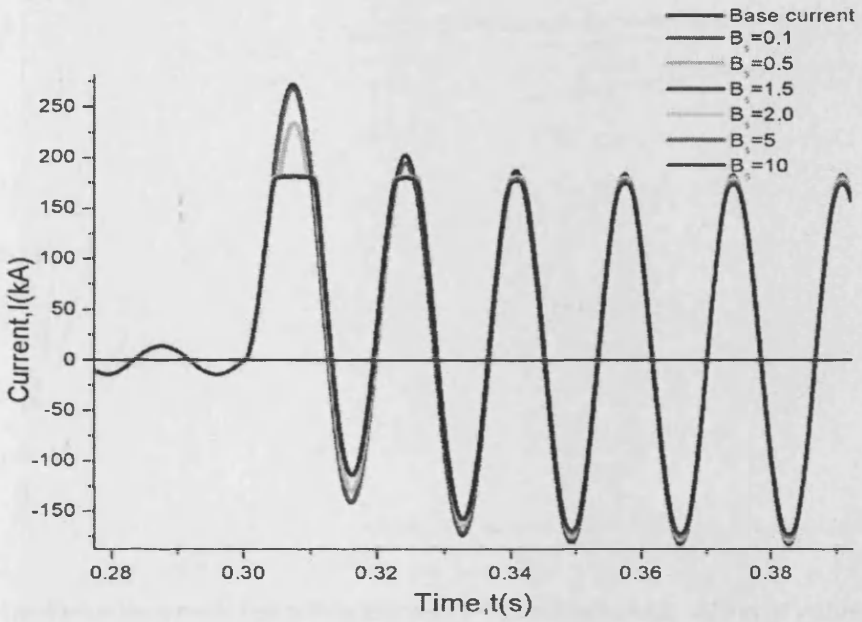

Fig. 5.11: Comparison of current waveforms for different values of the B_s*-parameter.*

As shown in Fig. 5.11, there seems to be an optimum value for B_s, below which changes in B_s have little effect on the clipping of the current. In this test run, beyond B_s = 1.5, there is little functional gain in clipping the current when this value is increased. This implies that materials around this saturation magnetisation value could be the best for this FCL. This means it may be unnecessary to consider more expensive materials with higher saturation magnetisation. The analysis also point towards the possibility that particular materials (with particular values of B_s) could be optimum for particular ranges of currents limiting, at various levels of the power distribution grid.

5.5.3. Effect of the a-parameter

The ***a***- parameter is responsible for the slope (curvature) of the nonlinear BH curve, as shown in Fig. 5.12.

The effect of the ***a***-parameter on the clipping levels of the FCL is shown in Fig. 5.13:

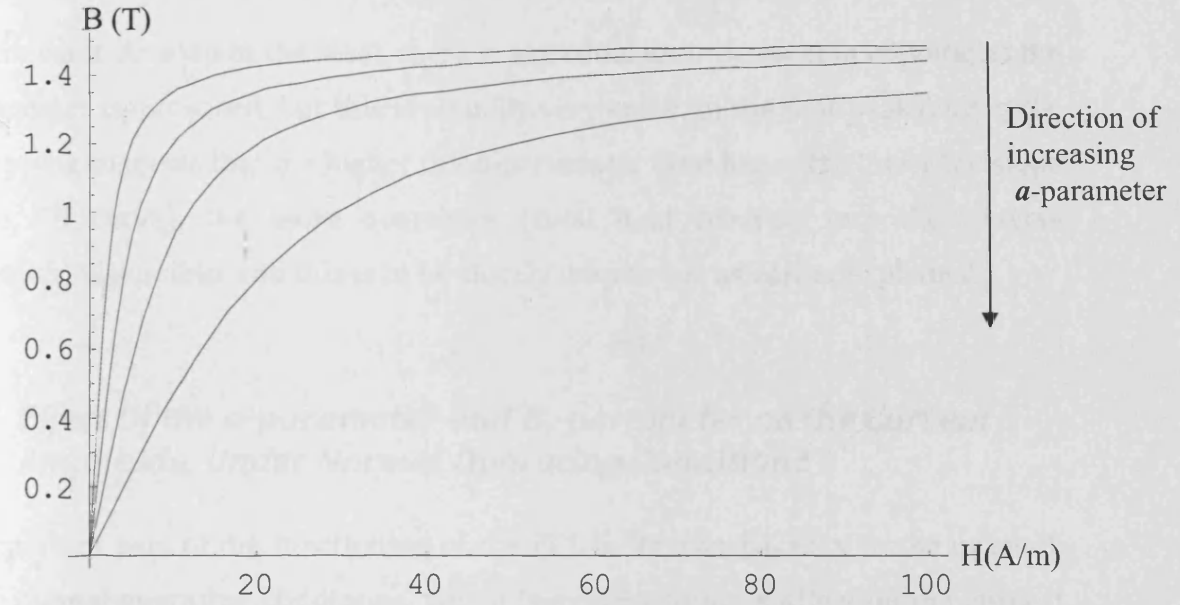

Fig. 5.12: Non-linear magnetic induction curves (1st quadrant) with different values of the **a***-parameter.*

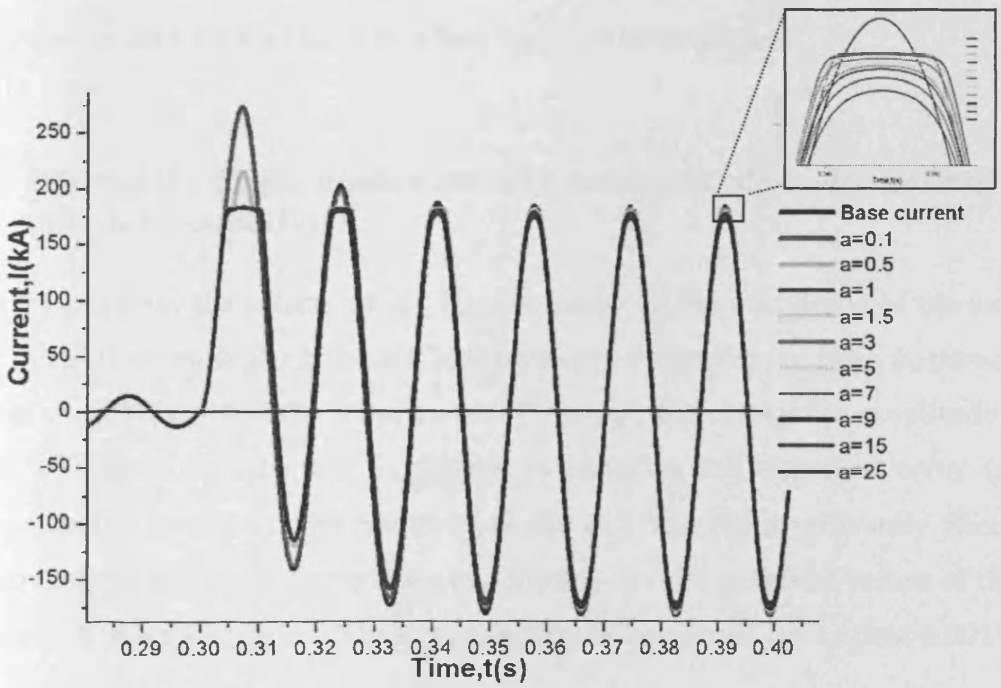

Fig. 5.13: Comparison of current waveforms due to different values of the **a***-parameter.*

The graph suggests that there is not a lot of difference in clipping current caused by changes in the a-parameter of the non-linear curve, as long as the operating point is

held constant. As seen in the inset, there is a gradual improvement in clipping as the a-parameter is increased, but this is actually very small. In the first peak fault cycle, the clipping suggests that the higher the a-parameter (and hence the lower the slope of the BH curve), the more overshoot (total field crossing into the reverse saturation) is possible, and this is to be closely monitored, as earlier explained.

5.6. *Effect Of the a-parameter and B_s-parameter on the Current Amplitude, Under Normal Operating Conditions*

An important part of the functioning of the FCL is its transparency to the network under normal operating conditions, which is evident from its effect on the current amplitude when there is no fault on the network. Ideally, there should be no reduction in the current amplitude at all, and this constraint makes it necessary to study how the core parameters can affect the current amplitude.

5.6.1. *Effect of the Bs-parameter on Current Amplitude under Normal Operating Conditions*

Table 5.1 presents the effects of the B_s-parameter on the amplitude of the current under normal operating conditions. It shows that the increase of the B_s-parameter reduces the amplitude of the line current. However, the changes in amplitude start in the 4th digit only and are negligible, considering the expected error in the measurements. Therefore, the presence of the FCL will not significantly affect the line current during normal operating conditions. For the practical values of the B_s-parameter (values less than 2.5T), the reduction in amplitude is less than 0.001%.

Table 5.1: The effects of the Bs*-parameter on the amplitude of the current, under normal operating conditions. Note that the change in amplitude starts in the 4th digit only.*

Case studied		**Current Amplitude, kA**
No FCL	Base current	13.972850
FCL with B_s =	0.1	13.972845
	0.5	13.972831
	1.5T	13.972793
	2.01T	13.972774
	5T	13.972660
	10T	13.972469

5.6.2. *Effect of The a-parameter On Current Amplitude under Normal Operating Conditions*

Table 5.2 presents the effects of the a-parameter on the amplitude of the current under normal operating conditions. It shows that the increase of the a-parameter value reduces the amplitude of the line current. However, the changes in amplitude start in the 4th digit only and are negligible; therefore, the presence of the FCL will not significantly affect the line current during normal operating conditions.

Table 5.2: The effects of the a*-parameter on the amplitude of the current, under normal operating conditions. Note that the change in amplitude starts in the 4th digit only.*

Case studied		**Current Amplitude, kA**
no FCL	Base current	13.972850
FCL with a =	0.1	13.972816
	0.5	13.972809
	1.5	13.972799

	2.01	13.972723
	5	13.972685
	10	13.972647

What emerges from this analysis is a comparison of the effects of the a-parameter and the B_s-parameter with respect to their influence on the current waveform amplitude values. Under normal operating conditions, the B_s-parameter has more influence, albeit very small; on the AC line current than the a-parameter as shown in Tables 5.1 and 5.2.

However, both parameters change the amplitude negligibly (less than 0.001 %); therefore, it can be concluded that the ferromagnetic material characteristics of the FCL do not significantly affect the line current during normal operating conditions.

5.7. *Frequency Response of Model Parameters in Relation to SCFCL Functionality*

An examination was also carried out on the effects that the material parameters under investigation had on the frequency of the current system in which the FCL will be functioning. Specifically, the effects of the FCL parameters on line frequency both during the fault and during normal operating conditions were analysed. Such an analysis will give a qualitative estimate as to how the choice of material and circuit parameters can affect frequency, given that little or no frequency distortion is permissible for the application of such a device on the power network.

The differences caused by the parameters were compared with each other using the frequency of the base current frequency waveform as a standard, i.e. the fault waveform generated for an electrical system without an FCL. The frequency change from the base current was calculated using the frequency difference Δf such that,

$$\Delta f = frequency_{parameter\ value} - frequency_{base} \qquad (5.19)$$

where the parameter value represents the frequency at the particular parameter value being investigated. As such, this frequency change is expressed as a percentage change:

$$Frequency\ \ change = \frac{\Delta f}{frequency_{base}} \times 100\% \qquad (5.20)$$

The study was carried out over 3 different fault cycles (1st, 5th and 10th) of the waveform to ensure that the effects were studied under stable network conditions. This was needed in order to show that these are real effects as opposed to simply transient responses. Additionally, the results of variation of B_S- and α-parameters on the frequency of the base current, i.e. the current under normal operating conditions, were analysed.

5.7.1. Frequency Change in the First Cycle

In performing the analysis using the WVM, special attention was paid to the method of fault inception and its possible effect on the frequency analysis, for establishing a good base case to which all the other frequency values could be compared. The base frequency analysis shows an inherent frequency change in the waveform during the first cycle of the fault in Fig. 5.14. This was discovered to be dependent on the X/R ratio and timing of fault inception.

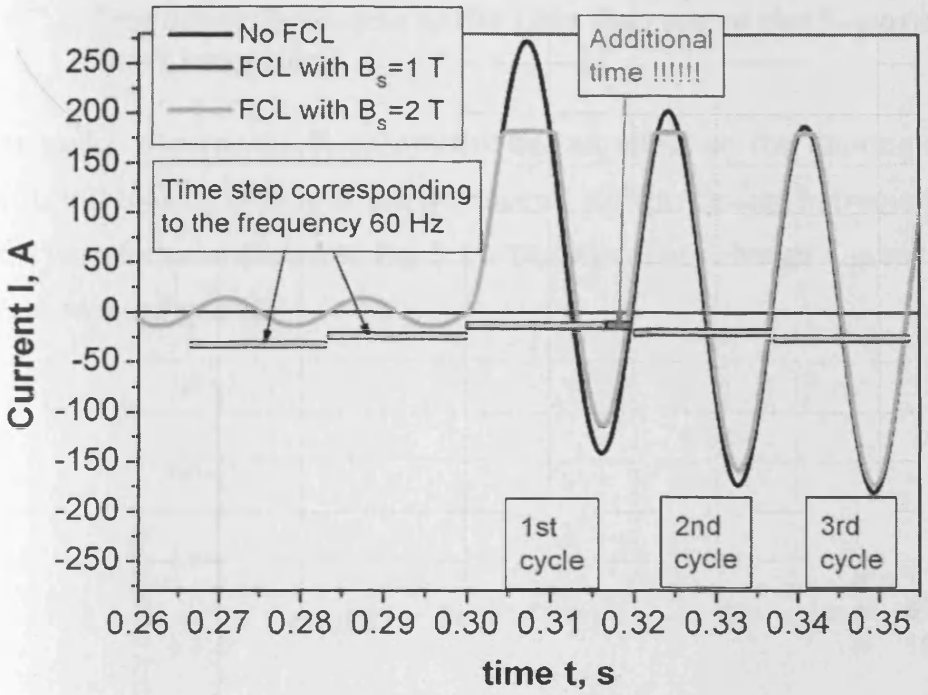

Fig. 5.14: Current as a function of time before and after the fault (which is introduced at t=0.3s). Note that the 1st cycle of the fault current is longer in time than all other cycles.

The frequency of the 1st cycle in this case was estimated to be 61 Hz compared with 60 Hz before the fault. Also, after this 1st cycle, all other fault cycles have frequency close to 60 Hz. In the mathematical algorithm, the total resistance of the system changed instantaneously (from a 'No Fault value'= 10^6 Ohms, to 'Fault value' = 0.08 Ohms), at the time of the fault (t=0.3 s, this number was chosen arbitrary in time but at the stable normal operation stage):

$$R = \begin{cases} No\ fault\ value, & t < 0.3\,s \\ Fault\ value, & t \geq 0.3\,s \end{cases}$$

It is important to note that this frequency shift is noticed for all the waveforms and so it can be judged as a natural consequence of the circuit. Hence it can be considered independent of the method of fault introduction. That is why the further analysis was carried out for the 10th fault cycle.

5.7.2. *Frequency Response of the Line Current to the B_s-parameter (After Fault Inception)*

As earlier shown, the B_s-parameter has an effect on the limiting capability of the FCL. But looking closely at the waveforms a slight change in frequency is noticed on the waveform, as shown in Fig. 5.11. The frequency change due to the B_s-parameter is shown in Fig. 5.15.

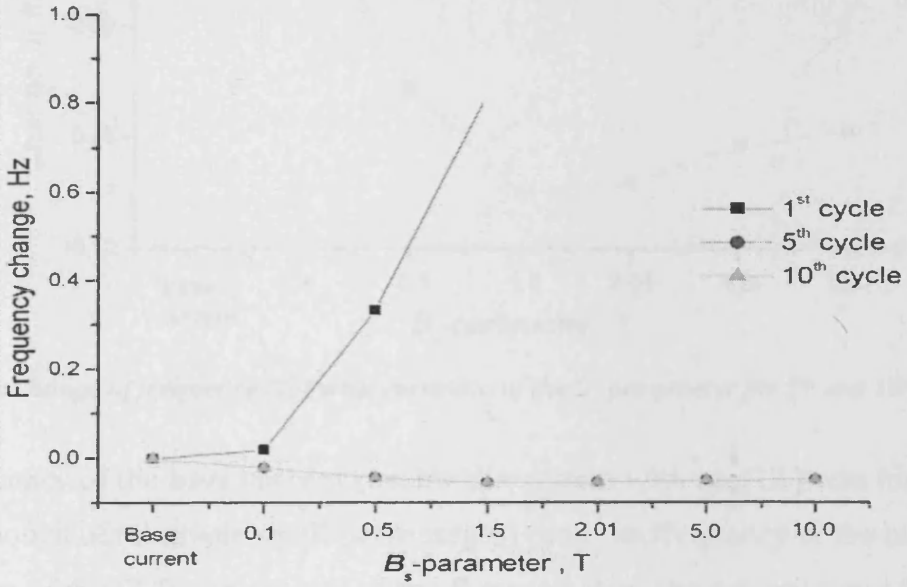

Fig. 5.15: Frequency change Δf as a function of the B_s-parameter after fault inception over different wave cycles.

The first cycle has the largest frequency variations from the base current as was shown in the Fig. 5.15, but as the wave progresses to the 5th through the 10th cycle, it is noticed that the frequency effects stabilise to a more consistent pattern for all cycles.

For this reason, the frequency analysis was carried out at the 5th and 10th cycles. Fig.5.16 shows how changing the B_s-parameter changes the frequency under stable fault conditions.

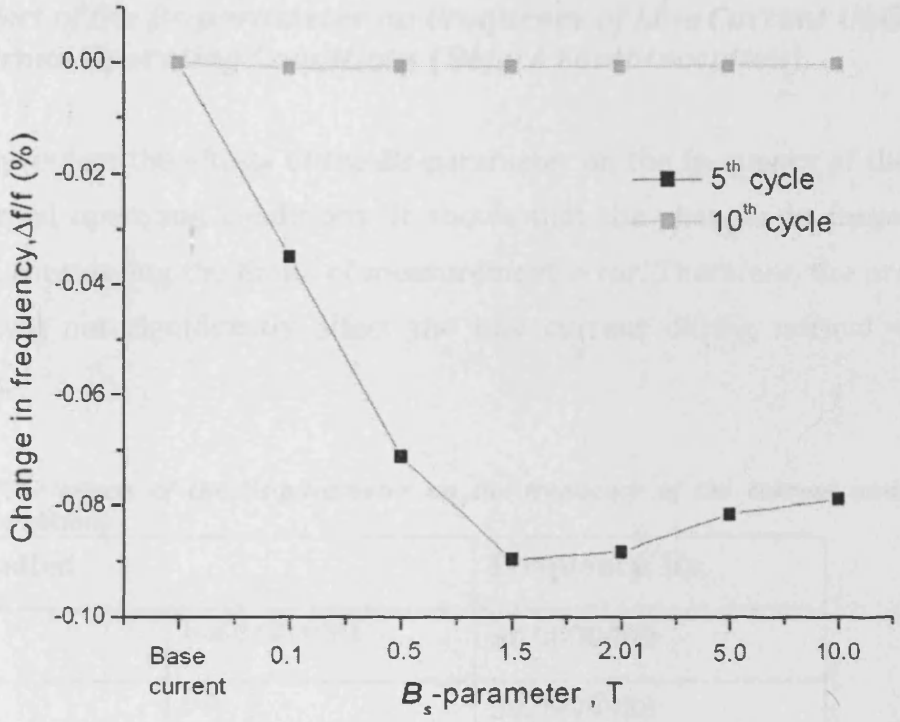

Fig. 5.16: Change of frequency Δf/f with variation of the B_s-parameter for 5th and 10th cycles.

The frequency of the base current (i.e. for the system with no FCL) was found to be larger (though of relatively small percentages) than the frequency of the current for the system with FCL for any values of the B_s-parameter. The general trend for the 5th cycle presented in Fig. 5.16 shows that as the values of the B_s-parameter increases, frequency change decreases to a certain value and then levels up. At the 10th cycle, it is seen that the frequency change is very small (less than 0.001 %) and shows no major pattern. Since the B_s-parameter represents the saturation induction, the trend suggests that the B_s-parameter has a very limited effect on the frequency of the waveform. But it should be noted that the real values for the M4 steel (B_s is 2.01 T) result in less than 0.002 % decrease in frequency.

5.7.3. *Effect of the Bs-parameter on Frequency of Line Current Under Normal Operating Conditions (Before Fault Inception).*

Table 5.3 presents the effects of the ***Bs***-parameter on the frequency of the current under normal operating conditions. It shows that the changes in frequency are negligible, considering the limits of measurement error. Therefore, the presence of the FCL will not significantly affect the line current during normal operating conditions.

Table 5.3: The effects of the Bs-parameter on the frequency of the current under normal operating conditions

Case studied		**Frequency, Hz**
no FCL	Base current	60.0000000
FCL with B_s =	0.1	59.9999988
	0.5	59.9999988
	1.5	59.9999952
	2.01	59.9999988
	5	60.0000024
	10	60.0000024

5.7.4. *Frequency Response of the Line Current to the a-parameter (After Fault Inception)*

The effect of the ***a***-parameter on the frequency was also analysed at various cycles of the waveform. The percentage change in frequency $\Delta f/f$ is presented in Fig. 5.17 and 5.18.

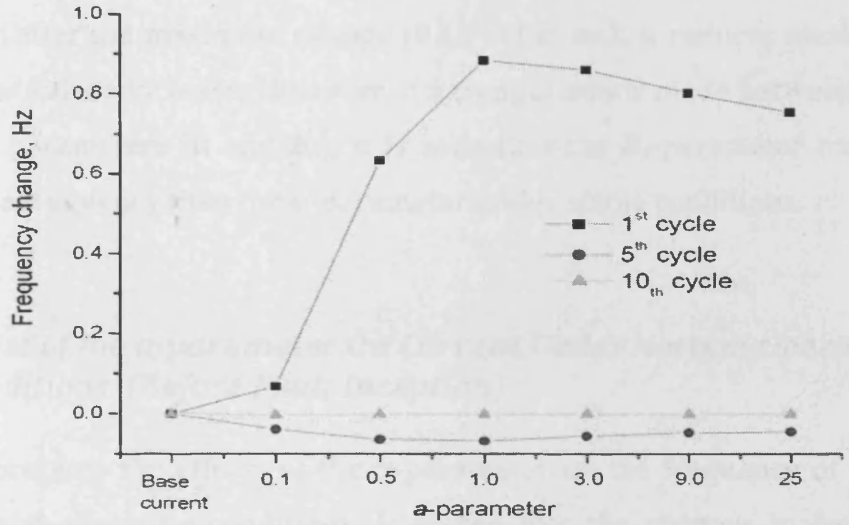

Fig. 5.17: Frequency variation due to the a-*parameter, over different cycles.*

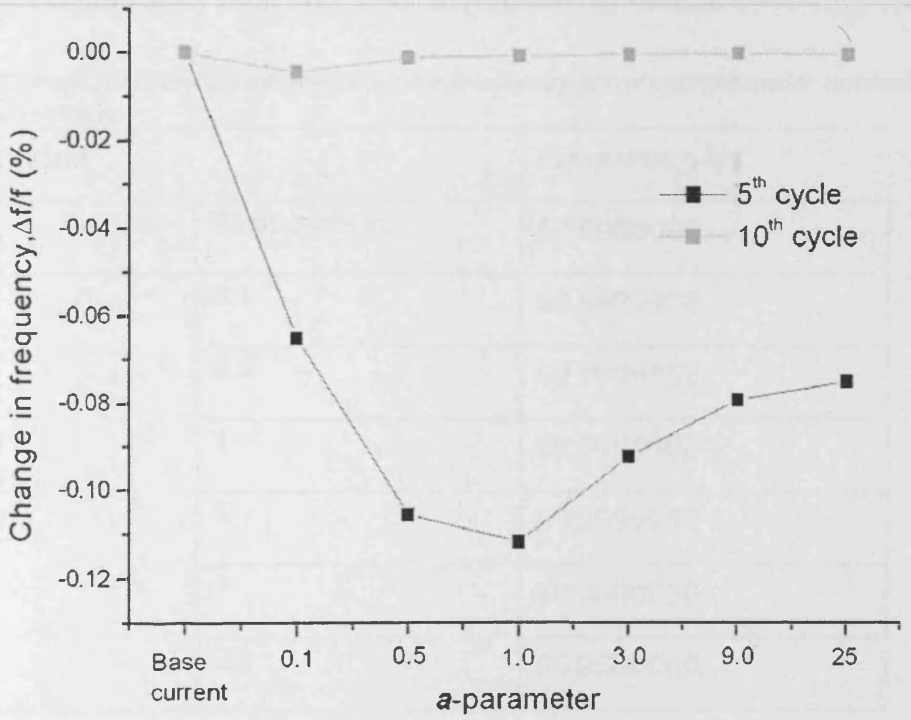

Fig. 5.18: Change of frequency (Δf/f x100%) with variation of the a-*parameter for 5th and 10th cycles.*

It is observed that the frequency change caused by this parameter is small (less than 0.1 %), and after the maximum change (0.12 %) at a=1, it reduces markedly as the a-parameter values increase. However, if a comparison is made between the effects of the two parameters (a and B_s), it is seen that the B_s-parameter has a smaller effect on the frequency than the a-parameter under stable conditions.

5.7.5. *Effect of the a-parameter On Current Under Normal Operating Conditions. (Before Fault Inception)*

Table 5.4 presents the effects of the a-parameter on the frequency of the current under normal operating conditions. It shows that the changes in frequency are negligible, within the limits of measurement error; therefore, the presence of the FCL will not significantly affect the line current during normal operating conditions.

Table 5.4: The effects of the a*-parameter on the frequency of the current under normal operating conditions*

Case studied		**Frequency, Hz**
No FCL	Base current	60.0000000
FCL with a =	0.1	59.9999988
	0.5	59.9999952
	1	59.9999988
	3	59.9999952
	9	60.0000060
	25	60.0000060

This analysis proves that the material representation parameters obtained from the anhysteretic representation of the M4 steel material; do have influences on the total frequency response of the FCL to a network. But these influences have been proven

to minute, and hence the choice of ferromagnetic material can be said to have no direct effects on the frequency at this low frequency levels, even when the fields involved are very high.

5.8. Summary

This chapter reports on an analytic VDM that was built and analysed for the equivalent circuit representation of the FCL in a real power system, using the Mathematica™ software. The model algorithm was developed and was cyclically modified from a piecewise initial setup, into a model which could represent the nonlinear continuous equations and ODEs involved in the FCL analysis. The assumptions needed have been pointed out and mathematical constraints necessary were made to produce a more realistic line waveform before and after fault inception. The direct effects of the ferromagnetic material parameters on waveform amplitude, frequency, and the general clipping capacity of the FCL were examined.
The model provided a basis for studying the FCL functionality and performance directly in a network, and formed a basis from which improvements, both in material, core design and structural modifications could be further investigated by altering the model parameters.

The next Chapter will examine in more detail some of the structural considerations and modifications that are possible when modelling is carried out with the FEM package, and gauge their effects on field distribution and ferromagnetic core performance. Such examination will invariably lead to improvements in the design efficiency of the electromagnetic device, by identifying the key structural components of the design, and studying ways of improving on such components, not only to improve the design on the device but also to improve the confidence in the modelling software being used.

[1] S. M. Rao, Time Domain Electromagnetics, Academic Press, 1999, Chapter 1, Pg. 13

[2] S. Tretyakov, Analytic Modelling In Electromagnetics, Artech House, 2003, Chapter 1, Pg 1

[3] Minseok J., T. K. Kuk, Novel Design And Operational Characteristics Of Inductive High-Tc Superconducting Fault Current limiter, IEEE Trans., On Applied Superconductivity, Vol. 7, No. 2,Pg 1005-1008, June 1997

[4] Mathematica™, Wolfram Group, http://www.wolfram.com/products/ Mathematica/ index.html, 2007

[5] D. Cvoric, S.W.H De Haan, , J.A.Ferreira, Comparison Of The Four Configurations Of The Inductive Fault Current Limiter,IEEE PESC 2008, Pg 3967-3973,August 2008

Chapter 6. *Structural Design and Analysis Using FEM in High Power Devices*

6.1. Introduction

Finite element modelling (FEM), has become an important tool in electromagnetic design and analysis over the last few decades, with the advent of increased computing capacity. Hence it has been used in the design of electromagnetic devices for both structural and functional study. In this thesis section, the FEM software MagNet™, is used along with measurements, to investigate structural design modifications of the FCL. The investigations were carried out ultimately to optimise the design of the device but also to understand the electromagnetic interactions during the fault cycles. FEM analysis using the static solver (which gives a 'snapshot' solution of the model at a particular time step, usually when the system has stabilised) were carried out on the core. This was to investigate a couple of design modifications in order to evaluate the improvements, if any, that such modifications bring to the FCL design.

6.2. FEM Analysis of Structural Modification to FCL Ferromagnetic Core

The initial design for the FCL that consists of 6 closed electromagnetic cores of M4 steel, 2 per phase, was the de facto design used in this structural analysis. This design, termed the 'spider' design described in the earlier chapters, had the obvious advantage of being a closed magnetic circuit construct. Hence there was minimal flux leakage and all the cores were magnetised by a singular DC bias coil.

Earlier FE-aided analysis uncovered some problems with such a design, for example, the uneven field distributions and hence uneven saturation of the core for its current limiting purposes. The design required even more DC coil current for the

core to be adequately saturated, and the insertion impedance was higher than required for the device in a power network. Non-technical disadvantages like device size, weight and cost made a revision of the design even more necessary.

FE analysis using MagNet ™ permitted such structural studies of various possible modifications using the fundamental flux couplings of the DC and AC coils in order to better understand the electromagnetics of the device and investigate possible improvements which could eliminate some of the disadvantages listed above.

Another important point in modelling of the FCL was to acquire a full quantitative description of the flux densities in all directions at normal operating conditions (saturated core) and in fault mode (non-saturation) in the cores of the FCL. Finite Element Modelling (FEM) was used to analyze the magnetic flux density of the core as a function of field under different conditions at different positions of the core. A major target was to obtain an accurate understanding of the flux interactions in the core of the device in order to better predict device behaviour under whatever operational conditions arise, using a consistent model.

6.3. FEM Analysis on Magnetised Core Limb Size

The first structural design modification investigated was the core limb size modifications. Given the core investigations in Chapter 4, it was noticed that due to the non-uniform magnetisation of the spider model, the right limb (unmagnetised limb) usually was not magnetised to the required level of magnetic flux density commensurate with the DC bias field produced, and this costs the device in terms of functionality by reducing its current limiting capacity. The technical background to this study points towards the fact that the reluctance of the core circuit can be increased by reducing the limb area hence forcing more of the flux into a smaller limb area, thus causing it to reach saturation faster. The M4 core model was built in

MagNet™ , with dimensions in mm as shown in Fig. 6.1. The dimensions were obtained from the spider model prototype. The aim of the study was to understand what gains in core limb saturation could be made by reducing the areas of this limb. Given the symmetry of the limb a 2D- FE study was used for this quantitative study.

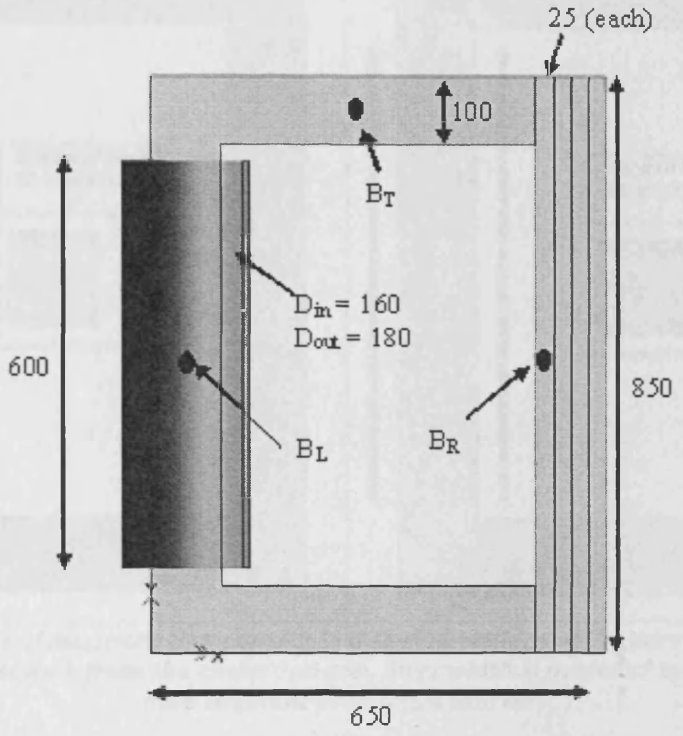

Fig. 6.1:The modelled structures of the FCL with the DC bias coil magnetising one limb only (spider model). All dimensions are given in mm. Three values of B ***were recorded at different positions:*** B_L ***(corresponds to the centre point of the left/magnetised limb),*** B_R ***(right), and*** B_T ***(top).***

The thickness of the core in the z-direction in Fig. 6.1 was 100 mm. The points where ***B*** was calculated: $\boldsymbol{B_L}$ corresponds to the centre point of the left limb, $\boldsymbol{B_R}$ the right limb, and $\boldsymbol{B_T}$ the top limb (values for top and bottom were identical due to central positioning of magnetising coil). The magnetising coil was set to 20 mm (inner diameter is 160 mm and out diameter is 180mm). The coil had 171 turns. The current was increased from 10 A to 100 A, in order to investigate the effect of the field distribution on sections of the core with different widths. The "width" of the unmagnetised right limb was changed from the original 100 mm, to 75 mm, 50 mm and 25 mm, which correspond to 100 %, 75 %, 50 % and 25 % width, respectively.

The nonlinear ***B-H*** anhysteretic characteristics obtained for the M4 material from Chapter 3 were used to represent the M4 material.

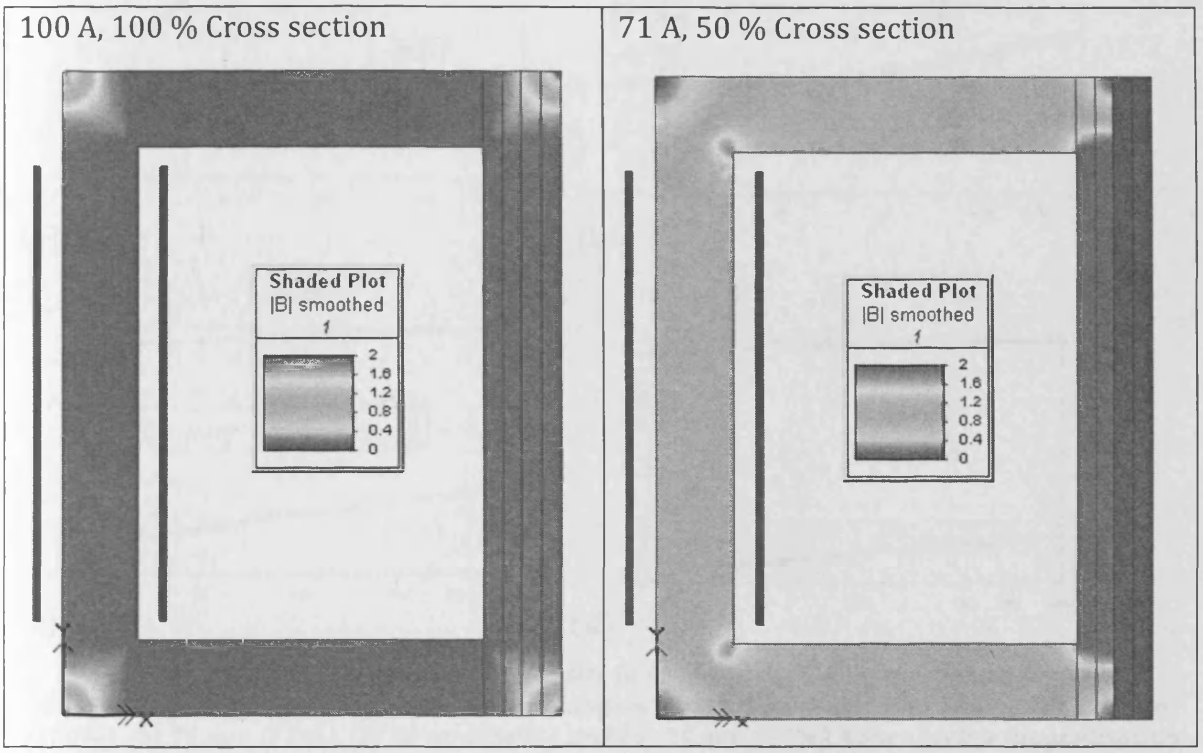

Fig. 6.2: 2D FEA plots of magnetic flux density in different regions of the core for different widths of core in the furthest limb from the excitation coil. 50% width is achieved by converting last two limb segment properties into air.

The typical screen-shots of the flux density distribution at 100 A, and 71A excitation are shown in Fig. 6.2. This suggests the same saturation magnetisation on the right or unmagnetised limb as on the magnetised limb can be obtained using less DC magnetising current, if the size of the limb is reduced by 50%. Furthermore, the flux density values as a function of magnetising current are shown in Fig. 6.3. The results look physically realistic for all the calculated cases.

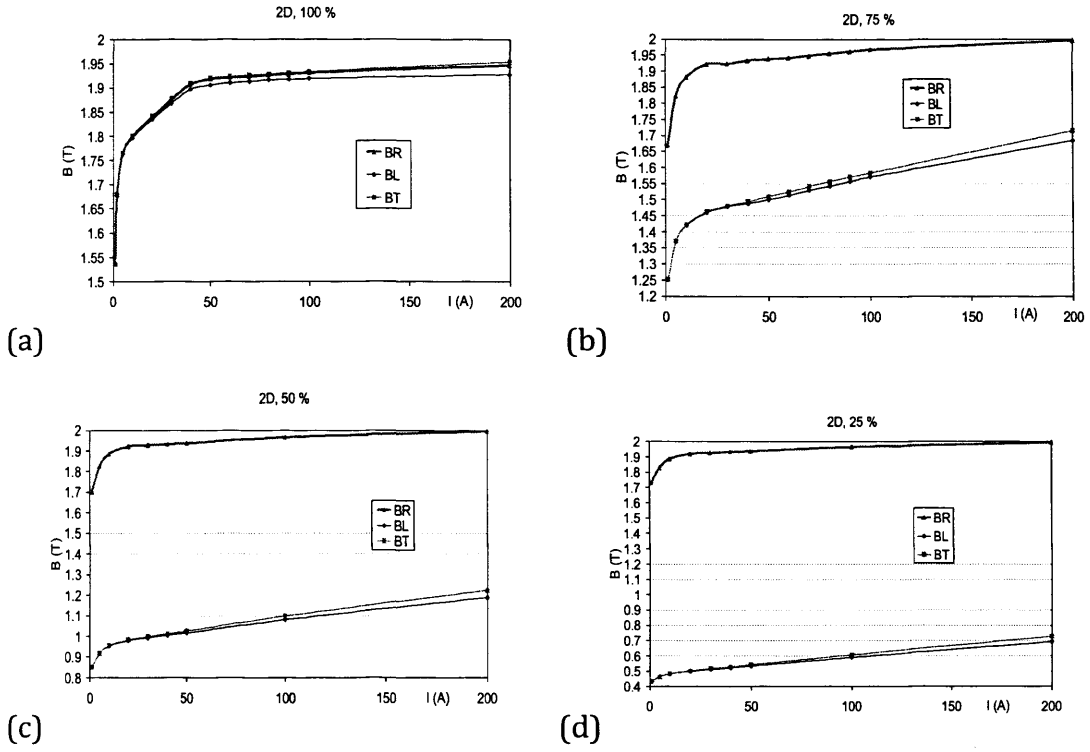

Fig. 6.3: 2D FEM plots of magnetic flux density in different regions of the core as function of magnetising current for the width of the unmagnetised right limb (AC limb) being (a) 100 mm (100%), (b) 75 mm (75%), (c) 50 mm (50%) and (d) 25 mm (25%).Notice higher magnetisation in right limb with reduction in limb size percentage.

Figs. 6.3 shows that by consistently decreasing the limb cross-sectional area, the magnetisation increases and it follows that for a smaller magnetising current, the same level of saturation magnetisation can be obtained on the unmagnetised limb as is on the magnetised limb. Alternatively, by reducing both the magnetising current and the limb size, only the unmagnetised limb could be made to attain saturation. This is very important for the functioning of the FCL for two reasons:

a) All the three other limbs are unsaturated and hence provide a better low reluctance path for the flux, hence channelling most of the flux produced by the DC bias coil to the unmagnetised limb with little flux leakage.

b) The unmagnetised limb which is the limb where the current limiting function actually takes place is saturated hence producing little insertion inductance, making the FCL transparent to the network

under normal operating conditions which is desirable for such a device.

This is consistent with the theory, and suggests a possible modification to the spider model which was to change the size ratio of the limbs from 1:1:1 (left: top: right) to a more asymmetric one (1:1:0.75) such that the benefits listed above could be realised.

6.4. *Investigative Measurements Of Air Gap Introduction In Spider Core Design*

Modelling of various air gaps in the core facilitated an insight into how their presence affected the functionality of the FCL by means of affecting the saturation levels and consequently the inductance introduced into the circuit during fault limiting. From first principles, introduction of an air gap will increase the reluctance of the circuit and hence increase the magnetising force needed to saturate the core. The FCL functions on the idea that the magnetomotive force produced by the fault current opposes that produced by the DC bias current, and the resultant mmf determines the saturation state of the core and hence its inductance. This inductance then limits the fault current in the circuit. So the idea of increasing the bias magnetising force by using an air gap arises, as this will mean a larger fault current can be limited since the operating point can be pushed further into saturation. Fig. 6.4 shows a single closed core showing the setup for the air gap investigations. The thick arrows show how the flux density distribution was measured. Search coils were used on different parts of the core for the ***B***-field measurements.

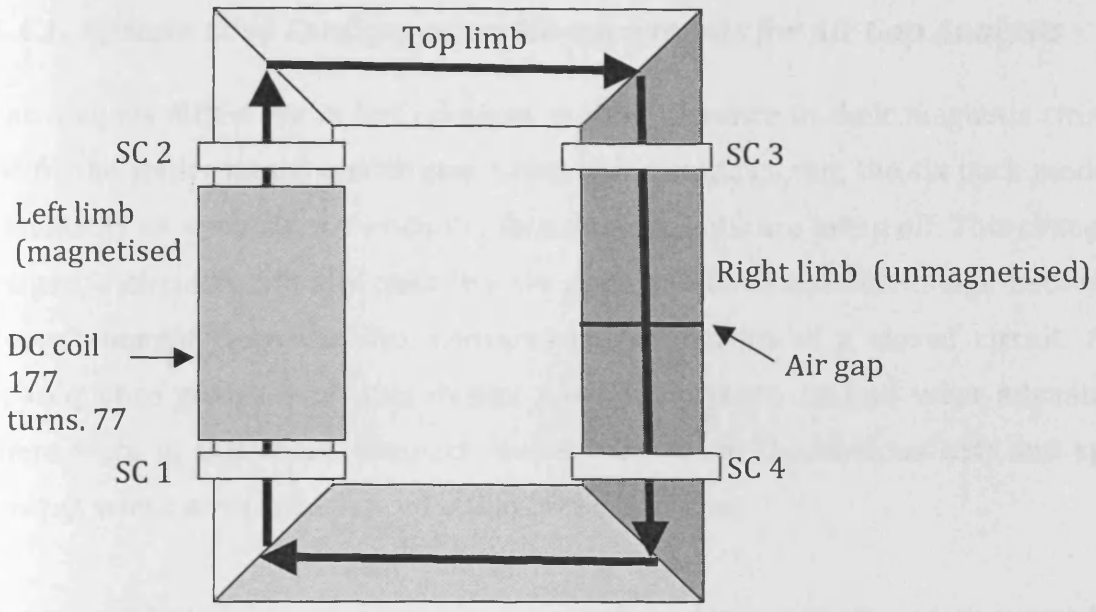

Fig. 6.4: Ferromagnetic core from spider model, as used in the air gap investigations

Another reason behind the air gap study was to examine the merits of a newer design of the FCL, known as the 'six pack model' as opposed to the 'spider model' that introduced in Chapter 5. In this new design the core is open with the top and/or bottom flux closure limbs taken off. This configuration saves on material, and improves on the compactness of the system. Furthermore, the limbs are both magnetised by an external DC coil that encloses both limbs. In addition, the right and left limb both have AC coils attached to them such that they limit the opposite cycles of the fault. Hence in this new design, three 'open' cores are used to limit the current instead of the six 'closed' cores which were required for the spider model.

The investigations are therefore performed to assess whether the overall performance of the FCL suffers significant loss in efficiency by introducing the new ferromagnetic core structure.

6.4.1. Epstein Core Configuration Measurements for Air Gap Analysis

The obvious difference in both designs is the difference in their magnetic circuits. While the spider model constitutes a closed magnetic circuit, the six pack model is essentially an open circuit when the flux closure limbs are taken off. This change in magnetic circuitry initially puts the six pack model at a disadvantage because it doesn't benefit from the flux conservation properties of a closed circuit. As a consequence analyses on this design were undertaken to find what advantages there were in this more compact model apart from the obvious cost and space savings which are due to the reduction in the core size.

Air gap analysis measurements were carried out using a representative core built from Esptein frame strips representing a closed ferromagnetic core. The air gap was introduced in the setup by cutting through the middle of the strips that constitute the right limb (or unmagnetised limb) before putting them back together with adhesive tape. The spacing between both halves of this limb (which constituted the air gap) was then varied by moving the pieces apart to the required separation. The magnetisation measurements were then performed on the core after running a demagnetisation routine. For simplicity of measurement, only the first quadrant of measurements was taken with increasing magnetic field. The air gap was varied between 0, 3, and 6 mm (0mm is the situation where both halves of the right or limiting limb -which was cut to introduce the air gap- are pressed into contact with no assumed space between them).

Fig. 6.5 shows that just by cutting a core limb in two parts and bringing them back together (even if the limb halves are polished and contact is re-established between them), there will be a non-negligible drop in flux densities across the core, but most notably on the limb with the where the cut was made on the electrical steel. By comparing the values acquired from SC 3 located on the unmagnetised limb, it is

evident that a reduction in the B_s parameter results as a consequence of introducing an air gap in the unmagnetised limb.

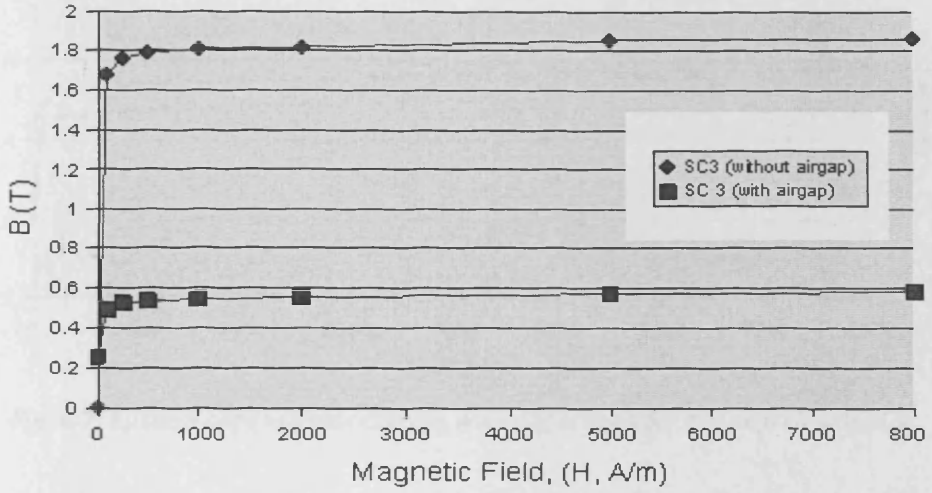

Fig. 6.5:Epstein core comparison with and without air gap for the search coil SC 3.

Fig. 6.6 shows measurements at the various search coils around the coil with 0 mm .

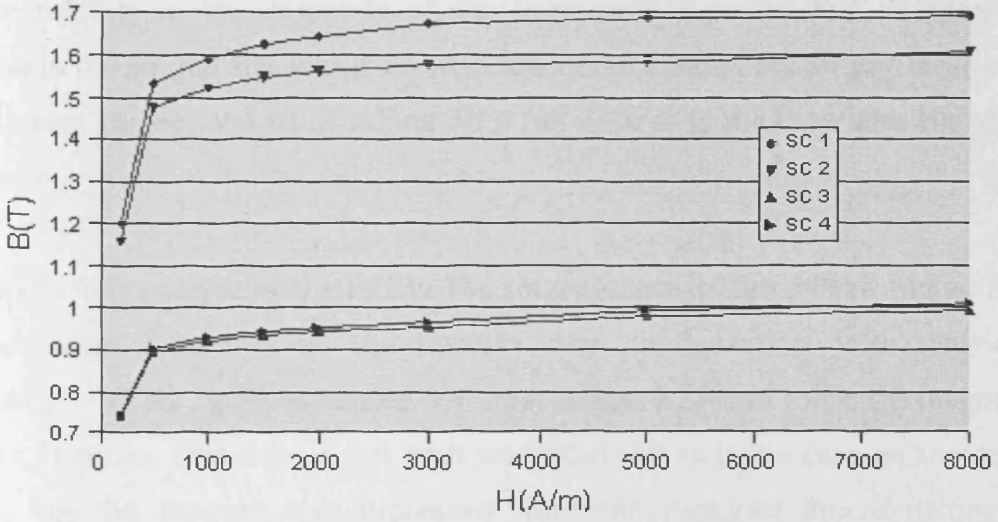

Fig. 6.6: Epstein core measurements for 0 mm.

Finally, the air gap was varied by increasing the spacing between the halves of the unmagnetised limb. Measurements were taken at the SC 3 and a comparison is made between them. This comparison reveals that as expected, the larger the air gap the higher the drop in B_s as shown in Fig. 6.7.

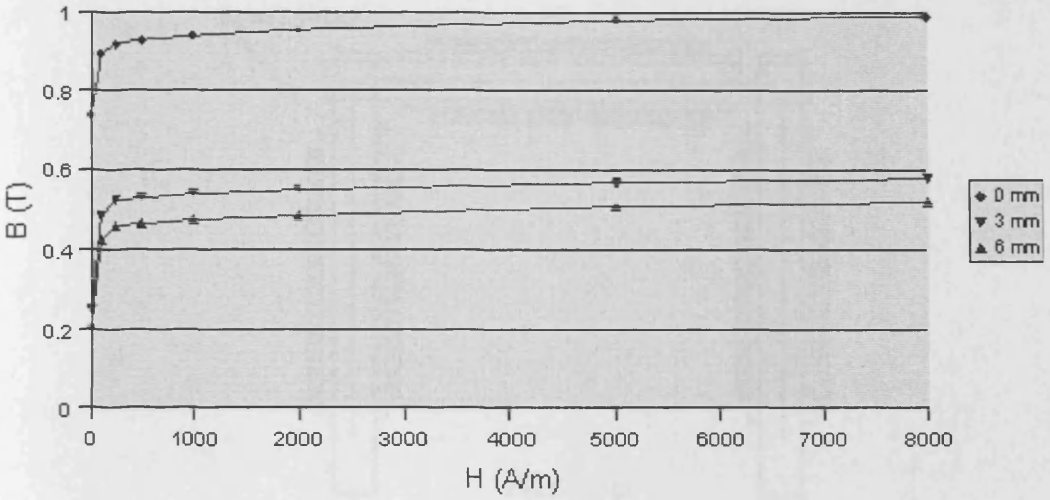

Fig. 6.7: Epstein core measurements with different s for the search coil SC3.

The initial Epstein core test above for investigating the airgap helped in understanding what the effect on the fault clipping would be. By using the single core six pack design (instead of the original spider design), and what its magnitude will be relative to the demands of the performance of the FCL. A progressive increase in the air gap size was used with the aim of making the air gap large enough to represent the equivalent of taking off a full limb as is the case with the six pack design.

In order to fully analyse how effective the six pack core design will be, higher field ***B-H*** loops were measured on the Epstein strip configuration, with magnetising Frequency = 50 Hz , grain-oriented M4 steel strips, 0.27 mm thick, DC magnetising coil of 171 turns. This time, a full limb was taken off as is the case on the six pack model. The DC current was increased until the required flux densities were achieved, and a full ***B-H*** loop was obtained. Measurements where carried out up to 1.5T (due to the limitation of the magnetising coil rating). Fig. 6.8. and Fig. 6.9 show the setup and a comparison of the ***B-H*** loops of the two configurations, magnetised to 1.5T (full core as represented by the normal Epstein configuration and semi-capped core -one limb taken off- as represented by the Epstein configuration with one limb missing).

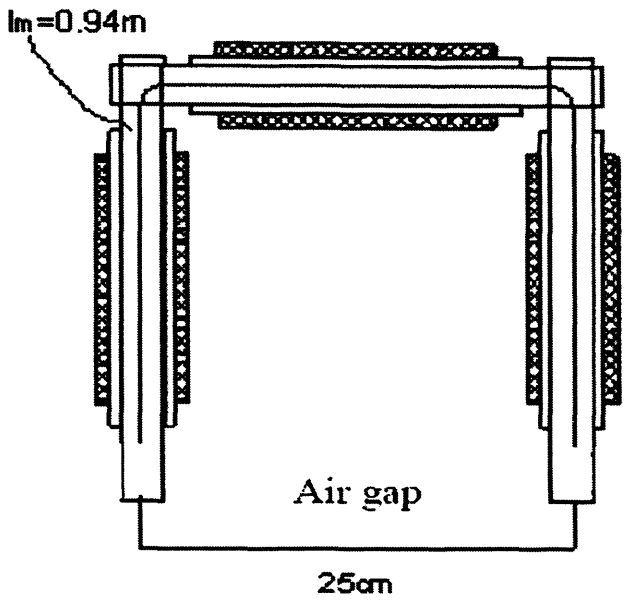

Fig. 6.8: Epstein frame -one limb missing configuration used in the experiment, where l_m denotes magnetic path length.

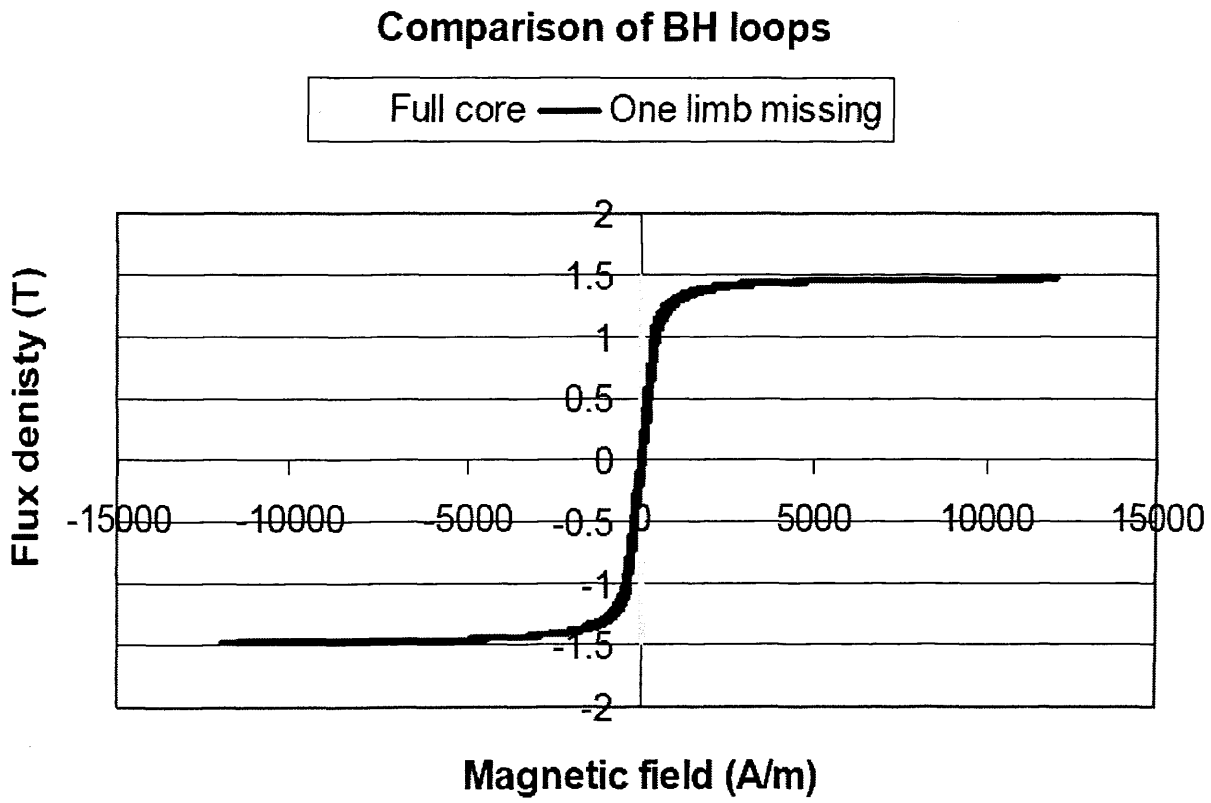

Fig. 6.9: Comparison of BH loops for full core and semi-capped (one limb missing) configurations magnetised at 1.5 T, 50 Hz.

Fig. 6.9 does answer some of the concerns about using an open magnetic circuit core in the FCL, because it points to the fact that although there is a reduction in the amount of differential permeability which can be obtained from the core (a reduction in the slope of the ***B-H*** curve), there still is adequate change in permeability to result in significant fault clipping in the FCL.

The full core does have a steeper slope of the magnetisation curve and hence greater differential permeability than the semi-capped configuration. The subsequent loss in clipping potential is countered by the gains in cost and space saving, and insertion impedance (the reduced impedance visible to the network from the device when there is no fault, during normal operating conditions) of the FCL. Furthermore, Fig. 6.9 shows a reduction in the B_s parameter for the semi-capped compared to the full core configuration. Investigations from Chapter 5 point out that this change does not significantly affect the clipping capacity of the device.

6.5. FEM investigations for the Six pack FCL Design.

6.5.1. Introduction

Having initially examined experimentally the measured effects of an air gap on the ferromagnetic core of the FCL using a constructed Epstein strip representation, more research on the functional impact of the air gap and the flux interaction carried out on the six pack model using finite element methods. An examination on where on the core to introduce the air gap in order to retain or improve efficiency was performed. The measurements taken above on the Epstein strip involved progressively introducing larger air gaps up to the point of completely taking off a limb of the core (this configuration was termed the semi-capped configuration of the core). Using FEM, this direction of researched could be further pursued with faster

results, and the added benefit of possessing a more complete picture of the DC and AC flux interactions. Thus FEM was used in continuing the air gap study.

The six pack design contains three two-limb "open circuit" cores with each limb wrapped with AC windings. These opposing limbs of the core, are both enclosed in the DC magnetising coil as shown in Fig. 6.10, and are responsible for limiting the opposing cycles of the fault current. Instead of a closed top and bottom limbs, the core magnetic circuits in this design can be completed by inserting end caps of the same material in the place of the top and bottom limbs as seen in Fig. 6.10. These end caps were used to investigate the effects of the airgap in this design by either their presence or absence.

One of the concerns with designs that incorporate open circuit cores is the additional energy needed to bias them into saturation, compared with closed circuit core models. Hence inserting both caps completes the magnetic circuit. These end caps were considered as low reluctance bridges between the two functional limbs of the core.

The capped configuration ensures that magnetic flux produced by the AC winding from one limb flows into the other limiting limb and either reinforces or opposes the magnetic flux in this limb produced by its own AC winding. In either case, the presence of the end cap reduces the magnetic reluctance of the whole magnetic circuit. With this established, another question arose over what material should be used for the end caps. An examination of this question from the perspective of materials with different values of permeability and saturation magnetization was then carried out.

6.5.2. FEM Six Pack End Cap Investigation

The 3D-Finite element modelling package MagNet was used to model FCL core constructions based on the six-pack model. Using a DC coil with a magnetisation output of 29 kAmp.turns, the AC coils on both limbs were modelled with 20 turns and an incoming current of 250 A. In the subsequent calculations (Figs. 6.11 - 6.15) the only difference was the material used in the end caps.

Successive materials were put into the end caps and their effects on the field values were recorded and compared with each other. Three different configurations were tried and compared with each other to see what their effects will be including: no cap (air gap between limbs), capped (both caps of different materials) and semi-capped (one cap of different materials and the other of air).

6.5.2.1. No Cap Configuration Analysis

In this configuration, the AC coils are wired in opposite sense so that the fields produced by incoming fault currents are produced in opposite directions at any instant in time. The value of the AC currents for this first configuration, were chosen such that there is a cancellation of the field in the limiting limb (Fig.6.10). This was so that the field generated by the AC current neutralises the DC magnetising field when we have the two core limbs separated by air gaps at the top and bottom, instead of end caps. This configuration with air gaps provided a reference from which to compare the effects of different cap materials (hence different material permeabilities) on the performance of the FCL. The magnetic field ***H*** and magnetic flux density ***B*** readings quoted were taken at the middle of the right limb. This limb is also called the limiting limb, because the comparisons of flux interaction will be taken at this limb.

It was observed that the flux density in the limiting limb was reduced well below saturation because the magnetic fields of the AC coil and the DC bias coil opposed each other. Due to this opposition, the field at the centre of the AC coil was reduced

to H = 0.5 A/m (almost no net field), while in non-limiting limb for this particular half cycle where the fields reinforce each other, the magnetic field strength was 26 A/m.

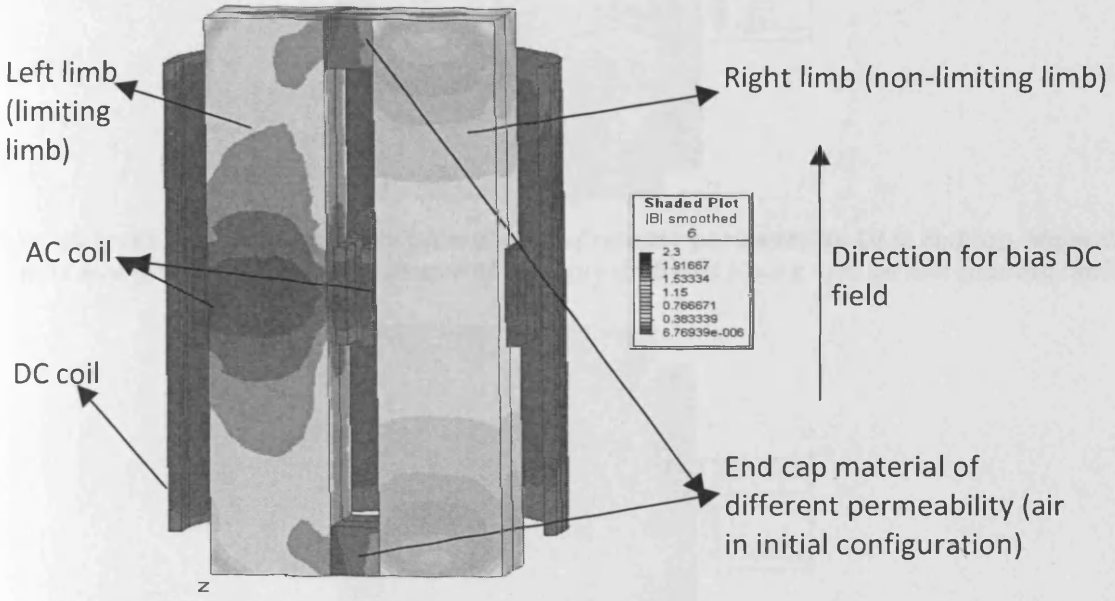

Fig. 6.10:Part of FCL of the six-pack design, with air (relative permeability = 1) in place of end cap. This shows one unsaturated limiting limb and one nearly saturated limb. The net magnetic field strength is 0.5 A/m in limiting limb and 26 A/m in non-limiting limb.

6.5.2.2. Semi-capped Configuration Analysis

In this configuration, one of the caps was removed hence introducing an air gap on one side with a cap on the other side of the configuration. The properties of the end cap material were then changed and in particular the permeabilities were increased, and the effects on the fields were recorded.

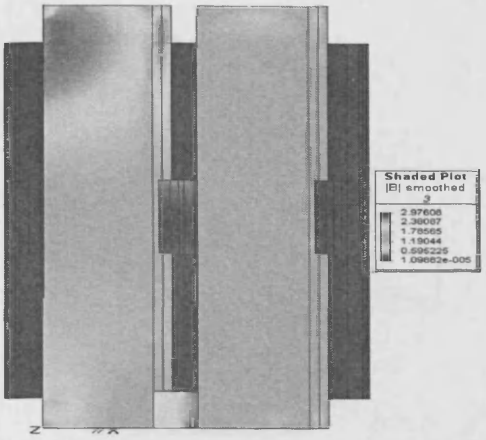

Fig. 6.11: FCL semi-capped core with material of relative permeability 10 in end cap. Magnetic field strength. H = 16.4 A/m at centre of limiting limb and H = 62 A/m on non-limiting limb.

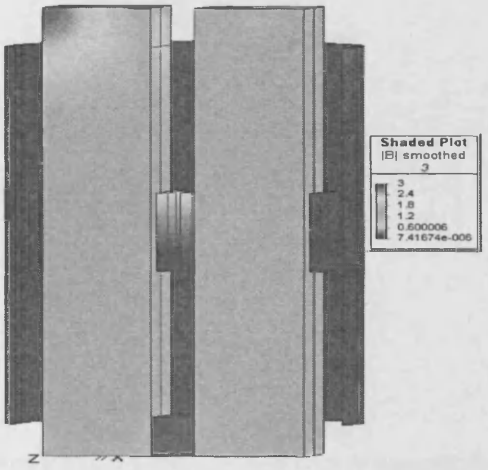

Fig. 6.12: FCL semi-capped core with material of relative permeability 1000 in end cap. Magnetic field strength H = 45.1 A/m at centre of limiting limb and H = 107.6 A/m non-limiting limb.

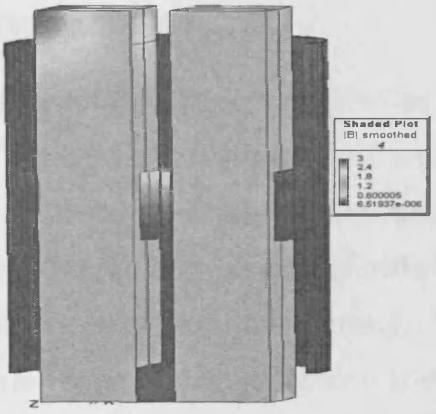

Fig. 6.13: FCL semi-capped core with material of relative permeability 10000 in end cap. Magnetic field strength H = 46.3 A/m at centre of limiting limb and H = 109.2 A/m non-limiting limb.

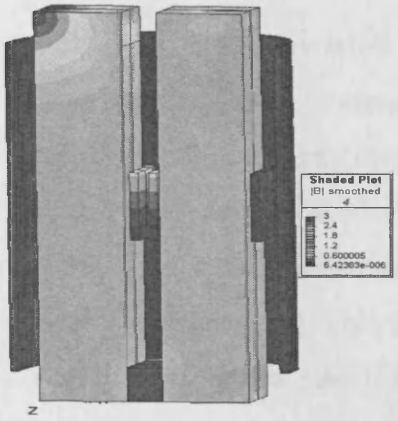

Fig. 6.14: FCL semi-capped core with material of relative permeability 100000 in end cap. Magnetic field strength H = 46.4 A/m at centre of limiting limb and H = 110.4 A/m non-limiting limb.

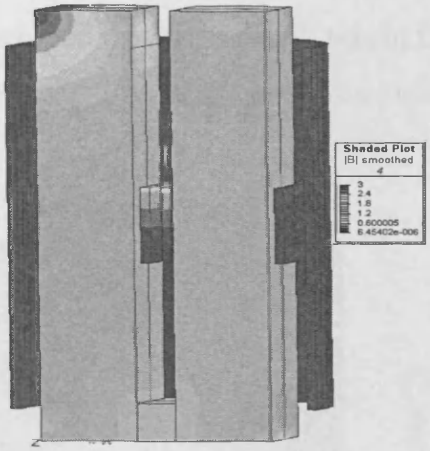

Fig. 6.15: FCL semi-capped core with M4 steel in end cap. Magnetic field strength H = 45.6 A/m at centre of limiting limb and H = 108.4 A/m non-limiting limb.

6.5.2.3. Capped Configuration Analysis

After establishing the baseline configuration using the 'no cap' configuration, the full capped configuration was analysed. It comprised of a closed core setup but with each of the right and left limbs performing limiting functions for the positive and negative cycles of the AC current. This is essentially different from the spider model as one core and not two, are used for the limiting of one phase current, and secondly, the DC coil is located around the whole core and not only on one limb. This improves the uniformity in bias magnetisation and reduces the DC current needed to properly bias the core into saturation.

For the capped configuration, the first material tried for the end caps was M4 electrical steel which was the same material used in constructing the limbs. With the same values for AC and DC currents, the flux density distribution shown in Fig. 6.16 was obtained. It is seen that for the same values of electrical current there is more flux circulating in the design of Fig. 6.16 than in the 'no cap' and the 'semi-capped' configurations using the same material (Fig. 6.15). This is due to the permeability of the M4 end caps. Thus the right limb, which has the AC flux contributed-field reinforcing or boosting its DC field, is driven further into saturation due to the addition of the circulating magnetic fluxes from the left limb, during this half cycle. Figs. 6.16 – 6.19 show the capped configurations, except that the permeability of the end caps has been increased from one to the other, as indicated.

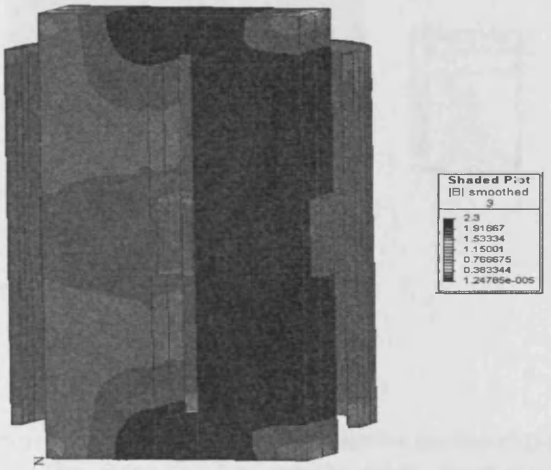

Fig. 6.16: FCL capped configuration with M4 electrical steel in end cap. This shows the effect of flux flowing from one limb on the other. The net magnetic field strength H = -883 A/m in limiting limb and H = 18440 A/m non-limiting limb.

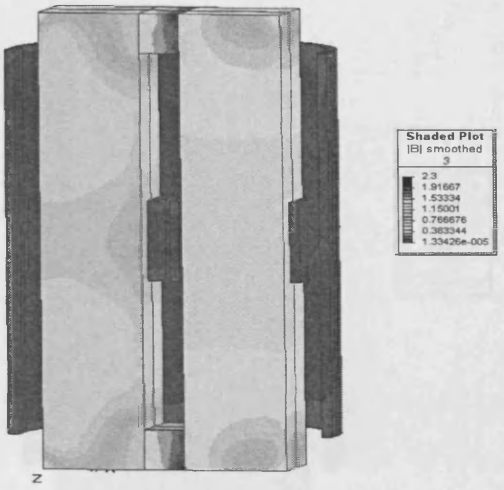

Fig. 6.17: FCL capped configuration with material of permeability 10 in end cap. This shows the effect of overflowing flux from one limb on the other. The net magnetic field strength H = 7 A/m in limiting limb and H= 26 A/m non-limiting limb.

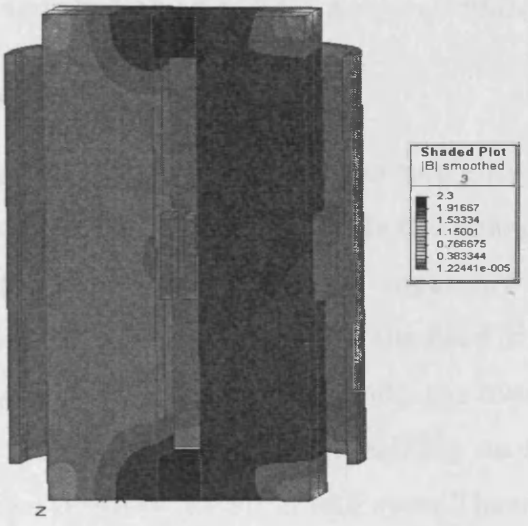

Fig. 6.18:. FCL capped configuration with material of relative permeability 10,000 in end caps. This shows effect of overflowing flux from one limb on the other. Magnetic field strength H = -634 A/m in limiting limb and H = 23700 A/m non-limiting limb.

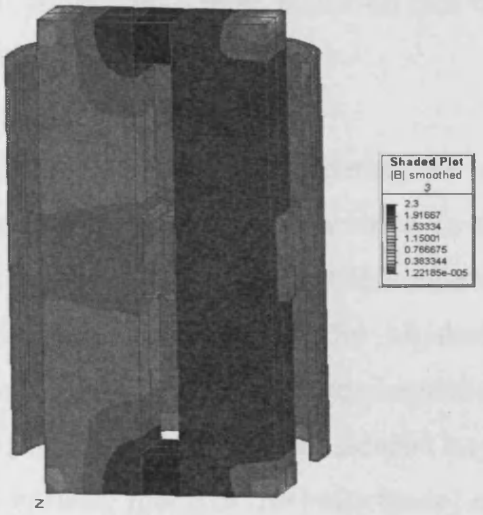

Fig. 6.19: FCL capped configuration with material of relative permeability 100,000 in end cap. This shows effect of overflowing flux from one limb on the other. Magnetic field strength H = -845 A/m in limiting limb and H = 23,734 A/m non-limiting limb

6.5.2.4. Results, Analysis and Discussion

The materials used in the end caps had different permeability from the material for the limbs (M4). What this effectively does is increase the linkage of flux between the limbs and hence augments their current limiting capability by pushing the non-limiting limb further into saturation (by increasing the field in that limb) in one half of the current wave cycle, while helping to shift the operating point of the ferromagnetic core into the region of high permeability on the limiting limb (by opposing the DC field in that limb) in the other half cycle. These alternate processing of helping one limb further into saturation while helping to remove the other from saturation are here termed the 'boost' and 'buck' processes.

The same process was repeated for the opposite limb during the next half cycle. This exchange of flux can essentially improve the functionality of the FCL by facilitating the boost and buck processes. Materials of high permeability which are more suitable to be used for the reluctance bridging are usually more expensive than the core material. Given the fact that the size of the cap is small, and it brings such an advantage in flux conservation (during normal operating conditions), and flux

reinforcement (during fault conditions), their inclusion into the six pack design has a technically sound basis, with economic merit.

Another way of viewing these results is by comparing the net gain in inductance presented to an incoming fault, due to the difference in the material (material permeability) in the end cap. Due to the fact that this effect is best seen with the capped model instead of the semi-capped model, the calculations are done with the capped model data. This comparison has been accomplished by normalising the calculated reactance (here the capacitance is considered negligible and hence the reactance is assumed to be entirely made of the inductance) obtained for each set of tests per material, over the AC current range 0-20 kA. This fault current range was chosen to represent the expected range of conditions for the FCL working in the MV power grid. This normalisation shows how the change in end cap material can improve the impedance of the FCL as the fault current in the AC coil changes. The highest gain was noticed with the highest permeability material, as shown in Fig. 6.20.

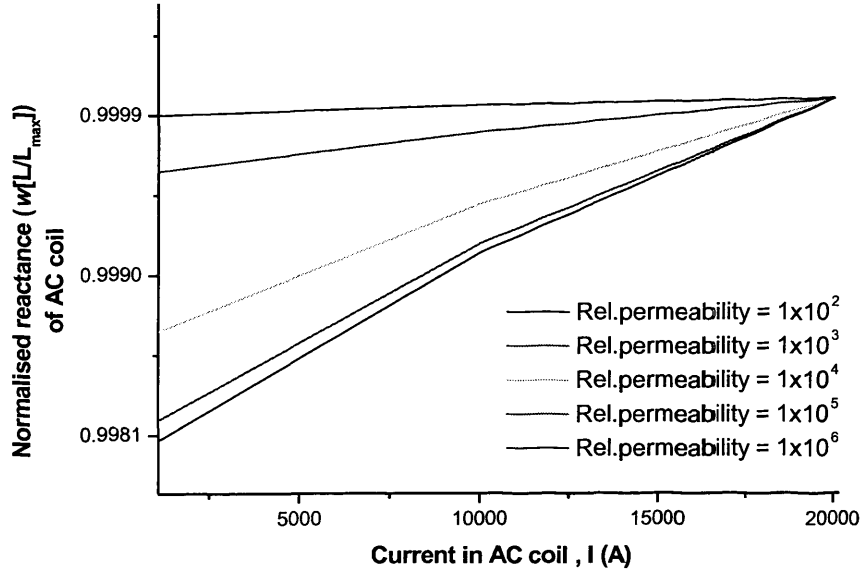

Fig. 6.20: Normalised reactance as a function of AC current for end cap materials with different permeabilities.

Fig. 6.20 shows that as the permeability of the end cap increased, the saturation of the non-limiting limb also increased. This pushes the operating point further into saturation thereby requiring a higher fault current to bring it into a region of high permeability. This thus increases the current rating of the FCL, as higher currents can be handled by the device without increasing the number of DC turns. Hence it can be deduced that using an end cap material of high relative permeability would be a good addition to the six pack FCL design.

Furthermore, it is worth noting that between Fig 6.18 and Fig 6.19 the increase in magnetic induction and saturation is not very large given the tenfold increase in permeability. This suggests a law of diminishing returns on increasing the permeability of the end caps, suggesting an optimum end cap material permeability, beyond which including higher permeability material does not bring a commensurate increase in flux density and consequently any benefit to the current rating of the device.

Supposing that the cost of the end cap material increases with the permeability (supermalloy for example), then a trade off has to be realised in which the chosen end cap material achieves the desired purpose of high magnetic flux density, but lies within an acceptable cost range for a commercially viable FCL.

6.6. *Flux Model Summary of Six Pack Design Improvements*

Considering the analysis that has been carried out for the six pack configurations, a flux model was used to explain how the improvements were achieved using the end cap configurations, and how this understanding can help optimise the design even further for better performance. The inherent disadvantages of the design, some of which were highlighted above, needed to be analysed from a fundamental electromagnetic perspective.

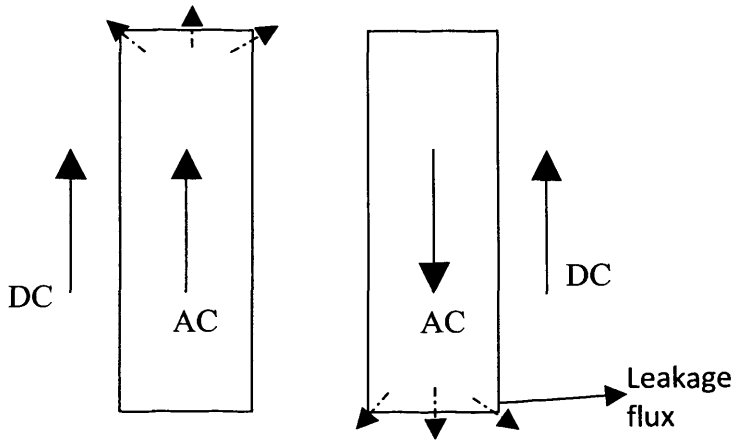

Fig. 6.21: Schematic for six pack (one phase), showing general direction of flux during one half cycle of fault. From the diagram above, the major problem of leakage flux with no path between both cores is easily visualised.

The flux diagram shows that the leakage flux in the non-capped model from the AC windings could be a cause for concern in the basic six pack design. Flux leakage from one phase could interfere with another phase since there is no designated easy path for it to flow through. One major improvement to this was the addition of a cap to the six-pack device between the two cores of any one phase that will greatly reduce most of this leakage flux, channelling it to the other limb instead as a boosting flux, thereby increasing the flux linkage of the coil on that limb. Furthermore, the opposite limb experiences a flux which helps bring it out of saturation - by opposing the DC produced field - into a zone of high permeability herein called the bucking flux, thereby increasing its sensitivity and ability to limit a fault current. The capped and semi-capped analysis above gives reason to suggest that this will result in some advantages (improved current rating of device) over the true open loop system because it allows for field reinforcement in both AC limbs at different times in the fault current cycle. This therefore leads to greater sensitivity for the device and greater dynamic range of switching field.

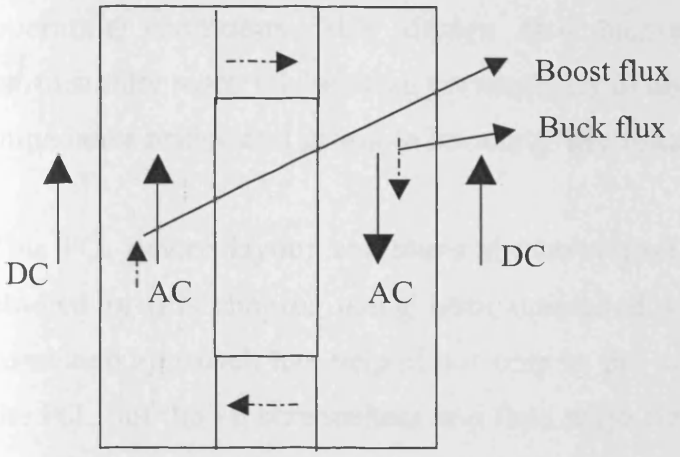

Fig. 6.22: Schematic of six-pack core with cap added, showing flux model of boost and buck flux.

As noticed in Fig. 6.22, this end cap simply functions as a yoke in the magnetic circuits serving the purpose of completing the circuit and thereby eliminating the obvious disadvantages that came with the original six pack design with no end caps.

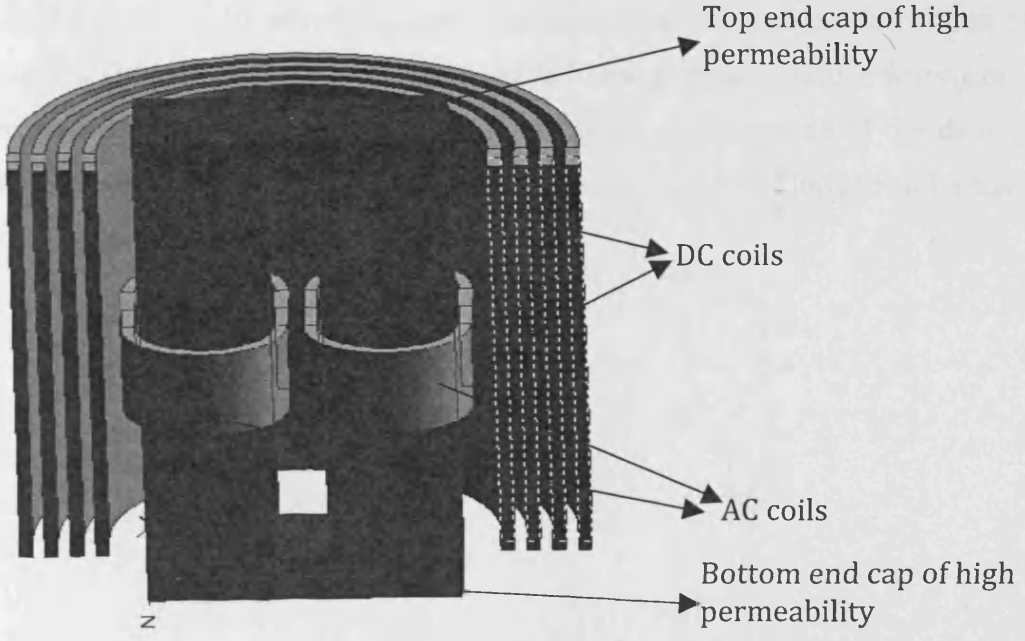

Fig. 6.23: Capped six pack design,with multiple DC coils.

Fig.6.23 shows the possible design improvements discussed to far with the six pack design. These include a multi-layered DC coil for increased DC current, as the design inherently needs more magnetising current to get magnetised under normal

operating conditions. This design also incorporates the end caps made of permeability material (relative permeability of about 10,000) to implement the low impedance bridge and promote boosting flux linkage between the two core limbs.

This FCL device layout combines the structural improvements which have been studied in this chapter using both measured values and FEM calculations. The combined approach has helped not only in the understanding of the functioning of the FCL, but the FE screenshots and field maps helped in the establishing of the flux model explanation for these improvements.

6.7. Summary

This chapter has studied and discussed the use of static FEM solver and prototype core measurements in assessing and implementing various modifications to the structure of the two FCL designs. The merits of each design feature were examined and explanations given for why they improved the performance of the device. The modified design for the six pack FCL with end caps has been judged to be the most improved of all the configurations studied.

Chapter 7. FCL Performance Analysis Using Inductance Calculations and FEM transient Methods

7.1. Introduction

In the electromagnetic design of the FCL, the performance of the device and its possible designs can be quantitatively compared by determining the inductance generated by the device during normal operations and during its fault limiting operation. Given the non-linearity of its core and other components, using the usual definitions for the calculation of inductance will be fraught with errors as they generally do not take into account aspects of nonlinearity, saturation and leakage flux [1] which are all involved in the electromagnetic design and analysis of the FCL.

This Chapter analyses the calculation for inductances used in all of the electromagnetic models that have been built for the FCL along with the calculations performed in FEM software, in order to provide a consistent basis of comparison and device evaluation. FEM transient simulation is also used in the Chapter to evaluate the current clipping capacity of the various FCL designs. The Chapter finishes with a comparative study between FEM software in their inductance calculations, along with some important aspects such as time step considerations and incremental inductance step size that need to be considered when simulating transient models using FEM software like MagNet™.

7.2. Some Considerations for Inductance Calculations In Nonlinear FCL core

7.2.1. Types of Inductance Measurements

The inductance of a coil or a system is usually calculated using one of three different methods including [2]:

a) the flux linkage per ampere in a coil

$$L = \frac{N\phi}{I} \qquad (7.1)$$

where Φ is the flux generated by the coil, I is the current in the coil, and N is the number of turns in the coil. In a non-linear system (with nonlinear magnetisation characteristic representing the core), it is analogous to the slope of the line from the 'point of origin' to the 'point of operation' on the curve. The point of operation is described as the point of interest at which the inductance needs to be calculated. It is sometimes referred to as the secant or absolute inductance, and usually assumes complete flux linkage from the coil current. In hysteretic systems the use of this expression is less useful than the differential, $Nd\Phi/dI$ for determining the inductive response

b) the back electromotive force induced in a coil

$$\varepsilon = -L\frac{dI}{dt} \qquad (7.2)$$

where I is the current flowing in the coil, and ε is the emf in the coil. This definition is analogous to the inductance at a point of operation, usually referred to as the differential inductance. It is calculated by using a small increment in either direction of the point of operation. This definition of inductance is comparable (and proportional) to the differential permeability.

And finally,

c) the magnetic energy stored in a magnetic field produced by current I

$$W = \int \varepsilon dt = \int LdI = \frac{1}{2}LI^2 \qquad (7.3)$$

This is analogous to the area between the nonlinear ***B-H*** characteristic and the vertical axis.

These definitions yield the same results in linear systems, but vary in nonlinear systems where there are aspects like saturation, flux leakage, and (in the FCL) varying currents and fluxes that affect the formulas and hence their accuracy in predicting the appropriate inductance of a system [3].

7.2.2. Inductance Calculations for FCL Models with Location and Magnetic Field Considerations

In the mathematically based FCL model –the voltage driven model (VDM)-developed in Mathematica™ during the earlier stages of this work (see Chapter 5), an absolute inductance scheme was adopted and modified accordingly. This was because it was not possible to numerically approximate the leakage fluxes. As a consequence, the flux loss effects on the inductance response had to be taken into account differently in the mathematical model. This was done by considering a non-uniform field distribution around the ferromagnetic core, which took into account the leakage fluxes.

The usual formulation for inductance used in engineering applications is

$$L = \frac{\mu_0 \mu_r N^2 A}{l}, \qquad (7.4)$$

where ***l*** is the length of the solenoid, ***A*** is the cross sectional area of the coil, μ_r is relative permeability, and μ_0 is the permeability in free space. Given the dependence of the relative permeability on the ***H***-field distribution of the core, a more accurate formula for the inductance was needed to include the variation of inductance along the core limb (limiting limb). Such a formulation will include the magnetic field

dependence on location, and also account for the leakage fluxes, and nonlinearity of the core.

Assumptions have been made in deriving the standard equation (Eqn. 7.4), which are not necessarily applicable to the present device. If the inductance ***L*** varies with position ***x*** along the length of the coil then consider an infinitesimally small element *dx* of coil, generating a contribution to the inductance ***dL***. By substituting $\Phi = BA$ and $B = \mu_0\mu_r H$, where ***H*** is the local value of magnetic field, Eqn. 7.4 becomes,

$$dL = \frac{\mu_0 \mu_r HA}{I}\frac{N}{l}\,dx \qquad (7.5)$$

Both field ***H*** and relative permeability μ_r can vary with position ***x*** in the core, and therefore integrating along the entire length of the coil gives,

$$L = \frac{\mu_0 A}{I}\frac{N}{l}\int_{x=-\frac{l}{2}}^{x=\frac{l}{2}} \mu_{r(x)} H_{(x)}\,dx \qquad (7.6)$$

This represents a generic equation for the inductance of a solenoid which magnetises a core with variable field distribution and hence permeability. Eqn. 7.4 can easily be deduced from the above by making the assumption that the permeability of the core is constant, and the magnetic field is uniform, then $H = \frac{NI}{l}$, and Eqn. 7.6 results in Eqn. 7.4. That is :

$$L = \frac{\mu_0 \mu_r A}{I}\frac{N}{l}.\frac{Ni}{l}\int_{x=-\frac{l}{2}}^{x=\frac{l}{2}} dx = \frac{\mu_0 \mu_r A}{l}\frac{N^2}{}$$

Thus if the modified expression for the ***H***-field distribution discussed in Chapter 4 is substituted in the equation, the expression for inductance used in modelling the absolute inductance in the VDM becomes,

$$L = \frac{\mu_0 A}{I}\frac{N}{l}\int_{x=-\frac{l}{2}}^{x=\frac{l}{2}} \mu_{r(x)}\left[\frac{(l+2x)}{2\sqrt{D^2+(l+2x)^2}} + \frac{(l-2x)}{2\sqrt{D^2+(l-2x)^2}}\right]dx \qquad (7.7)$$

An important implication of Eqn. 7.7 is the fact that with an accurate calculation for the field can be undertaken at any point on the ferromagnetic core. It should be noted that the incremental inductance response which can be calculated using the slope of the current-flux curve will the most accurate calculation for the inductance. But for initial model simplicity and given the dependence of the inductance on the varying permeability and time Eqn. 7.7 is essentially used as the inductance calculation, which for the nonlinear mathematically modelled FCL, was the more appropriate method to use.

Furthermore this suggests that if the permeability of the core can be controlled along its length, the inductance and hence impedance can also be controlled which raises the new idea of a multi-layered or composite core, with different permeabilities at different positions along the core. Such a core would allow the insertion impedance of the FCL to be controlled. It would mean more materials engineering of the core, but a study of the relative advantages and disadvantages of such a core, to see if it would be commercially viable, could be a good direction for future research.

7.2.3. Incremental Inductance calculations in transient FEM

As discussed above, inductance calculations have a tendency of varying, depending on the method of calculation of the characteristics of the magnetic material. After

acquiring measurements from industrial partner obtained from a prototype [4], it was of interest to calibrate and verify the FCL modelling in FEM, by comparing the measured values in order to ascertain the validity of the modelling carried out, using the transient analysis solver. This also provided a basis for comparing the functional merits of one model over another.

Due to the nonlinearity of the materials being used and the functioning principles of the FCL, the resultant inductance of the circuit is a function of the applied current (since the applied current directly determines the magnetic fields on the core). Faraday's Law still holds but inductance is different whether one calculates circuit parameters or magnetic fluxes.

From *Faraday*'s law we have, for the case of a single-turn coil with no internal resistance,

$$\varepsilon = -\frac{d\phi}{dt} \qquad (7.8)$$

If the coil is replaced by an **N**-turn closely wound coil, each loop will be linked by the same flux and will thus be the location of an induced *emf* given by Eqn. 7.8. Since all these *emf*'s are in the same direction, they will add up in series so that the total *emf* induced in the coil will be

$$\varepsilon = -N\frac{d\phi}{dt} = \frac{d\Lambda}{dt} \qquad (7.9)$$

where $\Lambda = N\Phi$ is the total flux linking the coil.

Now, assuming that the only time-varying quantity is the coil's current, we have.

$$\Lambda = \Lambda(I(t), B_{DC}(x)) \tag{7.10}$$

where $\boldsymbol{B}_{DC}(x)$ is the non-uniform, position on core dependent, DC bias magnetic field which is present even when the line current $I(t) = 0$. Let this flux be denoted $\boldsymbol{\Lambda_0}$ which is nonzero and constant with time. Substituting Eqn.7.10 into Eqn. 7.9 and using the chain rule leads to

$$\varepsilon = -\frac{d\Lambda}{dI}\frac{dI}{dt} \tag{7.11}$$

If the incremental inductance is assumed to be dependent on the DC field bias field and the AC field produced by the AC current per time step, then

$$L = L(I(t), B_{DC}(x)) = \frac{d\Lambda}{dI} \tag{7.12}$$

Thus Eqn. 7.2 can this be obtained by substituting Eqn. 7.12 into Eqn. 7.11. Thus the most appropriate formula to be used for the inductance calculation follows from Eqn. 7.12 as follow;

The incremental inductance gives the change in flux corresponding to a small change in current (i.e. it is the local slope of the $\Lambda(I)$ curve) around a specific operating point ($I(t)$, $\boldsymbol{B}_{DC}$), as well as the proportionality factor between the voltage and the rate of change of the current. In such a context of small-signal analysis, the incremental inductance can be used in a nonlinear context [5].

The transient solver implements a static solution at two small time steps in either direction of the point of interest in order to obtain fluxes $\boldsymbol{L_1}$ and $\boldsymbol{L_2}$ corresponding to two different excitation currents $\boldsymbol{I_{1(t)}}$ and $\boldsymbol{I_{2(t)}}$. Inserting these values in Eqn. 7.10 gives;

$$\Lambda_1(t_1) = LI_1 + \Lambda_0$$
$$\Lambda_2(t_2) = LI_2 + \Lambda_0 \qquad (7.13)$$

and subtracting these equations finally leads to,

$$L = \frac{\Lambda_2(t_2) - \Lambda_1(t_1)}{I(t_2) - I(t_1)} \qquad (7.14)$$

This equation produces the incremental inductance of the FCL per solver time step, and dependent on the current on the AC line. This formulation of the incremental inductance produces the most accurate value of inductance for this particular electromagnetic device.

7.3. *Transient Inductance Mapping for Circuit Parameter Selection, Using FEM Calculations*

In order that functional comparisons between models can be carried out, a method of comparing the inductances calculated for the configurations without any dependence on the structure of these configurations was examined, and the resultant procedure herein has been called an inductance map.

The inductance map is a 3-dimensional graph of the expected absolute inductances at a defined operation point which is dependent on the interaction between the AC and the DC coil currents. The assumption made here is that in comparing different possible configurations of AC and DC currents, combinations with the optimal inductance gain can be located, and these could be integrated into possible FCL designs. Such a map was made to provide a database of possible inductance values for different changes in AC/DC turns. This could be used as a reference to determine

what combination of AC/DC currents will produce what kind of inductance, for the particular six pack model under study.

The shortcoming of the map however, is the fact that it takes only the current effects at a particular operation point into consideration, and hence cannot be considered as giving the complete picture of what the possible AC/DC current value combinations will produce. It is also very design-specific.

The transient solver was used to introduce the AC sinusoidal current waveform into the six pack model. The range of values used for both coils was from 1 A – 20 kA. In order to focus directly on the current effects on the inductance, one turn coils were used for both coils so that the results will reflect only the current influences. The AC currents were defined at 50 Hz, and the DC current was defined as a constant value per test run.

These test runs were used to produce a 3-dimensional graph (Fig. 7.1) of absolute values of the inductances, which show areas of higher and lower inductance in relation to the current magnitudes on the limiting limb (limb with AC coil).

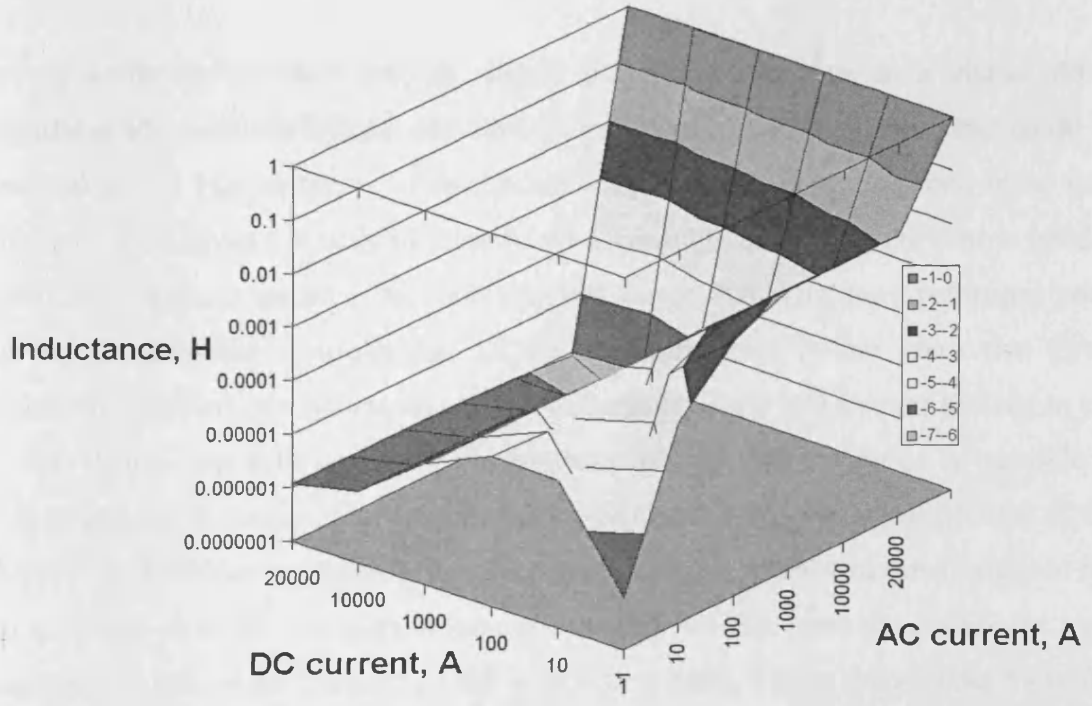

Fig. 7.1: Inductance map from transient solver showing inductance map for 1 coil turn AC and DC.

These graph values provide a visual aid from which combinations of suitable AC/DC excitations for the FCL could be obtained and tried in the model configurations. This inductance map, which essentially is a magnetisation force (*N*x*I*) map (since it is one turn per coil), shows an increase in inductance with a simultaneous increase in both the DC and AC magnetisation forces produced by both coils. This reveals that for higher fault currents (which on the graph is represented by the AC current), a larger DC magnetisation force is needed and that invariably produces a larger net inductance.

Secondly, it is also seen from the graph that a high level of inductance can be obtained with lower values of DC current (around 100A) than that for the AC currents, which are around the 1000A-10000A range. This gives us an indication of a possible optimum matching between the AC and DC coils, and provides a start point from which models can be compared, by building in these numbers into the FCL design.

The use of the inductance map is simply indicative and acts as a visual aid in recognising the possible DC/AC coil and magnetisation combinations that could be beneficial to the FCL in terms of the inductance which can be obtained from such combinations. It gives not only an idea to what amount of DC bias current is needed to limit a particular amount of AC fault current, but it also provides a reference point from which different non-obvious DC/AC combinations (other than the direct proportion relation) can be assessed. The inductance map is however limited in the fact that it does not take as many parameters into consideration as is possible in predicting the inductance, and hence cannot be trusted to give a full picture of the inductances of the device. Furthermore it is core-design specific in the sense that the map is useful only for the particular core model (in this case the initial six pack design specifications of Chapter 5) for which it is built. These drawbacks however

do not obviate its use as a good visual tool to be used in choosing the AC/DC combinations for the FCL.

7.4. *Study of the Effects of DC magnetisation on Insertion Inductance of the FCL*

7.4.1. *Investigating the Optimum Increment for Differential Inductance Calculations*

Due to the non-linearity of the inductance calculations used in the transient solver shown earlier in this Chapter, choosing an appropriate incremental change in current around the point of interest in these calculations becomes very important. In calculating the incremental inductance about a point using Eqn. 7.14, the increment ΔI, has to be such that it is not selected too large to get out of the region with a linear slope about the point of interest. Also, it cannot be too small such as generate numerical round up errors. To achieve this balance in choosing the appropriate ΔI for the transient calculations herein, many measurements at different ΔI values were attempted in order to find an appropriate ΔI for the inductance calculations.

Fig. 7.2 shows the result of changing the current increment values on the inductance calculations.

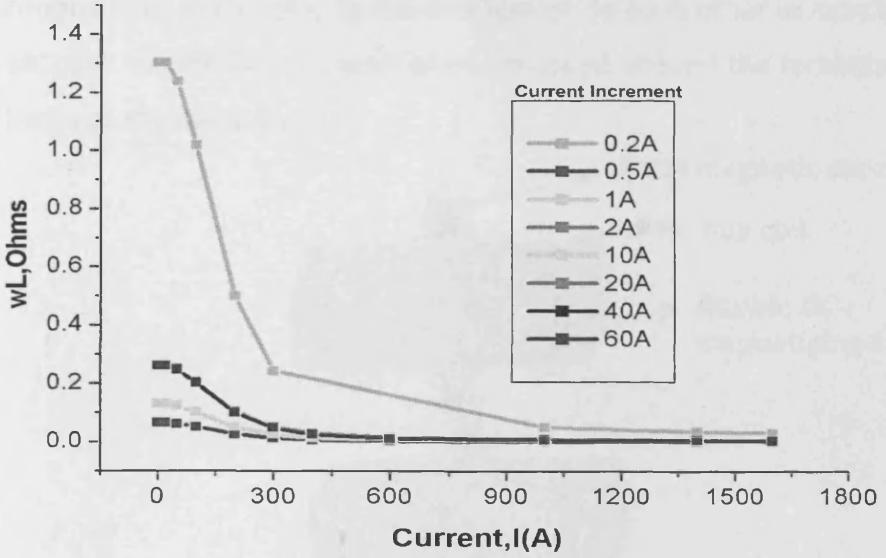

Fig. 7.2: Incremental inductance calculations using different current increments ΔI, against the current value at point of interest. Deviation of inductance value shows inappropriate ΔI in use.

As seen in the graph, different ΔI result in different calculated inductance values for the measurement range up to 1.6 kA , differential increments below 2A and above 60A were found to be inappropriate for these calculations. For example the large deviation of the inductance curve from the rest of the curves noticed when a ΔI of 0.2A I used makes this increment unsuitable for use compared with say 10A. The consistency of the graphs with ΔI between 2A and 60A (as shown by the overlaying of their graphs), makes them possible for making ΔI choices for the calculations. Thus the current increment to be used for this particular study was chosen to be 4A. With this choice, the inductance calculations for the model, and the comparison with the prototype measured values were done.

7.4.2. Comparison between Measured and Calculated Inductance for Modified Six pack Design

The initial prototype under study consists of the six pack model with a modification of having 4 DC coils of 100 turns each magnetising the cores. Furthermore the cores

are placed opposite to each other instead of alongside each other as was the case in the initial six pack model. The AC coils were wrapped around the ferromagnetic M4 steel core limbs as shown in Fig. 7.3

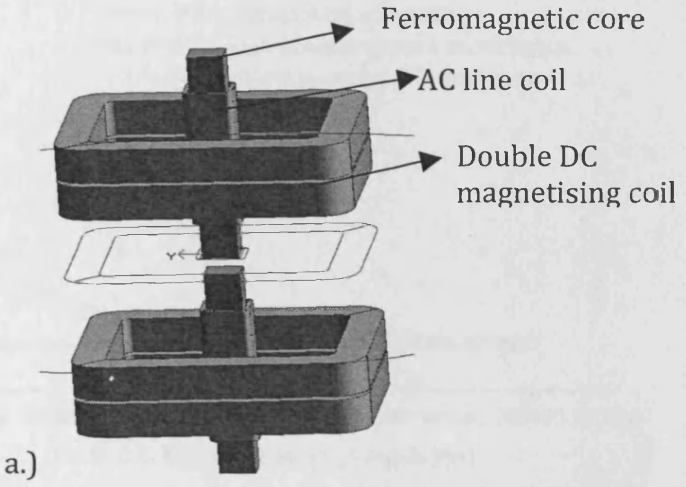

Fig. 7.3: a) Schematic of prototype six pack design modification used in the insertion impedance calculations;

Other circuit parameters included:

- Number of AC turns, N_{ac} = 60,
- Area -core = 0.0064m^2,
- Number of DC turns, N_{dc} = 4x100,
- Height of AC coil, Ht_{ac} = 390mm
- Measured aircore inductance = 92.2 μH

The measurements and calculations were taken independently of each other. The inductance measurement on the FCL prototype were provided by the industrial partner [6]

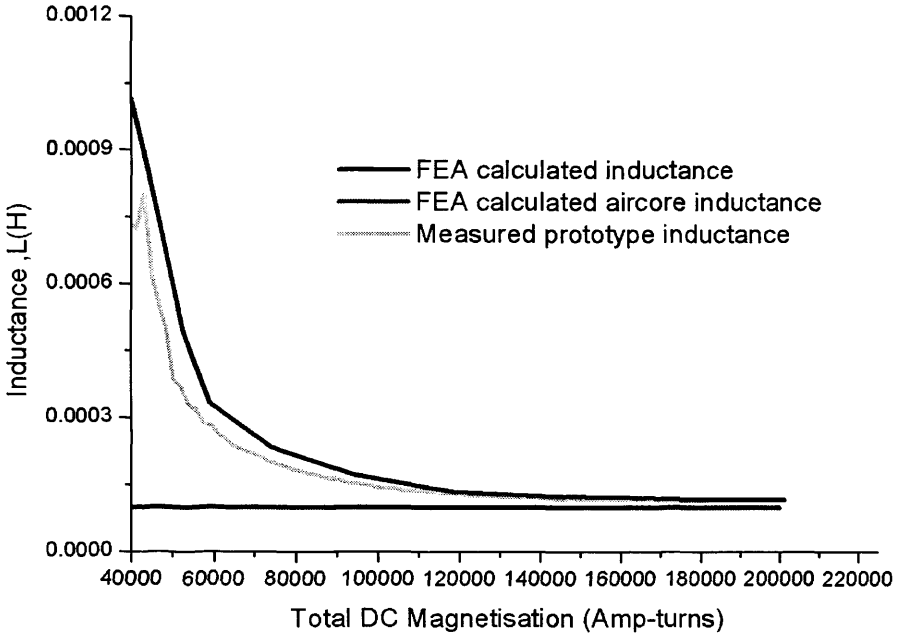

Fig. 7.4: Insertion inductance measured and calculated for FCL design in Fig 7.3 showing agreement.

There is a reasonable agreement of both measurement and calculated values, with the agreement improving with the magnetisation force, as shown in Fig. 7.4. The measurements and calculations are both compared to the aircore inductance that is the inductance of the FCL model when the ferromagnetic core is removed, hence making the model an aircore FCL. The discrepancies between the values can be attributed to some measurement errors and also the intrinsic differences that exist between the real steel core, and its modelled anhysteretic representation in the FE software. Below 40 kAmp-turns, there is significant noise in the measured values and hence these values were not included in the analysis.

Another method used in establishing agreement between the inductance calculated and that measured was to match the measured inductance and the permeability curve being used in the modelling simulations. The reason for using this is that if all other factors are kept constant in the modelled system but for the core material's level of magnetisation, then the inductance (and hence impedance) calculated has to

be comparable with the permeability curve ($L\alpha K.\mu$), where K is $\frac{AN^2}{l}$.This agreement as shown in the Fig. 7.5 confirms the agreement between the modelled and measured FCL models.

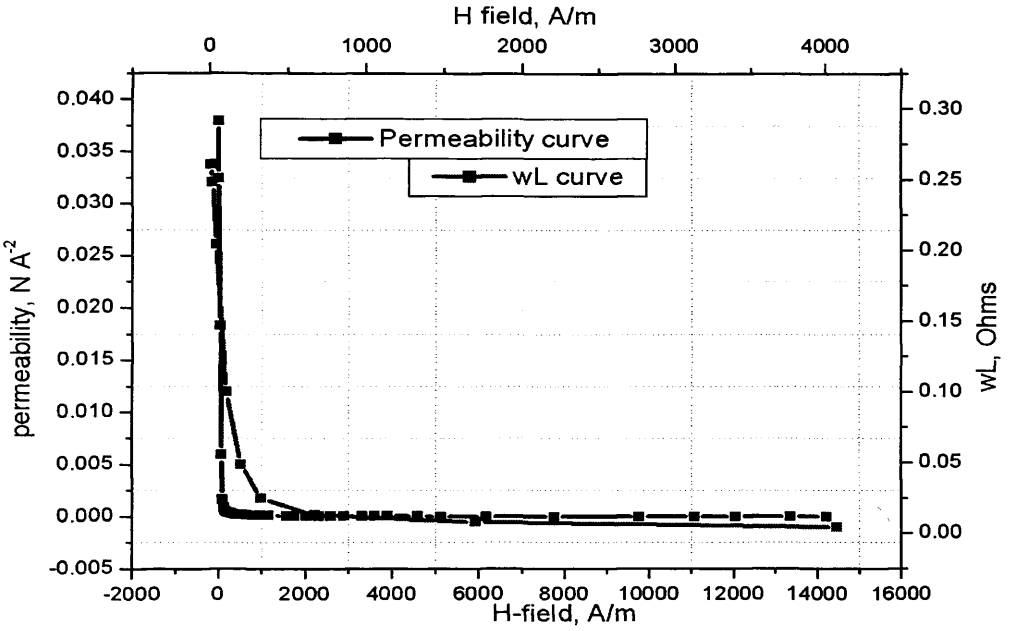

Fig. 7.5: Graph of permeability of core, against measured insertion inductance (reactance) showing good agreement.

With this agreement, the model built in the FEM software can be judged to give an appropriate representation of the FCL design prototypes, and hence more studies could be carried out on the models with a high level of confidence in the results.

7.4.3. Comparison of Six Pack Design Calculated Insertion Inductance between Different FEM software packages

In the course of constructing the FCL model and preparing for its use in external networks, characterizing its insertion inductance is of utmost importance. The insertion inductance is the inductance which the FCL presents to the power network under normal operating conditions. Ideally, the device should be electrically

'transparent' under normal operating conditions so as not to add to the impedance of the circuit.

This study examines the amount of DC magnetisation necessary to achieve such transparency and how the insertion inductance changes with different FE software (MagNet™, ANSYS™ and COMSOL™). These software packages were chosen for comparison because they are the most commonly used packages for design of electromagnetic devices such as the fault current limiter. The study was aimed at finding out not only if the inductance calculations vary from one FEM package to another, but also to make sure the quoted insertion inductance (which is an important parameter for this particular device) could be confidently and independently verified, no matter the software in use.

After adopting the incremental inductance method of measuring the inductance of the coil, the linkage flux at every current level is obtained by integration of the flux over the internal surface of the AC coil (including the surface of the ferromagnetic core). This result is in turn divided by the ΔI introduced in the AC coils while the DC circuit provides the external permanent field, and the inductance is calculated as per Eqn. 7.14.

A comparison of the insertion inductance (calculated at the AC coil) will give confidence in the transient measurements and current clipping capability studies to be carried out subsequently.

Insertion inductance measurements were performed for a single phase double core prototype with two different DC biasing types; symmetric and asymmetric, and compared to the FE calculated values. The symmetric bias includes exciting all 4 DC coils in the same direction while the asymmetric bias entails exciting both pairs of coils with DC currents in opposite directions. Further calculations were carried out

while modifying the design by inserting an end cap (whose other advantages have earlier been discussed) between the two cores, in order to quantify the improvement of the end cap in lowering of the insertion inductance of the device.

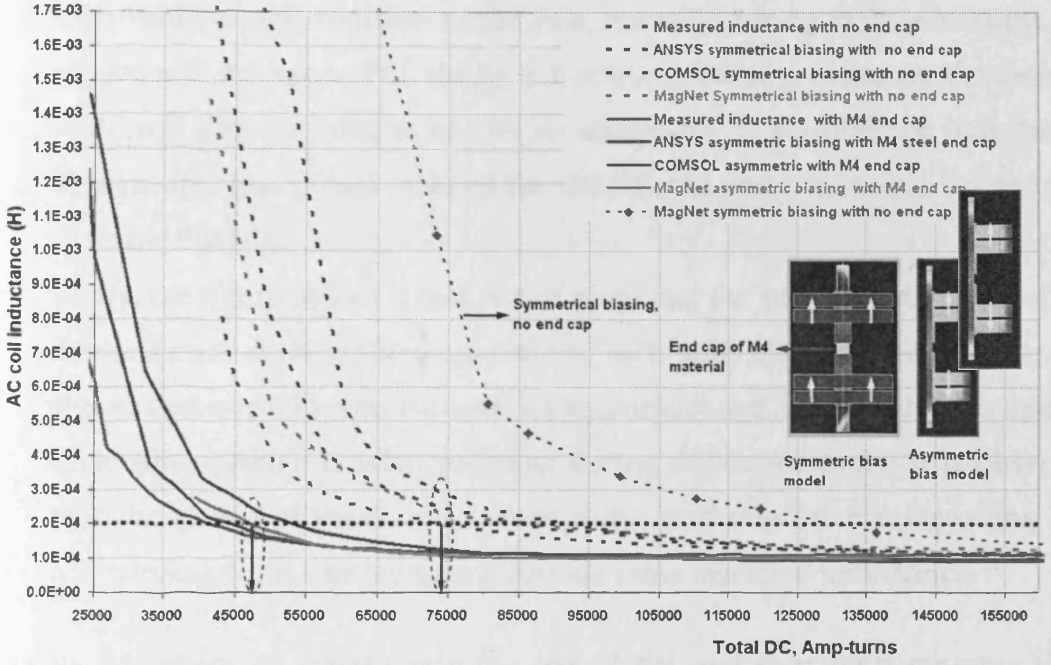

Fig. 7.6: Insertion inductance measurement comparison for different FEA programs for asymmetric and symmetric biasing

Fig.7.6 yielded many results which justify the usefulness of asymmetric biasing and the end caps in the FCL design. These include:

- Firstly, there is relative agreement with different configurations of the model using the three different FEA packages. The differences can be attributed to the model construction differences in all of the packages. They all do however agree that increasing the ampere turns on the DC coil will reduce the insertion impedance of the FCL on the network as seen by the reduced slope in all the simulations with increase in magnetising force.
- Secondly, they point to the fact that when an end cap (of a ferromagnetic material) is added between the FCL cores limbs, it takes less ampere turns of magnetising force to obtain the same insertion inductance (as shown by the

black dotted line). This is seen by the difference in symmetrically biased inductance calculations for the MagNet simulations between the model with and without the end cap. This supports the fact that an end cap is a favourable design addition to the FCL, not only during fault conditions (on capped and uncapped FCL studies), but also in helping to reduce the amount of DC coil turns needed to ensure an acceptably small insertion inductance. This means, less power needed for the DC coil and hence, less operational costs for the FCL.

- Lastly, the figure shows a test run of reversing the bias on both cores of the device, hence making them opposite to each other during operation. Fig. 7.6 shows that once the bias is made asymmetric such that the coil fields oppose each other (which is what happens during fault conditions) it is observed that the group of measured curves shifts to the left hence signalling less magnetising force needed to achieve the same insertion inductance.

The study has given an insight into the use of the end caps by comparing their influence on the insertion inductance values. Furthermore the discrepancies between different packages, though in agreement with one another, pointed towards the idea of using a single FEM software only, throughout the project as a standard to foster consistency in calculations and analysis. It has also revealed the advantage of asymmetric DC biasing over the symmetric model, in this particular FCL design.

7.5. Transient FEM study of the FCL's Fault Clipping Perfomance (Single Phase Six Pack Model)

After establishing the baseline for the insertion inductance and comparing their values between the various FEM software packages in use on the project, a study into the actual performance of the FCL was necessary.

A large amount of the FE work done so far was geared at understanding the functional aspects of the FCL, and how the various parameters could affect the FCL. In addition, some design considerations were looked into and the initial FCL designs were modified with the aim of providing possible improvement ideas to the building of the FCL. Hence an FE transient model for an MV power circuit was built in MagNet™ to analyse how the FCL functioned and evaluate its fault clipping capacity. The transient model circuit tests were designed with the following specifications:

- DC voltage,V_{dc} = 195,kV
- DC circuit resistance = 1000 Ohms.
- Total DC bias = 4 DC coils x 100 turns per coil x195Amps = 78 kAmp-turns
- Frequency = 50 Hz.
- Line voltage, V_{rms} = 660 *sqrt(2) V
- Load resistance, R_{load}=9.6 Ohms.
- AC coil resistance, R_{ac} = 0.021 Ohms
- Source Inductance L_s = 707 μH ;(Xs = 0.222 Ohms)
- Source resistance, R_s = 0.014 Ohms.

The following steps were used in setting up the circuit to simulate the basic MV circuit with the specifications listed above:

- The FCL model built in MagNet was represented by the two AC coils of the FCL over which the inductance introduced by the FCL can be calculated. These coils are used in limiting the positive and negative half cycles for one FCL phase in the MV circuit. The circuit consists simply of a voltage source and a purely inductive load. A switch is used to introduce a short circuit before the load branch, hence introducing a fault current into the setup. The DC circuits for both pairs of DC coils on the FCL are independent circuits with a direct DC current source.(Fig. 7.7)

- The voltage across the AC coil terminals (V_{ac1} and V_{ac2}) are calculated and summed up to provide the total voltage across the terminals of the FCL as a function of time, and the fault current in the AC circuit as a function of time, was calculated from this value.
- The model was run with the normal load resistance for one cycle (20 milliseconds) to establish stable conditions for the FCL-included MV circuit (that is, with low insertion inductance as evidence by a negligible steady state rms current amplitude reduction in the circuit).
- To introduce the fault, the load resistance is changed to zero (by use of a switch on a line of zero resistance). Thus, the source impedances and the back emf across the FCL are the only elements controlling the current that now flows, which is in fact, the circuits' fault current.
- A voltage source and a resistance combination are employed to produce the biasing DC current to the coils rather than a pure current source. This is in order to make the circuit attain steady state quickly without adversely influencing results or increasing simulation run time.
- It should be noted that the air core inductance of the AC coils in series, without any ferromagnetic material, will have a natural fault current limiting effect on the AC line current. This was earlier measured from the prototype to be 92.2 μH for a single coil or 184.4 μH for both coils in series. To establish a base AC line current waveform, the line current is calculated without any FCL in the circuit by simply eliminating the AC coils from the fault generating MV circuit. This provides a baseline current waveform to which the current limited waveform that results from including the FCL can be compared.

The MV circuit setup for this study is presented in Fig. 7.7:

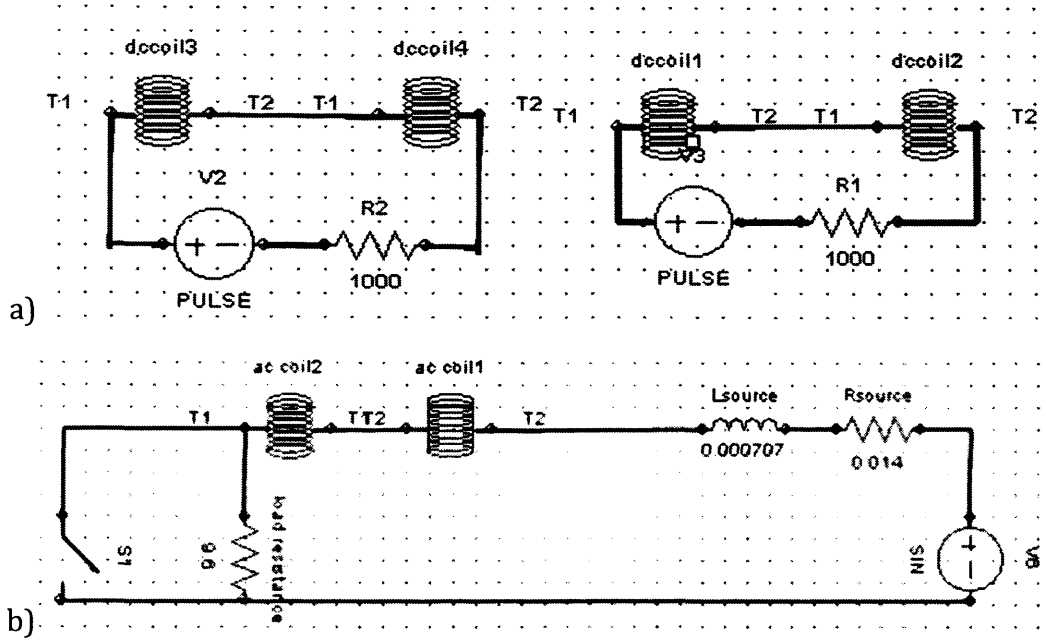

Fig. 7.7: **a)** *DC circuit and,* **b)** *AC circuit setups for transient study. Pulsed voltage sources (V2 and V3) are used along with resistances R1 and R2 to provide constant DC current. Switch S1 introduces short circuit.*

With the setup in Fig. 7.7 and circuit specifications, the simulations were run to ascertain what was the current clipping capacity of the FCL both with and without the ferromagnetic material. A time step of 0.001s was used with the fault current inception after one cycle (which takes effect once load resistance is shorted by switch S1) and it was left to run for 4 more cycles.

A preliminary test of the DC setup was run is to check the output for the DC current to make sure it was constant as needed.

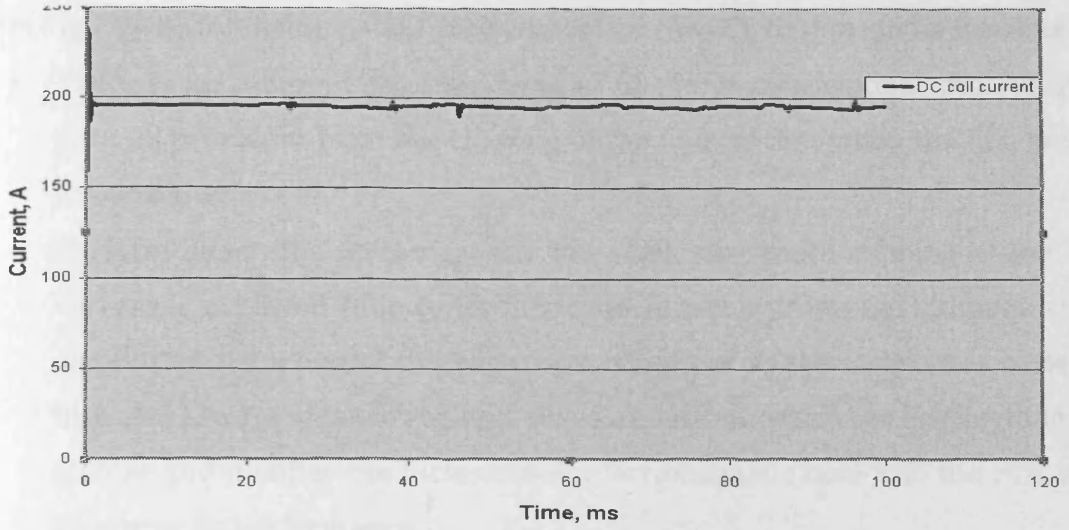

Fig. 7.8: DC current output from one of 4 DC coils, showing constant DC current throughout transient solver test simulation. Steady state conditions are arrived at very quickly as expected.

Apart from an initial stabilizing time at start of the simulation, the rest of the experiment runs virtually on a constant DC bias current as expected at 195A per coil as shown in Fig. 7.8. The spikes on the erstwhile constant DC current do show that there is an interaction between the DC circuit and the AC circuit, but it is not big enough to alter the DC coil's prevailing magnetisation direction.

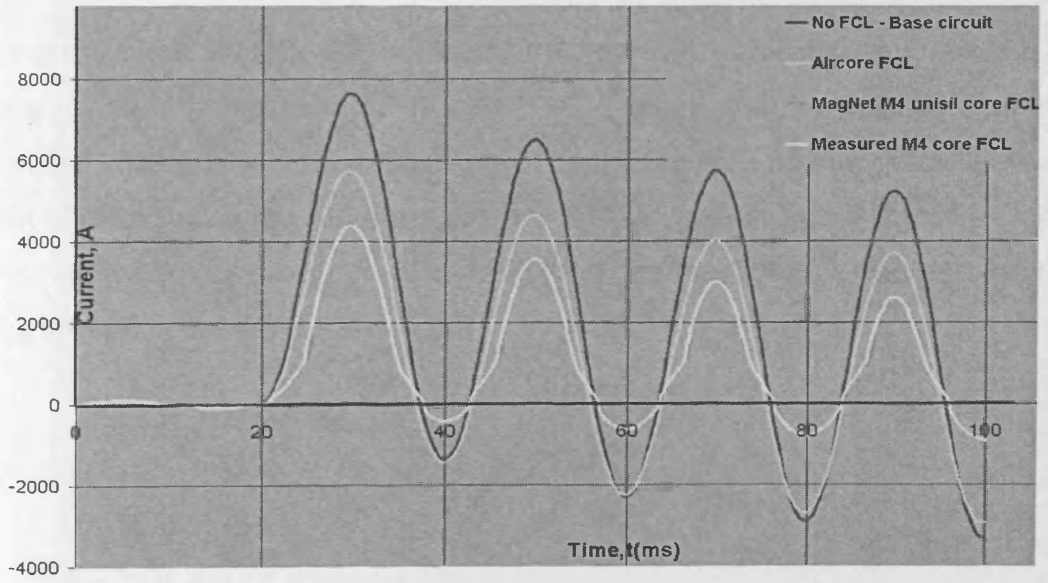

Fig. 7.9: Current waveforms from FCL transient study on FEM, showing the circuit with and without the FCL. A waveform with an aircore FCL is also included to show the limiting capacity it exhibits without a ferromagnetic core.

From Fig 7.9, the following points are deduced for the FCL design model simulated:

- There is an inherent limiting capacity of the aircore without the M4 steel core, as is evident from the clipping of the line current when the FCL has no ferromagnetic core.
- By introducing the ferromagnetic M4 steel core, more clipping of the line current is achieved (due to its flux concentration properties), though some amount of distortion of the waveform is noticed as the core cycles between high and low impedance regions. The core introduces more clipping than the aircore and justifies the inclusion of a ferromagnetic core into the FCL, as it enhances its performance.
- Two representations of the M4 material are used in the study; one being the native M4 steel representation in the Infolytica Magnet™ software, and the other being the measured M4 anhystereric material representation from Chapter 3. Both substitutions give consistent and similar results hence validating the point the M4 steel anhysteretic representation and characterisation done earlier is consistent with those done in industry.

Without the cores, there is a 25% reduction in the fault current accomplished by the aircore, or self inductance of the AC coils. When the ferromagnetic core is introduced, there is a 44% reduction in the peak fault current. This shows the benefit of introducing the core during the fault. With proper biasing of the DC circuit (higher saturation of core), the effects of such high inductance can be minimised during normal operating conditions.

7.6. *Performance Analysis Circular Compact model Using FEM Transient Solver (3-phase Simulations)*

FE transient solver simulations and analysis were performed on a 3-phase circular compact FCL model, in a bid to analyse the performance expected of the whole device in the network where it is implemented. This circular model is a simple variation of the six pack model, but with the ferromagnetic cores all arranged in a circular manner, and the DC coils (two) enclosing all six ferromagnetic core limbs (two per phase). The FCL was to be placed in a MV network with 1.25 kA nominal load current, and 19.6 kA peak asymmetric fault current. In the previous studies, only single phase simulations have been carried out because of their simplicity and under the assumption that the phases are independent of each other. In this set of simulations 3-phase tests were undertaken this time in order to confirm the absence of inter-phase interactions, and also to get a complete picture of FCL performance. Figs. 7.10 and 7.11 respectively are the FCL model structure and the network in which it was implemented.

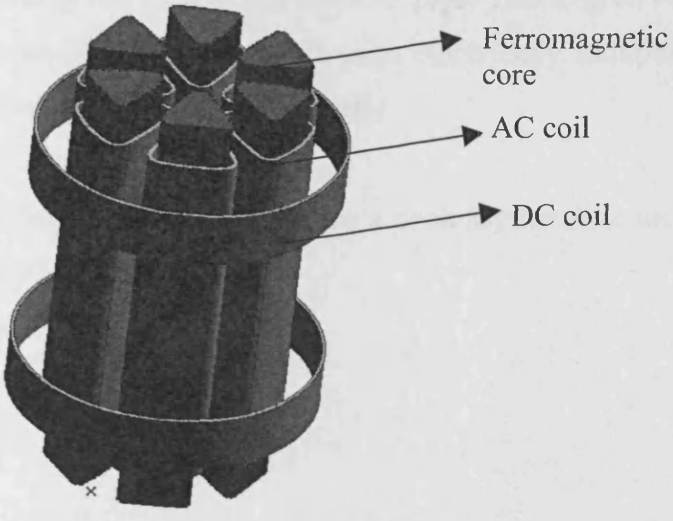

Fig. 7.10: Structure of new circular compact FCL.

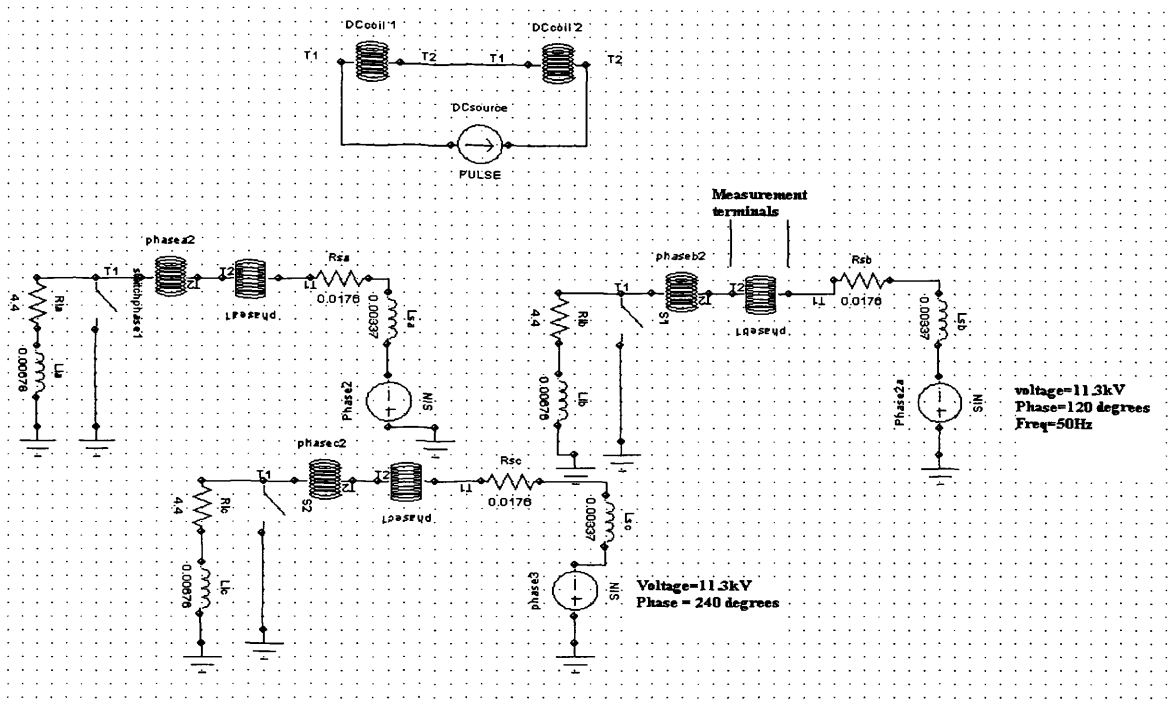

Fig. 7.11: Schematic of circuit constructed in MagNet, implementing 3-phase circular compact model of FCL in MV network.

The circuit was constructed simply by isolating each phase into its separate circuit and distinguishing them by making the AC voltage sources to be 120 degrees out of phase with each other. Hence each of the phases, though electrically independent from each other, were able to interact electromagnetically.

The values used for the circuit were modified to assure a peak asymmetric medium voltage typical fault level of 19.6 kA as follows:

Source voltage = 11.3 kV (L-L)

Source resistance = 0.0176 Ohms

Source inductance = 0.00337 H

Load resistance = 4.4 Ohms

Load inductance = 0.00678 (calculated from X/R ratio of 60).

Furthermore, the measured anhysteretic M4 characteristic being used was made into an anisotropic material with the orthogonal direction being incorporated into the material properties.

Fig.7.12 shows the 3-phase results obtained by selecting a time step of 0.001 ms

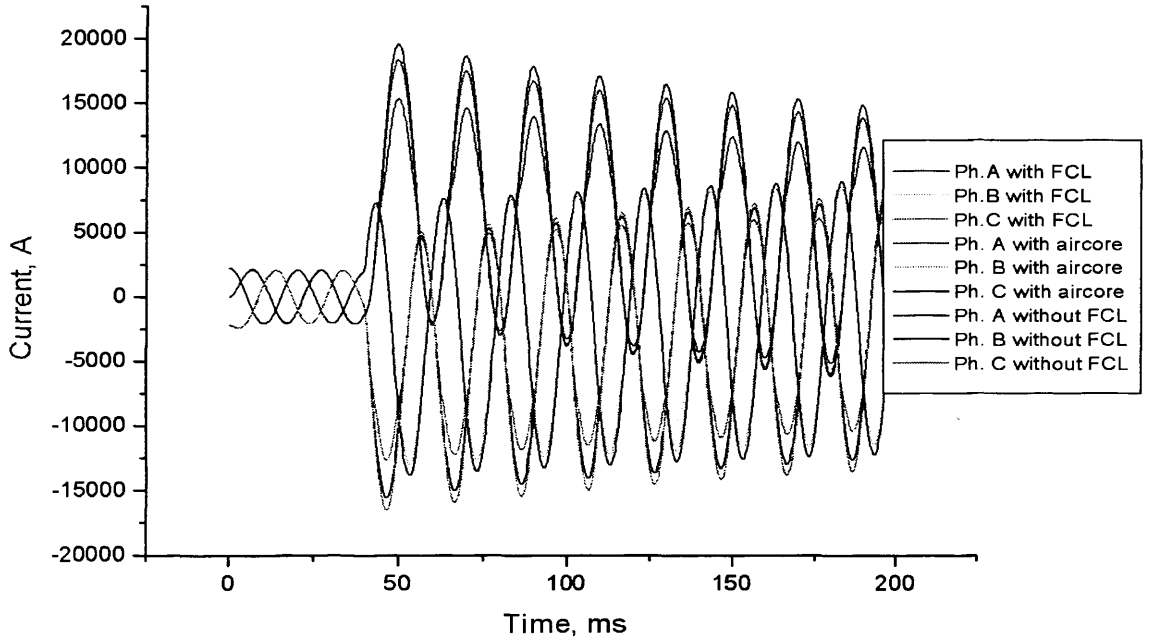

Fig. 7.12: Compact FCL current waveform showing current limiting for 3-phase circuit, at 0.001 ms.

As seen in Fig. 7.12, the aircore impedance offered to the circuit, clips the current from 19.6 kA to 18.4 kA (6.1%), while the M4 steel FCL clips the fault current to 15.3 kA (21.4%) at peak fault. Under steady state, the aircore clips the current from 15 kA to 14 kA (6.7%), while the M4 steel FCL clips the current from 15 kA to 11.7 kA, a 22% current limiting capacity. It is good to note here that because of the independence of the 3 circuits, there is no inter-phase influence seen in the results. The results further confirm that the ferromagnetic core definitely helps the performance of the FCL.

If we compare the phase A of the previous six pack configuration (Section 7.5) with that of the current FCL configuration, it is evident that the previous design limited

more of the fault current (44% to 21.4%). But the fault levels which are limited are higher, and the DC bias is also smaller in present design. These aspects can lead to better size and cost benefits, and hence make the circular compact design a very viable design to be used in the FCL.

7.7. *FEM Transient Solver Investigation of Performance of Circular Compact Model with Copper Shield*

Considering the large amounts of fields produced by the AC and DC coils, and the potential of disruptive coupling between these fields (especially on the DC side of the model), FEM analysis was carried out to investigate what the effects of such field interactions will have on the DC coils and the performance of the FCL as a whole. Ideally, the FCL should consist of two independent electrical circuits which are electromagnetically coupled only at the core limbs for maximum inductance gain, but the fact is that negative emf will be induced in the DC coils, hence bringing down the effective magnetisation.

A solution to this is the eddy current cancellation method [7] of passive shielding by the introduction of a grounded conductor (in this case copper) between both circuits, in order to shield the AC circuit field effects on the DC circuit side. Here the eddy currents produced in the shield by the AC current in turn generate magnetic fields that cancel out the incident AC fields. A cylindrical copper shield of 4cm thickness was introduced into the FCL design of the circular compact model as shown in Fig.7.13.

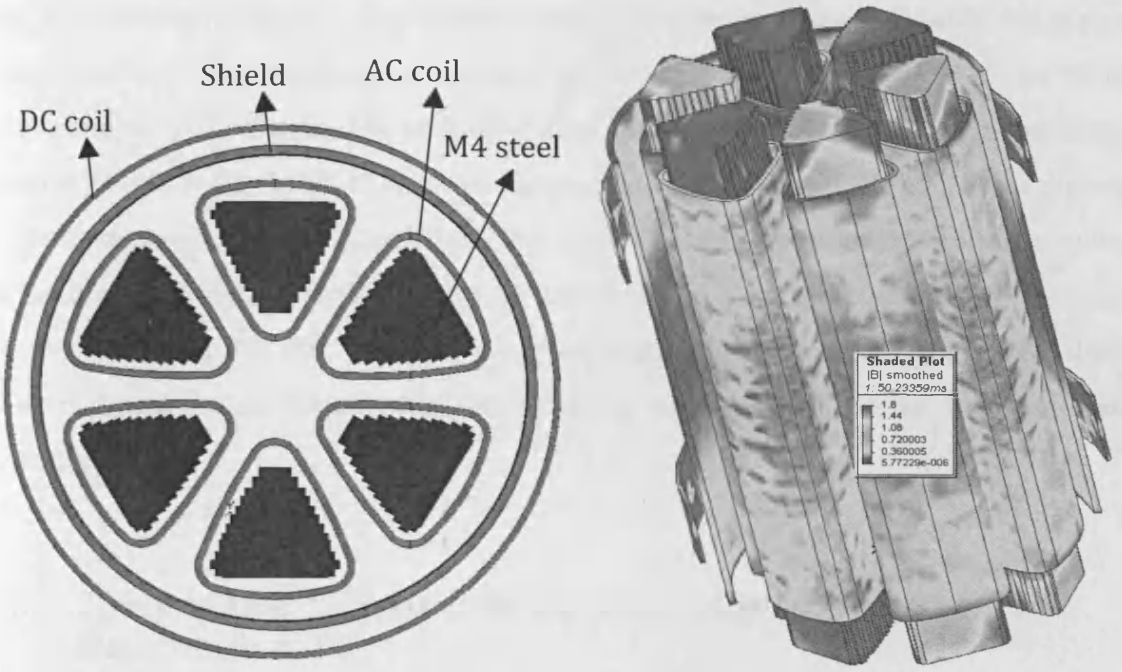

Fig. 7.13: Top and side view for shielded FCL at 50ms in the transient simulation with half of the DC and copper shield removed.

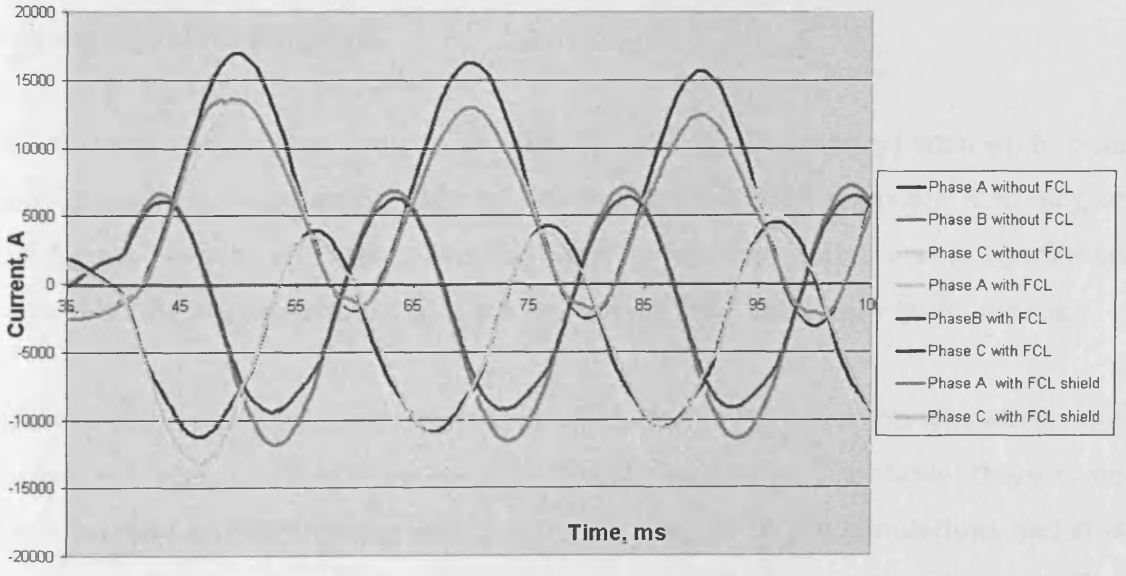

Fig. 7.14: Transient solution for FCL AC line current clipping performance with and without protective copper shield.

Fig. 7.14 shows no significant reduction in performance of the FCL with the copper shield present. The maximum current clipping still occurs at 13.4 kA of the 17 kA peak prospective current. The shielding does however help in limiting the disruptive coupling with the DC coil. It however introduces some distortion in the waveforms at the first current wave cycle. This effect seems more a result of the transient solver difficulties and issues with numerical convergence parameters, than to an actual physical effect of the FCL. From these simulations, we can conclude that the shield does not affect significantly the performance of the FCL, at least in its clipping capacity.

7.8. Effect of FEM Transient Solver Time Step in Performance Simulation of FCL

In the course of simulating the FCL in various test runs using the transient solver, the dependence on the accuracy of the solution on the chosen time step was encountered and investigated.

Given that the simulations are run at 50Hz (power line frequency) with each cycle taking 20 ms, the tests were made to run for 200 ms, with transient sampling of about 0.5 ms , which represents 40 samples per cycle. The switch was programmed to shut at 80 ms, thus introducing lower resistance path, and hence fault current.

Unlike the static measurements for inductance where a linear region was sought out to obtain the right current increment as shown in Section 7.4 above, there is no precise method of determining which time step to use in the simulations and this can result in large errors , if the choice is not properly researched and chosen. The choice of time step has to be an approximate decision which is dependent on the knowledge of the functional principles of whichever device is being modelled.

In the example of the FCL being modelled, due to the magnetic 'softness' (high permeability and low hysteresis) of the ferromagnetic material in use, the area of highest incremental permeability (steepest part of anhysteretic curve) and hence highest inductance is easily reached when magnetised. The H-field (approx. 89 A/m) needed to approach saturation is quite small, hence a wrong choice in time step could easily cause the simulation to skip over this area of maximum inductance gain, and hence severely limit the clipping capacity of the model during simulation. This means that the sampling rate of the AC line current (on which the AC fields are dependent) are not adequately sampled, and areas of high current magnitude on the sinusoidal waveform were not considered. Subsequently, the AC line current never opposes the DC field enough to bring the operating point into the area of high inductance. This can result in large simulation errors and hence is a point of major consideration during any transient simulation of an electromagnetic device.

To illustrate this point, the initial simulation time step used on the FCL was chosen arbitrarily as 0.5 s (40 samples per cycle).

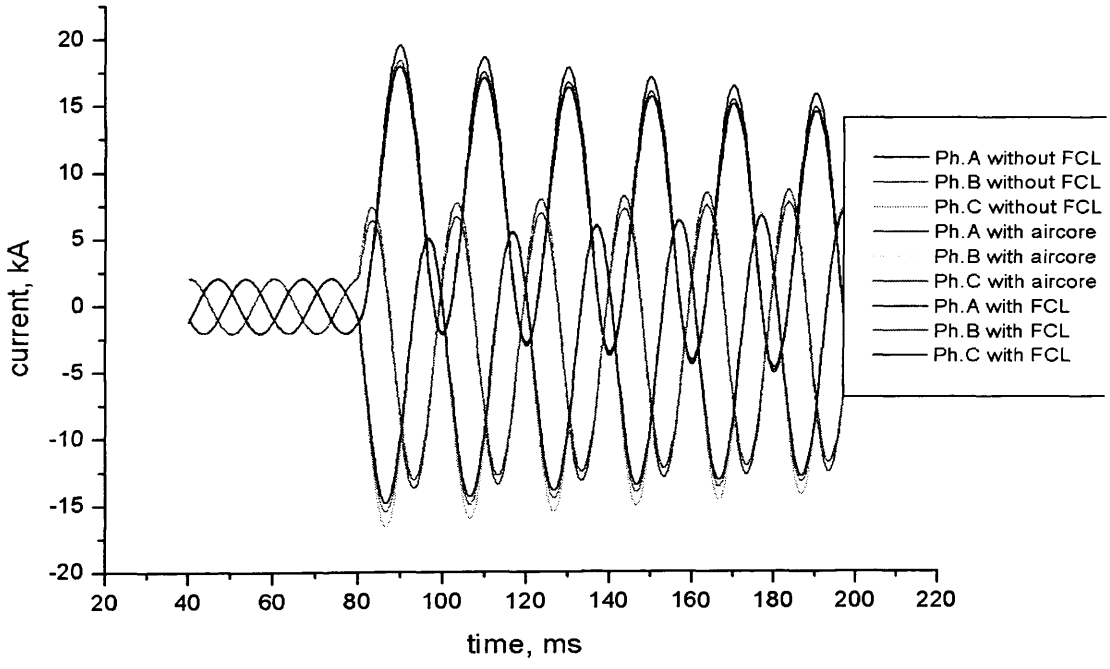

Fig. 7.15: Initial transient tests showing circuit with, and without FCL with 0.5 s time step.

As can be seen from Fig.7.15, the fault clipping due to the full FCL is not as large as expected (8.1% at peak and 9.55% at steady state), and the aircore FCL clips almost as much as the M4 steel core FCL. This is an erroneous simulation as a larger current clipping value of 24.1% at peak current and 22% at steady state, is expected as earlier shown in Section 7.6.

In order to further investigate this anomaly, the DC current was varied between 1A and 500A of DC current in order to eliminate the circuit parameters as the source of the anomaly. The reasoning being that if the problem was FCL circuit model-based, then varying the DC current would not change the clipping at all during the run. It would also serve a purpose of confirming that the FCL is functioning as required, if at low DC (1A), there is noticeable clipping during normal operation. This will prove that the fault clipping is being carried out as it is supposed to be, given that under normal operating conditions, the ferromagnetic core at the operation point will be in a region of high permeability (not fully saturated), and hence there will be a large inductance present on the circuit, leading to current clipping for the normal load current (not desirable for real FCL implementation). Furthermore, a higher DC current which will bias the core even further into saturation should result in little or no increase in current clipping over the aircore FCL, given that the bias point moves even further into saturation, hence increasing the capacity of the FCL to clip the current. Fig. 7.16 shows the results of this DC current study.

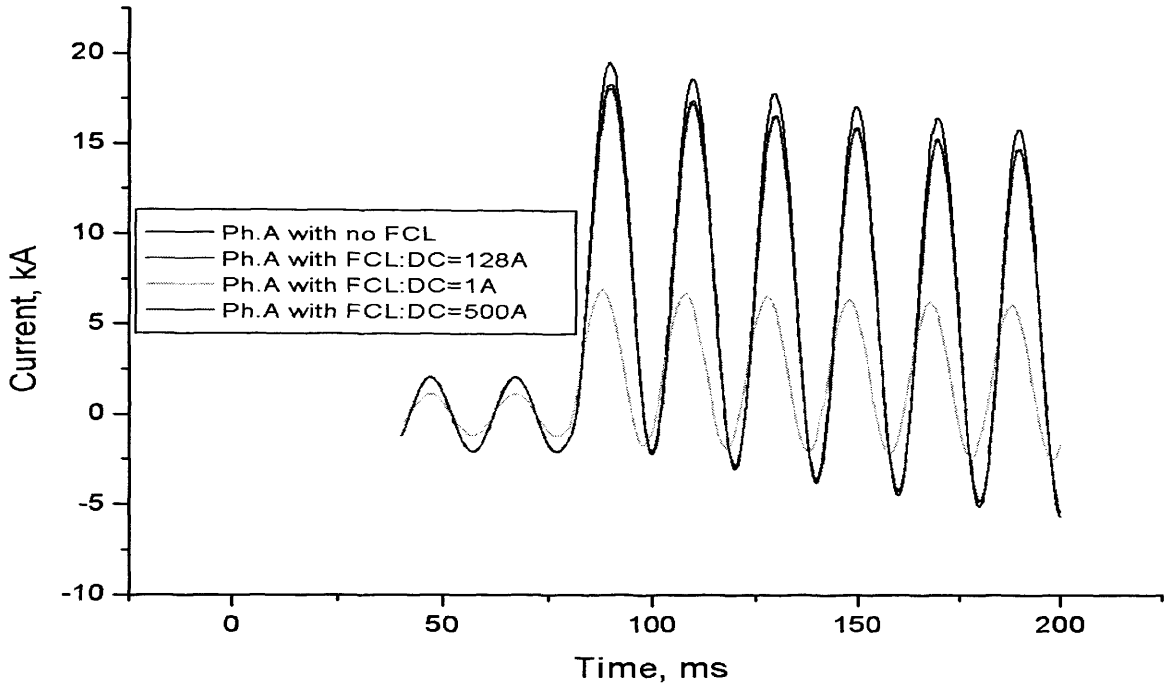

Fig. 7.16: FCL test current waveform, with varying DC current (1 A and 500 A), with a 0.5 ms timestep.

As shown in Fig. 7.16, when the DC coil current is reduced, the operating point of the FCL is moved into an area of high insertion impedance and hence there is clipping of the current waveform even under normal operating conditions as expected. Also, when the DC coil current is increased to 500A, a slight increase in clipping is noticed, as expected. These simulation runs show that the FCL is working as expected, and hence the FCL model setup is not the cause of the erroneous fault clipping results.

As a consequence, the next set of simulations comprised changing the time step through different values (0.5 ms to 0.0001 ms) and comparing the effect it has on the phase A line current of the FCL.

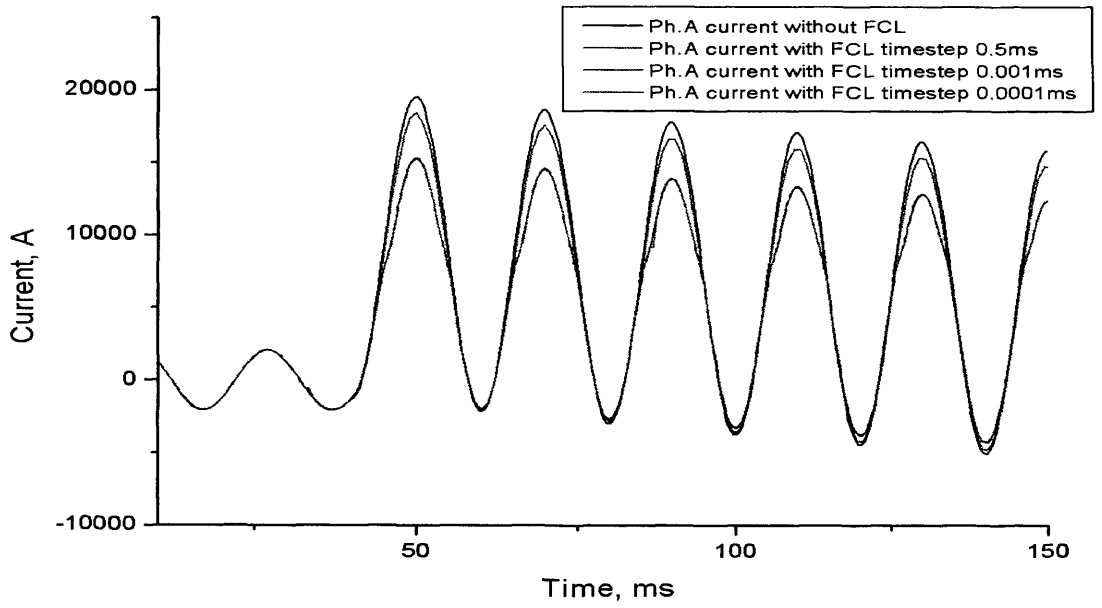

Fig. 7.17: Compact FCL phase A current waveform showing effect of different time steps.

Fig. 7.17 points to the fact that the choice of time step will change the results obtained in a transient simulation, hence care should be taken when conducting such simulations in FEM. The fault clipping levels changed as the time step was made smaller from 0.5ms to 0.001ms. Furthermore, Fig. 7.17 shows that this decrease in time step has a lower limit below which further reduction in the time step will not increase the accuracy of the simulation any further (0.001 ms to 0.0001 ms). But given the extra time and computing resources required for every reduction in time step, a compromise time step has to be chosen which gives enough accuracy in an accepted amount of modelling time. In these simulations, the time chosen was 0.001 ms.

7.9. Summary

In this chapter, the inductance types and calculations have been examined in order to find the appropriate method of comparing the inductances of various FCL design models. The insertion inductance of the FEM models were compared to those

measured from actual prototypes in order to authenticate the FCL models. The performance of various models and design modifications were then assessed using the FE transient solver. Finally, an examination was carried out on the effects of the choice of time step in transient simulations and how they altered the results of the modelling of the FCL.

[1] Rader, L. T.; Litscher, E. C., Some Aspects Of Inductance When Iron Is Present, AIEE Trans., Vol. 63, 1944,Pg 133-139

[2] Frederick W. Grover, Inductance Calculations: Working Formulas And Tables, Dover Publications, 1973,Ch. , Pg 9-17

[3] Rader, L. T.; Litscher, E. C., Some Aspects Of Inductance When Iron Is Present, AIEE Trans.,Vol. 63, 1944,Pg 133-139

[4] Franco Moriconi, Zenergy Power Inc Test Report:ZP/TR-2008/01,2008, pg. 9-15

[5] Calculation of inductance, Infolytica Corp, http://www.infolytica.com/ secured/ customer/elite/livedocs/, March 2009

[6] Franco Moriconi, Zenergy Power Inc. Test Report:ZP/TR-2008/01,2008, pg. 17

[7] Peter Stavroulakis, Biological Effects of Electromagnetic Fields, Springer-Verlag Heidelberg, 2003, Chapter 4, Pg. 380

Chapter 8. MV Power System Modelling of FCL in PSCAD and FCL Model Comparison (PSCAD and VDM)

8.1. Introduction

In the mathematical modelling of the FCL and the study of the use of FEM in the design of the FCL, there has been a recurring limitation to these methods. This is the limitation of being unable to appropriately model the power network in which the FCL will be utilised. This aspect of the FCL model development is very important as it presents the actual setup in which the device will be implemented. Building a more realistic model of a typical MV network in which the FCL can be implemented will provide the best conditions under which the FCL model's applicability can be assessed, and its functionality evaluated.

In this Chapter, a model of the FCL is constructed in a power system simulator PSCAD™ . Some of the problems encountered while constructing this model have been examined, and its functionality in a network has been studied. Finally, the PSCAD model has been compared to the VDM mathematical model of the FCL, in order to evaluate the consistency and accuracy of these models in relation to the values measured from real prototype tests. This Chapter will point out the limitations of the PSCAD model, and also highlight the disparities encountered from model to model in this anhysteretic design development.

8.2. Use of FCLs in Medium Voltage Power System

Distribution networks are generally divided into zones which contain protective equipment that are responsible for the protection of the given zone [1]. This switchgear equipment should prevent distribution network component overstress

or failure, by maintaining the quality of power that is supplied to customers whilst considering the safety of personnel [2].

The continuous growth of the electricity demand around the world has invariably led to an increase in short circuit currents on the power grids [3],[4]. This is because the additional loads and generators (usually decentralised generation) that have been added to the power network generate more voltage overloads and sags than the original switchgear were rated to handle. The penetration of this distributed generation (DG) poses challenges for the protection coordination of passive networks [5], one of such challenges being their significant contribution to an increase in the fault currents. Although inverter based DG may contribute limited fault currents, synchronous DG systems may feed higher sustained currents if they lack control capabilities through the use of power electronic interfaces [6]. Induction generators fail to sustain a high fault current due to the absence of a self-excitation system [7].

A questionnaire based survey from CIGRE WG A.310, acquired 53 responses from 14 countries in the European Union from which 84% identified the need for current limitation in HV or MV levels [8]. A number of techniques exist to limit the fault currents as discussed in Chapter 2, which include the use of FCLs [9].

8.3. Development of the PSCAD FCL Model

8.3.1. PSCAD Module Construction

PSCAD™/EMTDC™ is the power system simulator used in developing the model which could be directly implemented in power system networks. The FCL model was developed using a FORTRAN subroutine [Appendix 1]. This model (implemented as a control module in the software) represented the FCL on the network as an externally controlled variable inductor, whose value changed with the input current. The computational efficiency and simplicity of this model resides

in the derivation of mathematical expressions for the non-linear behaviour of the ferromagnetic material and the magnetic field profiles. These expressions have been developed in previous Chapters. Expressions incorporated into the module include the material function, H-field distribution function, and the inductance calculation function.

8.3.2. Material Function

The material function developed in Chapter 3 represents the properties of the soft ferromagnetic core material used in the device as a flux concentrator. This was comprised of a non-hysteretic ***B-H*** curve;

$$B(H) = B_s\left(\coth\left(\frac{H}{a}\right) - \frac{a}{H}\right) + \mu_0 H \qquad (8.1)$$

In PSCAD this mathematical function though mathematically well defined, encountered numerical difficulties at the origin (to be further explained in next section) and was modified appropriately.

This analytic function, fitted to measured data, is differentiated to obtain an equation for the non-linear permeability of the core dB/dH in Eqn. 8.2, which controls inductance such that:

$$\frac{dB}{dH} = \mu_0\left(\frac{B_s}{\mu_0}\left(\frac{a}{H^2} - -\frac{1}{a}\operatorname{cosech}^2\left(\frac{H}{a}\right)\right) + 1\right) \qquad (8.2)$$

to avoid possible numeric difficulties, as the field approaches zero, Eqn. 8.2 is described as

$$\frac{dB}{dH} \approx \mu_0 + \frac{B_s}{3a} \qquad (8.3)$$

with the ***a***-parameter controlling the inclination of the curve.

8.3.3. H-field Distribution Function

After extensive FEM modelling and measurements in Chapter 4, a mathematical expression was derived for the field distribution in the core. This expression takes into consideration all the design parameters of the coils and the core, including the positions of the coils, therefore providing a more accurate calculation of the inductance. The magnetic field H as a function of distance x from the magnetizing coil centre for either coil (AC or DC) can be written as:

$$H = \frac{NI}{L}\left[\frac{(L+2x)}{2\sqrt{D^2+(L+2x)^2}} + \frac{(L-2x)}{2\sqrt{D^2+(L-2x)^2}}\right] * f_{shape}(x) \qquad (8.4)$$

where N is number of turns of the coil, L is length of the coil, I is current in the coil, and D is diameter of the coil. The shape function $f_{shape}(x)$ is taken as unity to a first approximation.

The resultant magnetic fields; $H_+ = H_{DC} - H_{AC}$ and $H_- = -H_{DC} - H_{AC}$, are used for the positive and negative half cycles respectively. Here, H_{AC} and H_{DC} are the magnetic fields produced by the interacting AC and DC currents respectively.

8.3.4. Inductance Function

The response of the FCL device to the AC line current is a change in the inductance of the variable resistor following the equations discussed in Chapter 7 and this is calculated from a derived equation:

$$\Gamma i(t)] = \frac{\mu_0 AN}{i.l} \int_{x=-\frac{l}{2}}^{x=\frac{l}{2}} \mu_{r(x,t)} H_{(x,t)} dx \qquad (8.5)$$

where ***A*** is the cross-sectional area of the AC coil, ***N*** is the number of turns in the AC coil, ***l*** is the path length, and $\mu_r(x)$ is the relative permeability of the core material at a distance ***x*** from the point of interest or operating point on the core.

All these component equations were combined in the inductance equation (Eqn. 8.5) governing the FCL function to produce an electrical model that was easy to use and fast in its calculation of inductance and integration in external systems. Fig. 8.1 presents a schematic diagram of the control module and its constituent input and output components.

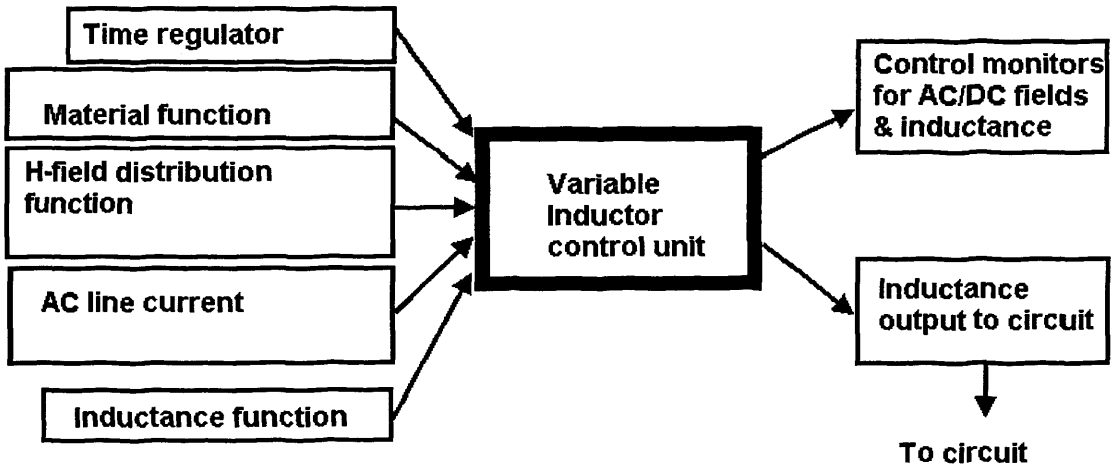

Fig. 8.1: FCL model schematic showing components input and output components.

The time regulator component is a simple time initialisation routine for the inductance at time t=0. This was necessary to introduce so that the inductance had a value at the start of the power system test run. A very small constant value (10^{-8}H) was input at time t=0, after which the module calculated its output value from the constitutive inductance equation.

The control monitors were graphs plotting the field, the line inductance and material functions in real time.

8.4. Mathematical Challenges and Solutions for PSCAD module: The Singularity Problem and the a-value Problem

In building the PSCAD model, mathematical challenges as per the validity of the equations used, were encountered. They constituted mainly of the mathematical limits to which the software could be taken, and solutions had to be sought in order for the model to be able to function around these numerical difficulties. These problems include the singularity problem and the ***a***-parameter problem:

8.4.1. The Singularity Problem

This consisted of an undefined value for magnetisation of the model when the total cumulative field H_{total} (sum of AC and DC fields at any time) equalled zero. It was noticed that the module functions as expected in the region where $|H_{DC}-H_{AC}|=0$. The PSCAD screen snapshot below shows the distortion in the waveform whenever this region of the ***B-H*** curve was approached, which meant the H_{AC} could not go higher than the H_{DC} as shown in the Fig 8.2a.

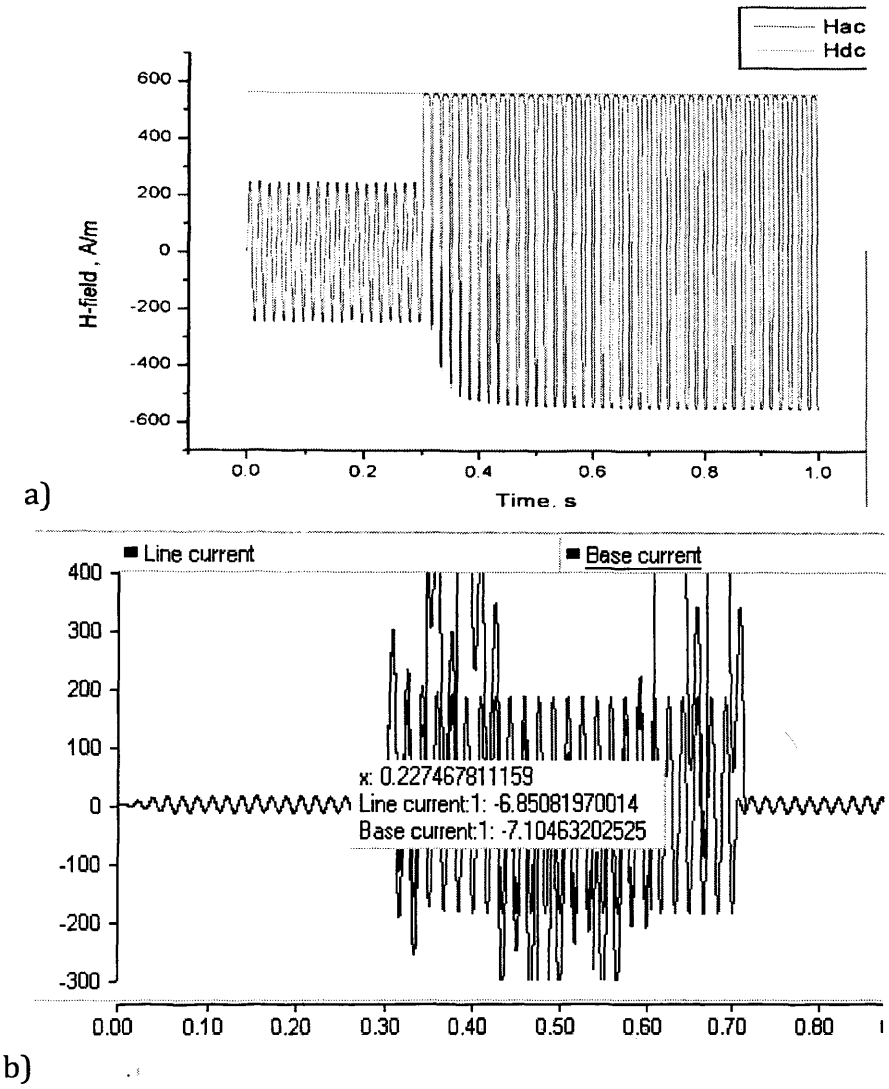

Fig.8.2: **a.)** ***Total H-field output when H_{AC}> H_{DC}, showing an erroneous limiting of H_{AC} by H_{DC} and hence*** **b.)** ***False distorted clipping of line AC current, compared to the base current with no FCL model in circuit.***

The problem was investigated and discovered to be due to the implementation of the material function in the PSCAD model. It was noticed that as H-> 0, the inductance function became unstable and was no longer representative of the material at such points (due to the numerical limits of the software). Also, bearing in mind that this curve of the M4 material in use was fitted as an approximate representation over a very large range, the inaccuracies of such a fitting around

point zero were preventing the PSCAD model from doing a fair representation of the FCL function.

The solution utilised for this problem was to approximate the material function using a linear equation as the ***H***-fields approached zero. The function Eqn. 8.1 was approximated by the first term of its Taylor expansion such that

$$B(H) = B_s \frac{H}{3a} + \mu_0 H \qquad (8.6)$$

as ***H*** tends to zero in order to make it a well-behaved function where ***B*** is the magnetic induction, ***a*** the anhysteretic curve parameter, ***H*** the magnetic field, μ_0 the permeability of free space and B_s the induction saturation is used.

This formulation solved the singularity problem at $H_{total}=0$ but revealed another problem, here-termed the ***a***-parameter problem

8.4.2. The a-parameter Problem

This problem caused the differential permeability to increase to extremely high values during the simulation run (with μ_r increasing up to 350000, due to the very low value of the ***a***-parameter), and this in turn completely clipped the current, giving an artificial perfect clipping of the line current. The problem was traced to the fact that the ***a***-parameter (which determined the inclination of the ***B-H*** anhysteretic curve) is a variable around the whole curve rather than being a constant value as is represented in the material function equation. Hence the input value being used, though a good approximate for most of the modelling becomes unrealistically small for the steeper part of the curve (region with highest permeability). Thus the existing initial material function, though reasonably representative over the whole anhysteretic curve falls short in properly representing the material when the

accuracy of the FCL is being investigated at the steepest part of the curve in PSCAD™.

The solution devised for this problem was to improve on the present Langevin function used for the material by introducing a second function that more closely represents the material behaviour at the steepest part of the curve.

By going back to measured curves and investigating which mathematical expression could be used, a piecewise approach was adopted. Two functions, a Lorentzian curve and the derivative of the Langevin function derivative were combined into a piecewise representation of the material permeability. These are joined together at values where both functions intersected. The Lorentzian equation is itself made to be piecewise to account for both the positive and negative ***H***-fields. This is achieved by implementing the transformation f(x) = f(-x) which is true for even functions.

The modified Lorentzian function thus used is:

$$\mu = B_0 + \left(\frac{2A}{\pi}\right)\left(\frac{\omega}{4(H - Hc)^2 + \omega^2}\right) \qquad \textbf{for H > 0 and}$$

$$\mu = B_0 + \left(\frac{2A}{\pi}\right)\left(\frac{\omega}{4(-H - Hc)^2 + \omega^2}\right) \qquad \textit{for H<= 0} \qquad \textit{(8.7)}$$

The parameter values obtained for the M4 steel from the curve fitting with the initial anhysteretic curve were: $\mathbf{B_0}$ = -346.7 , $\mathbf{H_c}$ = 6.75 , ω = 6.7 , **A** = 1,312,031

Combining both functions at their intersection (at ***H*** = 24.2, and ***H*** =-24.1) produced the material function represented in the following composite graph:

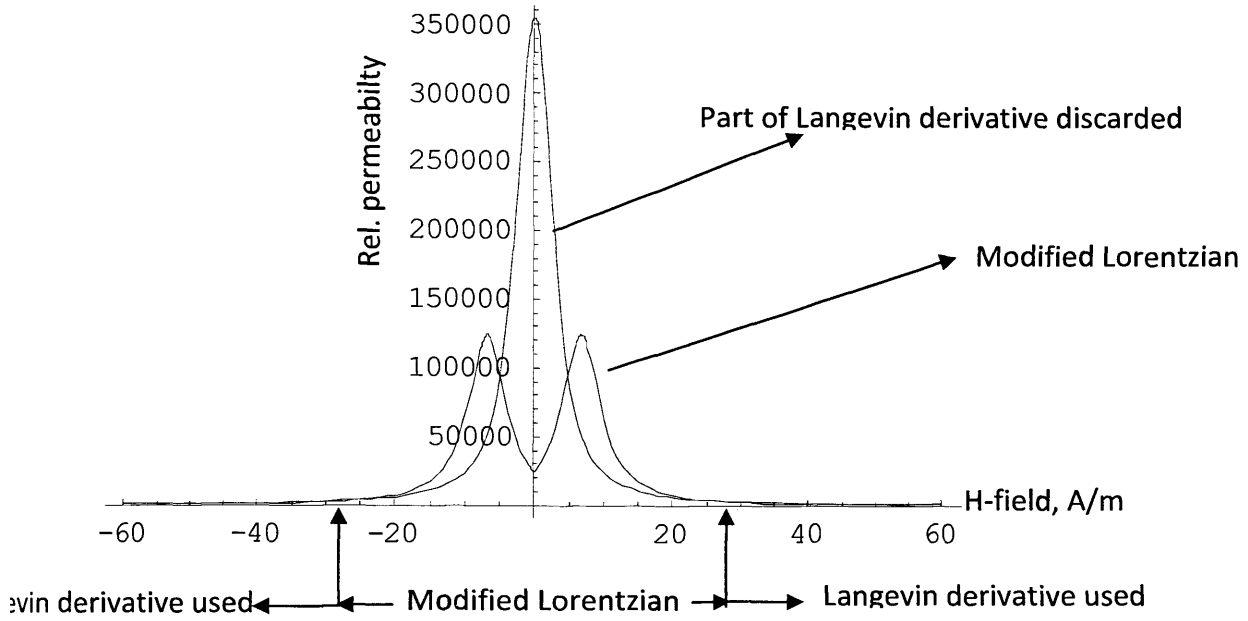

Fig. 8.3: Graphical representation of how the two functions are used in representing the permeability of the M4 steel material.

This implementation gives us a better representation of the magnetisation between the ***H***-field limits and a more realistic representation of the inductance even when the $H_{AC} > H_{DC}$.

After these mathematical issues were resolved, the PSCAD model was analysed, tested and validated against measured data from an FCL prototype. It was then used to study the performance of the FCL in a generic model of a real UK MV power network.

8.5. Examination of PSCAD FCL model Functionality

For the analysis shown here included, the FCL parameters used were:

I_{DC} = 1 kA ,

N_{DC} = 500 turns,

N_{AC} = 10 turns,

Mean path length = 2.6m

AC/DC cross-sectional area = 0.015m^2

AC and DC coil height = 0.35m

AC and DC coil diameter = 0.2m

ACMultfac = 1 (This was given this value in order to eliminate its effect on the analysis.)

All other parameter values were left unchanged as per the test network implemented in Chapter 7, with only the X/R ratio being adjusted to give a peak prospective asymmetric current of 47 kA. These values closely represent the real FCL prototype.

8.5.1. Fault Analysis and PSCAD Model Performance

8.5.1.1. Triple Phase Fault Investigation Using PSCAD FCL Model

The first scenario tested was the worse possible faults – 3-phase line to ground faults. The fault was introduced simultaneously on each phase, and neither phase was at its zero crossing of axis. The diagram in Fig. 8.4 shows the results of this simulation.

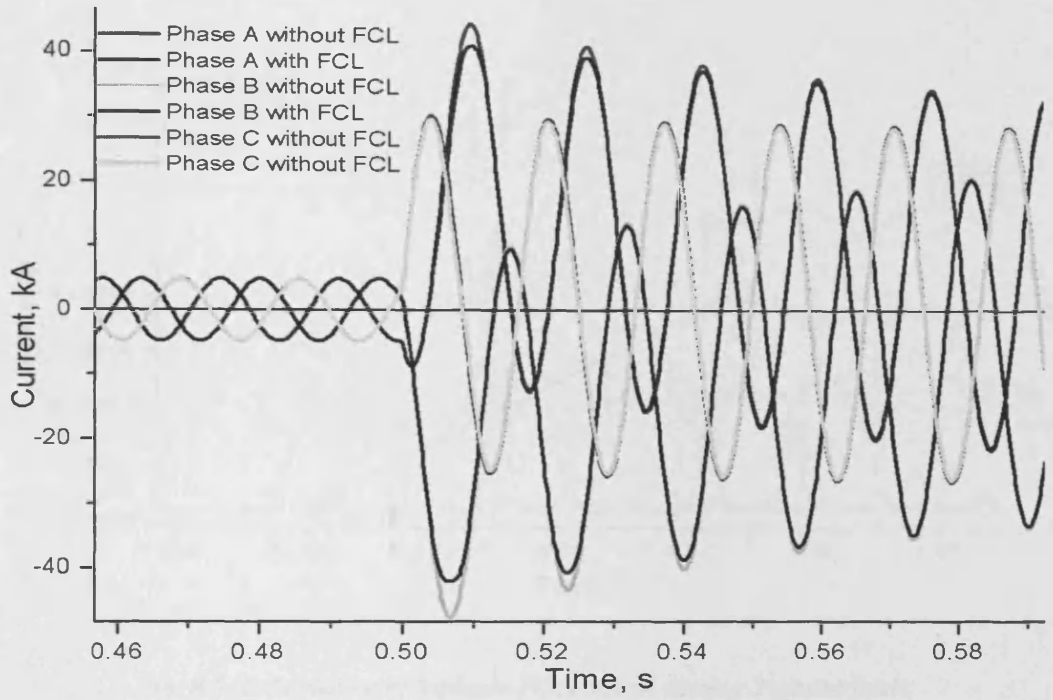

Fig. 8.4: 3-phase fault current showing clipping by FCL module in test power network.

The current clipping is performed for both positive and negative sequence faults to approximately 42kA from the 47 kA peak fault current. This represents a 13.1% clipping capacity, which is the 'worst case scenario'. It is worth noting that the ACMultfac which usually compensates for the inaccuracies in calculating the fields (as discussed in Chapter 5) has not been factored into this analysis. Secondly, it was readily seen that under normal operating conditions, the line current is not disrupted, and hence the FCL can be classified in this model as being 'transparent' to the network.

A closer look at the real-time functionality of the model as shown by the real time monitors, indicate how the model changes the line inductance with respect to the line current values as shown in Fig. 8.5:

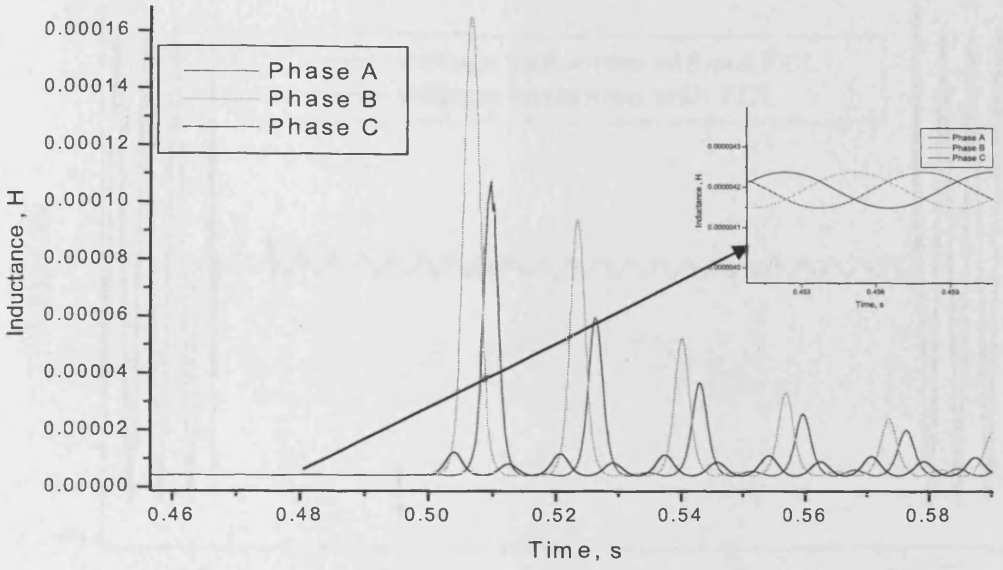

Fig. 8.5: Inductance of 3-phase FCL control during 3-phase fault.

The graphs show that there is an increase in inductance of about 1600% from normal operating conditions when a fault is introduced into the circuit. This increase varies per phase, depending on the maximum fault current in that phase. The inset shows that under normal operating conditions, the FCL contributes a very small but expected amount of inductance (insertion inductance) to the line.

Another area of interest was the effect of the insertion inductance, on the line voltage. An ideal FCL should have no over voltages during the transient stage of fault limiting. In the 'worst case scenario' for faults introduced above, Fig. 8.6 represents the voltage response of the power circuit, as examined on phase A:

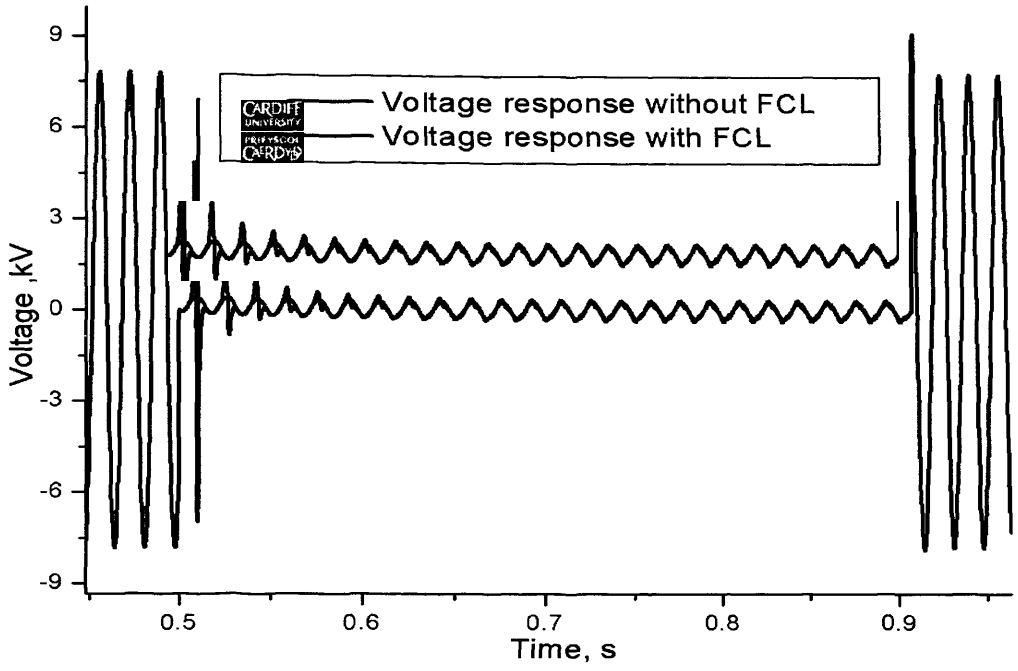

Fig. 8.6:Voltage response to fault with and without FCL on phase with time of fault inception at 0.5s.

The graph shows some transient effects on the voltage when the FCL is introduced. But not only are these events very short in duration, they are also not large in magnitude. In fact, the transient effects noticed at fault inception are well below the usual line voltage. Hence the FCL model reveals that the FCL poses no danger to a network in terms of over-voltages during fault currents.

A look at the ***H***-field variations over the course of the simulation run shows how the AC and DC fields interact (see Fig. 8.7).

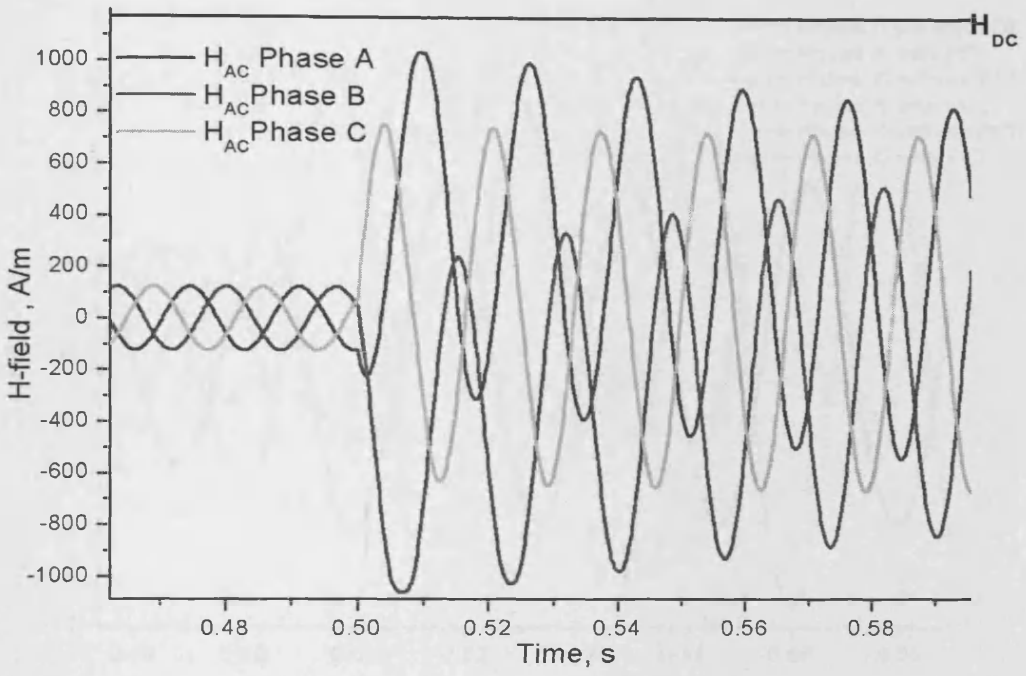

Fig. 8.7: H-field interaction between H_{DC} and H_{AC} during 3-phase fault.

It was noticed from numerous runs of the PSCAD simulation that the condition $H_{AC} \sim H_{DC}$ was critical for the functioning of the FCL as the optimum performance of the FCL resulted when the $H_{DC} \sim H_{AC}$ condition was satisfied.

8.5.1.2. Single Phase Fault Investigation Using PSCAD FCL model

A series of simulation were undertaken with only single-phase line-to-ground fault on only one of the phases (Phase A). The fault currents due to such faults are usually markedly lower than those on 3-phase faults (worst case scenario). For this single line fault the FCL parameters were not changed from the 3-phase settings, in order to investigate how the FCL will behave towards smaller faults in a case where the parameters are set to limit of the 'worst case scenario' fault currents.

In Fig. 8.8, a line-to-ground fault was introduced on phase A only at time 0.5s, which are the same conditions as for the 3-phase faults.

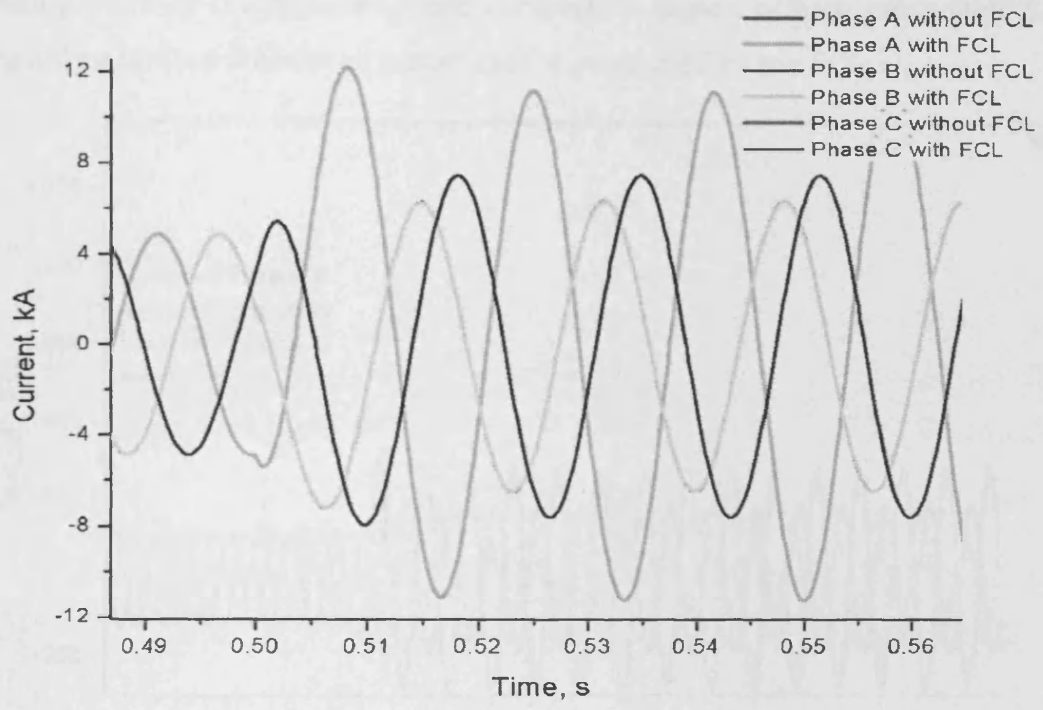

Fig. 8.8: Single-phase fault current, showing waveforms with and without FCL.

With no changes in the FCL parameter settings, the smaller fault currents are not as limited as the large faults, but are limited by about 0.3% (not visible on graph). This means that the FCL still functions normally, although it would be relying on other power protection equipment (circuit breakers) to handle smaller fault currents if it is set to perform in the higher fault range. It is a positive to this FCL model that it is still able to contribute some amount of fault clipping, albeit very small, even at these low fault current levels.

This study shows that the FCL settings are fault-level specific in that, they would be more effective at a set fault current range, and not as effective on others lower fault levels. A look at the ***H***-field graph of this setting as seen in Fig. 8.9 shows the reason for the limited clipping. Given that the DC bias field had been set to limit worse case scenario faults, single-phase faults do not produce enough ***H***-field to move the

operating point of the ferromagnetic core into a region of high permeability, and hence only a limited amount of inductance is generated by the FCL.

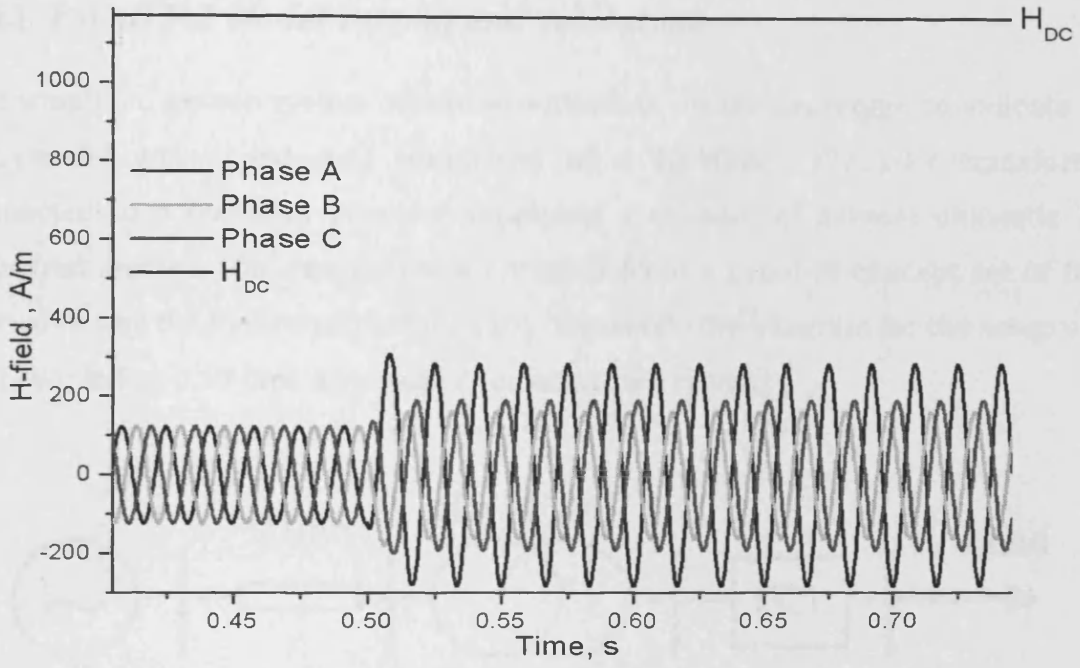

Fig. 8.9: H-field interaction between H_{DC} and H_{AC} during 1-phase fault.

Fig. 8.9 shows that the AC line current produced by the single phase fault does not generate not enough ***H***-field to reach the H_{DC} bias field, and hence the inability of the FCL to significantly limit the fault current with those settings.

Contrasting Figs. 8.7 and 8.9 shows the reason for a visible clipping on the higher fault levels is the AC current-generated ***H***-fields which are large enough to move the bias point into the region of maximum inductance gain as shown in Fig. 8.7. This capacity to be selective in limiting faults allows the model and hence the FCL to apply to various levels and magnitudes of fault currents.

It is desirable to rate the FCL for the 'worst case scenario' fault on the power line, given that the other switchgear and protection equipment can handle the smaller faults.

8.6. PSCAD model Validation and Performance Testing in Typical UK MV Power Network Setup

8.6.1. PSCAD FCL Model Testing and Validation.

The simplified power system where experiments on the prototype to validate the FCL model were conducted comprised of a 45-MVA, 132/11-kV transformer connected to a common bus bar supplying a mixture of several domestic and industrial feeders. The results were obtained from a proof-of-concept set of tests carried out by the industrial partner [10]. The single line diagram for the setup used is shown in Fig. 8.10 [See Appendix 2 for expanded circuit]

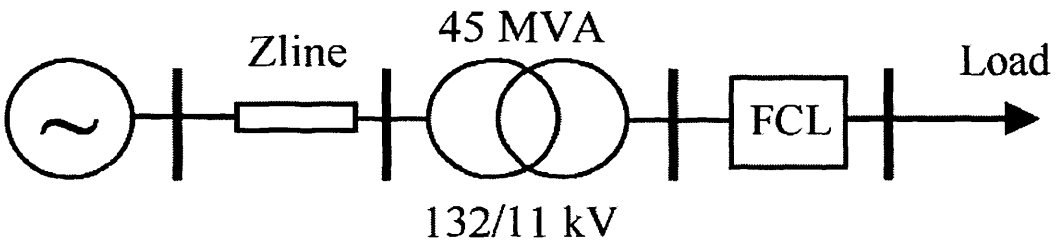

Fig. 8.10: Single line diagram for the validation test runs of the FCL prototype in the medium voltage network.

The experimental procedure included a large range of tests, six of which are shown in Table 8.1. These tests were duplicated in simulation as closely as possible (exact numbers were not achieved due to possible impedances in real network which were unaccounted for in testing report), using the FCL model to examine the behaviour of the model in the simulated network. This was in order to test the minimum limiting capacity of the FCL for the particular circuit.

Multiple fault tests were conducted, along with insertion impedance (inductance) testing, to confirm that the voltage drop due to the insertion inductance of the prototype was within industrial standards. For this specific device, the voltage drop ratio was 0.8% of the line voltage.

Table 8.1: FCL Testing Experimental and Simulated Results

Experimental Results *(Industrial Partner)*				
Test ID	**Line X/R ratio**	**Peak Phase Prospective current (kA)**	**Maximum Clipped Current (kA)**	**Peak Clipping (%)**
1	22.9	7.4	6.2	11.1
2	19.8	20.8	18.7	10.2
3	19.7	31.4	27.6	12.2
4	26.3	40.3	20.9	15.1
5	21.6	52.4	43.5	16.8
6	44	63.1	53.1	15.7
Simulation Results *(Current work)*				
Test ID	**Line X/R ratio**	**Peak Phase Prospective Current (kA)**	**Maximum Clipped Current (kA)**	**Peak Clipping (%)**
1	22.9	6.6	6.15	9.9
2	19.8	21.3	18.7	11.5
3	19.7	31.94	27.54	13.8
4	26.3	39.85	34.36	14.6
5	21.6	50.81	43.38	1.8
6	44	60.1	51.07	15.02

Table 8.1 shows good agreement between the simulated and experimental results, as all recorded values were within a 4% error margin. Differences between the actual material and its modelled mathematical representation, coupled with the inherent differences in the circuit simulation and the real-time testing conditions, can be cited for the disparities noticed in the values.

8.6.2. Application of SCFCL in the UK Generic Network

A UK radial MV generic network was used to evaluate the behaviour of the FCL model. This specific distribution network serves 18,432 residential consumers, through a primary substation of 33/11.5 kV. The fault current levels of the modelled network were computed and verified towards the simulation results published in [11]. Fig.8.11 provides the network schematic.

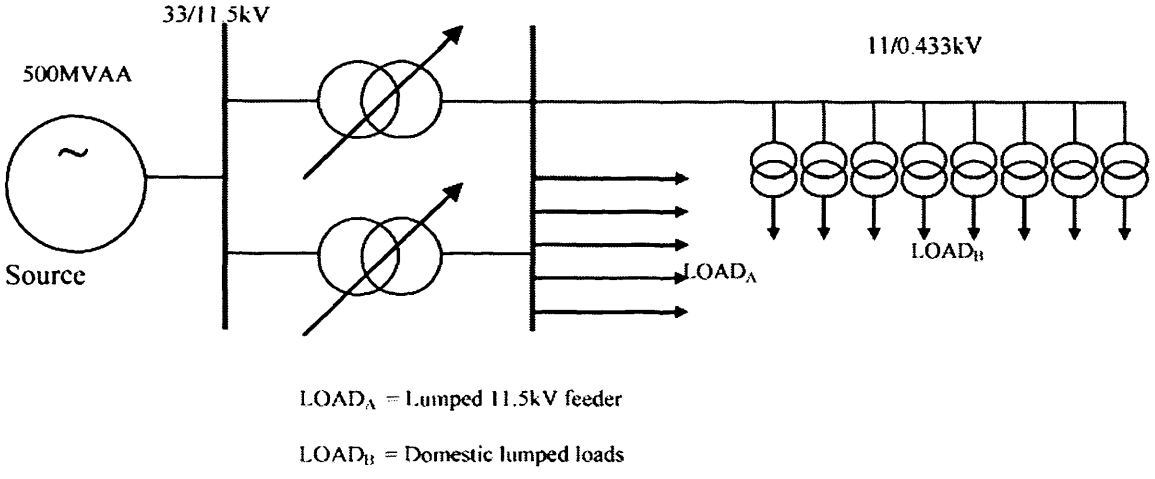

Fig. 8.11: UK Generic MV Distribution Network into which PSCAD model is implemented.

In this network simulation, an equivalent DG model of 4.5MW was connected to the 11kV substation busbar. The FCL's location is shown in Fig. 8.12. This location was selected to limit the fault current contribution from both the grid infeed and the DG. This way, a new DG installation combined with FCL installation could defer existing switchgear updates.

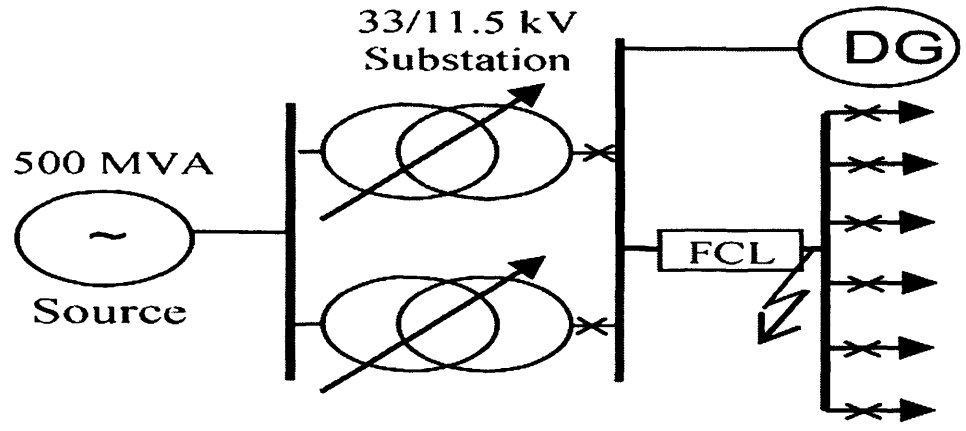

Fig. 8.12: Schematic of the simulated network showing location of FCL.

8.6.3. Results and Discussion of FCL Model Implementation in Generic UK Network

The On Load Tap Changer (OLTC) mechanisms of the transformers shown in Fig. 8.12 are adjusted to keep the voltage between 1 and 1.01 p.u. The first requirement tested for, was the transparency of the device in real-time, because the voltage drop caused by an FCL during normal operating conditions is of great importance for the utilities. The model showed negligible voltage drop (i.e. approximately 0.5%) during normal operating conditions. Fig. 8.13 shows the voltage (rms) during a three phase fault with and without the FCL model. The measurement was taken at the position of the fault (Fig. 8.12).

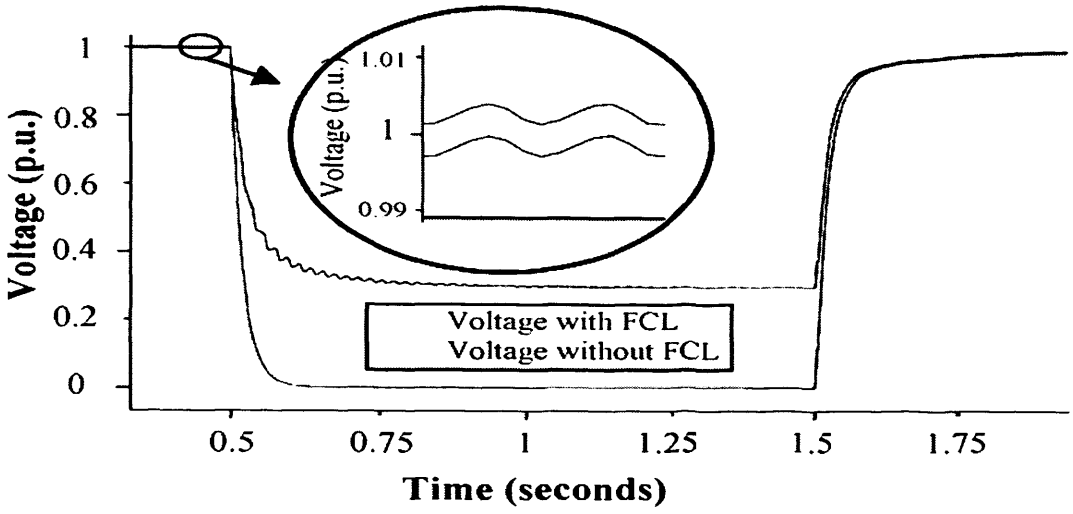

Fig. 8.13: Voltage drop during a 3- phase fault on UK network with and without FCL model.

The maximum clipping capacity was then tested to evaluate the behaviour of the model during a fault. The first peak short circuit current was clipped by approximately 50% in less than 7 micro-seconds as shown in the Fig.8.14 inset. This showcases not only the FCL's ability to clip a large percentage of the current, but it does so in the first half cycle, thereby enabling other protection equipment to function normally.

A test for repeatability and reliability constituted of simulating a double fault with a 1s interval. This test was to analyse the model's ability to provide fast recovery for multiple operations. Fig. 8.14 shows the results of a multiple operation test, with the SCFCL not suffering any loss in performance.

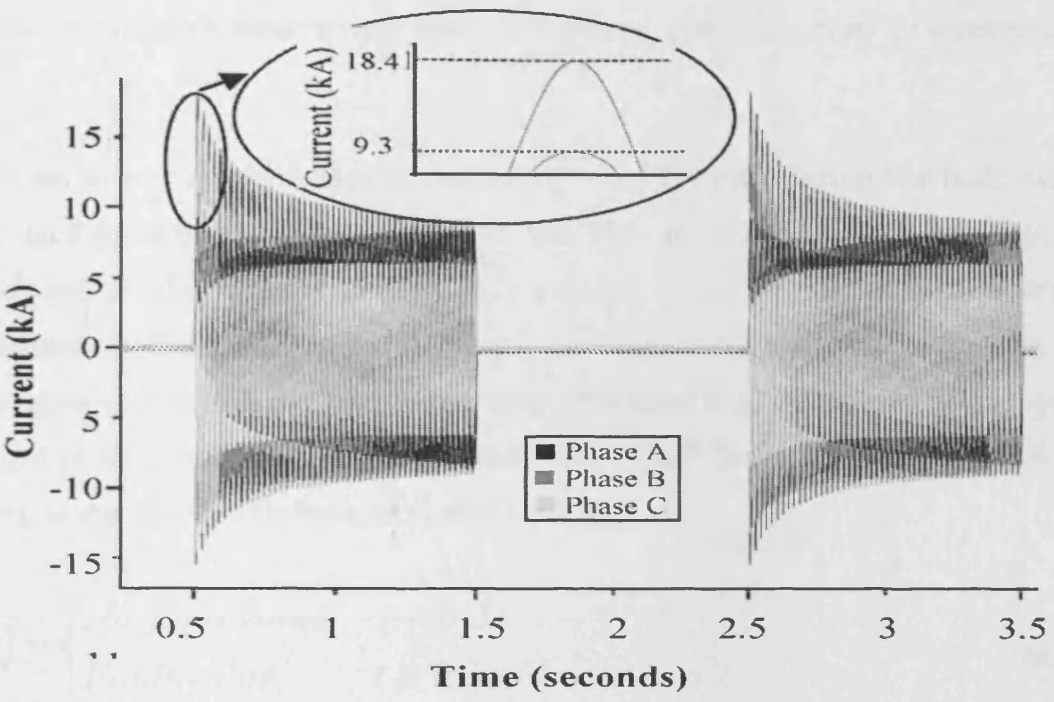

Fig. 8.14: Fault current during three phase fault with and without the FCL

It is evident that the network PSCAD model displayed the required characteristics necessary for the FCLs' deployment in the UK networks viz; device transparency under normal operating conditions, a fast response time, substantial clipping capacity, and the ability to automatically recover for repeated operation.

In general, the model results were consistent with experimental test results, within tolerable error margins, and hence could be used to represent the device in modelled power networks.

8.7. PSCAD model Comparison with VDM Model

8.7.1. Study of the Base Currents Before and After Fault Inception

After designing the PSCAD FCL model, and implementing it in an identical circuit as that is used in the VDM model, it was logical to perform a comparative study of both

models to establish their similarities, differences and limitations in modeling the FCL.

The same power network layout and values used for introducing the fault current were used in both modelling setups. In the VDM model of the FCL, the fault was introduced at the end of a current waveform cycle during normal operating conditions. In the PSCAD model it was introduced by short-circuiting the load impedance with a low resistance pathway. The total load resistance of the system changed instantaneously (from 'No Fault value'= 10^6 Ohms, to 'Fault value' = 0.08 Ohms), at the time of the fault inception (t=0.3):

$$R_{load} = \begin{cases} No\ fault\ value, & t < 0.3\,s \\ Fault\ value, & t \geq 0.3\,s \end{cases} \qquad (8.8)$$

On the other hand, the PSCAD model introduced the fault current by use of a fault module into the circuit. These different methods of fault introduction into the models constituted a possible area of disparity between the base current waveforms of the models. A look at these base waveforms in both models (without the FCL) highlighted a series of differences in the models which were examined for their effect if any, on the comparative analyses carried out for both models.

A closer view of the current waveforms at the inception of the line current shows some of the differences which exist as a result of the difference in the methods in which both model current waveforms are generated.

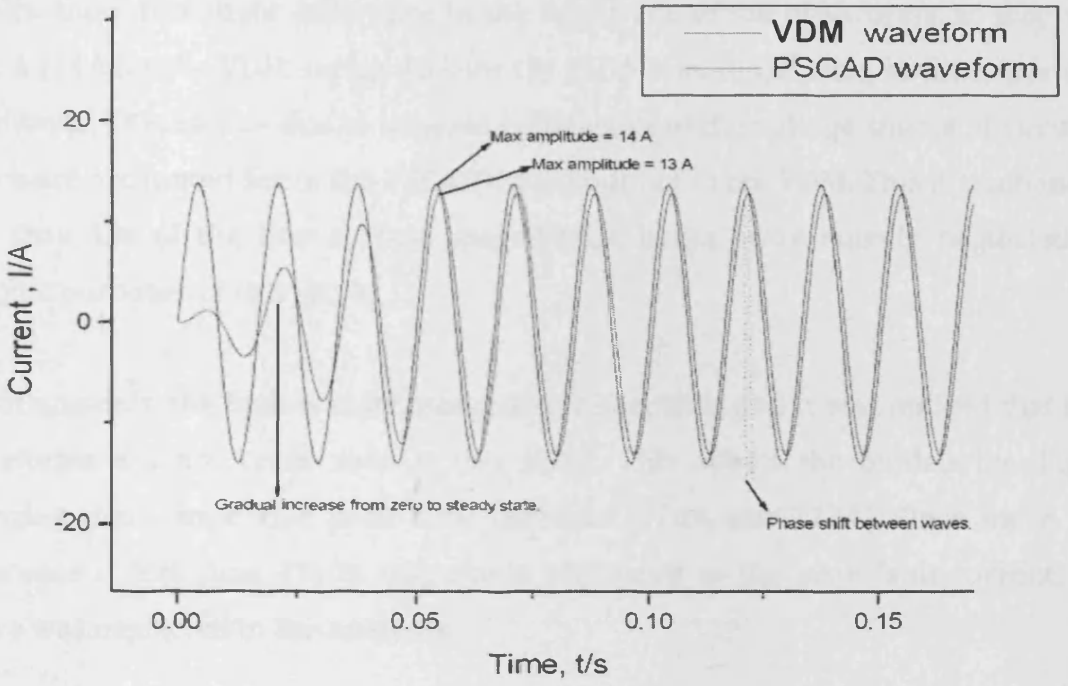

Fig. 8.15: Comparison between PSCAD and VDM waveform under normal operating conditions.

As seen in the diagram, the PSCAD model is more realistic in its representation of the base current waveform as its amplitude gradually increases into a steady state current as opposed to the VDM which starts up already in steady state. This disparity is however not significant to the analysis being carried out as it has no influence on current clipping of the FCL, as both models were allowed to get into stable state conditions before the faults were introduced.

The second noticeable difference is the slight phase shift between the two waveforms as shown in Fig. 8.14. This can be attributed to how the voltage supplies are configured and implemented in the two models. This shift is negligible when looking at the macroscopic influence of the FCL and does not significantly affect the results since the frequencies of the current waveforms in both models remain unaffected.

Finally, there is a slight difference in the amplitude of the waveforms, as they vary by 1 A (14A for the VDM versus 13A for the PSCAD model) during normal operation conditions. This can be due to internal resistances of the voltage source of circuitry, which are accounted for in the PSCAD model but not in the VDM. This discrepancy is less than 1% of the line current magnitudes, hence were equally neglected for analytic purposes of this work.

In both models, the fault was introduced at 0.3 seconds and it was noticed that both waveforms did not cross zero at this point. This affects the models by slightly changing their respective peak fault currents (270A and 272A). Once more, this difference is less than 1% in magnitude compared to the peak fault current, and hence was neglected in the analyses.

Another interesting point of investigation was the additional time that arose on the first waveforms of both models after fault inception as shown in Fig. 8.16. Because of this, the first fault wave cycle has a lower frequency than the subsequent wave cycles, although the frequency of 60Hz is supposedly determined by the power source. It was of interest that this wave characteristic was also present in the PSCAD model, confirming that it was a natural occurrence (due to change in X/R ratio), and not a problem with either of the FCL implementations.

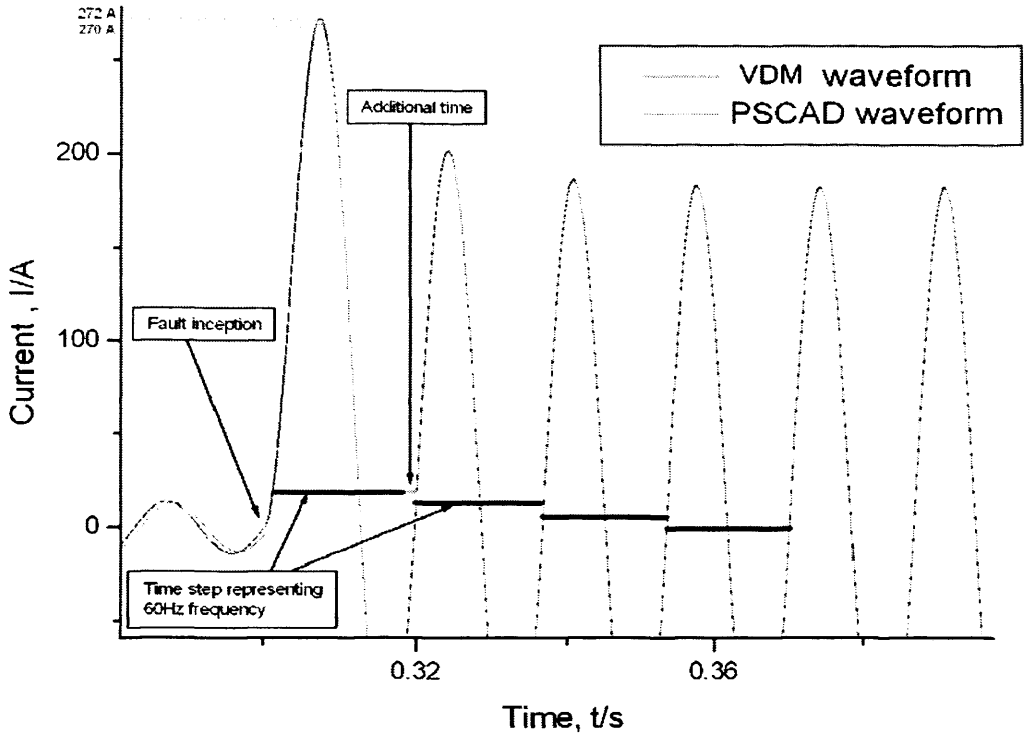

Fig. 8.16: Comparison of PSCAD and WVM after fault inception, showing first few cycles.

Unlike under normal operating conditions, there is little or no phase shift between the model waveforms after the fault in introduced. This is advantageous to the analyses as most of the interest in device performance is actually based on the fault current waveforms after fault inception.

8.7.2. Comparison Of Current Clipping Perfomance between the PSCAD and VDM Models of the FCL

After highlighting the differences in the waveforms, a comparison has been made between the clipping capabilities of both models. Both models incorporate the ACMultfac parameter (which is less than one percent of the actual magnetic field) as a way of correcting for the AC/DC field balance (which varies from model to model as seen in Chapter 5).

Given the differences introduced between the model circuits as discussed above, a new metric was developed which could be used to compare the two models while recognising their intrinsic differences. The ***clip ratio*** parameter was thus defined such that:

$$clip\,ratio = \frac{line\ current}{base\ current} \qquad (8.9)$$

This represents the capacity of each of the FCL models to clip the fault current under its own unique set of circuit circumstances. It provides a way in which the two models that are built using different software can be compared, at a particular value of the field correction parameter ACMultfac. The clip ratio is equivalent to comparing the current clipping percentage of each model, calculated from the magnitudes of the currents before and after the FCL is inserted into the circuit.

The clip ratio was used to compare both models under two conditions along the current waveform. These were during the "sub-transient" fault cycle (first cycle after fault inception), and then when the fault waveform attained steady state (taken as the fourth cycle after fault inception) as shown in Fig. 8.17.

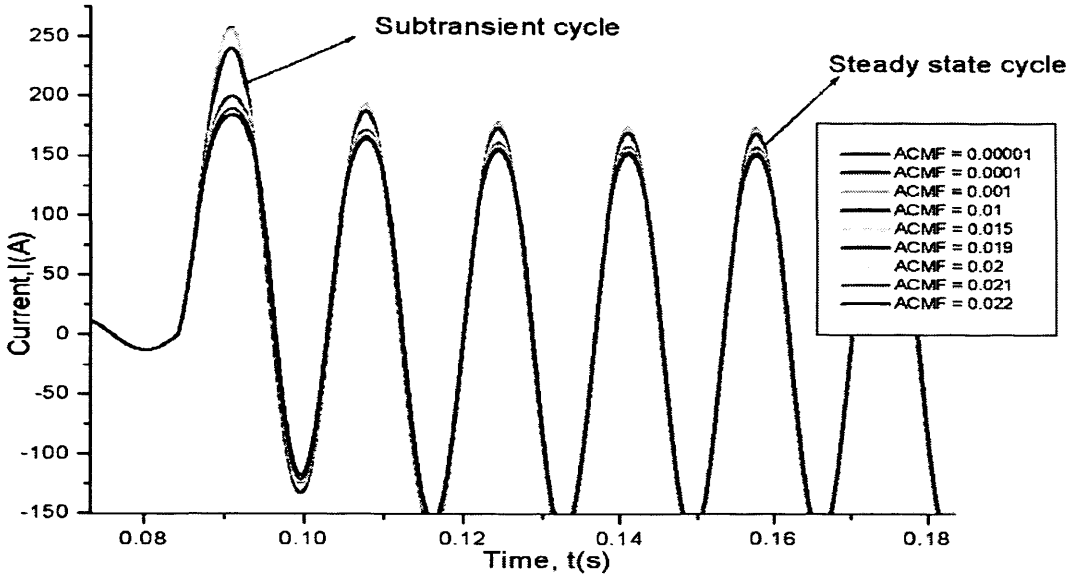

Fig. 8.17: Current waveform showing comparison regions for PSCAD and VDM FCL models at different parts of fault waveform, at different ACMultfac values.

Using Eqn. 8.8 for the clip ratio, the comparison in the Figs. 8.18 and 8.19 were performed.

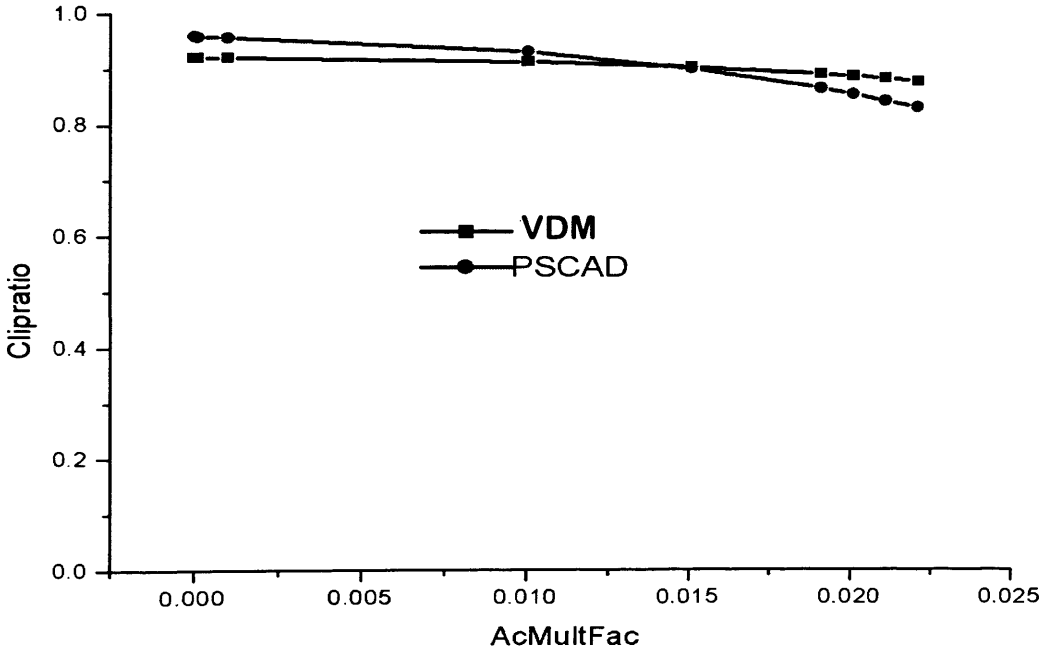

Fig. 8.18: Subtransient fault cycle comparison of the PSCAD and VDM models, showing an agreement over a range of values for the ACMultfac.

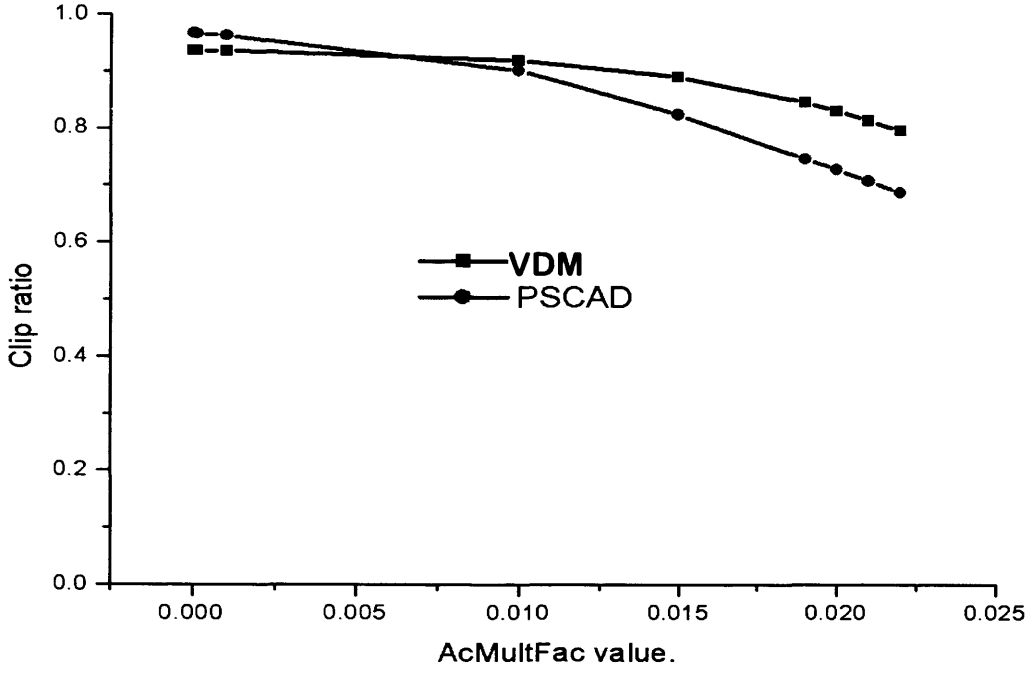

Fig. 8.19: Steady state fault cycle comparison of the PSCAD and VDM models, showing an agreement over the range of values for the ACMultfac.

This particular range of values of ACMultfac (0 to 0.022) was compared because it was the range over which visible clipping was experienced in both models, above which the models had numeric problems in dealing with the input values of the FCL modules.

Figs. 8.18 and 8.19 show a comparable relationship between the models in that their clip ratios are consistent with each other inside a small error limit. A larger deviation in the clip ratios occurs under steady state than in the subtransient region. An argument can be made that since this device is mainly concerned with clipping (limiting) the highest fault current (which occurs in the subtransient cycle and not the steady state), the effectiveness of the models should be judged at the first cycle of the fault profile.

With this assumption, it can be concluded by within the limits of the intrinsic differences of the two model circuits constructed, the two model formulations for

the FCL perform consistently with one another in the functional area defined by the ACMultfac. It also validates the methods and approximations used in each model in achieving an appropriate representation of the FCL and its performance in a power circuit.

8.8. Summary

In this Chapter, an electrical power simulator PSCAD has been used in developing a model for the FCL, and has been used in more realistic power circuitry to assess its performance. The mathematical challenges resolved in the construction of this model due to software limitations were examined, before the model was validated against measured data. The PSCAD model was then used to analyse the performance of the FCL in a real generic network. Finally, a comparative study was carried out between the two models which have been developed so far in this Thesis, in order to validate a consistency in the methods and approximations used in representing the FCL and its constitutive equations.

[1] A. Oudalov, A. Fidigatti, Microgrid Protection And Modern Protection Devices, Advanced Architectures And Control Concepts , EU-More Microgrids Report, 2009

[2] E. Lakervi, E. J. Holmes, Electricity Distribution Network Design, P. Peregrinus Ltd. Press for IEE, 2003 , Pg 115-117

[3] G.A. Putrus, M.M.R. Atimed, L. Ran, K.R Chul, And T. Funabashi, Integration Of Fault Current Limiters In Power Distribution Networks, 8th IEE Conf. on Developments in Power System Protection, Vol. 1, Pg. 311-314, April 2004

[4] W. Paul, J. Rhyner, And F. Platter, Superconducting Fault Current Limiters Based On High Tc Superconductors, IEE Colloquium On Fault Current Limiters - A Look At Tomorrow , Pg 1-4, June 1995

[5] N. Jenkins, R. Allan, P. Crossley, D. Kirschen, And G. Strbac, Embedded Generation, The Institute Of Electrical Engineers, London, UK, 2000

[6] K. Kauhaniemi, And L. Knmpnlained, Impact Of Distributed Generation On The Protection Of Distribution Networks, 8th IEE Conf. on Developments in Power System Protection, Vol. 1, Pg. 315-318, April 2004

[7] T. Burton, D. Sharpe, N. Jenkins E. Bossanyyi, Wind Energy Hand Book, John Wiley, 2001, Pg 590-592

[8] H. Schmitt, Fault Current Limiters Report On The Activities Of CIGRE WG A3.16, 2006

[9] J. R. S. S. Kumara, A. Atputharajah, J. B. Ekanayake, F.J. Mumford, Over - Current Protection Coordination Of Distribution Networks With Fault Current Limiters, IEEE Power Engineering General Meeting, 2006

[10] Franco Moriconi, Zenergy Power Inc Test Report:Zp/Tr-2008/01,2008, Pg. 89-171

[11] S. Ingram, S Probert, The Impact Of Small Scale Embedded Generation On The Operating Parameters Of Distribution Networks, P B Power, Department Of Trade And Industry (Dti), 2003

Chapter 9. Conclusions and Future Work

In this Thesis an examination of the development and application of modelling methods and the use of FEM tools in the design of an electromagnetic device – the saturable core fault current limiter (SCFCL) has been undertaken. It has resulted in two consistent models - a mathematical model (in Mathematica™) and a power electronic circuit simulator module (in PSCAD™) for this device - using expressions and electromagnetic parameters obtained from data measurements. The model development focused principally on the unique problems associated with modelling non-linear magnetic devices and proposed solutions to the challenges and shortcomings of the existing mathematical and FE tools used in investigating and improving the design of the device. Both models were proven to yield good agreement with the measurements performed on the FCL prototypes that were built and tested, and the independent application of each model gave different perspectives on the functioning of the FCL and hence provided a more complete picture of the FCL.

Furthermore, FEM analysis was used as tool for understanding the device functionality, and subsequently improving its design. FEM analysis was shown to be an adequate tool for performance analysis of the electromagnetic FCL using both transient and static solvers.

The conclusions drawn from the work have been arranged in two general categories:

9.1. Data Acquisition and Preparation for Modelling

- The conventional Ampere's Law model equation used for calculation of H is not accurate enough for modelling of novel devices which depend on non-

linear properties of electrical steels and for which the field coil is not uniformly distributed.

- A combination of measurement and modelling methods have to be used to provide a solution to this problem at high fields and high flux densities where the equation's shortcomings are most apparent.
- The analytic approximation derived here - which adds a model-specific dimension to the much used standard Ampere's law equation, combined with precise material measurement data - provides excellent agreement with the FEM calculated fields and provides an expression for faster field calculations for device design in the high field regime.
- Such solutions are device model-specific but extendable to other core designs, and give fast and accurate results which are needed in many applications.
- For extrapolation of magnetization curves to high fields the Straight Line Extrapolation (SLE) procedure shows significant discrepancy from the predictions of the other extrapolation procedures, which include more measured data and seem to give more robust solutions. Therefore, caution in using the SLE is advised for calculated extrapolations in the magnetic high field regime. Among the other extrapolation procedures, the Law of Approach to Saturation procedure (LAS) and Exponential Law Extrapolation (ELE) have been found to give better results and good agreement with each other. On this basis these are recommended for use for reliable extrapolation of magnetisation data to high fields.

9.2. Model Development Performance Analysis

- An improved model for SCFCL has been developed, with analytic expressions relating to the magnetic behaviour of the core materials. A mathematical model representing the operation of the FCL was developed in PSCAD, for

power electronics circuit simulations. The model was validated against experimental results obtained from measured values of the device prototype from testing in a medium voltage substation, for one phase and three phase faults. The results showed good agreement between measurement and simulation results.

- The real time modelling and validation of the FCL showed that the PSCAD model developed gave a valid representation of the actual device as the simulations with the model were in agreement with prototype test results within tolerable error margins. Furthermore, the installation of the FCL within the generic UK medium voltage model network displayed the required characteristics necessary for the FCLs' deployment in the UK networks .

- FEM modelling studies can be used in design improvement of electromagnetic devices such as SCFCLs. Here it proved that strategic placement of high permeability material in cores increases inductance transfer in the FCL, hence improving its efficiency and electromagnetic compatibility.

- Mathematical modelling encounters the limitations of not only the constituent equations and expressions for the device materials being approximate, but also the intrinsic mathematical capacity of the platform in which they are built (as shown with the a-parameter and singularity problems). Hence consistency in usage of the same software provides a continuity and consistency necessary in building good electromagnetic models.

9.3. *Future Work*

- More analysis should be carried out on the proposed analytic function for the H-field distribution in closed cores to improve on the first approximation for the shape function. Further tests, including different core sizes and shapes, should result in a better approximation for this function, making it less model specific and hence more applicable to a range of magnetic closed cores.
- In the mathematical VDM model for the FCL, incorporation of hysteresis is essential as this will improve the accuracy of the general model. It will also increase the range of applicability of the model to include other magnetic materials which for which the use of anhysteretic representation cannot be considered sufficient.
- Further work to investigate FCL characteristics during operation in different power network scenarios to ascertain their usefulness and compatibility with existing protection equipment should be done. These should include testing the component in different locations of the network, or simulating the fault at a number of additional locations on the network, relative to the FCL position to determine the FCL location of maximum efficiency in the power grid.
- Given the suggestion of the generalised inductance equation derived in Chapter 7 (Eqn. 7.7) that the inductance can be improved with an increase in the spatial permeability of the core, a study should be conducted to investigate this further. This will involve FEM studies and the construction of a composite core with materials of increasing permeability stacked on one another in the direction of the applied field. This should improve the inductance gain of the core and consequently the performance of the FCL.

APPENDIX 1

FORTRAN Subroutine code for PSCAD model, showing implementation of constituent functions to produce variable inductance.

! Variable Definition

```
#LOCAL REAL Hm,#LOCAL REAL Hp,#LOCAL REAL Hma, #LOCAL REAL Hpa
#LOCAL REAL Hm2,#LOCAL REAL Hp2,#LOCAL REAL Bsmu,#LOCAL REAL Inva
#LOCAL REAL IndA,#LOCAL REAL IndB,#LOCAL REAL Indtotal,
#LOCAL REAL Indconst,#LOCAL REAL Ind,#LOCAL REAL pi,#LOCAL REAL a1,#LOCAL REAL
a2#LOCAL REAL a3,#LOCAL REAL a4,#LOCAL REAL b1,
#LOCAL REAL b2,#LOCAL REAL b3,#LOCAL REAL b4,#LOCAL REAL Ms,
#LOCAL REAL test,#LOCAL REAL muo,#LOCAL REAL as,#LOCAL REAL Bs,
#LOCAL REAL xacA,#LOCAL REAL xdcA
```

! Module constants

```
muo= 0.0000012566,as = 1.5,Bs = 2.01,pi = 22/7,Ms = 120029.51694,
a1 = -0.09186,a2 = 0.10459,a3 = -0.02272,a4 = 0.00199,b1 = -0.16728
b2 = 0.01735 ,b3 = -0.00184,b4 = 0.00018 ,xacA = 0,xdcA = 2.4379
```

! Field distribution profiles

```
$Hac=($NacA*$CurA/$HacCA)*(($HacCA+2*xacA)/(2*($DiaACA**2+($HacCA+2*xacA)**2)**0.5)+
($HacCA-2*xacA)/(2*($DiaACA**2+($HacCA-2*xacA)**2)**0.5))
```

! DC field profile including form shape function

```
$Hdc=80000 !((0.03*$Imax
+0.3)*$NdcA*$IdcA/$HdcCA)*(($HdcCA+2*xdcA)/(2*($DiaDCA**2+($HdcCA+2*xdcA)**2)**0.5)+
($HdcCA-2*xdcA)/(2*($DiaDCA**2+($HdcCA-2*xdcA)**2)**0.5))

Hm=$Hdc-$Hac
Hp=-$Hdc-$Hac
Hma=Hm/as
Hpa=Hp/as
Hm2=as/Hm**2
Hp2=as/Hp**2
Bsmu=Bs/muo
Inva=1/as
Indconst=(muo*$AacA*$NacA**2)/$lA  ! (Inductance constant
test = b2*Hm**2
```

! Induction equation using Lorentzian fit for material permeability curve.

```
IF (Hm.GE.0) THEN

 $IndA = Indconst*((Ms*((1 + b1*Hm + b2*(Hm)**2 + b3*(Hm)**3 + b4*(Hm)**4)*(a1 + Hm*(2*a2 +
Hm*(3*a3 + 4*a4*Hm)))-(1 + a1*Hm + a2*(Hm)**2 + a3*(Hm)**3 + a4*(Hm)**4)*(b1 + Hm*(2*b2 +
Hm*(3*b3 + 4*b4*Hm)))))/(1 + b1*Hm + b2*(Hm)**2 + b3*(Hm)**3 + b4*(Hm)**4)**2 + 1)
```

```
ELSEIF (Hm.LT.0) THEN

$IndA = Indconst*((Ms*((1 + b1*(-Hm) + b2*(-Hm)**2 + b3*(-Hm)**3 + b4*(-Hm)**4)*(a1 + (-
Hm)*(2*a2 + (-Hm)*(3*a3 + 4*a4*(-Hm))))-(1 + a1*(-Hm) + a2*(-Hm)**2 + a3*(-Hm)**3 + a4*(-
Hm)**4)*(b1 + (-Hm)*(2*b2 + (-Hm)*(3*b3 + 4*b4*(-Hm))))))/(1 + b1*(-Hm) + b2*(-Hm)**2 + b3*(-
Hm)**3 + b4*(-Hm)**4)**2 + 1)

ENDIF

IF (Hp.GE.0) THEN

$IndB = Indconst*((Ms*((1 + b1*Hp + b2*(Hp)**2 + b3*(Hp)**3 + b4*(Hp)**4)*(a1 + Hp*(2*a2 +
Hp*(3*a3 + 4*a4*Hp)))-(1 + a1*Hp + a2*(Hp)**2 + a3*(Hp)**3 + a4*(Hp)**4)*(b1 + Hp*(2*b2 +
Hp*(3*b3 + 4*b4*Hp)))))/(1 + b1*Hp + b2*(Hp)**2 + b3*(Hp)**3 + b4*(Hp)**4)**2 + 1)

ELSEIF (Hp.LT.0) THEN

$IndB = Indconst*((Ms*((1 + b1*(-Hp) + b2*(-Hp)**2 + b3*(-Hp)**3 + b4*(-Hp)**4)*(a1 + (-
Hp)*(2*a2 + (-Hp)*(3*a3 + 4*a4*(-Hp))))-(1 + a1*(-Hp) + a2*(-Hp)**2 + a3*(-Hp)**3 + a4*(-
Hp)**4)*(b1 + (-Hp)*(2*b2 + (-Hp)*(3*b3 + 4*b4*(-Hp))))))/(1 + b1*(-Hp) + b2*(-Hp)**2 + b3*(-
Hp)**3 + b4*(-Hp)**4)**2 + 1)

ENDIF

$Indt=$IndA + $IndB

IF($EnabA.EQ.0) THEN

$Ind = 0.000000001

ELSE

$Ind=$Indt

ENDIF
```

APPENDIX 2

PSCAD screen snapshot of FCL module test network, showing 3-phase control and introduction of FCL on circuit. Two circuits used with and without FCL.

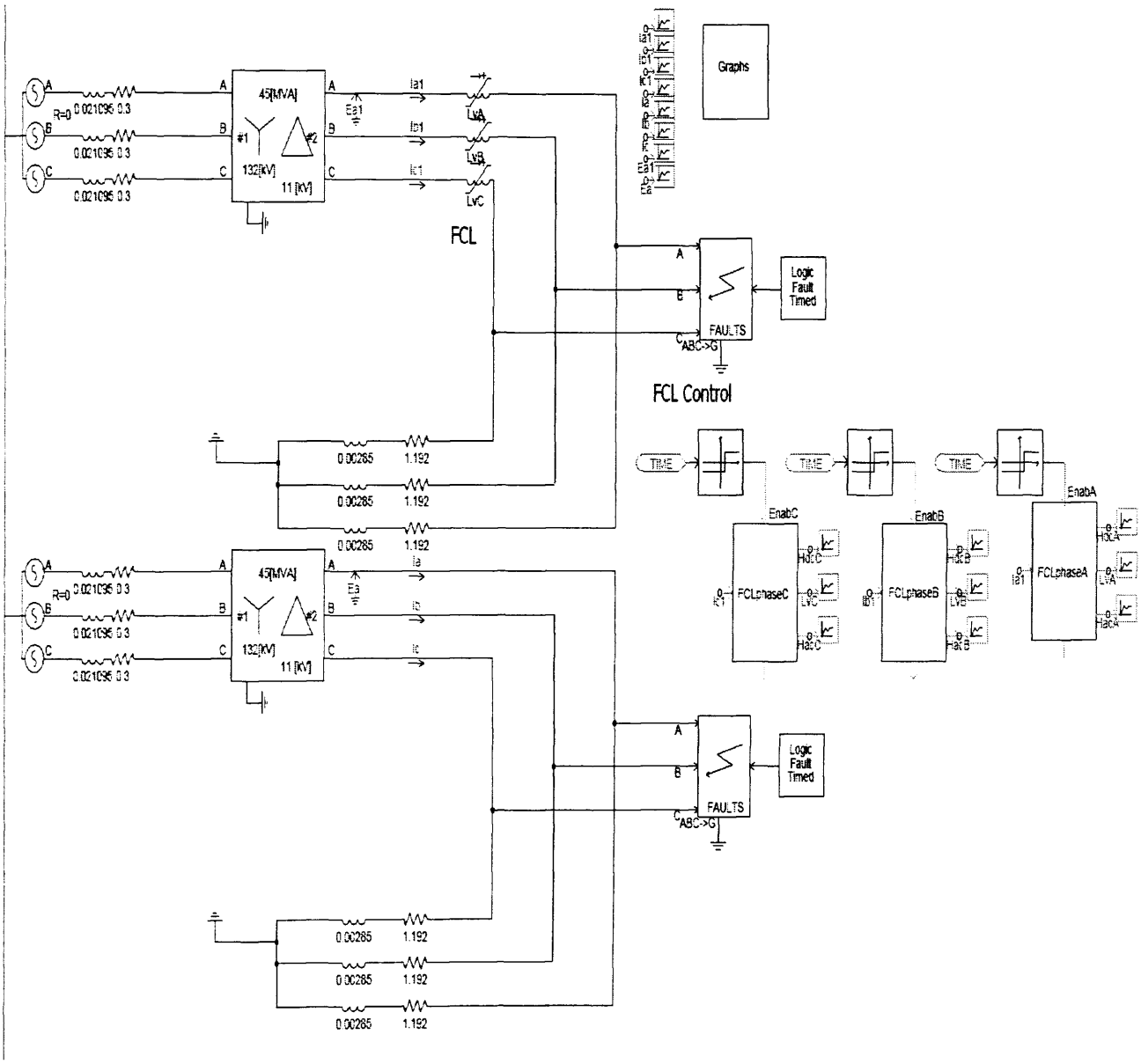

APPENDIX 3

1. Publications

- Effectiveness of a New Inductive Fault Current Limiter Model in MV networks, ***A. E. Umenei, P. Papadopoulos, I. Grau, R. Williams, L. Cipcigan, Y. Melikhov, IEEE 45th UPEC 2010, August 2010, Pg. 1-5.***

- Analytic Solutions for Variations of Magnetic Fields in Closed Circuits: Examination of Derivations from the 'Standard' Ampere's Law Equation, ***A. E. Umenei, Y. Melikhov, D.C. Jiles, (Accepted for publication), IEEE Trans. Magn., 2010.***

- Methods of Extrapolation of Magnetisation Data on Magnetic Cores to High Fields, ***A. E. Umenei, Y. Melikhov, D.C. Jiles, (Submitted for publication), IEEE Trans. Magn., 2010.***

2. Conference Papers

- Development of Field Coils for Diagnostic Applications of Transcrannial Magnetic Stimulations, ***D. C. Jiles, P.I. Williams, A.E. Umenei, P. Marketos and L. Crowther, XVth International Workshop on Electromagnetic NDE, Poland, June 2010.***

- Modelling, Validation and Implementation of Non-linear Magnetic Switching for Device Application, ***A. E. Umenei, Y. Melikhov, D.C. Jiles, 55th Annual Magnetism and Magnetic Materials Conference, Atlanta, Georgia, November, 2010*** .

- Improved Model for Inductive Switching Devices In Power systems, ***A. E. Umenei, Y. Melikhov, D.C. Jiles, GW-05, Pg. 275, 11th Joint InterMag/MMM conference, Washington DC, January 2010.***

- Modelling of Improvement in Impedance Transfer for Inductive Switching Devices, using high permeability soft materials , ***A. E. Umenei, Y. Melikhov, D.C. Jiles,*** **H2-22, 19th Soft Magnetic Materials conferenc , Torino, Italy, September 2009.**

- Design and Modeling of Improved Functionality, of Switching Inductive Devices using Non-linear Behaviour of Core Materials, ***A. E. Umenei, Y. Melikhov and D.C. Jiles, FU-08. InterMag Conference, Sacramento, California, May 2009.***

- Variation of Magnetic H-field in Closed-loop Magnetic Circuits: Problems with the Ampere's Equation. ***A. E. Umenei, Y. Melikhov, D.C. Jiles, http://meetings.aps.org/link/BAPS.2009.MAR.W32.13, American Physics Society Conference, Pitssburgh, March 2009.***

- Modelling of the Analytic Approximation of Magnetic Properties at High Magnetic Fields in Electrical Steel Cores, ***A. E. Umenei, Y. Melikhov, S. Zurek, D.C. Jiles, 53rd Annual Magnetism and Magnetic Materials Conference, Austin, Texas, November, 2008*** .

- Measurement and Modelling of Magnetic Properties of Electrical Steels at High Flux Densities, ***A. E. Umenei, S. Zurek, Y.Melikhov, D. C. Jiles, International Workshop on 1 & 2 Dimensional Magnetic Measurement and Testing (2DM) Cardiff, Wales, UK, 2008.***

- Modelling of Magnetic Inductive Fault Current Limiters, ***A. E. Umenei, Y. Melihkov, S. Zurek, D.C. Jiles, Speaking of Science Conference, Cardiff University, Cardiff, UK, 2008.***

APPENDIX 4 : PAPER 1

(Accepted for publication in UPEC Conference Proceedings 2010)

Effectiveness of a New Inductive Fault Current Limiter Model in MV networks

A.E. Umenei, P. Papadopoulos, I. Grau, R. Williams, L. Cipcigan, Y. Melikhov

*Email:umeneiae@cf.ac.uk, papadopoulosp@Cardiff.ac.uk

***Abstract*- A realistic model for a novel saturable core superconducting FCL (SCFCL) prototype is presented, and incorporated into time-domain power simulation software PSCAD™/EMTDC™. The present work incorporates non-linear material properties data of the magnetic core with inductance to produce a limiting effect on the line current in real time. The novelty of this core design is the inclusion of a superconducting material as the magnetisation DC coil to saturate the core, instead of using the superconductor directly within the magnetic circuit. The FCL model's accuracy was validated against experimental test results, and its performance analysed by its placement in a UK generic network at MV level. Implementation simulations showed the device could achieve a 50% current clipping capacity, when placed in an MV network. Other standard FCL tests were performed on this model and their results presented.**

Index Terms—Distribution Networks, PSCAD™/ EMTDC™, Superconducting Fault Current Limiter

I. INTRODUCTION

Distribution networks are generally divided into zones which contain protective equipment that is responsible for the protection of the zone [1]. This switchgear equipment aims to prevent distribution network component overstress or failure, by maintaining the quality of power that is supplied to customers whilst considering the safety of personnel[2].

The continuous growth of the electricity demand corresponds to an increase in short circuit currents [3, 4]. The penetration of Distributed Generation (DG) poses challenges for the protection coordination of passive networks [5], one being their contribution to fault currents. Although inverter based DG may contribute limited fault currents, synchronous DG systems may feed higher sustained currents if they lack control capabilities through the use of power electronic interfaces [6]. Induction generators fail to sustain a high fault current due to the absence of self-excitation system [7].

A questionnaire based survey from CIGRE WG A.310, acquired 53 responses from 14 countries from which 84% identified the need for current limitation in HV or MV levels [8]. A number of techniques exist to limit the fault currents: (i) network splitting, (ii) use of current limiting reactors or high impedance transformers, (iii) sequential network tripping, (iv) switchgear uprating and (iv) use of Fault Current Limiters (FCLs) [9]. The first four techniques are considered to decrease flexibility and increase the cost and complexity [10]. FCLs are considered as a promising emerging technology. The advantages that FCLs offer and the different technology types together with the preferred network locations they can be installed are well documented in [11].

A saturable core superconducting inductive FCL has been developed by Zenergy Inc.[12]. Primary experimental testing has been completed, and installation of the device onto the Southern California Edison grid has been carried out with promising results [13]. A PSCAD™/EMTDC™ dynamic model of the device was developed to simulate the behaviour of the actual prototype. The novelty of this core design is the inclusion of a superconducting material as the magnetisation DC coil. This produces the magnetisation field necessary to saturate the core, instead of using the superconductor directly within the magnetic circuit. The approach harnesses the power of the superconductor in producing high magneto motive forces with smaller coils (relative to standard copper coils), while circumventing the many problems related to superconducting coils used in magnetic circuits [14].

Section II discusses the requirements for ideal FCLs and presents electromagnetic considerations used in building the FCL model. Two sets of study cases were used to gauge the performance of this FCL model within PSCAD™/EMTDC™. The first set of simulations is a validation test for the model, compared to experimental results from the actual FCL prototype. The second set of performance analysis simulations was based on a UK generic network to evaluate the behaviour of the FCL model in a UK representative distribution network.

II. FAULT CURRENT LIMITERS

A. Overview and criteria

Fault Current Limiters are devices which are connected in series to power lines in order to limit the fault current to network specific acceptable levels. This is done by an increase of their impedance. When this impedance is low during normal operating conditions and increases only during the fault, the device is theorised as active. FCLs are generally categorised into transmission and distribution

ll this components were combined in the physical quations governing the FCL function to produce and nalytic model which is easy to use and fast in its alculations and integration in external systems. Fig. 1 resents a schematic diagram of the control module and its onstituent input and output components.

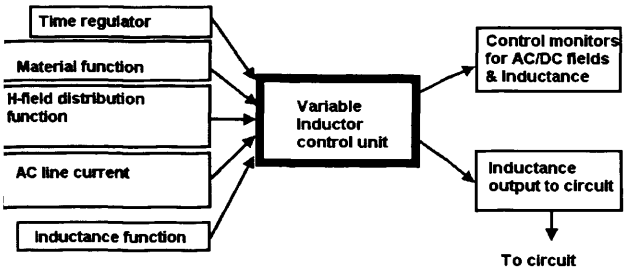

ig.1: FCL model schematic showing components input and output omponents.

II. CASE STUDIES

Two sets of simulations were carried out with the model - a validation set, and a performance set of simulations. ,. n the first set , experimental data was obtained from a real mplementation of the FCL (base capacity tests), and the nodel was tested by comparing the experimental and the imulated results.

I. *FCL model testing and validation.*

The simplified system where the validation experiments vere conducted comprises a 45-MVA, 132/11-kV ransformer connected to a common bus bar supplying a nixture of several domestic and industrial feeders. The esults were obtained from a proof-of-concept set of tests arried out by the company (*see* **). The single line liagram for the setup used, is shown in Fig.2.

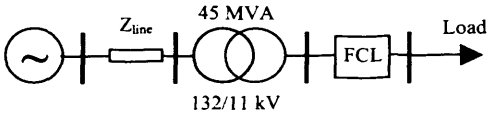

ig 2. Single line diagram of validation test network.

The experimental procedure included a large range of ests, six of which are shown in Table II. These tests were luplicated in simulation as closely as possible (exact umbers were not achieved due to possible impedances in eal network which were unaccounted for in testing eport), using the FCL model, to examine the behaviour of he model for the simulated network. This was in order to est the **minimum limiting capacity** of the FCL at lifferent current levels for the particular circuit.

Multiple fault tests were experimentally conducted, long with insertion impedance testing, to confirm that the oltage drop of the device was within industrial standards. For this specific device, the voltage drop ratio was 0.8% of the line voltage.

TABLE II
FCL TESTING EXPERIMENTAL AND SIMULATED RESULTS

Experimental Results				
Test	*Line X/R ratio*	*Peak Phase Prospective Current (kA)*	*Maximum Clipped Current*	*Peak Clipping (%)*
1	22.9	7.4	6.2	11.1
2	19.8	20.8	18.7	10.2
3	19.7	31.4	27.6	12.2
4	26.3	40.3	20.9	15.1
5	21.6	52.4	43.5	16.8
6	44	63.1	53.1	15.7
Simulation Results				
Test	*Line X/R ratio*	*Peak Phase Prospective Current (kA)*	*Maximum Clipped Current*	*Peak Clipping (%)*
1	22.9	6.6	6.15	9.9
2	19.8	21.3	18.7	11.5
3	19.7	31.94	27.54	13.8
4	26.3	39.85	34.36	14.6
5	21.6	50.81	43.38	1.8
6	44	60.1	51.07	15.02

** EXPERIMENTAL RESULTS COURTESY ZENERGY POWER INC.

Table II shows good agreement between the simulated and experimental results, where all recorded values were within a 4% error margin. Differences between the actual material and its modelled representation, coupled with the inherent differences in the circuit simulation and the real-time testing conditions, can be cited for the disparities noticed in the values. In this research work, silicon steel was used as the core material from which the material parameters were obtained.

B. *Application of SCFCL in the UK Generic Network*

A UK radial MV generic network was used to evaluate the behaviour of the SCFCL model. This specific distribution network serves 18,432 residential consumers, through a primary substation of 33/11.5 kV. The fault current levels of the modelled network were computed and verified towards the simulation results published in [21]. Details of the model parameters can be found in [21]. Fig. 3 provides the network schematic.

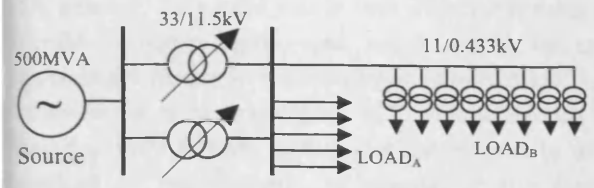

LOAD$_A$ = Lumped 11.5kV feeder
LOAD$_B$ = Domestic lumped loads

Fig. 3. UK Generic LV Distribution Network

Distribution Network Operators (DNOs) usually require wind farms to be connected at 11 kV voltage level [22]. Conventionally, DG connections at 11kV voltage level are limited to 5MW [23]. In this paper, an equivalent DG model of 4.5MW was connected to the 11kV substation busbar. The FCL's location is shown in Fig. 4. This location was selected to limit the fault current contribution from both the grid infeed and the DG. This way, a new DG installation combined with FCL installation could defer existing switchgear updates.

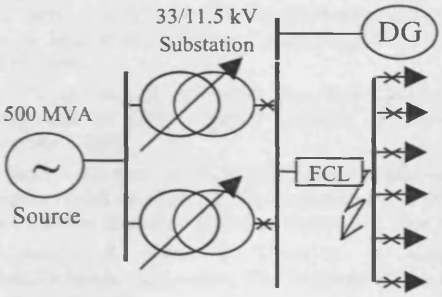

Fig. 4. Schematic of the simulated network

IV. RESULTS AND DISCUSSION

The On Load Tap Changer (OLTC) mechanisms of the transformers shown in Fig. 4 are adjusted to keep the voltage between 1 and 1.01 p.u. [21]. The first requirement tested for, was the transparency of the device in realtime, because the voltage drop caused by an FCL during normal operating conditions is of great importance for the utilities. The model showed negligible voltage drop (i.e. approximately 0.5%) during normal operating conditions. Fig. 5 shows the voltage (RMS) during a three phase fault with and without the FCL model. The measurement was taken in the position of the fault (Fig. 4).

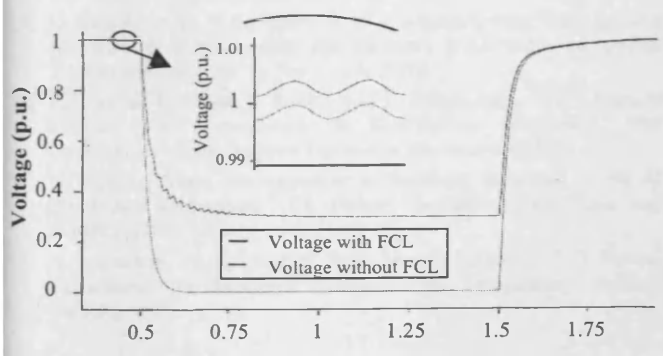

Fig. 5. Voltage drop during a three phase fault

Maximum clipping capacity was then tested for as the three phase fault was simulated with the FCL in the network, to evaluate the behaviour of the model during a fault. The first peak short circuit current was clipped by approximately 50% in less than 7 μseconds as shown in the Fig.6 inset. This showcases not only the SCFCLs ability to clip a large percentage of the current, but it does so in the first half cycle, thereby enabling other protection equipment to function normally.

A test for repeatability and reliability constituted of simulating a double fault with a 1s interval. This test was to analyse the model's ability to provide fast recovery for multiple operations. Fig. 6 shows the results of a multiple operation test, with the SCFCL not suffering any loss in performance.

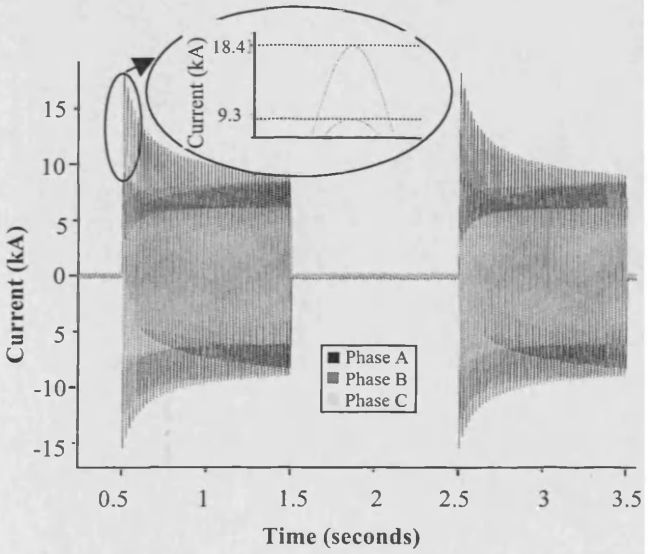

Fig. 6. Fault current during three phase fault with and without the FCL

V. CONCLUSIONS

It is evident that FCL technology can be used to mitigate the fault current levels within a network. Results obtained from the individual case studies of the modelled SCFCL show that; (i) the FCL model used during the simulations was a valid representation of the actual device, and (ii) the installation of the FCL within the generic UK Distribution Network model displayed the required characteristics necessary for the FCLs' deployment in the UK networks viz; device transparency under normal operating conditions, a fast response time, substantial clipping capacity, and the ability to automatically recover for repeated operation.

In general, the model was in line with test results, within olerable error margins, and hence could be used to epresent the device in modelled power networks.

Further work to investigate FCL characteristics during peration may include testing the component in different locations of the network, or simulating the fault at a number of additional positions relative to the FCL device.

VI. ACKNOWLEDGEMENT.

Special thanks for Franco Moriconi of Zenergy Power Inc. for providing 'base capacity' results of experimental tests on the prototype SCFCL.

VII. REFERENCES

[1] A. Oudalov, and A. Fidigatti, "Microgrid protection and modern protection devices, Advanced Architectures and Control Concepts for More Microgrids", 2008.

[2] E. Lakervi, and E. J. Holmes,*Electricity Distribution Network Design,* Institution of Electrical engineers, 2005, pp 115-117, ISBN 0863413080.

[3] G.A. Putrus, M.M.R. Atimed, L. Ran, K.R Chul, and T. Funabashi, "Integration of Fault Current Limiters in Power Distribution Networks", 2004.

[4] W. Paul, J. Rhyner, and F. Platter, "Superconducting Fault Current Limiters Based on High Tc Superconductors", *IEE Colloquium on Fault Current Limiters - A look at Tomorrow,* June 1995, pp 1-4.

[5] N. Jenkins, R. Allan, P. Crossley, D. Kirschen, and G. Strbac,*Embedded generation,* The Institute of Electrical Engineers, London, UK, 2000.

[6] K. Kauhaniemi, and L. Knmpnlained, "Impact of Distributed Generation on the Protection of Distribution Networks", 2004.

[7] T. Burton, D. Sharpe, N. Jenkins E. Bossanyyi, *Wind Energy Hand Book,* John Wiley, 2001, pp 590-592.

[8] H. Schmitt, "Fault Current Limiters Report on the Activities of CIGRE WG A3.16", 2006.

[9] J. R. S. S. Kumara, A. Atputharajah, J. B. Ekanayake, and F.J. Mumford, "Over Current Protection Coordination of Distribution Networks with Fault Current Limiters", 2006.

[10] A. J. Power, "An Overview of Transmission Fault Current limiters", 1995,pp 1/1 -1/5.

[11] CIGRE WG A3.10 "Fault Current Limiters, Report on the activities of CIGRE WG A3.10 ", 2003.

[12] S.B. Abbott, D. A. Robinson, S. Perera, F. A. Darmann, C. J. Hawley, and T. P. Beales, "Simulation of HTS saturable core-types FCL for MV distribution systems", *IEEE Trans. Power Delivery,* vol. 21, pp.1013, 2006.

[13] L. Sanford , 'First FCL goes in US grid', Modern Power Systems, www.modernpowersystems.com,May 2009.

[14] L. Salasso et al., ' Comparison of superconducting fault limiting conceopts in electric utility applications', IEEE trans. on applied Superconductors, Vol. 5, No. 2, june 1995.

[15] R.Parashar, C. Sasse, R. Banks, and L. Falkingham, "Fault Current Limiters For Transmission & Distribution Networks", *18th International Conference on Electricity Distribution,*2005.

[16] S. Ingram, "New Technologies to facilitate increased levels of Distributed Generation." PB Power. Department of Trade and Industry (DTI), 2006.

[17] A. Neumann, Application of fault current limiters, P B Power, Department for Business Enterprise and Regulatory Reform (BERR), 2007.

[18] B. Marchionini, N. K. Fall, andM. Steurer, "An Assessment of Fault Current LimiterTesting Requirements", *U.S. Department of EnergyOffice of Electricity Delivery and Energy Reliability,* 2009.

[19] M. Steurer, "New IEEE Task Force on Fault Current Limiter Testing", Presented during the DOE HTS Peer Review onAug 4-6, 2009, Alexandria, VA.

[20] J. Jäger,"Interaction Between Fault Current Limiters andProtection - A Glance at the Final Report ofCIGRE WG-A3.16", 2006.

[21] S. Ingram, and S Probert, "The impact of small scale embedded generation on the operating parameters of distribution networks", P B Power, Department of Trade and Industry (DTI), 2003

[22] Ecotricity Wind Turbine at Swaffham: A Connection Case Study, West Green Associates, Department of Trade and Industry (DTI), 2000.M. Mac Donald, 2004, "Innovation in electricitydistribution networks", *OFGEM report 212281.*

APPENDIX 5: PAPER 2

(Accepted for publication in IEEE Trans. Mag. 2010)

Analytic Solution for Variations of Magnetic Fields in Closed Circuits: Examination of Deviations from the 'Standard' Ampere's Law Equation

A. E. Umenei, Y. Melikhov, and D.C. Jiles

Wolfson Magnetics Research, School of Engineering, Cardiff University, CF24 3AA, Cardiff, United Kingdom

The calculation of magnetic fields in devices with a non-uniform distribution of magnetomotive force (mmf) and with nonlinear magnetic components has proven problematic within electromagnetic systems. This is caused by insufficiently precise determination of the dependence of magnetic induction B, on magnetic field H. This paper develops a method for analytically calculating the variation of magnetic fields H, in magnetic circuits by introducing a specific expression into the Ampere's Circuital Law formula to take into account non-uniform mmf. The new formula uses a conformal mapping procedure which allows calculation of the magnetic field at different displacements from the field generating coil. The analytic approximation proposed is developed for the specific problem of a closed circuit magnetic core. This analytic model gives accurate results faster than can be achieved in FEM software.

Index Terms—**Magnetic field distribution, ferromagnetic cores, FEM simulation, Ampere's Law equation, magnetic modeling.**

I. INTRODUCTION

With the expanding demands on the power industry, more magnetic materials are being used in the manufacture of equipment needed to meet the ever increasing energy demands. These demands in turn place great significance on the quality and the efficiency of power related devices. Requirements such as the accuracy in measuring magnetic properties – B-H characteristics – at very high magnetic fields of electrical steels - have become more important, to improve the design and functioning of electromagnetic devices like transformers and fault current limiters. One of the principal predictive tools used in this regard is Finite Element Modeling (FEM) which requires meshing of the spatial domain, including the device and surrounding air boundaries, and providing solutions in 3D. The accuracy of FEM simulations of electromagnetic devices is affected by the quality of nonlinear magnetic information input into the software model. The method is also time consuming [1-2]. Also, challenges are encountered in attempts to fit laboratory measurements to model equations for the purposes of mathematical modeling of such devices.

Ampere's law equation, which is widely used in field calculations [3], and which has even been generalized to take into account effective fields due to stress [4], has been found to be lacking, at least in the form that is normally used, especially when applied to large magnetic core field distributions in these devices, when the mmf is not evenly distributed. This paper describes this problem as found in non-uniform mmf (magneto motive force) magnetic cores, and proposes an analytic method of calculating such fields with extensions to Ampere's law equation.

II. AMPERE'S LAW

Ampere's circuital law in materials provides a relationship between the magnetic field H around a current carrying conductor and its current source. In integral form, [5]

$$\oint_C H \,.\, dl = I \tag{1}$$

where I is the current in the conductor, and integration is performed over a closed path C enclosing the conductor. If we assume that there are N such conductors arranged in a form of a long thin solenoid, the magnetic field H produced in the centre of the solenoid is uniform throughout the whole length L of the solenoid, so Eqn. 1 becomes

$$H = \frac{N.I}{L}. \tag{2}$$

Eqn. 2 is the usual 'standard' of Ampere's law derivation used in most engineering applications. In the characterization of materials, it is usual to maintain good uniformity of magnetization over a closed path of the material. A commonly used method for ensuring uniform mmf, and therefore applicability of Eqn. 2, is by making the solenoid toroidal in shape, hence wrapping it completely around the magnetic core material [6]. While this process yields good results, it suffers from the major drawbacks of tedious preparation of such circuits, and the stresses that could be induced on the core materials due to bending.

lence it is not the usual technique used in laboratory measurements or in the design of electromagnetic devices in industry. The more practical standard Epstein frame configuration is preferred for magnetic material measurements, which maintains these uniform fields by having the coils wound on each of the core limbs. The field remains relatively uniform except around the edges of such configurations.

Practical cores in devices on the other hand, generally do not have this uniform distribution due to the location of the energizing coils and device design in general. With uneven mmf in such cases, a non-uniform field profile around the core is a consequence, and Eqn. 2, which his widely employed for such calculations, cannot be used.

This failure is even more significant in terms of the error magnitudes when calculations are needed in higher field regimes for simulation or design for power devices such as transformers and fault current limiters. The fact that in such devices the mmf produced by the applied current source is non-uniform and non-local, applying Eqn. 2 to field calculations or measurements for such devices that require accurate values for magnetic field for their proper calibration and functioning, can lead to significant error in design and prototyping. A careful look into this problem and a proposal for a more realistic variation of Ampere's law, to improve the accuracy of such calculations is the focus of this work.

II. Problem Discussion with Experimental Results

The Amperian approach to field generation is most commonly used in laboratory closed circuit measurements for ferromagnetic materials, due to their practicality and the ease of current-controlled field generation [5]. In some device models, the exact spatial field distribution variation along their component cores is needed for calculations such as inductance and magnetic induction, *B*. A common element of such devices is the magnetization of the steel cores by a localised magnetizing coil that doesn't extend over the entire core. This results in non-uniform mmf around the core, and hence uneven field distribution across the cores, thus violating the principal assumptions of the Ampere's law derivation, Eqn.2. Furthermore, most field calculations using this standard derivation are made with the magnetizing coil as a reference point instead of at the point where the electromagnetic interactions in the device take place, for example, in inductance calculations on transformers. Consequently, for larger ferromagnetic cores, the field distribution can become highly non-uniform and hence vastly different from the analytically calculated values using Eqn. 2. Measurements taken on such cores in the laboratory or industry, using the Ampere's law derivation (Eqn. 2) erroneously assume the law works for such cases, and hence a major source of error in magnetic measurements is overlooked.

To illustrate the problem, a scaled-down prototype of a ferromagnetic core stack was built with standard laminated Epstein-size strips of M4 non-oriented steel, 30x3x0.03 cm each. The core was 3 cm thick. Only one limb had a magnetizing DC coil around it, referred to as the magnetizing limb. Search coils (SC) were wrapped at various points around the length of the core as shown in Fig. 1. A similar model was built in FEM to reflect the locations of the search coils as included on the prototype. The field distribution was taken as a function of displacement, x, around the core from the FEM calculated model, while the field values as specific points on the prototype were measured with search coils as shown in Fig 1.

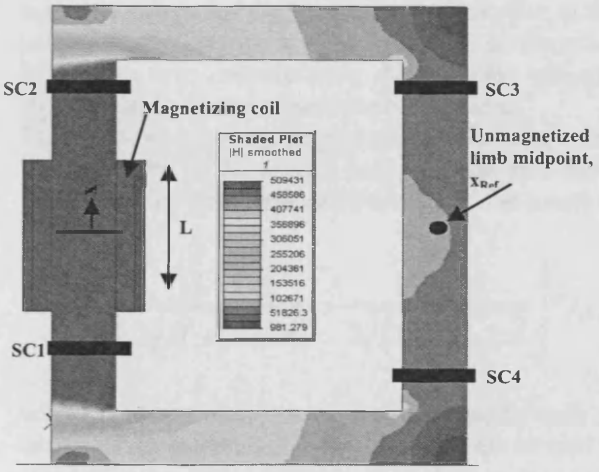

Fig. 1: FEM snapshot of magnetic field in a core taken on slice though middle of core model, showing model of actual constructed prototype with difference in H-field distribution on opposite limbs.

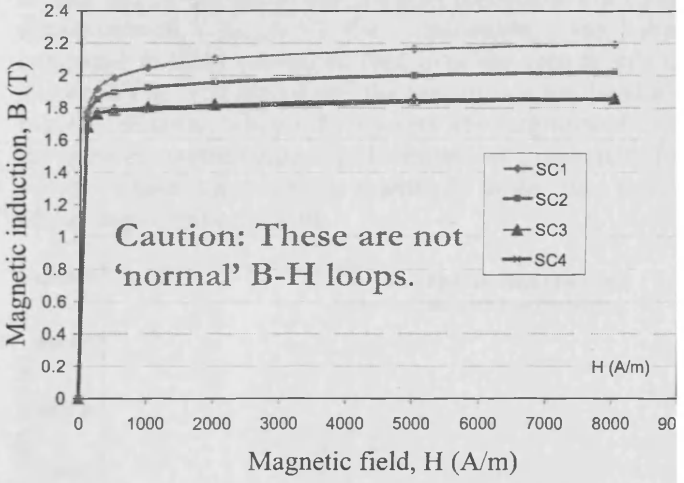

*Fig. 2: Flux density measurement, **B**, on miniature prototype core at various locations vs field values, **H**, obtained at 50Hz, using the 'standard' form of Ampere's law, at the coil, i.e. Eqn. 2.*

Fig. 2 shows the danger involved in obtaining B-H measurements in such situations. Different curves are obtained when the measurements are taken at different parts of the constructed prototype core. This is because the assumption of uniform mmf around the closed circuit is not

net. The magnetic field ***H*** is inhomogeneous around the closed path of the core, varying significantly from the prediction of Eqn. 2, and hence the ***H***-values calculated at the coil location are not the effective ***H***-values at the various search coils. This equation relates the average **H**-values produced by the current carrying conductor over the length of the solenoid, but accounts neither for the finite dimensions of most practical solenoids, nor the geometric effects of the core on the field distribution. Thus, magnetic field values at some parts of the core can drop to less than 1% of their peak value between the magnetized and un-magnetized limbs. An FEM model to illustrate this was also constructed as shown in Fig. 1. These measurements and simulations on the prototype reveal the inadequacy of the usual formula, which will apply to all other ferromagnetic cores of similar configuration.

A proposed alternative to accurately calculate the effective magnetic field at a particular location of a core becomes essential, given the errors that can arise for the primary B-H loop measurements and also for derived or secondary measurements like inductance.

IV. AMPERE'S LAW GENERALISATION PROCEDURE

In order to overcome the problem, we suggest the formula based on a combination of measurements and modeling to make up the procedure to provide a better solution, especially at high fields and flux densities where the shortcomings of Eqn. 2 are more prominent. The first step of the procedure entails obtaining accurate closed circuit measurements for the core material, up to the maximum attainable magnetic field, **H**, available. DC measurements following the IEC 60404-2 Epstein standard using a 2T Epstein frame tester, with maximum achieved field at about 15kA/m. The BH information obtained herein was then incorporated into FEM and H-field distribution profiles were obtained over a large range of current values around the core (0-25kA). Calculation of field distributions were made, starting from the middle of the magnetized limb and tracing the displacement, x, around the core to an arbitrary point of interest, x_{Ref}, along the core length (for this case, taken as the midpoint of the unmagnetized limb due to symmetry, as shown in Fig.1).

Beginning from the field distribution of a locally magnetised ferromagnetic bar, an assumption is made that a similar distribution will hold if the ends of such a core were magnetically closed to form a closed circuit. This assumption is validated by FEM calculated results around the simulated core.

This assumption is core-specific and would need to be mathematically transformed to represent more complex core structures. For this purpose, the closed core is to be then transformed conformally as those for non-uniform media, since both structures are planar (z-direction potentials are unchanged) and the analytic function is well-behaved [6].Therefore, the edge or fringing effects are to be accounted for by a differential analytical function, which is introduced into the proposed Ampere's law extension as a shape function The H-I graph which results from this transformation, can then plotted alongside the prediction based on Ampere's law derivation function for the same current value range. Fig. 3 shows the plot for the simplistic core used in our prototype with the shape function assumed as unity..

The hypothesis for the method is that the field is better calculated with the analytic solution for a finite solenoid extension of Ampere's equation [7], to compare with the field profile around the whole core is now considered. The equation solves for the magnetic field, H, due to the finite solenoid at a distance x from the centre of the solenoid. It also takes into consideration the solenoid characteristic like height, L, diameter and number of turns.

Fig . 3 shows great agreement of the values for such a core calculated by FEM over a large current and field range (used to investigate large applicability of the function).

$$H=\frac{NI}{L}\left[\frac{(L+2x)}{2\sqrt{D^2+(L+2x)^2}}+\frac{(L-2x)}{2\sqrt{D^2+(L-2x)^2}}\right]*f_{shape}(x) \quad (4)$$

where D is the diameter of the magnetizing coil, L is the length of the solenoid, x is the displacement around the core mapped into a linear distance equivalent to the path length l.

The shape function $f_{shape}(x)$ (which is equivalent with the conformal function **w**) is introduced to allow for the effect of the shape and fringe effects of the core on the field as transcribed by the conformal mapping procedure. For a first approximation, $f_{shape}(x)$=1.The expression was then compared to FEM calculated data over the core profile as shown in Fig. 3. It shows that the assumption for the shape function as unity, while offering very good agreement over the general current range, can be improved , especially for devices whose cores operate essentially at the knee point of the magnetisation curves.

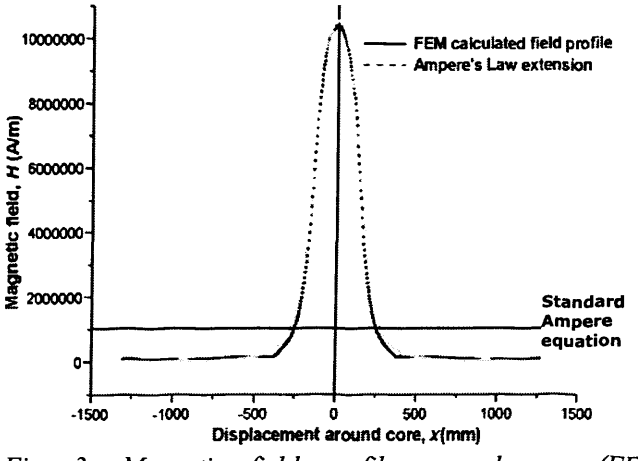

Fig. 3: Magnetic field profile around core (FEM calculated) compared to the new generalised Ampere law extension (Eqn. 4) and the standard Ampere's law equation (Eqn 2).

Furthermore, at the reference point x_{Ref}, a linear dependence of field H, on current I, was obtained by fitting our proposed linear extension equation (Eqn. 4) to H-field values produced over a large range of current values.

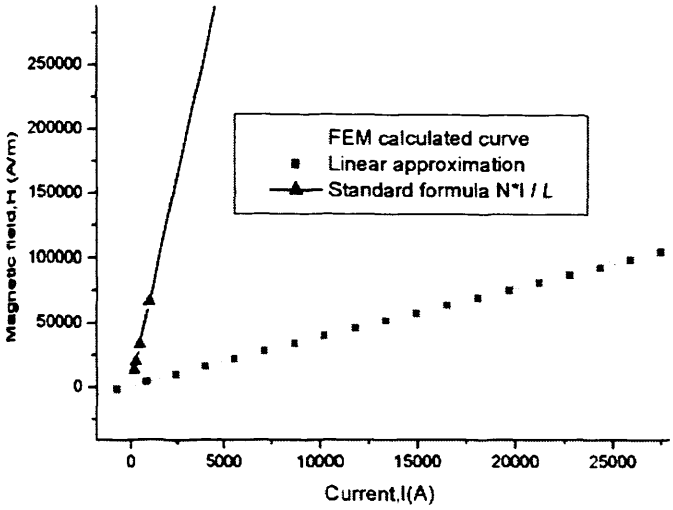

Fig. 4: New generalized linear extension (Eqn.4) fitting for H-I data contrasted with standard Ampere's derivation (Eqn.2) results for H-field values (FEM calculated) over large coil current range.

The agreement shown in Fig.3 between FEM-calculated values and Eqn. 6, proves not only how consistently the new generalised equation models the field distribution over a large amount of current values, but also the difference between the calculated values and the usual ampere's law derivation equation (Eqn. 2).

Fig. 4 shows the FEM generated field distribution profile of the core, compared to the Ampere's law equation and the modified equation derived in Eqn 4. It confirms the fact that the ampere's law extension can be used for a larger range of field values – from low to high fields –with more accuracy than the original ampere's law equation. The accuracy of this modified analytic expression is much improved over the usual ampere's law formulation, and cuts down on the time resources needed for magnetic field computations using complex FEM analysis. Furthermore, the edges of both graphs show that our first approximation of the shape function as unity, though good, has room for improvement.

This makes the analytic function adaptable, accurate and applicable to various specific core geometries. An analytic function with such a high level of accuracy in predicting the field distribution on a closed core can easily be incorporated into larger system modelling. Analytic formulations such as this are model/problem-specific, but the approach can be extended to other core models, and is certainly faster than relying on FEM calculations.

CONCLUSION

The usual 'standard' Ampere's Law derivation used fo calculation of magnetic fields **H** in magnetic circuits, is nc accurate enough for calculations or modeling for device which depend on non-linear properties of magneti materials at high magnetic fields and with non-uniforr mmf. A combination of measurement and modelin methods was used to provide a solution to this proble especially at high fields and flux densities, where th equation's shortcomings are most prominent. The analyti approximation derived here - which adds a model-specifi dimension to the much used standard Ampere's la equation, along with precise material measurement data provides better accuracy for field calculations and devic design in the high field regime. The calculations describe above were formulated for a specific example but ar extendable to other core designs, and give fast and accurat results which are needed in many applications.

REFERENCES

[1] K. Boughrara, R. Ibtiouen, O. Touhami, "*Numerica Analysis of Brushless Permanent Magnet Motors usin Lagrange Multiplier*", Industrial Electronics Society, 2005 IECON 2005, 32nd Annual Conference of IEEE, 6-1(Nov. 2005, pp. 2575-2578.

[2] Peter Virtic, Peter Pisek, Tine Marcic, Miralen Hadziselimovic, Bojan Stumberger, *"Analytical Analysi of Magnetic Field and Back Electromotive Force Calculation of an Axial-Flux Permanent Magne Synchronous Generator With Coreless Stator*", IEEE Trans Magn., Vol. 44, NO. 11, Nov 2008.

[3] N. Takahashi, S. Miyabara, K. Fujiwara, "*Problems ir practical finite element analysis using the Preisach Hysteresis mode",* IEEE Trans. Magn., Vol. 35 (3),Pg 1243-1246 1999.

[4] D.C. Jiles, C.C.H. Lo, "*The role of new materials in the development of magnetic sensors and actuators", Sensors and actuators* A 106, 2003, pg. 3-7.

[5] R. Bansal,"*Fundamentals of engineering electromagnetics*", CRC press, 2006, Chapter 3.

[6] Stan Zurek, Faris Al-Naemi, and Anthony J. Moses," *Finite-Element Modelling and Measurements of Flux and Eddy Current Distribution in Toroidal Cores Wound From Electrical Steel*", IEEE Trans. Magn., Vol. 44, NO. 6, June 2008

[7] F. Fiorillo, "*Measurement and characterization of magnetic materials*", Elsevier Academic press, 2004, Chapter 2.

[8] Roland Schinzinger, Patricio A., A.Llaura,"*Conformal mapping: Methods and Applications"*, Dover Publications, 2003, Chapter 6, pg 186.

[9] D.C. Jiles, "*Introduction to magnetic materials*", Chapman & Hall, 1998, Chapter 1, Pg 25.